

THÈSE

En vue de l'obtention du

DOCTORAT DE L'UNIVERSITÉ DE TOULOUSE

Délivré par :

Institut National Polytechnique de Toulouse (Toulouse INP)

Discipline ou spécialité :

Génie des Procédés et de l'Environnement

Présentée et soutenue par :

Mme CHLOÉ GUZELOT

le mercredi 7 décembre 2022

Titre :

Etude de systèmes auto-assemblés à base de tensioactifs commerciaux non-ioniques non-polymérisables: application à la synthèse de matériaux membranaires polymères réticulés nanoporeux

---

Ecole doctorale :

Mécanique, Energétique, Génie civil, Procédés (MEGeP)

Unité de recherche :

Laboratoire de Génie Chimique (LGC)

Directeur(s) de Thèse :

M. JEAN-CHRISTOPHE REMIGY

M. JEAN-FRANÇOIS LAHITTE

Rapporteurs :

M. DENIS BOUYER, UNIVERSITE DE MONTPELLIER

M. PATRICK GUENOUN, UNIVERSITE PARIS-SACLAY

Membre(s) du jury :

M. PATRICE BACCHIN, UNIVERSITE TOULOUSE 3, Président

M. DAMIEN QUEMENER, UNIVERSITE DE MONTPELLIER, Membre

M. JEAN-CHRISTOPHE REMIGY, UNIVERSITE TOULOUSE 3, Membre

M. JEAN-FRANÇOIS LAHITTE, UNIVERSITE TOULOUSE 3, Membre

M. KEVIN ROGER, TOULOUSE INP, Invité(e)

MME BARBARA LONETTI, UNIVERSITE TOULOUSE 3, Membre

MME MARTINE MEIRELES-MASBERNAT, UNIVERSITE TOULOUSE 3, Invité(e)

MME VÉRONIQUE RATAJ-NARDELLO, Université de Lille, Membre

Abstract

Membrane performances in liquid filtration are characterised by the permeability and selectivity of the material. However, the classical techniques for membrane synthesis are unable to combine both a high permeability and a good selectivity. Composite membranes have therefore been investigated to further improve membrane filtration. The present research project focuses on the manufacture of a nanostructured polymer material for deposition as a thin-film coating on supporting membranes.

To that end, acrylate monomer self-assembled systems were synthesised using commercial non-ionic non-polymerisable surfactants. The microstructure of these monomer systems was investigated by determination of birefringence, as well as by conductimetric, NMR-PGSE and SAXS analyses. Few interesting formulations were subsequently polymerised, using three different initiation methods (chemical and photochemical processes). We evidenced that, depending on the formulation and the initiation method, the resulting polymer structure can actually be nanoporous and interconnected – but will however differ from the monomer structure. We have thus highlighted the crucial impact of the initiation method on the polymer structure. Finally, we investigated the permeabilities of the synthesised materials and carried out some preliminary work on their deposition as thin-film on supporting flat-sheet membranes.

A last axis of this research work presents the numerical simulation of the dip-coating process of bicontinuous microemulsions on hollow-fibre membranes. We evidenced the difficulty to achieve thin microemulsion coatings without causing a capillary penetration phenomenon prior to polymerisation, and thus without impacting on the homogeneity of the deposit as well as the composite permeability.

Globally, this research project reported experimental conditions to achieve a nanoporous interconnected cross-linked material from a self-assembled system stabilised by non-ionic non polymerisable surfactants. Subsequent work is needed to precisely determine the experimental performance of the resulting polymeric materials, which may *a priori* exhibit atypical elastic properties under the application of water pressure.

Keywords: *bicontinuous structure, cross-linked polymer membrane, dip-coating process, nanoporous material, non-polymerisable surfactants, self-assembled system*

Résumé

La performance des membranes pour la filtration liquide est caractérisée par la perméabilité et la sélectivité du matériau. Cependant, il est impossible à l'heure actuelle de synthétiser un matériau polymère présentant à la fois une forte sélectivité et une perméabilité élevée. Pour contrer ce problème, la synthèse de membranes composites a été étudiée. Le projet de recherche présenté dans ce manuscrit se concentre sur la fabrication d'un matériau polymère nanostructuré et poreux pour le dépôt de couche-minces à la surface de membranes supports.

Pour ce faire, des systèmes de monomères acrylates auto-assemblés à base de tensioactifs commerciaux non-ioniques et non-polymérisables ont été synthétisés. L'identification de la structure des solutions de monomères a été réalisée par détermination de la biréfringence, ainsi que par analyses conductimétrique, RMN-PGSE et SAXS. Plusieurs systèmes auto-assemblés ont été ensuite été sélectionnées pour polymérisation. Différentes méthodes de polymérisation (chimique et photochimique) ont été employées afin de transformer cette structure monomère, en un réseau polymère interconnecté nanoporeux. Si l'obtention de ce réseau a été prouvée, ce dernier reste tout de même différent de la structure initiale. Nous avons également démontré que le choix de la méthode de polymérisation est crucial, car il impacte l'évolution de l'interface de tensioactifs, et donc la microstructure, au cours de la polymérisation. Les performances membranaires des matériaux synthétisés ont ensuite été évaluées théoriquement et expérimentalement à l'aide de mesures de perméabilité à l'eau.

Enfin, une dernière partie de ce travail de recherche consiste en la simulation numérique du procédé d'enduction de microémulsions bicontinues sur membranes fibres creuses par procédé dip-coating. Nous avons mis en évidence la difficulté de réaliser des dépôts de microémulsions sur des membranes poreuses, sans entraîner un phénomène de pénétration capillaire préjudiciable à l'homogénéité et la perméabilité de la membrane composite.

De manière générale, ce projet de recherche a permis de déterminer les conditions expérimentales pour la synthèse d'un réseau polymère interconnecté nanoporeux réticulé à partir de de structures auto-assemblées stabilisées par des tensioactifs commerciaux non-ioniques et non-polymérisables. Des travaux futurs sont nécessaires pour déterminer avec précision les performances expérimentales des matériaux polymères obtenus, pouvant *a priori* présenter des propriétés élastiques atypiques sous l'application d'une pression d'eau.

Mots-clés: *matériau nanoporeux, membrane polymère réticulée, procédé dip-coating, structure auto-assemblée, structure bicontinue, tensioactifs non-polymérisable*

Contents

ABSTRACT I

GLOSSARY IX

GENERAL INTRODUCTION 1

CHAPTER 1 – BIBLIOGRAPHIC STUDY 7

1.1 ORGANISED SURFACTANT-BASED SYSTEMS 11
1.1.1 Colloidal and (micro-)emulsified systems 11
1.1.2 Liquid crystal systems 13
1.1.3 Modification of the surfactant interface 16
1.2 STRUCTURAL CHARACTERISATION OF SURFACTANT-BASED ORGANISED SYSTEMS 24
1.2.1 Characterisation of liquid crystals 25
1.2.2 Characterisation of microemulsions 27
1.3 POLYMERISATION OF NANOSTRUCTURED POLYMER NETWORKS 35
1.3.1 RedOx polymerisation 35
1.3.2 UV polymerisation 36
1.4 MEMBRANES FOR LIQUID AND GAS FILTRATION 39
1.4.1 Operating principles 39
1.4.2 Membrane classification 40
1.4.2.1 Filtration range 40
1.4.2.2 Membrane porosity 41
1.4.2.3 Membrane materials 41
1.4.2.4 Membrane module geometry 42
1.5 MEMBRANE SYNTHESIS FROM SURFACTANT-BASED ORGANISED TEMPLATES 44
1.5.1 Synthesis of membrane materials from monomer microemulsions 44
1.5.2 Synthesis of membrane materials from monomer liquid crystals 52
1.6 CONCLUSION 60
REFERENCES 61

CHAPTER 2 – MATERIAL AND METHODS 77

2.1 MATERIAL 81
2.1.1 Monomers and cross-linker 81
2.1.2 Non-ionic surfactants 82
2.1.3 Initiators 82
2.1.4 Oxygen scavengers 83
2.1.5 Organic solvents 83
2.1.6 Membranes 83
2.2 METHODS 84

2.2.1 Polymerisation of the microemulsion 84
2.2.2 Surfactant removal and polymer cleaning 85
2.3 ANALYSIS 86
2.3.1 Elaboration of pseudo-ternary phase diagrams 86
2.3.2 Temperature monitoring UV-light 89
2.3.3 Contact angle determination 89
2.3.4 Small Angle X-ray Scattering (SAXS) 89
2.3.5 Scanning Electron Microscopy (SEM) 90
2.3.6 Cryo-scanning Electron Microscopy (Cryo-SEM) 91
2.3.7 Attenuated Total Reflectance Fourier-Transform Infrared Spectroscopy (ATR-FTIR). 91
2.3.8 Water permeability 92
REFERENCES 93

CHAPTER 3 – ELABORATION OF PSEUDO-TERNARY PHASE-DIAGRAMS OF THE MONOMER SYSTEMS BY SAXS AND DOSY-NMR ANALYSES 95

3.1 INTRODUCTION 99
3.2 SYSTEM COMPOSITION 100
3.3 NON-IONIC QUATERNARY SYSTEM INVESTIGATION 102
3.3.1 Elaboration of the pseudo-ternary phase diagrams 102
3.3.2 Impact of the co-surfactant on the microstructure of the system 107
3.4 NON-IONIC QUINARY SYSTEMS INVESTIGATION 110
3.4.1 Elaboration of the pseudo-ternary phase diagrams 110
3.4.2 Evolution of the microstructure upon water dilution 113
3.5 CONCLUSION 125
REFERENCES 129

CHAPTER 4 – POLYMERISATION AND CHARACTERISATION OF SELF-ASSEMBLED SYSTEMS STABILISED BY NON-POLYMERISABLE SURFACTANTS 135

4.1 INTRODUCTION 139
4.2 COMPLETE CASE STUDY: $(21:23:56)_{62:19:19}$ COMPOSITION 140
4.2.1 Polymer microstructure characterisation 141
4.2.2 Membrane performances 157
4.3 INVESTIGATION OF $(46:8:46)_{62:19:19}$ AND $(46:8:46)_{33:33:33}$ COMPOSITIONS 174
4.3.1 Microstructure of the polymer depending on the initiation method 174
4.3.2 Analysis of the $(46:8:46)_{62:19:19}$ UV-TQ150 sample 178
4.4 CONCLUSION 182
REFERENCES 186

CHAPTER 5 – MICROEMULSION DIP-COATING ON HOLLOW-FIBRE MEMBRANE: AN INDUSTRIAL PROSPECT? 193

5.1 INTRODUCTION 197
5.2 DESCRIPTION OF THE DIP-COATING PROCESS FOR HOLLOW-FIBRE MEMBRANES 198
5.3 MODELS OF FLUID DEPOSITION ON FIBRES 200
5.3.1 Newtonians fluids coating 200
5.3.2 Complex surfactant-based solutions 203
5.4 SIMULATION OF HOLLOW FIBRE COATING - APPLICATIONS TO MICROEMULSIONS ON MF-PES (MICROPES™) AND UF-PS (ZEEWEED™) HOLLOW-FIBRES 210
5.4.1 Operating conditions for the control of the deposited coating 211
5.4.2 Photopolymerisation of the monomer microemulsified coating 215
5.4.3 Coating perturbation after deposition on the fibre 219
5.4.4 Efficiency of the dip-coating process for microemulsions 233
5.5 CONCLUSION 236
REFERENCES 240

GENERAL CONCLUSIONS AND PERSPECTIVES 245

APPENDICES I

APPENDIX 1 – TECHNICAL DATA SHEET OF THE MICROPES™ TYPE 2F FLAT-SHEET MEMBRANE V
APPENDIX 2 – EMISSIVITY SPECTRA OF UV LAMPS USED IN THE LABORATORY VI
APPENDIX 3 – TUNING OF THE POROUS MATERIAL PROPERTIES: A NON-EXHAUSTIVE SURVEY OF THE POLYMERISATION OPERATING PARAMETERS VII
3.1 Oxygen elimination prior to polymerisation VIII
3.2 UV-initiation parameters XII
3.3 Polymer washing parameters XIV
APPENDIX 4 – EVOLUTION OF THE MICROSTRUCTURE OF THE ACRYLATE MONOMER SYSTEM UPON MMA:SURFACTANT PHASE DILUTION XVIII
APPENDIX 5 – TECHNICAL DATA SHEETS OF HOLLOW-FIBRE MEMBRANES DISCUSSED AS PART OF THE NUMERICAL SIMULATION XXII

Glossary

Symbols

a_{min}	Minimum surface area of the surfactant head-group	m^2
a_o	Surface area of the surfactant head-group	m^2
A	Acid number of the fatty acid	-
A_2, C_1, C_2	Constants	-
B	Scattering background	-
Bo	Bond number	-
c	Surfactant volume concentration	$mol.L^{-1}$
C_{ST}	Molar concentration of the surfactant	$mol.L^{-1}$
Ca	Capillary number	-
Ca_ϕ	Capillary number threshold	-
d	Teubner-Strey periodicity	Å
$d_{colloid}$	Colloid particle diameter	m
d_m	Molecular size	m
D	Chemical self-diffusion coefficient	$m^2.s^{-1}$
D_0	Chemical self-diffusion coefficient in pure liquid	$m^2.s^{-1}$
E	Weight percent of ethoxy functions	wt.%
$E_{surfactant-oil}$, $E_{surfactant-aqueous}$	Interactions of the surfactant film with the organic and aqueous phases	-
f_a	Amphiphilicity factor	-
g	Gravitational acceleration	$m.s^{-2}$
g_m	Magnetic gradient strength	$kg.C^{-1}.s^{-1}$
Ma	Marangoni number	-
h_0^*	Minimum coating thickness to avoid Plateau-Rayleigh instability	m
h_0	Liquid coating thickness	m
h_c	Thickness at which the liquid flattens out under the effect of gravity	m
h_m	Membrane thickness	m
$h_{reservoir}$	Liquid reservoir height	m
h_{HV}	Thickness of the sol-gel coating obtained at high speed	m

h_{LV}	Thickness of the sol-gel coating obtained at low speed	m
H_I, H_{II}	Normal and inverted hexagonal structure	-
I	Signal intensity	cm^{-1}, UA
I_0	Unattenuated signal intensity	cm^{-1}, UA
I_I, I_{II}	Normal and inverted discontinuous cubic structure	-
I_{UV}	UV irradiance	$W.m^{-2}$
J_0	Evaporative flux	$kg{\cdot}m^{-2}{\cdot}s^{-1}$
J_{20}	Permeate volume flow at 20°C	$m^3.m^{-2}.s^{-1}$
J_T	Permeate volume flow at temperature T	$m^3.m^{-2}.s^{-1}$
k_B	Boltzmann constant	$kg.m^2.s^{-2}.K^{-1}$
$k_p.\xi$	Polydispersity factor	-
l_c	Capillary length	m
l_h	Length of the hydrophobic tail of the surfactant	m
l_S	Effective length of the surfactant	m
L	Lamellar structure	-
L_3	Sponge phase	-
L_{cap}	Capillary penetration of the liquid	m
L_d	Droplet size	m
L_0, L_i	Dimension of the material for an applied stress	m
L_{P20}, L_{P25}	Water permeability at 20°C and 25°C	$m^3.m^{-2}.s^{-1}.bar^{-1}$
L_{UV}	Length of the UV module	m
m	Mass of compound	kg
M_w	Molecular weight of a compound	$g.mol^{-1}$, Da
n	Number of carbon in the hydrophilic tail of the surfactant	-
N_a	Avogadro number	mol^{-1}
ΔP	Applied pressure	bar
P	Weight percent of polyol functions	wt.%
P(q)	SAXS form factor	-
P(%)	Lamp power	%
q	SAXS scattering vector	$Å^{-1}$
q_{UV}	UV dosis	$J.m^{-2}$
Q_I, Q_{II}	Normal and inverted bicontinuous cubic structure	-
Q	Volumetric flow rate of liquid	$m^3.s^{-1}$

$r_{dewetting}$	Dry-zone radius during dewetting	m
r_{fibre}	Hollow-fibre radius	m
r_m	Pore radius	m
r_{hydro}	Hydrodynamic radius of a suspended particle	m
$r_{reservoir}$	Liquid reservoir radius	m
R	Ideal gas constant	$J.K^{-1}.mol^{-1}$
R_m	Retention coefficient	-
R_W	Winsor ratio	-
S	Membrane surface	m^2
S_p	Number of ester saponification	-
S(q)	SAXS structure factor	-
Δt	Duration	s
T	Temperature	K
v_{fibre}, $v_{substrate}$	Hollow-fibre/substrate velocity	$m.s^{-1}$
V_i^*	Critical divergence speed	$m.s^{-1}$
V_e^*	Critical liquid expulsion droplets speed	$m.s^{-1}$
V_o	Volume of the hydrophobic tail of the surfactants	m^3
V_P	Dry volume of the sample	m^3
We	Weber number	-
x_∞	Meniscus radius	m

Greek letters

α	Thickening factor	-
β	Coordination number for aqueous and organic phases	-
β′	Coordination number of the surfactant molecules	-
γ	Surface tension	$N.m^{-1}$
γ_{LV}	Surface energy at the liquid-vapour interface	J
γ_{SL}	Surface energy at the solid-liquid interface	J
γ_{SV}	Surface energy at the solid-vapour interface	J
γ_m	Gyromagnetic ratio of the observed nucleus	-
Γ_{max}	Surface excess concentration	$mol.m^{-2}$

δ	Deformation of a material under stress	m
δ_m	Length of the magnetic gradient	s
Δ_m	Diffusion time	s
Δ_{ρ^2}	SAXS contrast of the sample	$Å^{-2}$
ϵ	Strain	-
η	Dynamic viscosity	Pa.s
θ	Liquid-solid contact angle	°
θ_D	Dynamic contact angle	°
θ_E	Static contact angle	°
θ_S	Static meniscus angle	°
θ_{SAXS}	SAXS scattering angle	°
κ_C	Curvature rigidity of the surfactant film	$kg.m^2.s^{-2}$
κ_{SANS}	Renormalized bending elastic constant	$kg.m^2.s^{-2}$
λ	Wavelength	m
ν	Poisson's ratio	-
ν^*	Intrinsic velocity	$m.s^{-1}$
ξ	Teubner-Strey correlation length	Å
ρ	Density	$kg.m^{-3}$
σ	Electric conductivity	$S.m^{-1}$
σ_c	Compressive stress	MPa
τ	Relaxation time	s
τ_{PR}	Plateau-Rayleigh instability characteristic duration	s
ϕ_i	Volume fraction of particles i	-
ϕ_m	Maximum filling ratio of the particle stack in the suspension	-
Φ_V	Volume fraction of the dispersed particles	-

Abbreviations

AA	Acrylic acid
AIBN	Azobisisobutyronitrile
AIPS	3-((11-acryloyloxyundecyl)imidazolyl) propyl sulfonate
APS	Ammonium persulfate

ATR-FTIR	Attenuated Total Reflectance – Fourier-Transform InfraRed spectroscopy
AUDMAA	(((Acryloyloxy)undecyl)dimethylammonio)acetate
AUTEAB	((Acryloyloxy)undecyl)triethylammonium bromide
AUTMAB	((Acryloyloxy)undecyl)trimethylammonium bromide
CMC	Critical Micellar Concentration
CPP	Critical Packing Parameter
Cryo-SEM	Cryo-Scanning Electron Microscopy
CTAB	Cetyltrimethylammonium bromide
C_nTAB	n-Alkyltrimethylammonium bromide
DBK	DiBenzyl Ketone
DDAB	Dimethyldidodecylammonium bromide
DMAEMA	2-(Dimethylamino)ethyl methacrylate
DMPA	2,2-dimethoxy-2-phenylacetophenone
DOSY	Diffusion Ordered SpectroscopY
DSC	Differential scanning calorimetry
DTAB	Dodecyltrimethylammonium bromide
EGDMA	Ethylene glycol dimethacrylate
FEG-SEM	Field Emission Gun – Scanning Electron Microscope
FF7	Bruggolit 7
GIFT	Generalised Indirect Fourier Transformation
HEMA	2-hydroxyethyl methacrylate
HLB	Hydrophilic-Lipophilic Balance
HMP	2-Hydroxy-2-méthylpropiophenone
HPF	High-pressure freezing
iCVD	Initiated Chemical Vapor Deposition
IR	InfraRed
LED	Light-Emitting Diode
LC	Liquid Crystal
LLC	Lyotropic Liquid Crystal
TLC	Thermotropic Liquid Crystal
LGC	Laboratoire de Génie Chimique (Toulouse)
MAA	Methacrylic acid
MF	Microfiltration

MMA	Methyl methacrylate
MWCO	Molecular Weight Cut-Off
NA11-EAAU	11-(N-ethylacrylamido)undecanoate
NF	Nanofiltration
NMR	Nuclear Magnetic Resonance
O/W	Oil in Water emulsion
RO	Reverse Osmosis
LLD	Landau-Levich-Derjaguin
PEO	Poly(ethylene oxide)
PEO-R-MA-40	ω-Methoxy poly(ethylene oxide)$_{40}$ undecyl-α-methacrylate
PES	PolyEtherSulfone
PSU	PolySUlfone
PUD	Potassium 10-undecenoate
PVDF	PolyVinyliDene Fluoride
SANS	Small Angle Neutron Scattering
SAXS	Small Angle X-ray Scattering
SDS	Sodium Dodecyl Sulfate
SEM	Scanning Electron Microscopy
SFS	Formaldehyde sulfoxilate
SLD	Scattering Light Density
TBHP	Tert-butyl hydroperoxide
TEA	Triethylamine
TEOA	Triethanolamine
TEM	Transmission Electron Microscopy
TMEDA	Tetramethylethylenediamine
UF	Ultrafiltration
UP	UltraPure
UV	Ultraviolet
W/O	Water in Oil emulsion
WI, … , WIV	Winsor 1, Winsor 2, Winsor 3, Winsor 4
XRD	X-Ray Diffraction

General introduction

Membrane performances are characterised by two main properties: its permeability – how much liquid or gas can go through the membrane per unit of time, pressure and surface – and its selectivity – how good particles of defined size can be retained by the membrane. Unfortunately, usual phase inversion techniques cannot be used to manufacture a membrane with both a good permeability and a high selectivity. A possibility to overcome this problem is to deposit a selective thin-film on a highly permeable supporting membrane. This support allows the newly formed composite membrane to exhibit both high mechanical resistance and high permeability, while the deposited thin-film increases the composite selectivity.

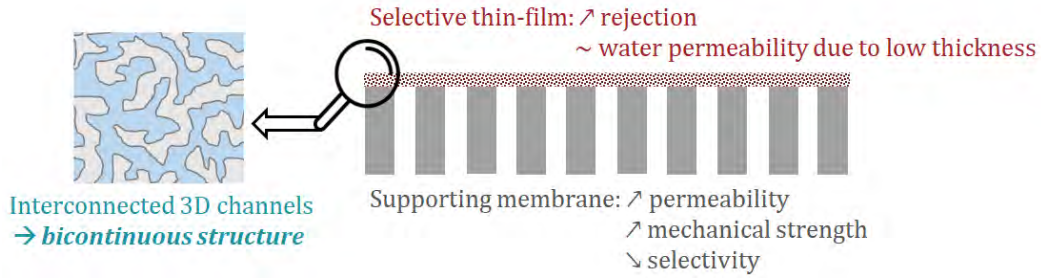

Figure I.1 – Schematic representation of the composite membrane developed in this research project.

In the context of this work, we will only focus on the synthesis of bicontinuous nanostructured polymer thin-film, and more specifically to the polymer templated from microemulsion and liquid crystal nanostructures, cf. Figure I.1. The synthesis of bicontinuous polymer structures have been widely investigated the last three decades and proven successful when polymerisable surfactants are used to bring structuration to the system. These compounds, however, are expensive to produce and the process is difficult to scale up. In order to counteract this problem, systems based on non-polymerisable surfactants have been investigated. However, the inability to immobilise these compounds into the forming polymer network led to the modification of the system microstructure during polymerisation. Therefore, at present time only few non-polymerisable surfactant systems have been proven usable.

The present project is a continuation of the work carried out by our research team in the Laboratoire de Génie Chimique (Toulouse, France). A non-ionic microemulsion based on a non-polymerisable surfactant mix has proven to result in a bicontinuous nanometric structure, which would meet the criteria to be good candidate as a bicontinuous nanostructured polymer thin-film. The present research aims to study this formulation and to investigate the mechanisms leading to the obtention of a bicontinuous polymer nanostructure upon polymerisation of a microemulsion stabilised by a non-ionic, non polymerisable, commercial surfactant mix.

The present manuscript is organised as follows:

Chapter 1 describes the state of art of membrane synthesis using surfactant-based self-assembled monomer systems. A specific attention will be paid to the membrane performances resulting from microemulsion and liquid crystal templating presented in the literature. The various characterisation techniques used to investigate such systems will then be presented.

Chapter 2 presents the materials and methods used as part of this project to formulate, polymerise and characterise the nanostructured polymers from surfactant-based systems.

Chapter 3 focuses on the characterisation of monomer systems prior to polymerisation. The investigation of various compositions formulated with an equimassic mix of the Synperonic™ A11 and Tergitol™ 15-S-12 non-ionic, non-polymerisable commercial surfactant mix has led to the identification of liquid crystal as well as non-birefringent transparent solutions, whose microstructure will be discussed.

Chapter 4 then addresses the evolution of a few selected self-assembled monomer samples upon polymerisation. Several polymerisation initiations have been investigated and based on the resulting characterisation of the membrane, the accuracy of each method is discussed. The possibility to synthesise a bicontinuous nanometric structure to enhance the performances of membrane filtration by polymerisation of a monomer self-assembly formulated with non-polymerisable surfactant is then assessed.

In Chapter 5, the application of one bicontinuous monomer formulation to the dip-coating of hollow-fibre membranes is reported. A numerical simulation is conducted to predict the outcome of the dip-coating process, depending on the operating conditions considered. The industrial prospects of microemulsion dip-coating and photopolymerisation are then reviewed based on our results.

Finally, we present a general conclusion of this research work and discuss some perspectives regarding the synthesis of composite membranes based on the deposition of a thin bicontinuous monomer template.

Chapter 1

Chapter 1 – Bibliographic study

CHAPTER 1 – BIBLIOGRAPHIC STUDY 7

1.1 ORGANISED SURFACTANT-BASED SYSTEMS 11
1.1.1 Colloidal and (micro-)emulsified systems 11
1.1.2 Liquid crystal systems 13
1.1.2.1 Hexagonal LC 14
1.1.2.2 Lamellar LC 15
1.1.2.3 Cubic LC 15
1.1.3 Modification of the surfactant interface 16
1.1.3.1 Surfactant 16
1.1.3.2 Co-surfactant 21
1.1.3.3 Aqueous phase 21
1.1.3.4 Organic phase 22
1.1.3.5 Temperature 23
1.2 STRUCTURAL CHARACTERISATION OF SURFACTANT-BASED ORGANISED SYSTEMS ... 24
1.2.1 Characterisation of liquid crystals 25
1.2.1.1 Cross- polarised light microscopy 25
1.2.1.2 X-ray diffraction 26
1.2.2 Characterisation of microemulsions 27
1.2.2.1 Conductivity 27
1.2.2.2 Diffusion Ordered Spectroscopy (DOSY) 28
1.2.2.3 Small Angle X-ray Scattering (SAXS) 31
1.3 POLYMERISATION OF NANOSTRUCTURED POLYMER NETWORKS 35
1.3.1 RedOx polymerisation 35
1.3.2 UV polymerisation 36
1.4 MEMBRANES FOR LIQUID AND GAS FILTRATION 39
1.4.1 Operating principles 39
1.4.2 Membrane classification 40
1.4.2.1 Filtration range 40
1.4.2.2 Membrane porosity 41
1.4.2.3 Membrane materials 41
1.4.2.4 Membrane module geometry 42
1.5 MEMBRANE SYNTHESIS FROM SURFACTANT-BASED ORGANISED TEMPLATES 44
1.5.1 Synthesis of membrane materials from monomer microemulsions 44
1.5.2 Synthesis of membrane materials from monomer liquid crystals 52
1.6 CONCLUSION 60

REFERENCES 61

1.1 Organised surfactant-based systems

1.1.1 Colloidal and (micro-)emulsified systems

Colloidal systems are composed of insoluble particles dispersed in a continuous medium. These particles have a size between 10 nm and 1 µm. Both the dispersed and continuous medium can exist in the three different states of matter: gas, liquid and solid. Colloidal systems are used in numerous industrial applications, as presented in Table 1.1.

Table 1.1 – Colloidal system types and their common implementations [1].

Continuous medium	Dispersed phase	Common application
Gas	Liquid	Varnish
Gas	Solid	Pharmaceutical inhaler
Liquid	Gas	Fire extinguishing product
Liquid	Liquid	Margarine
Liquid	Solid	Paint
Solid	Gas	Zeolite
Solid	Liquid	Asphalt
Solid	Solid	Composite material

According to Stockes and Evans (1996) [1], colloidal systems originate from the Brownian motion of approaching dispersed particles which coalesce under the action of long-range attractive forces. This non-reversible phenomenon gives rise to dimers, which later spontaneously combine with one another to create agglomerates: the homogenous system then becomes polyphasic. De facto colloidal suspensions are thermodynamically unstable but can be kinetically stabilised by electrostatic and steric repulsive forces.

An emulsion is a colloidal system consisting of two immiscible liquids – an aqueous and an organic phase – randomly dispersed in solution and stabilised by the addition of a surfactant. This last compound possesses a hydrophobic tail and a hydrophilic

head-group, which allow its spontaneous adsorption onto the interface between the aqueous and organic phases, resulting in a decrease of the interfacial tension and therefore a stabilisation of the system [1], [2].

Above the critical micellar concentration (CMC), the interface becomes saturated with surfactants which self-organise into diverse microstructures to reach a lowest energy state, defined according to their amphiphilic geometry [3]. The rearrangement of the system results in a spontaneous emulsification phenomenon and the creation of numerous thermodynamically stable dispersed objects. Some surfactants do not lower the interfacial enough to reach a spontaneous emulsification and need the addition of an alcohol compound called a co-surfactant. This alcohol will further lower the interfacial tension of the interface and will allow the system to reach the targeted CMC. The surfactant usually represents at least 10 to 20 wt.% of the solution.

Depending on the size of the dispersed phase, two types of emulsions are to be distinguished: the microemulsions and the macroemulsions. The size of the dispersed phase is between 5 and 100 nm in the former, while it is above 100 nm in the latter [1], [2]. Due to this different ranges of size, microemulsions appear transparent to the human eye – the particle size being lower than the wavelength of visible light – while macroemulsions appear opaque. It is therefore quite easy to differentiate between macro- and microemulsions. These two types of emulsions are also different in terms of their properties and stability. Microemulsions are thermodynamically stable while the macroemulsions are only kinetically stable. The following bibliographic study only focus on microemulsions, to remain within the framework of this thesis work.

Hoar and Schulmann (1943) [4] are the first to bring to light the existence of microemulsions in 1943. This colloidal suspension will however be clearly identified and characterised 38 years later by Danielsson and Lindman (1982) [5]. Winsor (1947) [6] was the first to classify microemulsions according to their microstructure:

- **Winsor I (2) –** O/W systems: Biphasic system consisting of an organic phase with a low surfactant content and an aqueous phase comprising the majority of the surfactant with a small amount of organic phase structure in micelles.

- ⇨ **Winsor II ($\bar{2}$) –** W/O systems: Biphasic system consisting of an aqueous phase with a low surfactant content and an organic phase comprising the majority of the surfactant with a small amount of aqueous phase structure in micelles.
- ⇨ **Winsor III (3) –** triphasic systems: Triphasic system consisting of both aqueous and organic phases with low surfactant content and a third intermediate phase comprising most of the surfactant and small amounts of organic and aqueous compounds.
- ⇨ **Winsor IV (1) –** monophasic systems: Homogeneous single-phase solution whose structure can be bicontinuous depending on the various parameters impacting the solution microstructure.

Bicontinuous microemulsions present a zero mean-curvature of the interface, resulting in an interconnected structure of the two immiscible phases. Micellar structures in turn exhibit positive or negative radius of curvature, resulting in normal or inverse microstructures respectively [7].

1.1.2 Liquid crystal systems

The liquid crystal (LC) state – also called mesophase – is an intermediate state between liquid and solid crystal organisation. They possess solid crystalline characteristics, such as positional order and long-range orientation, but maintain at least one disordered spatial direction, which is typical of liquid solutions. One of the specificity of liquid crystals is the anisotropy of its tensorial properties (optical, dielectric, magnetic, mechanical, etc.) [8]. Even if several denominations can be used to describe the various LC conformations, the Luzzati's notation will be used in this manuscript.

Liquid crystals can be classified as a function of their structural ordination, as presented in Figure 1.1. If a long-range orientation order is obtained in the solution, but no long-range positional order, the liquid crystal is classified as nematic. Otherwise if the solution exhibit both long-range orientation and positional order in one spatial, the liquid crystal is classified as smectic and will contain a regular stacking of liquid layers. Finally, if a positional order in two spatial directions is observed, as well as a liquid order in the third spatial direction, the mesophase is classified as columnar and possesses a two-dimensional network of liquid tubes.

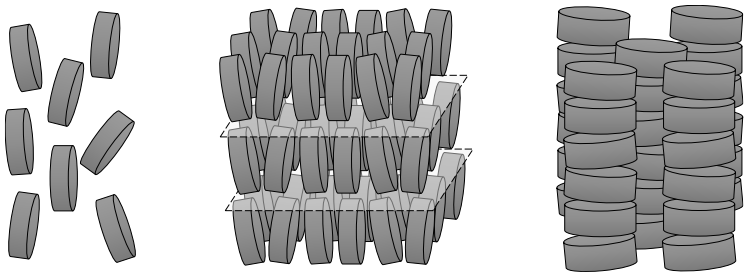

Figure 1.1 – Schematic representation of the various possible orders in the mesophases.

If the phase transitions of the mesophase are induced by variation of the temperature the solution is referred to as a thermotropic liquid crystal (TLC). If both the composition of the solution and its temperature are impacting the phase transitions, the solution is referred as a lyotropic liquid crystal (LLC). It is important to note that although LLCs result from the interactions of micelles at high surfactant concentrations, these mesophases are distinct from microemulsions and are by no means identical. Plus, some surfactants do not form microemulsions but liquid crystals [9].

1.1.2.1 Hexagonal LC

The hexagonal structure has only one axis of symmetry. Depending on the surfactant interface curvature (positive or negative), the structure is either normal or inverted. The normal hexagonal structure (H_I) is constituted of organic rod-shaped micelles assembled in a hexagonal lattice and separated by an aqueous medium. The inverted hexagonal structure (H_{II}) is constituted of aqueous rod-shaped micelles separated by an organic medium, cf. Figure 1.2 [10], [11], [12]. Normal hexagonal structures possess the ability to swell without significantly modifying the interfacial area per molecule, which is not the case for the inverted H_{II} structure.

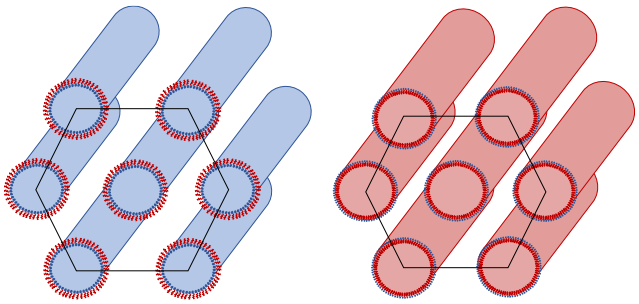

Figure 1.2 – Schematic representation of (left) an inverted hexagonal structure (H_{II}) and (right) a normal hexagonal structure (H_I).

1.1.2.2 Lamellar LC

Similarly to the hexagonal structures, lamellar LC structures only have one axis of symmetry. The surfactant interfaces exhibit a zero mean curvature and are arranged in a stack of bilayers separated by continuous, planar water networks, as presented in Figure 1.3. These bilayers can extend over long ranges – up to about a micrometre [11].

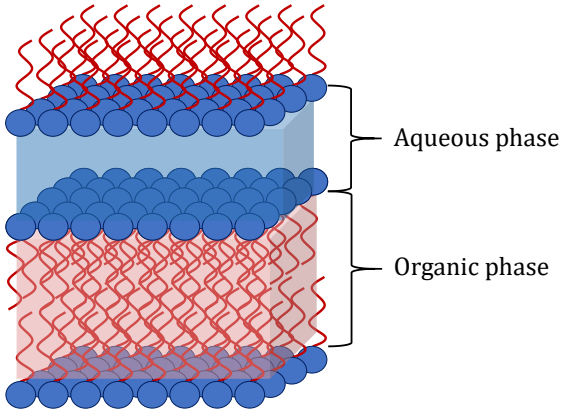

Figure 1.3 – Schematic representation of a lamellar structure (L).

1.1.2.3 Cubic LC

Cubic structures have four axes of symmetry and are mostly occurring as an isotropic viscous phase. Similarly to hexagonal structures, depending on the surfactant interface curvature, the structure is either normal or inverted. However, cubic structures can also be differentiated into bicontinuous (Q_I and Q_{II}) and discontinuous (I_I and I_{II}) structures, as depicted in Figure 1.4. Cubic structures are usually occurring as a narrow intermediate zone in composition and/or temperature, located between various domains of the phase diagrams [11], [13].

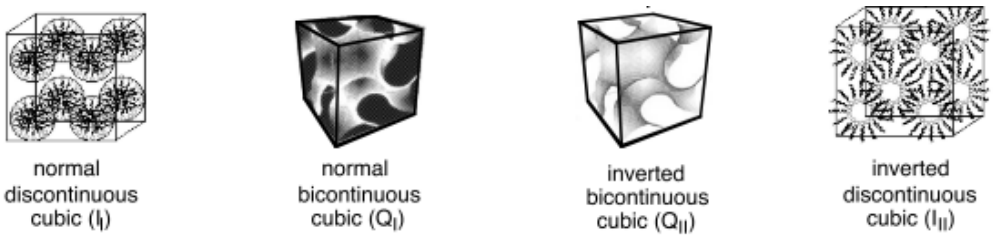

Figure 1.4 – Schematic representation of cubic I_I, Q_I, Q_{II} and I_{II} LLC. . Reprinted with permission from Zhou et al. (2007) [14]. Copyright 2007 American Chemical Society.

Cubic structures are the only liquid crystal structures which are optically isotropic – and thus non-birefringent under polarised light, [11], [13], and [14]. Plus, even if these

structures are usually highly viscous, fluid structures may occur depending on their conformation.

1.1.3 Modification of the surfactant interface

The surfactant interface of microemulsions and liquid crystals is the key factor dictating the microstructure adopted by the system. This interface can be affected by various elements, such as the composition of the surfactant-based solution or the temperature, as described in the following sections.

1.1.3.1 Surfactant

The surfactant is an amphiphilic molecule which lowers the interfacial tension between the organic and aqueous phase. Depending on its concentration in the system, this compound will give rise to a spontaneous and thermodynamically stable microemulsion. The choice of the surfactant – or mix of surfactants – is essential when formulating a microemulsion. This species controls a great number of attractive and repulsive interactions, which drive the flocculation and coagulation phenomena, and therefore the mechanical properties of the interfacial film and the coalescence rates [15]. Depending on the surfactant and its emulsifying capacity on a definite system, the surface tension of its interface might vary from several orders of magnitude [16].

Surfactants head group can either be ionic (anionic, cationic or zwitterionic) or non-ionic. Chieng et al. (1996) [17] and Peinado et al. (2006) [18] evidenced the impact of the surfactant ionic charge on a microemulsion by studying the stabilising power of both anionic and cationic surfactant on an identical system. While Gan reported higher pore size using an anionic surfactant (i.e. SDS) due to a higher interaction with monomers compared to the cationic surfactant (i.e. DTAB), Peinado highlighted a strong dependence of the self-acceleration of the phenomenon of polymerisation to the ionic charge of the surfactant when comparing SDS and CTAB. The variations due to the ionic charge of the polar head-group are related to a combination of several phenomena directly linked to the geometrical and chemical structure of the surfactant: its surface tension, bending strength and its spontaneous curvature [19]. Aveyard et al. (1986) [20] compared ionic and non-ionic surfactants by varying various factors including the length of the size of the oil molecules, the temperature and the electrolyte concentration. They evidenced that ionic and non-ionic surfactants with similar hydrocarbon tail possess a similar surface

tension. The ionic charge and size of the surfactant head-group however impact the system regarding the parameters modifying the phase inversion and the microstructure of the emulsion: non-ionic surfactants will be highly sensitive to temperature but not to concentration of the electrolyte, while ionic surfactants are sensitive to both parameters [19].

The number of hydrophobic tails and their length in a surfactant molecule impact on the spontaneous emulsification phenomenon, which can be hindered due to a too low curvature radius of the interface (e.g. no of co-surfactant and/or electrolyte solution for ionic surfactants or modification of the temperature for non-ionic surfactants). On the contrary, using a double-tailed usually dispenses with the need of a co-surfactant [1], [19], [21], [22]. Generally speaking, increasing the length of the tail favours lamellar structures while decreasing its length favours micellar dispersions and bicontinuous structures [19], [23], and [24]. Regarding the LLC structures, hexagonal lattices can be modified by modification of the length of the hydrocarbon tail – as well as the counter-ion type in case of ionic surfactant [10]. Plus, increasing or the number of hydrophobic tail, as well as its length, slightly decreases the temperature of occurrence of LLC [11].

As stated before, the LC structure is dictated by the curvature of the surfactant interface. Lamellar structures are the only liquid crystal structure to exhibit a zero-mean curvature. Hexagonal and cubic LCs can either have a positive curvature – resulting in normal structures – or a negative curvature – resulting in inverted structures. Zhou et al. (2007) [14] summarised the ideal evolution of the structure of a LLC system depending on the curvature of the interface, when increasing the water content (cf. Figure 1.5).

One must however note that not all surfactant-based systems can give rise to liquid crystal structures. Such structures can be obtained for high surfactant concentration, when the amount of energy required to bring together the micelles is sufficient to obtain a conformation extending over one (hexagonal), two (lamellar) or three spatial dimensions (bicontinuous cubic) [25]. Liquid crystals can also occur at lower surfactant concentration, if the osmotic pressure of the system is increased, or if non-ionic surfactants are used, as they lower the electrostatical repulsion at the oil-water interface [11].

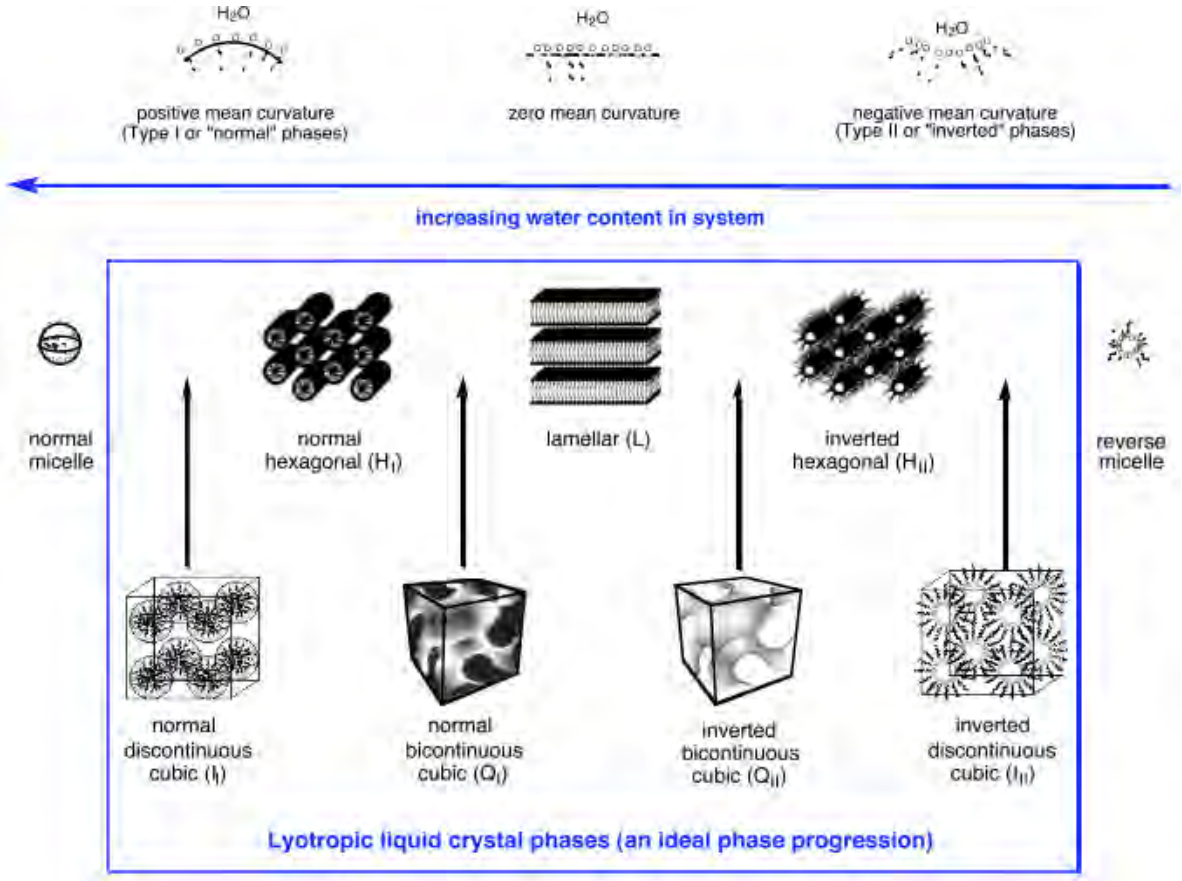

Figure 1.5 – Schematic representation of the ideal evolution of the structure of a LLC system depending on the curvature of the interface, when increasing the water content. Reprinted with permission from Zhou et al. (2007) [14]. Copyright 2007 American Chemical Society.

With regard to microemulsions, the curvature of the surfactant film – and the associated microstructures – can be predicted using the Hydrophilic-Lipophilic Balance (HLB) or the critical packing parameter (CPP). These parameters have been determined using empirical formula. In order to obtain a planar interface, which promote bilayer and bicontinuous structures, a HLB value around 10 and a CPP of 1 are required, as presented in Table 1.2. These two parameters can be calculated both for ionic and non-ionic surfactants, but the following will only develop the case of non-ionic surfactants.

Table 1.2 – Structure and application of microemulsions depending respectively on the CPP and the HLB of the surfactant used [26]–[29].

Structure	CPP	Application	HLB
Spherical and ellipsoidal micelles	$< \frac{1}{3}$	Antifoaming agent	2-4
Cylindrical and rod-like micelles,	$\frac{1}{3} - \frac{1}{2}$	W/O emulsifier	4-8
Vesicles and flexible bilayers	$\frac{1}{2} - 1$	Wetting agent	8-12
Bicontinuous structures and planar bilayers	~ 1	O/W emulsifier	12-16
Reversed structures	> 1	Solubiliser	16-20

Two major experimental formula arose in the 1950s in order to calculate the HLB of non-ionic surfactant molecules by Griffin (1949, 1954) [30], [31] and Davies (1963) [32]. The former is mostly used to determine the HLB of polyoxyethylene surfactant:

$$\mathrm{HLB} = \frac{\mathrm{E} + \mathrm{P}}{5} \qquad \text{Eq. 1.1}$$

Where E and P are the weight percent of ethoxy functions and of polyol functions respectively. Griffin also identified another equation to determine the HLB of fatty acid esters:

$$\mathrm{HLB} = 20\left(1 - \frac{\mathrm{S_p}}{\mathrm{A}}\right) \qquad \text{Eq. 1.2}$$

Where S_p is the number of ester saponification and A the acid number of the fatty acid.

Davies method to determine HLB values is widely used but does not describe polyoxyethylene non-ionic surfactants satisfactorily. The equation proposed is the sum of the unit value of each functional group constituting the surfactant molecule. The unit

values of several functional groups have been discussed by different research groups and some of the most common groups are listed in Table 1.3 [32]–[36].

$$\text{HLB} = 7 + \sum \text{unit value of hydrophilic groups} + \sum \text{unit value of hydrophobic groups} \quad \text{Eq. 1.3}$$

It should however be noted that the HLB method has been replaced by HLD method, which allows for a better determination of the curvature of the surfactant interface based on the amphiphilic geometry but also on its environment. This method will however not be detailed as part of this manuscript.

Table 1.3 – Structure and application of microemulsions depending respectively on the CPP and the HLB of the surfactant used. Adapted from Guo et al [34].

Functional group	**Davies and Lin et al.**	**Guo et al.**
Ester (free)	2.4	2.316
-OH (free)	1.9	2.255
$-CH_3$, $-CH_2-$, -CH-, -CH=,	-0.475	-0.475
$-CH_2-CH_2-OH$	-	0.479

The CPP is another method to determine the geometry adopted by the surfactant film, based on its intrinsic geometrical and electrostatically properties [35]:

$$\text{CPP} = \frac{V_o}{l_h a_o} \quad \text{Eq. 1.4}$$

Where V_o and l_h are respectively the volume and the length of the hydrophobic tail of the surfactants. Tanford (1972) [37] elaborated empirical formula based on the experimental work of Reiss-Husson and Luzzati (1964) [38], in order to determine the length and volume per hydrocarbon chain depending on the number of carbons in the hydrophobic tail:

$$V_o = 54.3 + 26.9n \text{ Å} \quad \text{Eq. 1.5}$$

$$l_h = 1.500 + 1.265n \text{ Å} \quad \text{Eq. 1.6}$$

Some authors suggest to determine a minimal surface area a_{min} for the surfactant head-group parameter in the packing parameter calculation. This minimal area is obtained using the equilibrium between surfactant molecules and the air-liquid interface before reaching the CMC value. The minimum surface area is then linked to the surfactant surface excess concentration calculated from Gibbs equation (Eq. 1.8) [39].

$$a_{min} = \frac{1}{N_a \Gamma_{max}} \quad \text{Eq. 1.7}$$

$$\Gamma_{max} = -\frac{1}{RT}\left(\frac{d\gamma}{d\ln C_{ST}}\right)_T = -\frac{1}{2.303RT}\left(\frac{d\gamma}{d\log C_{ST}}\right)_T \quad \text{Eq. 1.8}$$

1.1.3.2 Co-surfactant

Surface tension of surfactant films in microemulsions is usually around 50 $mN.m^{-1}$ but can be as low as 10^{-2} à 10^{-4} $mN.m^{-1}$ when using double chains surfactants. However in most cases, these so-called ultra-low values are not achievable without the use of co-surfactants. These species are said to have a bigger impact on the microstructure than the surfactant and organic phase [23].

The co-surfactant molecules are usually a medium chain alcohol or a short-tailed surfactant of a different chemical nature than the main surfactant, in order not to compete with one another [19]. A bicontinuous structure is usually favoured when using a short co-surfactant with a minimum of repulsive interaction with the main surfactant, promoting the co-surface adsorption in the surfactant interface.

1.1.3.3 Aqueous phase

Solvent constituting the aqueous phase must possess some specific properties, especially when ionic surfactants are used. Indeed, the solvent must be highly polar so its dielectric constant will be sufficient to dissociate the ions in the ionic amphiphilic molecules, while preventing their self-association. The aqueous liquid must also have a high solvency capacity, in order to favour dipole-dipole interaction instead of the association of ions of opposite charges. Finally for both ionic and non-ionic surfactant, the aqueous phase must be structured and must allow chemical interactions – such as hydrogen bonds – as well as

physical interactions – such as polarity. This last requirement is however not needed if the aprotic molecules of the system have sufficient polarity to structure the system [40].

Water is usually chosen as aqueous medium as it is a polar and protic solvent is highly structured and very stable while offering a low cost, a wide availability and low toxicity. Other polar media can however be chosen to replace water but their properties are sought to be close to those of water [40]. If not possible, a same type of surfactant –with a higher hydrophobic tail and a bigger hydrophilic head – can be used but its proportion will be increased in the system to compensate the poorer properties of the substitute phase [41]. For example, glycerol and ionic liquids have been studied as aqueous medium for microemulsions [42].

1.1.3.4 Organic phase

The organic phase – also called oil phase – is a made of one or more hydrocarbon compound(s), whose length is the determining factor in competitive adsorption processes of the organic and co-surfactant molecule onto surfactant interfaces. The shorter the hydrocarbon tail, the easier the penetration of the oil at the surfactant interface, which will increase the radius of curvature of the interface and promote micellar structures. In parallel with this phenomenon, a shorter oil tail will make the co-surfactant adsorption difficult [1], [23]. The structure of the hydrocarbon is of high interest as well: Ceglie et al. (1987) [23] highlighted that the use of an aromatic oil leads to bicontinuous microstructures, no matter the ionic charge of the surfactant and its hydrocarbon length.

In order to increase the stability of the colloidal system, the difference of interactions between the immiscible phases must be minimised. This difference is represented by the R-ratio described by Winsor (1947) [6], which determines the impact of the solvents on the interface curvature:

$$R_W = \frac{E_{surfactant-oil}}{E_{surfactant-aqueous}} \qquad \text{Eq. 1.9}$$

Where $E_{surfactant-oil}$ and $E_{surfactant-aqueous}$ represent the interactions of the surfactant film with the organic and aqueous phases respectively. As a result, when the cohesive energy of the aqueous phase is higher than the one of the organic phase, a bicontinuous structure is expected [19].

1.1.3.5 Temperature

As previously explained, the ionic charge of the surfactant impacts on the curvature radius of the interface and on the microemulsion phase inversion. Non-ionic surfactants are highly sensitive to the temperature parameter because of their chemical structure: increasing temperature dehydrate the ethoxylated functions of the non-ionic surfactant. Such a modification then decreases the affinity of the hydrophilic part of the surfactant with the aqueous phase, which penetrates less into the surfactant [19], [43]. The opposite phenomenon is observed for a temperature decrease cf. Figure 1.6.

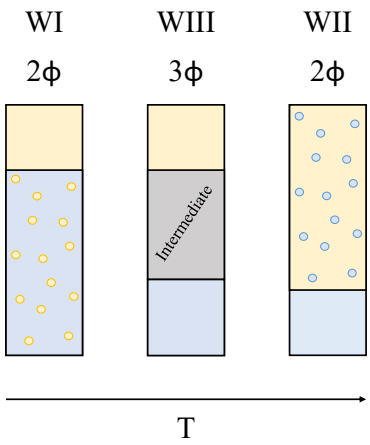

Figure 1.6 - Evolution of non-ionic microemulsion microstructures depending on the temperature.

Some head-groups exhibit low temperature dependence, notably the sugar-based surfactants [44]. Ionic surfactants, are sensitive to both concentration and temperature, the CMC being dependent on the temperature. These two parameters have an opposite impact on the curvature radius of the interface and must be studied separately to evaluate their respective influence on the surfactant film geometry.

1.2 Structural characterisation of surfactant-based organised systems

Liquid crystals and microemulsions may result from similar systems but with different relative composition and/or temperature. Several analyses allow to differentiate between these two possible structuration of the organised system. Based on these analyses, it is then possible to represent each system based on its composition and on its temperature.

The most accurate representation of the structures adopted by the surfactant-based systems is a quaternary phase diagram. Quaternary phase diagrams represent the structure of the solution versus its composition (triangular-based prism) and the temperature (prism height) for a constant pressure. Each side of the triangular-prism represent the mass fraction of one compound or composite phase. However, for practical reasons, ternary (or pseudo-ternary if using a composite phase) phase diagrams (cf. Figure 1.7) associated with fish-tail diagrams (cf. Figure 1.8) are most frequently used to describe the microstructure of microemulsions and liquid crystals depending on the composition and the temperature respectively.

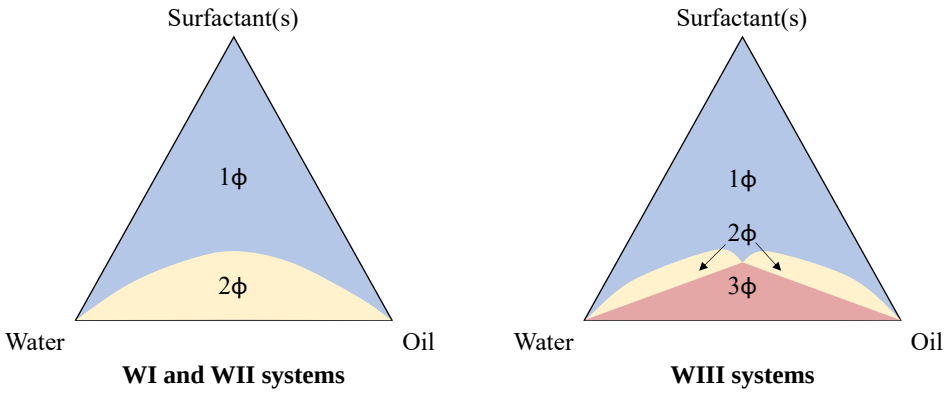

Figure 1.7 – Schematic representation of (pseudo-)ternary phase diagrams used for the description of surfactant-based systems (microemulsions and liquid crystals).

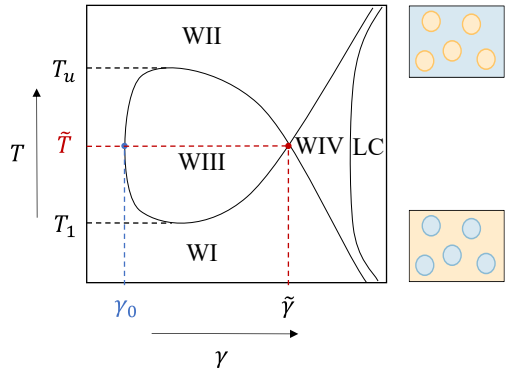

Figure 1.8 – Schematic representation of a fish-tail diagram T=f(surfactant concentration γ).

1.2.1 Characterisation of liquid crystals

Several techniques allow for the characterisation of liquid crystals. If some of the most common ones are cross-polarised light, electron microscopy and X-ray diffraction, fluorescence [14], DOSY-NMR [12], [14] and DSC [12] can also be used.

1.2.1.1 Cross- polarised light microscopy

Since both hexagonal and lamellar TLC and LLC are anisotropic, the first common technique for their identification is to verify whether the solution is birefringent under cross-polarised light. The liquid crystal solution will be perceived as coloured because of all the wavelengths of light that are not blocked by the analyser, cf. Figure 1.9 and Figure 1.10.

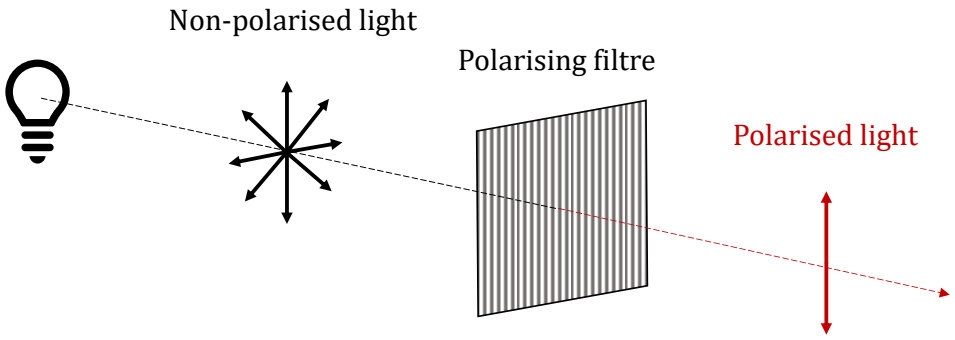

Figure 1.9 – Representative scheme of the formation of polarised light.

It should be noted that nematic liquid crystal are not perceived as colourful but as an arrangement of bright and dark areas. However, cubic structures, which are isotropic, appear completely black under cross-polarised light [12], [14].



Figure 1.10 – Birefringence of two liquid crystal samples under cross-polarised light.

1.2.1.2 X-ray diffraction

X-ray diffraction of liquid crystals allows for the identification of the three-dimensional configuration of the lattice, cf. Figure 1.11. Each peak results from a d-spacing, i.e. the distance between the planes of atoms that gives rise to the diffraction peak.

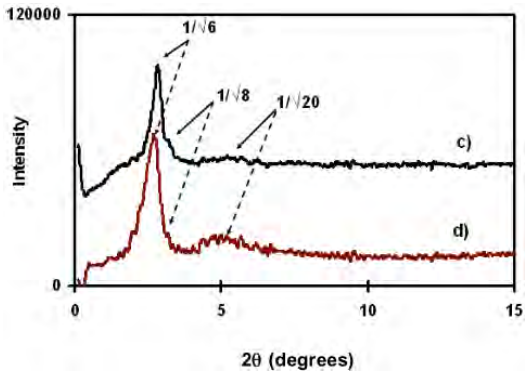

Figure 1.11 – XRD diffractogram of a bicontinuous cubic structure. . Reprinted with permission from Zhou et al. (2007) [14]. Copyright 2007 American Chemical Society.

Each liquid crystal structure can be characterised by measuring the specific ratios of the d-spacing to the lowest angle diffraction peak, as detailed in Table 1.4. However, due to the disordered nature of these liquid structures, XRD analyses can sometimes be difficult to interpret. To confirm the lattice structure identification, other techniques can be used, such as NMR or SAXS/SANS. Indeed, the peaks found in XRD diffractograms and their associated d-spacing can also be found in X-ray and neutron small angle scattering. This technique which will be described below.

Table 1.4 – Liquid crystal structure and their associated d-spacing in XRD diffractograms and SAXS scattering curves.

Liquid crystal structure	Diffraction peaks d-spacing ratios
Lamellar	$1:\frac{1}{2}$
Hexagonal	$1:\frac{1}{\sqrt{3}}:\frac{1}{\sqrt{4}}$
Cubic	$1:\frac{1}{\sqrt{6}}:\frac{1}{\sqrt{8}}\left(:\frac{1}{\sqrt{20}}\right)$

1.2.2 Characterisation of microemulsions

After differentiating between liquid crystal and microemulsions, several analyses allow to specify the microstructure adopted by the system: micellar or bicontinuous.

1.2.2.1 Conductivity

Conductivity measurement is a classical first approach used to determine the Winsor domains in a microemulsified sample. This characterisation technique has been widely used for the delimitation of micellar and bicontinuous structures. A confined aqueous structure – such as a micelle or a liposome – in an oil medium will lead to low conductivity measurements, which can be attributed to a Winsor II system. On the opposite, a continuous aqueous medium containing a dispersed organic phase will lead to high conductivity values, which can be then attributed to a Winsor I system, as shown by Fanun [45]. For mid-range conductivity values, an intermediate structure will be found and is often assumed to be bicontinuous. This phenomenon is based on the motion of ions in the aqueous phase from particle to particle. The transfer of ions will be enabled when the aqueous droplets merge. Those three ranges of conductivity values are delimited by two slope discontinuity indicating a significant change in the microstructure, as depicted in Figure 1.12. These discontinuities originate from the percolation theory that describes the behaviour of a network subject to random filling. The minimal temperature or composition for which a long-range connectivity between the different sites and a microstructural transition is obtained is called a percolation threshold [46].

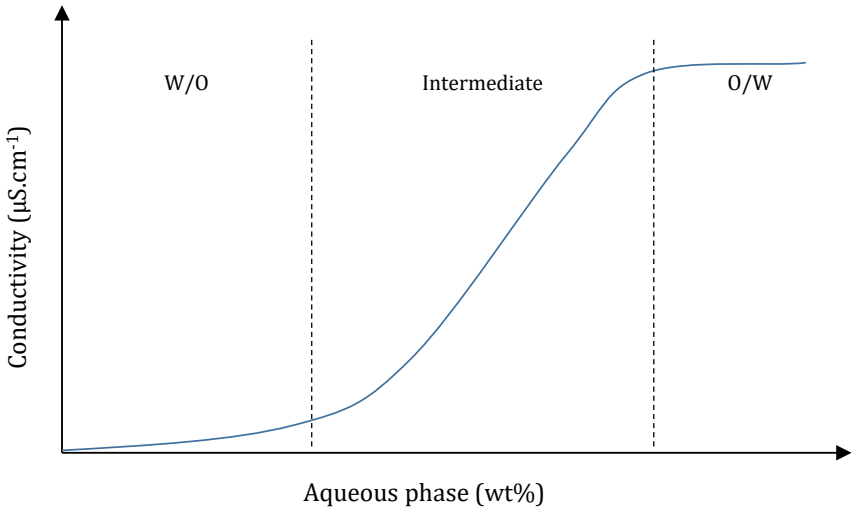

Figure 1.12 – Schematic conductivity curve versus the aqueous phase proportion in the emulsified monomer solution.

This simple method is however unable to identify precisely the intermediate structures and thus to differentiate between bicontinuous and other for example ordered structures such as cubic microstructures.

1.2.2.2 Diffusion Ordered Spectroscopy (DOSY)

The Nuclear Magnetic Resonance ^1H (^1H NMR) is a powerful method for the composition and structural analysis of solutions. Modern NMR spectrometers are equipped with a Z-gradient probe are able to perform 2D experiments, such as DOSY analyses. This technique is useful to determine the self-diffusion coefficients of molecules in solutions and homogeneous mixes. This determination is based on the measurement of the translational motion – also known as Brownian motion – of the molecules in the solution.

A first gradient is applied to determine the spatial position of each molecule in the sample. A second gradient is then applied after a diffusion period Δ, so the new position of the molecules can be identified. If some compounds have moved during the diffusion period a decay of the signal is observed. The attenuation of this signal will be determined for different the gradient strength g and the resulting signal intensity I will directly be related to the self-diffusion coefficient of the compound using the following equation [47]–[49]:

$$I = I_0 . e^{-D.\gamma_m{}^2.g_m{}^2.\delta_m{}^2.\left(\Delta_m - \frac{\delta_m}{3}\right)} \qquad \text{Eq. 1.10}$$

Where I_0 is the unattenuated signal intensity, γ_m the gyromagnectic ratio of the observed nucleus, τ the relaxation time, δ_m the length of the gradient, g_m the gradient strength and Δ_m the diffusion time. The small molecules and compounds move fast – hence a high self-diffusion coefficient – and their signal will decrease quickly, as opposed to large molecules. The DOSY spectra of a mixture of different chemical compounds allows for the attribution of each self-diffusion coefficient according to their associated chemical shift, as depicted in Figure 1.13.

The determination of self-diffusion coefficients in microemulsions provides microstructural information that enables normal and inverse micellar structure to be distinguished, as well as intermediate structure to be accurately identified. Both parameters are to be considered to carry out a complete analysis of the results obtained from DOSY measurements: the self-diffusion coefficient D and the relative self-diffusion coefficient $\frac{D}{D_0}$. The latter compares the self-diffusion coefficient in the mix to the one of the

pure compound and is comprised between 0 and 1. The higher the self-diffusion coefficient, the less obstructed the solution.

Micellar and bicontinuous structures are easily identified using the following rules, regarding the values of the self-diffusion coefficients and of the relative self-diffusion coefficients – also called obstruction factors – for the oil, aqueous (water) and surfactant molecules [50]–[54]. These rules are however to be considered carefully as they are based on geometric constraints occurring in ideal microemulsified network and do not consider the interactions that may arise in the system, e.g. the solvatation of non-ionic surfactant.

- Normal micellar structure (O/W):

  $D^{surfactant} \approx D^{oil} << D^{aqueous}$, with $D^{oil} \approx 10E\text{-}11\ m^2.s^{-1}$ and $D^{aqueous} \approx 10E\text{-}9\ m^2.s^{-1}$

  $\left(\frac{D}{D_0}\right)_{oil} \approx 0.3$ and $\left(\frac{D}{D_0}\right)_{aqueous} > 0.8$

  The organic phase being retained in small micelles, the obstruction is high and the self-diffusion coefficient of oil is really low compared to its value in pure organic phase (ca. one third). On the contrary, the aqueous phase being the continuous medium, the molecules encounter little to no obstruction and their self-diffusion coefficient is close to the one of the pure aqueous phase.

- Inverse micellar structure (W/O): opposite of the above description of normal micellar structure.

  $D^{oil} >> D^{aqueous} \approx D^{surfactant}$, with $D^{oil} \approx 10E\text{-}9\ m^2.s^{-1}$ and $D^{aqueous} \approx 10E\text{-}11\ m^2.s^{-1}$

  $\left(\frac{D}{D_0}\right)_{oil} > 0.8$ and $\left(\frac{D}{D_0}\right)_{aqueous} \approx 0.3$

- Bicontinuous structure:

  $D^{surfactant} < D^{oil} \approx D^{aqueous} \approx 10E\text{-}9\ m^2.s^{-1}$

  $\left(\frac{D}{D_0}\right)_{oil} \approx \left(\frac{D}{D_0}\right)_{aqueous} \approx 0.6$

  The microstructure being interconnected, both organic and aqueous phase molecules are free in two of the three directions of space. The self-diffusion coefficient of both phase is ca. 0.6 times the self-diffusion coefficient of the pure solution.

Other microstructures can be identified using the obstruction factors. As an example, in tubular structures, the relative self-diffusion coefficient of the dispersed phase is around $\frac{1}{3}$ because the molecules are only able to move in one direction of space. Generally

speaking, an increase of the obstruction factor of the organic phase and a decrease of the factor of the aqueous phase indicates a decrease in the interfacial film curvature, and vice versa [51], [53].

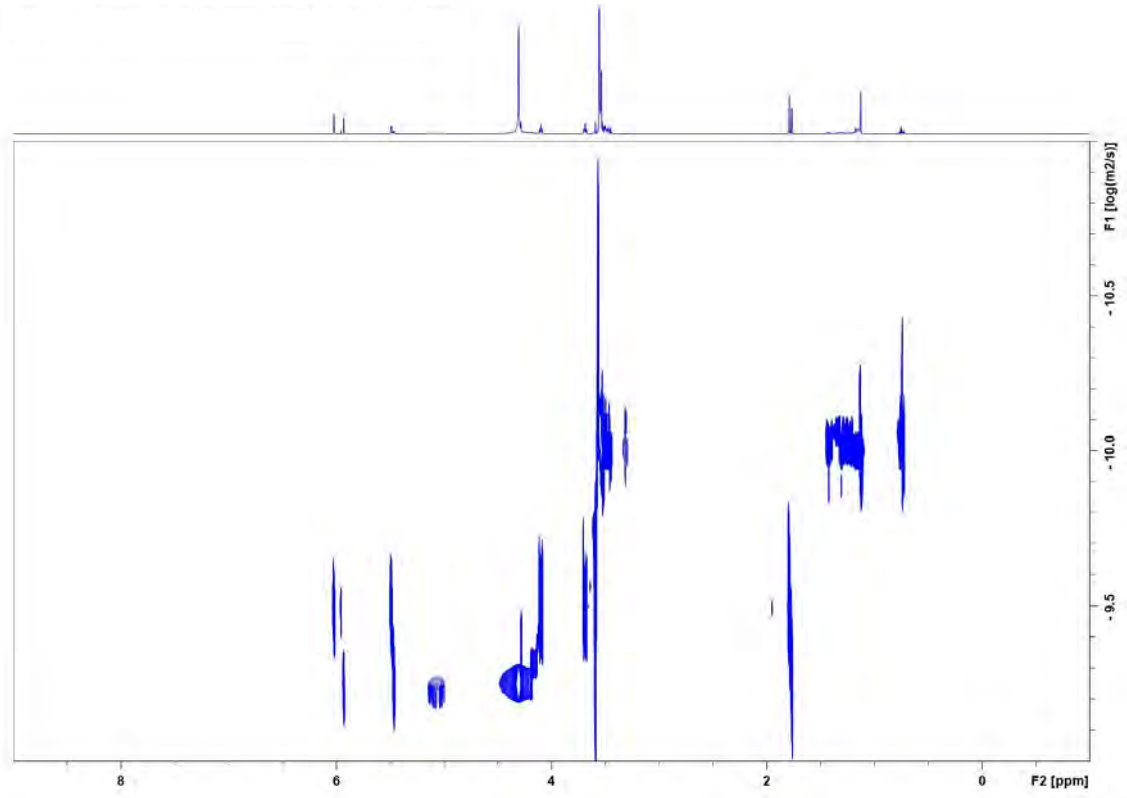

Figure 1.13 – ^{1}H NMR DOSY 2D spectrum of one acrylate microemulsion discussed in this work.

Relative self-diffusion coefficients of bicontinuous microemulsions can be predicted for a similar composition in organic and oil phases, depending on the coordination of both phases and the surfactant [47], [51], [55].

$$\frac{D_{oil}}{D^{0}_{oil}} = \frac{1}{3} + \beta\left(\Phi_{oil} - \frac{1}{2}\right) \quad \text{Eq. 1.11}$$

$$\frac{D_{water}}{D^{0}_{water}} = \frac{1}{3} - \beta\left(\Phi_{oil} - \frac{1}{2}\right) \quad \text{Eq. 1.12}$$

$$\frac{D_{surfactant}}{D^{0}_{surfactant}} = \frac{2}{3} - \beta'\left(\Phi_{oil} - \frac{1}{2}\right)^{2} \quad \text{Eq. 1.13}$$

Where β is the coordination number for aqueous and organic phases and β' is the coordination number of the surfactant molecules. β = 0.78 and β' = 1.80 for a coordination of 6, while β = 0.54 for a coordination of 4.

Depending on the correlation of the surfactant molecules, the interfacial film can either describes monolayers or bilayers. The previous equations have been determined for monolayers but are also verified for bilayered systems, such as cubic or sponge (L_3) systems.

It should be noted that the equations presented in this section only describe the geometrical obstruction in microemulsified systems and do not account for the solvatation effects, which can dramatically modify the relative self-diffusion coefficient values. The solubility of the surfactant in one of the two immiscible phases might also tamper the experimental value compared to the value obtained from the previous equations. This last phenomenon is more common for non-ionic surfactants, which present an affinity with the organic phase for higher temperature and with the aqueous phase for lower temperature. DOSY NMR must therefore be used in addition to other characterisation techniques, such as SAXS or TEM, to confirm the microstructure of the emulsified system.

1.2.2.3 Small Angle X-ray Scattering (SAXS)

Small angle scattering is a powerful non-destructive characterisation technique, which can indirectly give specific information about the morphology of microemulsions (and liquid crystals). This analysis can be performed using an X-ray (SAXS) or a neutron (SANS) emission source. This section will focus on the scattering of X-ray.

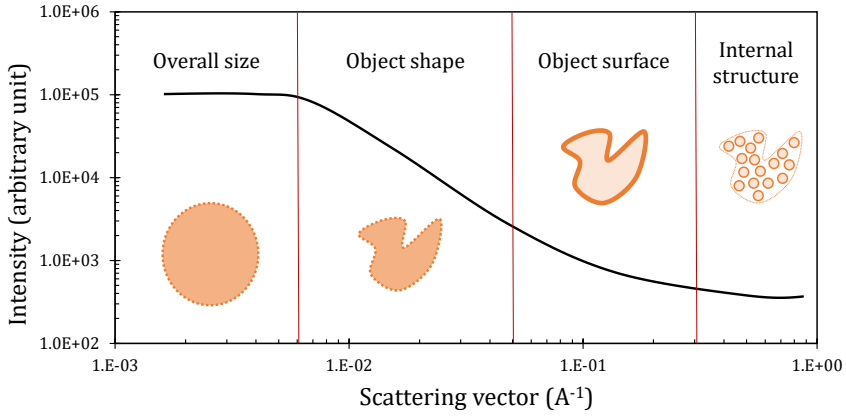

Figure 1.14 – Schematic representation of the type of information collected by SAXS analysis (case of monodispersed particles).

An X-ray beam is applied to the samples and will interact with the electronic density of the atoms composing the material. This interaction leads to a deviation of the beam,

whose diffused intensity is then collected on a detector. Depending on the scattering vector range, one can access to various information such as the size and the surface condition of particles, the internal morphology of the material, the size and polydispersity of the pores or the crystallinity of the polymer network, as presented in Figure 1.14 [56]. Each scattering curve is obtained by plotting the scattering intensity I(q) versus the scattering vector q.

$$q = \frac{4.\pi.\sin(\theta_{SAXS})}{\lambda} \qquad \text{Eq. 1.14}$$

Where λ is the wavelength of the emitted X-ray beam and θ_{SAXS} the scattering angle.

$$I(q) = \Delta_{\rho^2}.\Phi_V.V_P.P(q).S(q) \qquad \text{Eq. 1.15}$$

Where Δ_{ρ^2} is the contrast – which only depends on the equipment used – Φ_V is the volume fraction of the dispersed particles, V_P is the dry volume of the sample. P(q) and S(q) are respectively the form factor – which only depend on the geometry of the dispersed system – and the structure factor – which describes the correlations among particles.

The scattering curves are then fitted with well-defined models, depending on the microstructure of the sample, which has to be known beforehand. The mathematical description of those models allows for the characteristic parameters and variables associated with the structure of the sample to be determined.

In order to avoid the need for a prior knowledge of the structure of the sample, some methods have been established such as the generalised indirect Fourier transformation (GIFT) technique [56]–[58]. This method provides a lot of valuable information such as the distance pair distribution function, the radial distribution profile of a particle and thus its shape and structure factors. The main advantage of the GIFT technique is that it can be used in order to describe a wide variety of microstructures such as micellar or bicontinuous structures. This model allows for the study of the transition from one microstructure to another.

In the case of microemulsions, a lot of research work are based on the use of models requiring prior knowledge of the microstructure. The core-shell model [56], which provides a radial density profile varying in successive steps, allows for the visualisation of the different domains constituting a hydrophobic core surrounded by the head-group

of the surfactant interface for O/W microemulsions, and vice versa for W/O microemulsions. This model has been derived to represent spheres with multiples layers such as vesicles [59]. This model compiles a hardsphere structure factor S(q), using the Percus-Yevick closure relationship and a core-shell form factor P(q) [60], [61].

The Teubner-Strey model has been widely used for the analysis of SAXS and SANS scattering curves describing bicontinuous microstructure. The curve following this model present a large Bragg's peak followed by a plateau in the small angle range and presenting a steep slope in the wide-angle ranges following a Porod law. This mathematical model introduces two parameters describing the bicontinuous network: the periodicity d which defines the distance between two interconnected channels and the correlation length ξ, which defines the distance over which the local order is maintained. A_2, C_1 and C_2 are some constants and B is the scattering background.

$$I(q) \propto \frac{1}{A_2 + C_1.q^2 + C_2.q^4} + B \qquad \text{Eq. 1.16}$$

$$d = 2.\pi.\left[\frac{1}{2}.\left(\frac{A_2}{C_2}\right)^{\frac{1}{2}} - \frac{1}{4}.\frac{C_1}{C_2}\right]^{-\frac{1}{2}} \qquad \text{Eq. 1.17}$$

$$\xi = \left[\frac{1}{2}.\left(\frac{A_2}{C_2}\right)^{\frac{1}{2}} + \frac{1}{4}.\frac{C_1}{C_2}\right]^{-\frac{1}{2}} \qquad \text{Eq. 1.18}$$

However, one must keep in mind that the Teubner-Strey model has been developed per se for liquid microemulsions and not polymer network [63]. This model is also unable to distinguish between ordered and disordered microstructure. In order to fill this need, some authors have associated the Teubner-Strey parameters to mathematical assets in order to evaluate the system structuration with the amphiphilicity factor f_a and the polydispersity factor $k_p.\xi$ [62]–[65].

$$f_a = \frac{C_1}{\sqrt{4.C_1.C_2}} = \frac{1 - \left(\frac{2.\pi.\xi}{d}\right)^2}{1 + \left(\frac{2.\pi.\xi}{d}\right)^2} \qquad \text{Eq. 1.19}$$

$$k_p.\xi = \frac{2.\pi}{d}.\xi \qquad \text{Eq. 1.20}$$

The height of Bragg's peak also gives relative information regarding the rigidity and uniformity of the interfaces when comparing two samples [66], [67]. Schulreich et al. (2013) [67] used the d and ξ parameters extracted from the Teubner-Strey model in order to determine the renormalized bending elastic constant κ_{SANS} (cf. Eq. 1.21) while Tartaro et al. (2020) [68] linked the correlation length to the curvature modulus κ_C using the effective length of the surfactant l_s (cf. Eq. 1.22).

$$\xi = \frac{64.d}{10.\sqrt{3}.\pi}.\frac{\kappa_{SANS}}{k_B.T} \qquad \text{Eq. 1.21}$$

$$\xi = l_S.\exp\left(\frac{2.\pi.\kappa_{SANS}}{k_B.T}\right) \qquad \text{Eq. 1.22}$$

If the polydispersity of the droplet size is too important, the determination of the structure of the micellar microemulsion in SANS and SAXS is complicated: the micro objects will interact with one another and attenuate the typical oscillations of a micellar system. It is therefore necessary to combine small angle scattering analyses with other characterisation techniques, and more specially techniques that enable the visualisation and identification of the microstructure, such as (cryo-)TEM and (cryo-)SEM [16], [41].

1.3 Polymerisation of nanostructured polymer networks

It is commonly agreed that it is possible to set a microemulsified structure in order to reach a solid, nanostructured material [41]. Two main methods have been developed to reach the desired microstructure upon solidification of the structure. The first is an indirect templating and consists in the polymerisation of one of the two immiscible phases. The initial microstructure is not retained because of the destabilisation of the system. The second technique is a reversible gelification or freezing of the structure before its polymerisation, which allows for the initial microstructure to be retained [7], [69–71]. As part of this work, we will only consider the polymerisation of the monomer phase by free radical polymerisation.

Radical polymerisation can be performed using different type of initiators: thermic, RedOx or photoinitiators. Thermic initiators present however a few drawbacks compared to the RedOx and UV priming. The increase of the temperature can destabilise the colloids and decrease the polymerisation rate – and thus the yield – while increasing the particle size [72]. The thermal initiators have therefore mostly been substituted with RedOx and UV primers, which will be discussed in the following sections.

In order to reach high yields upon polymerisation, commercial monomers must be purified beforehand to eliminate the inhibitors. The self-assembled solution must also be flushed with an inert gas in order to eliminate all the oxygen of the air, which would preferentially react with the radicals and prematurely put an end to the propagation step [73–76].

1.3.1 RedOx polymerisation

Using a RedOx process compared to a thermic polymerisation process allows for a decrease in the induction period, a lower energy input to initiate the reaction, a high yield and a controlled reaction at low temperatures [73], [76].

In order to maximise the efficiency of the polymerisation process, the induction period must be as short as possible. This duration depends on the RedOx imitators chosen, as well as their concentration in the monomer system. This last parameter tailors the number of radicals initially created, the particle size, the polymerisation rate, the temperature of the system and the yield achieved [73], [74]. Common RedOx oxidising

agent are peroxides, persulfates, permanganates and transition metal salts. Some of the most used reducing agents for vinyl monomers are alcohols, aldehydes, amines, amides, ketones, acids and thiols [76]. Peroxides and nitriles emit undesirable volatile by-products, typically carbon dioxide and nitrogen, which leads to heterogeneous structures in the polymer samples [77]. Finally, the affinity between the monomers and the initiators is an essential parameter that will impact on the final polymer product. Kohut-Svelko et al. Highlighted that the RedOx couples TBHP/SFS and TBHP/FF7 were well suited to the polymerisation of peroxide systems, while APS/TMEDA were best suited to monomer systems containing a persulphate oxidant [73].

RedOx polymerisation of MMA monomers has been performed with several initiators such as the couples Ce(IV)/HNO_3 [76] and APS/AIBN [78]. However, the APS/TMEDA initiators have been found to limit the phase separation phenomenon during the polymerisation process, rendering this couple one of the most interesting choice for the RedOx process [79]. The priming mechanism of the TMEDA/APS couple is described in the following Figure 1.15.

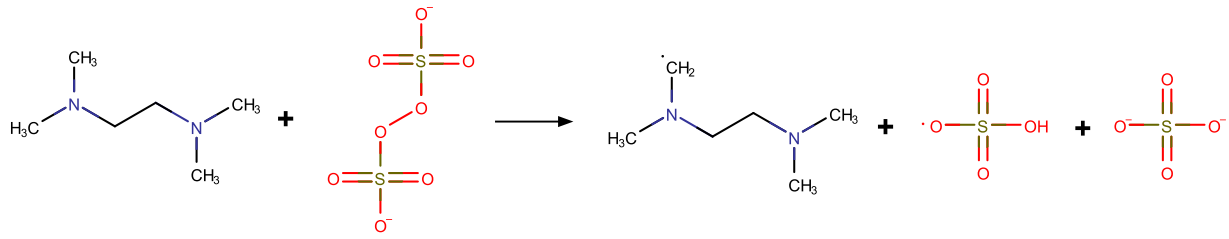

Figure 1.15 – Reaction scheme for the initiation of the RedOx couple APS/TMEDA.

1.3.2 UV polymerisation

UV polymerisation possesses several advantages compared to the RedOx polymerisation and is considered as a promising industrial technique for microemulsion and emulsion polymerisation. UV polymerisation can be performed at room temperature, similarly to the RedOx process, but exhibits a negligible induction period, as opposed to the RedOx process. This last characteristic makes UV polymerisation one of the most efficient process for the synthesis of cross-linked multifunctional polymer networks.

UV polymerisation is induced with the aid of a photoinitiator, which absorbs UV- radiations and generates radicals, which will then propagate in the medium. If

photosensitive species are in the solution, the polymerisation process can be further accelerated and set the system microstructure.

1.3.2.1 Norrish photoinitiators

The mechanism involved in the initiation step of UV polymerisation depends on the Norrish type of the photoinitiator. Norrish I photoinitiators allow for the direct cleavage of the molecule under UV-radiations, as presented in Figure 1.16. These initiators carry ketone or aldehyde function, which undergoes homolytic cleavage of the σ-bond, resulting in two radicals. DMPA, HMP as well as Irgacure® and Darocur® product lines are common Norrish I photoinitiators.

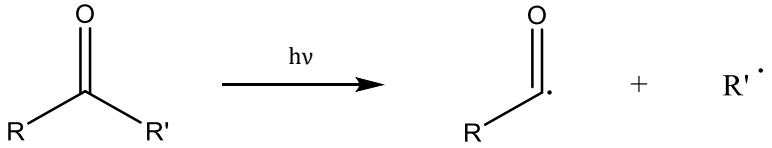

Figure 1.16 – Photochemical priming of a Norrish type I initiator.

Norrish II initiators must undergo a rearrangement of their structure before they can react with UV-radiations, in the same way as Norrish II initiators. This rearrangement requires a hydrogen donor, as presented in Figure 1.17. This donor can be found in the initiator itself, on a co-initiator or on the grafted substrate. Benzophenone and its derivates, as well as ITX are common Norrish II photoinitiators.

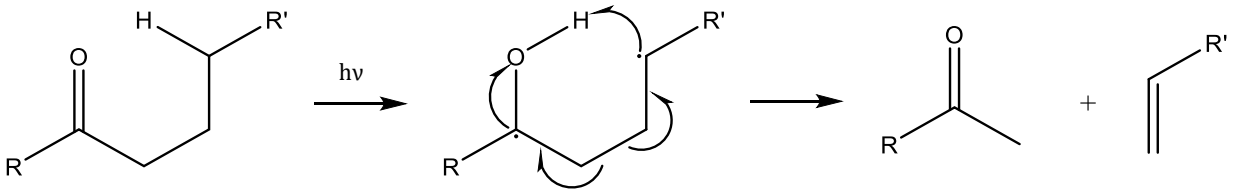

Figure 1.17 – Photochemical priming of a Norrish type II initiator.

1.3.2.2 UV grafting

Two distinct grafting types are to be considered when modifying a solid surface, such as a membrane: the “grafting-to” and “grafting-from” methods [80], [81]. The former requires the substrate to be functionalised so that the grafted group will react with the substrate. The latter consists in the functionalisation of the substrate prior to the grafting, as schematised in Figure 1.18.

In the case of membrane grafting, the "grafting-from" methods are the most commonly used. When photosensitive substrates are used, a simple UV-irradiation will generate the active sites, which will later react with the grafted groups. Non-photosensitive substrates can be functionalised using Norrish II photoinitiators prior to the UV exposition. Other functionalisation methods, which do not involve UV irradiation are summarised by Stamm et al. [81].

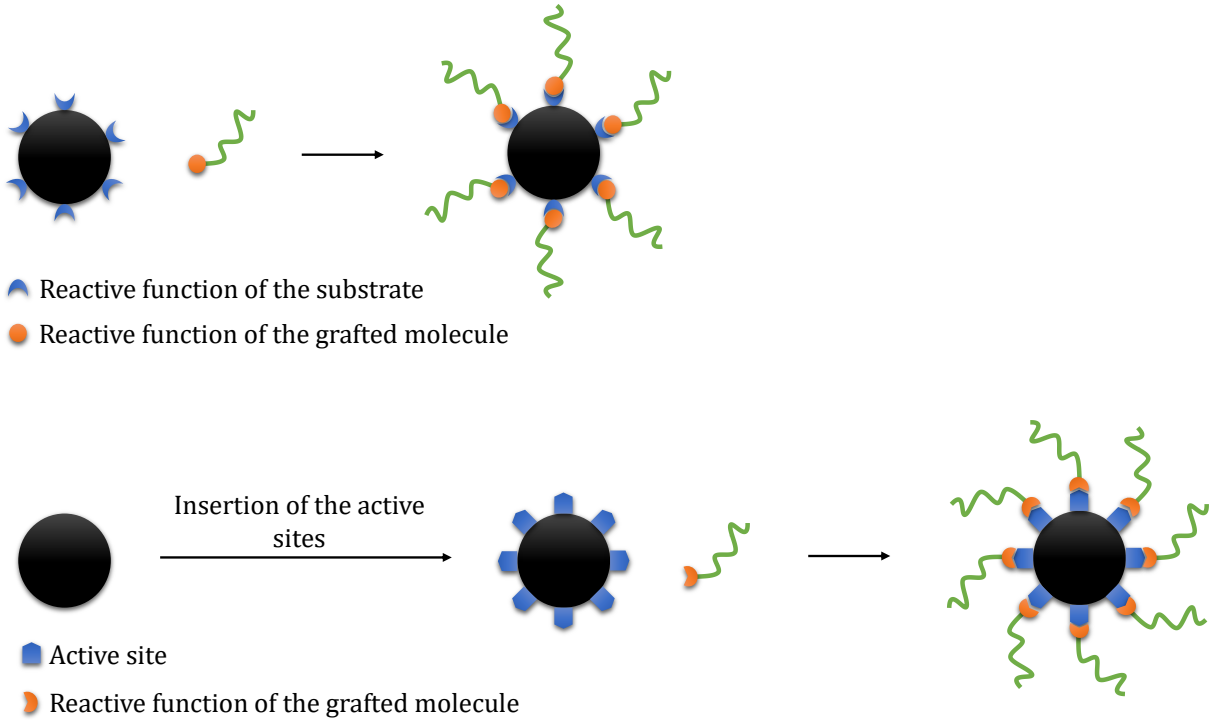

Figure 1.18 – Reaction scheme for the "grafting to" (top) and the "grafting from" (bottom) mechanism.

1.4 Membranes for liquid and gas filtration

In this Section, a general description of membranes process will be presented, including their structure, their filtration range, their common composition and their various module geometry.

1.4.1 Operating principles

Membrane filtration is a separating process based on the transfer of a fluid or a gas across a physical barrier: the membrane. This process is found in diverse industries (e.g. petrochemicals, solvent recovery or food processing, etc.) as well as in wastewater treatment and for biological and medical purposes (e.g. enzymes production, haemodialysis, etc.).

Two main types of membrane filtration are commonly encountered in the industry: the dead-end and the cross-flow filtration, as presented in Figure 1.19. The feed stream runs perpendicular to the membrane in the former case and parallel to the membrane in the latter case.

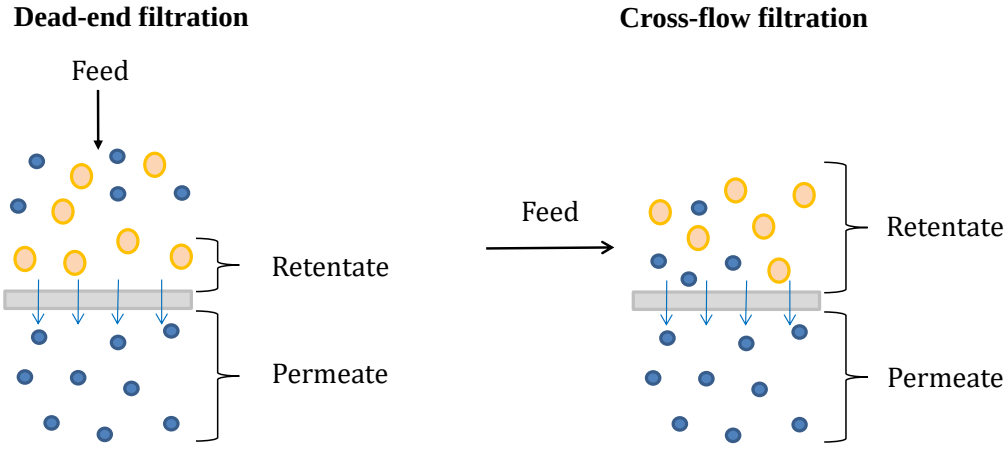

Figure 1.19 – Schematic representation of dead-end and cross-flow filtration.

Membrane filtration occurs under one or several driving forces such as a pressure (liquid filtration), a concentration (pervaporation), a temperature (membrane distillation) or an electrical potential gradient (electrodialysis). Membrane selectivity depends on the ability of liquid or solid molecules to be retained by the membrane under the action of the driving force.

Two major properties define how efficient a membrane is: its permeability and its selectivity to the stream flow. These characteristics depends partly to the geometry, the size and the density of the pores. While the membrane porosity is often depicted as ideal cylinders of spheres, the real porous structures present defaults and constrictions, which may be tortuous and even closed pores [82], as depicted in Figure 1.20.

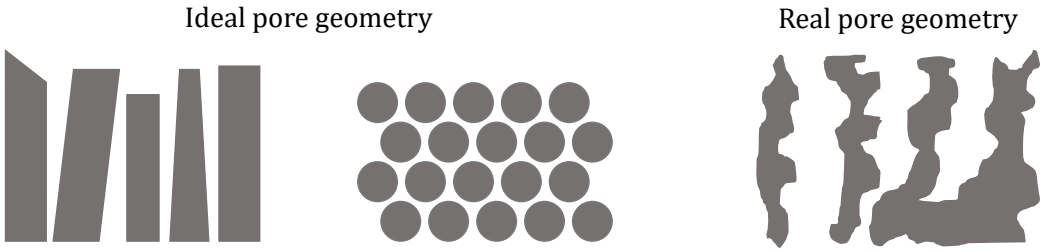

Figure 1.20 – Schematic representation of a membrane porosity.

1.4.2 Membrane classification

Membranes are generally classified according to their filtration range, their structure, their material(s) or their module geometry.

1.4.2.1 Filtration range

The membrane performance being dependant on its porosity, a first classification of membranes based on their pore size is often used to select a first range of filtration according to the desired field of use. In line with the subject matter of this study, only membrane processes occurring under a pressure gradient (cf. Figure 1.21) will be discussed in the following thesis.

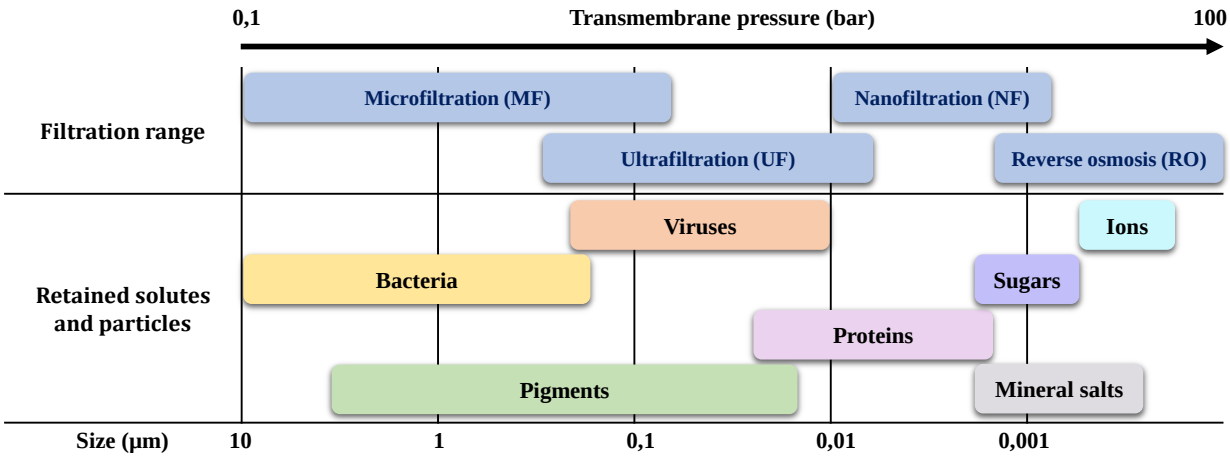

Figure 1.21 – Membrane filtration range and their common applications depending on the retentate size.

1.4.2.2 Membrane porosity

Membrane structure is divided in three categories: symmetric, asymmetric and composite structures, cf. Figure 1.22. Symmetric membranes are made of a unique homogeneous material which allows a uniform porosity over the membrane thickness, which acts as the selective layer. Depending on the elaboration process, symmetric membranes can either be porous or dense.

Asymmetric membranes thickness is divided into the selective and the porous layers. The porosity of the former is dramatically lower in the former and its thickness must be as low as possible in order to maintain good flux performances. This layer is responsible for the selectivity and the permeability performances of the membrane. The porous layer ensures the mechanical integrity of the membrane. Its porosity is usually really high (between 60 and 80%) and may fluctuate but has no impact on the selectivity and the permeability of the overall structure.

Composites membranes are composed of several layers made of different materials. These layers have an increasing porosity over the membrane thickness, which allows both a high selectivity and a high permeability. The structural integrity of the overall structure is usually ensured by the use of a non-woven support in UF and NF.

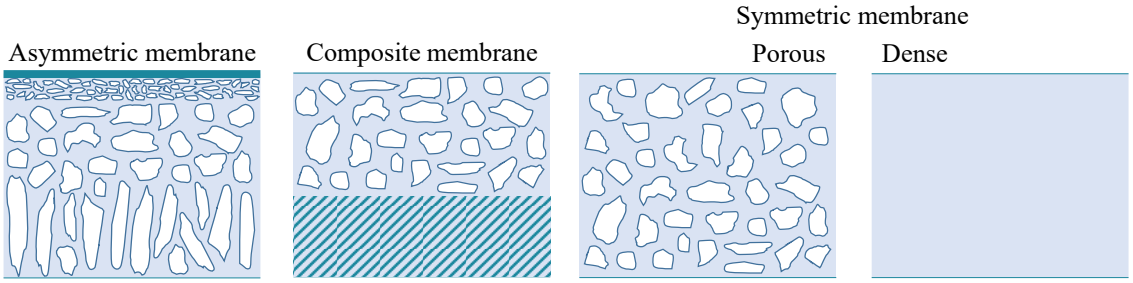

Figure 1.22 – Schematic representation of the internal structure of a membrane.

1.4.2.3 Membrane materials

Two material categories are mainly used for the manufacture of membranes: organic (polymers) and mineral (mostly ceramics) materials. The former represents ca. 80% of the membrane marker in the industry, due to the low production cost associated and the wide adaptability of the materials to various uses. Polymer membranes however exhibit a lower mechanical resistance, which makes them vulnerable to washings and therefore prone to fouling [83].

On the contrary, inorganic materials offer a very high mechanical, thermal and chemical resistance – and therefore less prone to fouling – but are expensive to produce and sensitive to cracks and shocks. Common operating properties of both types of material are listed in Table 1.5.

Table 1.5 – Comparison between organic and mineral membrane general operating properties.

Membrane type	Mineral	Organic
Filtration range	MF, UF	MF, UF, NF, ROP
Thermal resistance	T > 300°C	T < 100°C
Mechanical resistance	Shock sensitive	Flexible
Chemical resistance	Very high pH : 0 – 14	Poor No extreme or oxidizing pH values
Membrane module geometry	Limited plane and tubular	Large plane, tubular, spiral and hollow fibre
Service life	Long	Short
Production cost	Very high	Low

1.4.2.4 Membrane module geometry

The choice of the membrane module geometry is based on several factors such as its price, its volume or simply its feasibility at industrial scale. Two main module types prevail: plane and cylindrical geometry [83].

Both flat-sheet membranes and spiral modules derived from a planar geometry, cf. Figure 1.23. They can both be made of one or several materials but are mainly composite industrial membranes. Spiral modules are constituted of several flat-sheet membranes wrapped around an axis, which increases the compactness of the module but prevents backwashing because of its low mechanical resistance.

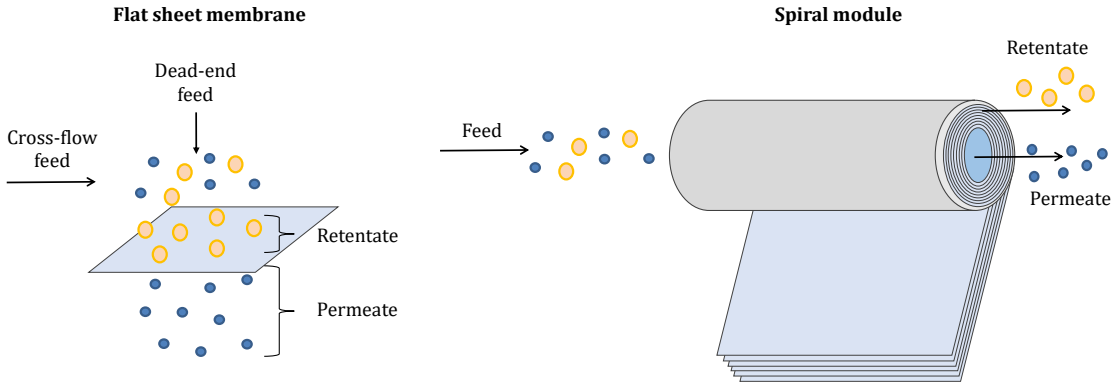

Figure 1.23 – Schematic representation of a flat sheet membrane and a spiral module.

Both hollow-fibre membranes and tubular modules have a cylindrical geometry, cf. Figure 1.24. Hollow-fibre membranes are self-supporting structures withstanding high transmembrane pressure and possessing a high active surface per volume unit, which is why this geometry is one of the most used in industry. They are commonly made of a unique organic material although composite fibres are also manufactured. Depending on the application, the selective layer may be on the external wall, on the internal wall or on both walls of the fibre. Tubular modules are made of one, or several, organic or mineral materials channel(s) and possess a selective layer deposited on the internal wall of the porous substrate, where the permeate flows. Backwashing is impossible to perform on this type of module.

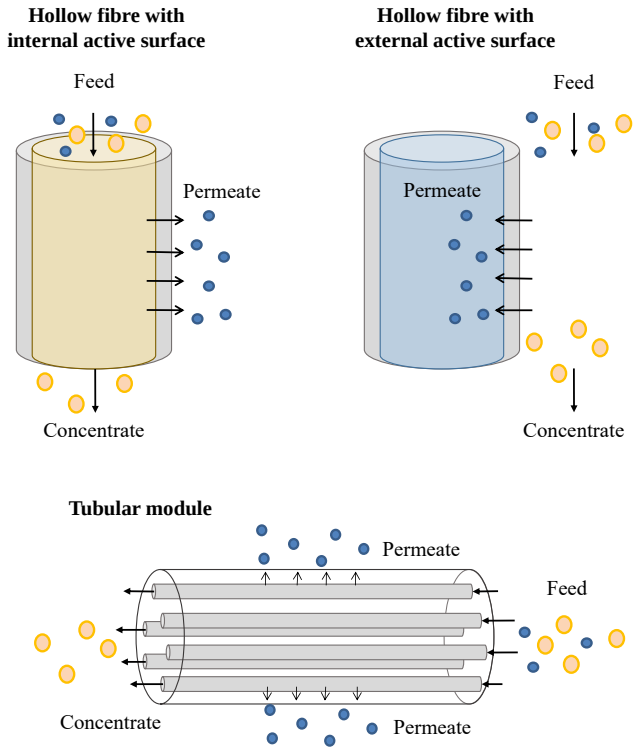

Figure 1.24 – Schematic representation of a hollow fibre membrane and a tubular module.

1.5 Membrane synthesis from surfactant-based organised templates

1.5.1 Synthesis of membrane materials from monomer microemulsions

Two different approaches have been studied regarding the polymerisation of microemulsified structures: using polymerisable surfactants, which will integrate the polymer network upon polymerisation, or non-polymerisable surfactants, which will be eliminated in the washing step. Using polymerisable surfactants is said to retain the microstructure of the solution during the polymerisation process, because the mean-curvature of the surfactant interface will not be modified. These surfactants can also be chosen in order to add some specific properties to the polymer network, such as antibacterial and antifouling properties [84], [85].

On the contrary, non-polymerisable surfactants are not incorporated into the polymer matrix during the polymerisation step, which leads to a destabilisation of the microstructure. Indeed, during polymerisation the affinities of the surfactant interface with the organic phase will be modified, and so will the microstructure. The prediction of the polymer microstructure using this type of surfactants is therefore complicated and limits their application in the industry. The synthesis of thin-film bicontinuous polymer network on supporting membranes have been widely studied for polymerisable surfactants, but only few research work have been performed on the use of non-polymerisable surfactants.

The surfactant and co-surfactant chosen for the formulation of the microemulsion are crucial as their properties will determine the size and the number of pores, the stability and the mechanical properties of the emulsion. If some authors have used a mix of surfactants for the synthesis of thin-film membranes [86], [87], most of the research has been carried out on systems comprising only one surfactant. In the case of the synthesis of microemulsions based on acrylate monomers, the use of acrylic acid (AA) and 2-hydroxyethyl methacrylate (HEMA) as co-surfactant has been widely studied. This last compound are of high interest because of their amphiphilic and polymerisable nature, which can increase the stability of the microstructure during the polymerisation. Plus, addition of HEMA has been proved to decrease the size of the water channels in bicontinuous structures, which can be interesting in order to tailor the porous microstructure range [79].

Our work will focus on the combination of HEMA and methyl methacrylate (MMA). The association of these monomers is mainly used in two specific areas of application: the synthesis of membrane materials and biomedical materials [88]–[99]. This combination is of high interest because if the PHEMA increases the biological response and cell integration and is subjected to biodegradation, it was found to be a poor mechanical medium [100]. Plus, the hydrophilic behaviour of PHEMA is interesting to decrease the hydrophobicity of membranes and thus their fouling ability. Polymem company (Toulouse, France) implemented the grafting of PMMA and PHEMA copolymers on PVDF fibres to give rise to their NEOPHIL™ hollow-fibres [101]. For all these reasons the combination of MMA and HEMA is of high interest in the domain of both membranes and bio-devices.

Regarding the synthesis of membrane materials, acrylate monomers have been used in combination with water and different types of surfactants. These systems have been studied in order to solve one of the major challenge in the field of synthesis of new materials for membrane filtration, which is the compromise between high flux and high selectivity [102]. To this end, some research focused on the synthesis of composite membranes using bicontinuous polymer material.

This nanostructured polymer networks aim to be deposited as thin-film on the surface of a porous supporting membrane, which ensures the mechanical strength of the composite. When a polymerisable surfactant is added into mix, the microstructure is expected to be retained during the polymerisation process, unlike when using non-polymerisable surfactants. Due to the difficulty to predict the microstructure upon polymerisation most of the work done in this field of application has been focused on the use of polymerisable surfactants. Different types of surfactants have been used to synthesise thin-film polymer membrane anionic [17], [103], [104] cationic [17], [21], [79], [84], [85], [105], zwitterionic [106], non-ionic [107], [108] and mixes of surfactants [86]. Table 1.6 gathers the work carried out on the polymerisation of acrylate-MMA systems for the synthesis of bicontinuous polymer network using both RedOx and UV polymerisation processes. To our knowledge, no research has yet dealt with the synthesis of bicontinuous acrylate network using non-polymerisable non-ionic commercial surfactants.

Table 1.6 – Composition of acrylate microemulsion systems containing MMA, their polymerisation process and associated application as presented in the literature.

Monomers	Cross-linker	Surfactant		Co-surfactant	Polymerisation process and initiator(s)	Applications	Reference
		Name	Ionic charge				
NON-POLYMERISABLE SURFACTANTS							
MMA (24 wt.%)	EGDMA (4 wt.% of monomers)	SDS (12 wt.%)	Anionic	HEMA (16 wt.%)	RedOx – APS/TMEDA	-	Chieng et al. (1996) [74]
MMA (18 wt.%)	EGDMA (4 wt.% of monomers)	SDS (4 – 8 wt.%)	Anionic	HEMA (42 wt.%)	RedOx – APS/TMEDA	-	Chieng et al. (1996) [17]
MMA (18 wt.%)	EGDMA (4 wt.% of monomers)	DTAB (6.8 – 12 wt.%)	Cationic	HEMA (42 wt.%)	RedOx – APS/TMEDA	-	Chieng et al. (1996) [17]
MMA (variable)	EGDMA (3 wt.% of monomers)	DTAB (20 wt.%)	Cationic	HEMA	RedOx – APS/TMEDA	Treatment of textile industry wastewaters	Galiano et al. (2018) [85]

AA:MMA (1:1.25 wt.%)	EGDMA (4 wt.% of monomers)	SDS (20 wt.%)	Anionic	AA	UV – DMPA	-	Palani Raj et al. (1993) [109]
MMA (6 – 57 wt.%)	EGDMA (4 wt.% of monomers)	SDS (1 – 10 wt.%)	Anionic	HEMA (20 – 54 wt.%)	UV – DBK	-	Chieng et al. (1995) [104]
MAA (2 – 44 wt.%) MMA (8 - 44 wt.%)	EGDMA (4 wt.% of monomers)	SDS (12 - 90 wt.%)	Anionic	-	UV – AIBN	-	Palani Raj et al. (1995) [110]
DMAEMA (21.25 – 29.75 wt.%) MMA (21.25 – 29.75 wt.%)	EGDMA (4 wt.% of monomers)	SDS (15 wt.%)	Anionic	-	UV – Irgacure® 819		Peinado et al. (2006) [18]
MMA (10 wt.%)	EGDMA (4 wt.% of monomers)	C_nTAB (10 wt.%)	Cationic	HEMA (40 wt.%)	UV – DBK	-	Chieng et al. (1996) [21]
DMAEMA (21.25 – 29.75 wt.%) MMA (21.25 – 29.75 wt.%)	EGDMA (4 wt.% of monomers)	CTAB (15 wt.%)	Cationic	-	UV – Irgacure® 819		Peinado et al. (2006) [18]

POLYMERISABLE SURFACTANTS							
MMA (21 – 33.6 wt.%)	EGDMA (2,5 – 4 wt.%)	AUTMAB (17.5 – 28 wt.%)	Cationic	HEMA (9 – 14.4 wt.%)	RedOx – APS/TMEDA	-	Li et al. (1996) [106]
MMA (29.4 – 42 wt.%)	EGDMA (1.4 wt.%)	AUTMAB (26.46 wt.%)	Cationic	HEMA (0 – 12.6 wt.%)	RedOx – APS/TMEDA UV – DMPA	-	Chew et al. (1998) [79]
MMA (21 wt.%)	EGDMA (3 wt.% of monomers)	AUTEAB (25 wt.%)	Cationic	HEMA (10 wt.%)	RedOx – APS/TMEDA	Treatment of textile industry wastewaters	Galiano et al. (2015) [84], (2018) [85]
AN (30.9 – 42.8 wt.%)	EGDMA (5 wt.% of monomers)	PEO-R-MA-40 (32.5-45 wt.%)	Non-ionic	-	RedOx – APS/TMEDA	Ethanol separation by pervaporation	Liu et al. (2000) [111]
MMA (21 – 33.6 wt.%)	EGDMA (2.5 – 4 wt.%)	AUDMAA (17.5 – 28 wt.%)	Zwitterionic	HEMA (9 – 14.4 wt.%)	RedOx – APS/TMEDA	-	Li et al. (1996) [106]
MMA (21 wt.%)	EGDMA (3 wt.% of monomers)	AUTEAB (25 wt.%)	Cationic	HEMA (0 – 10 wt.%)	RedOx – APS/TMEDA UV – DMPA	Gas separation	Figoli (2001) [105]

MMA (29.4 – 42 wt.%)	EGDMA (1.4 wt.%)	AUDMAA (26.46 wt.%)	Zwitterionic	HEMA (0 – 12.6 wt.%)	RedOx – APS/TMEDA UV – DMPA	-	Chew et al. (1998) [79]
MMA (5 – 35 wt.%)	EGDMA (4 wt.% of polymerisable compounds)	PUD (5 – 35 wt.%)	Anionic	-	UV – DMPA	-	Palani Raj et al. (1992) [112]
MMA (28 – 34 wt.%)	EGDMA (4 wt.% of monomers)	NA11-EAAU (21 – 25.5 wt.%)	Anionic	HEMA (21 – 25.5 wt.%)	UV – DBK	-	Gan et al. (1994) [113]
MMA (21 wt.%)	EGDMA (3 wt.% of monomers)	AUTEAB (25 wt.%)	Cationic	HEMA (10 wt.%)	UV – DMPA, Irgacure® 184	Treatment of textile industry wastewaters	Galiano et al. (2018) [114]
MMA (10 – 21.25 wt.%)	EGDMA (4 wt.% of monomers)	PEO-R-MA-40 (20 – 42.5 wt.%)	Non-ionic	HEMA (10 – 21.25 wt.%)	UV – DMPA	-	Gan et al. (1997) [108]
NIPAAm (0 – 25 wt.%) MMA (7.5 – 20 wt.%)	EGDMA (2 wt.%)	PEO-R-MA-40 (35 wt.%)	Non-ionic	HEMA (5 – 20 wt.%)	UV – DMPA	Cell transplantation and wound healing	Wang et al. (2006) [107]

MMA (20 – 60 wt.%)	EGDMA (0 – 4 wt.%)	AUDMAA (20 – 40 wt.%)	Zwitterionic	-	UV – DMPA	-	Gan et al. (1995) [115]
MMA (20 – 35 wt.%)	EGDMA (1 wt.%)	AIPS (29 – 34 wt.%)	Zwitterionic	-	UV – DMPA	-	Gan et al. (2005) [116]
SURFACTANT MIX							
MMA (18 wt.%)	EGDMA (4 wt.% of monomers)	SDS – NA11-EAAU (0 – 100 wt.% ; 100 - 0 wt.%)	Anionic	HEMA (18 wt.%)	UV – DBK	-	Chieng et al. (1996) [86]
MMA (5 wt.%)	-	DTAB-DDAB (3.75 wt.% - 1.25 wt.%)	Cationic	-	UV – AIBN	-	Bléger et al. (1994) [87]

To our knowledge the bicontinuous microstructure of the liquid MMA:water:HEMA:surfactant(s) systems as template for membrane synthesis have only been studied using conductivity, quasi-elastic light scattering (QELS) and viscosity measurements. Other bicontinuous and microemulsified systems have been successfully characterised using SAXS [52], [55], [63], [117], [118] and DOSY-NMR [47], [52], [53], [55] analyses. The resulting polymer microstructures were all probed using electron microscopy (SEM, TEM or cryo-SEM) and the filtration performances of the polymer network were only occasionally tested [17], [84], [85], [114], [119]. The measured permeability as a function of the material thickness were quite low, ranging from 0.07 to 5 $L.m^{-2}.L^{-1}.bar^{-1}$, except for Galiano (2012) [119] who reported a composited permeability of 200 $L.m^{-2}.L^{-1}.bar^{-1}$. The selectivity of the synthesised structures has however not been studied in depth.

Even fewer authors investigated the rejection abilities of their composite membranes. Galiano et al. [84], [114] synthesised a composite PES-AUTEAB microemulsion membrane and reported a drastic decrease in permeability, but no increase in humic acid (HA) rejection after coating. It is however debatable whether it is scientifically worthwhile to determine the selectivity of a coated membrane when the rejection of the commercial pristine membrane was already 89 ± 8.4% as stated by the authors. Galiano [119] also investigated the rejection of a Remazol Brilliant Blue and Acid Red 4 dye and observed a 27% and 36% increase in their rejection respectively, compared to the pristine commercial membrane, associated to a permeability decrease from 600 to 200 $L.m^{-2}.L^{-1}.bar^{-1}$. This author also tested the salt rejection of NaCl and $MgSO_4$ from a dense DTAB microemulsion coating deposited on the same PES commercial membrane. They reported a rejection of 75% and 88% respectively, while the salt rejection of the pristine PES membrane was 5 and 7% respectively. The permeability of their resulting DTAB-composite membrane was however dramatically reduced to 1.4-4 $L.m^{-2}.L^{-1}.bar^{-1}$. To our knowledge, no other research has been carried out on the investigation of microemulsion thin-film composite membranes.

We must also note – except for Galiano et al. (2015, 2018, 2012) [84], [114], [119] and Chieng et al. (1996) [21] – all of the authors listed in Table 1.6 who investigated on the synthesis of polymer networks based on microemulsion template containing non-polymerisable surfactants reported the obtention of opaque materials and/or

micrometric pore sizes upon the polymerisation of transparent microemulsions. This transition to a micrometric structure is an irrefutable proof of the modification of the structure from a nano- to a microscale and thus indicating the destabilisation of the initial monomer template structure during the polymerisation process. Dos Santos et al. (2011) [120] highlighted the evolution of the structure of acrylate counterions during the polymerization, using the cationic alkyltrimethylammonium ions as surfactant in aqueous media, and how phase diagram "comes alive" during the polymerisation process. One might therefore question the ability of the polymerisable co-surfactant and the cross-linker to actually preserve the original microstructure without the use of a polymerisable surfactants.

1.5.2 Synthesis of membrane materials from monomer liquid crystals

Liquid crystals may exhibit interesting optical and electrical properties and have been widespread in recent decades, for example in Liquid Crystal Display (LCD) for television screens [121]. In the field of membrane filtration, the synthesis of composite membranes using liquid crystals for gas and liquid separation has been investigated and proved promising. To our knowledge, limited work has been reported on the use of thermotropic liquid crystals (TLC) for membrane synthesis. Such thermosensitive structures are however widely found in electro-optical devices and thermography applications [119].

Lyotropic liquid crystals (LLC) allow for the synthesis of nanometric easily functionalisable structures, of great potential for catalytic applications or drug delivery systems [10], [25]. LLCs however require a polymerisation step to immobilise their microstructure prior to use. Similarly to microemulsions, the destabilisation of the system must be avoided during polymerisation. To that end, photopolymerisation processes combined with the use of a cross-linker are widely used. Plus, this UV-priming method allows for a low operating temperature, which can beneficial to some LLC structures that only occur in specific temperature ranges [10], [25], and [123].

Most of the structures investigated for membrane synthesis are cubic and hexagonal structures. Indeed, some authors reported [10], [124] a low mechanical resistance of lamellar polymers network. For the same reason, normal hexagonal structures (H_I) are of lower interest and will not be discussed in the following. On the contrary, polymerisation of inverted hexagonal structures (H_{II}) allow for a robust continuous polymeric network

containing aqueous channels. The resulting structures are of significant interest, due to their insolubility in most common solvent, as well as their low ability to swell. Inverted hexagonal polymer networks are considered as organic analogue to zeolites and mesoporous sieves. Plus they exhibit some catalytic potential due to the good accessibility to reactive sites they offer [10]. However, H_{II} composite membranes display limited performances due to the difficulty of aligning the pores on all layers of the membrane.

Bicontinuous cubic LLCs (Q) are an alternative to H_{II} structures due to their interconnected and symmetrical networks, which allows for a better material transfer between the membrane layers. These structures exhibit an organised structure with uniform lattice size. Due to the tortuous nature of their polymer networks, such structures are almost impossible to completely obstruct. However, the movement of the molecules through the composite membrane will be limited in return [25].

Because discontinuous cubic LLCs (I) do not possess an interconnected network, these structures will not be further discussed in this work. Both normal Q_I and inverted Q_{II} cubic LLC networks have been successfully polymerised. However Gan et al. (2001) stressed that the molecular design of reagents leading to Q_{II} LLC is more complicated than for the Q_I LLCs. Gin et al. (2001) [10] developed novel LLC precursors by substitution of the counter-ion and by the synthesis of "gemini" monomers. These "gemini" monomers allow for the polymerisation of the two hydrocarbon parts without changing the overall shape of the molecule. Wiesenauer et al. (2012) [25] also reported lower CMC for "gemini" precursors and a higher mechanical resistances of the resulting polymer networks, allowing no cross-linker to be used. Pindzola et al. (2003) [125] and Hatakeyama et al. (2010) [126] also synthesised Q_I structures based on the same "gemini" monomers concept. The latter aimed to produce an attractive "gemini" LLC precursor on an industrial scale, using an ammonium base instead of a phosphorus one, combined to the possibility to modify the hydrocarbon length.

Table 1.7 summarises several LLC precursors developed in the past few decades, as well as their aimed application. Due to their ionic nature, two main application fields have been investigated: nanostructured transport materials and nanostructured membranes. In all the presented cases, the liquid crystal precursors have been polymerised and cross-linked in order to give rise to nanoporous, monodispersed and highly resistant materials.

- **Liquid crystals for nanostructured transporting membrane materials**

Wiesenauer et al. (2012) [25] developed Q_{II} LLC precursors in a lithium salt-doped electrolyte and propylene carbonate, for materials with improved ionic conductivity (e.g. lithium batteries). Similarly, Ichikawa et al. (2011) [130], Frise et al. (2009) [128] and Soberats et al. (2015) [129], developed bicontinuous Q_{II} and H_{II} TLC precursors for the synthesis of ion-conductive polymeric films exhibiting interconnected ionic channels to enhance ion transportation.

- **Liquid crystals for aqueous membrane filtration**

Several authors highlighted the possibility to create composite membranes for water filtration, based on liquid crystal precursors. To that end, two main polymerisation methods have been mainly investigated: solvent-casting [14], [130] and hot-pressing. The latter allows to avoid water evaporation and thus a modification of the structure prior to polymerisation [123]. However, Carter et al. (2012) [131] demonstrated lower membrane performances when choosing the hot-pressing method over the solvent-casting one. Their research team therefore reported the use of low-volatile, water-miscible and non-toxic solvents to replace water in the solvent-casting process (e.g. glycerol). It should also be noted that only the solvent-casting method can be adapted to liquid crystal solution dip-coating on hollow-fibres, in order to further improve the performances of the composite membranes.

Some researchers reported the use of liquid crystals to improve the performances of membranes for water treatment, such Mahalingham et al. (2018) [132] who used graphene oxide liquid crystals, or Sakamoto et al. (2018) [133]. However, the research group of Douglas Gin and Richard D. Noble (CU Boulder, United States) is to our knowledge the team that has most extensively investigated the liquid crystals for membrane synthesis for separative applications. This research team reported the synthesis of composite membranes that demonstrated higher rejection than some commercial nanofiltration membranes, with little impact on the composite permeability.

Table 1.7 – Liquid crystals used for membrane synthesis and their application field, as presented in the literature.

Liquid crystal	Type	Structure	Applications	Reference
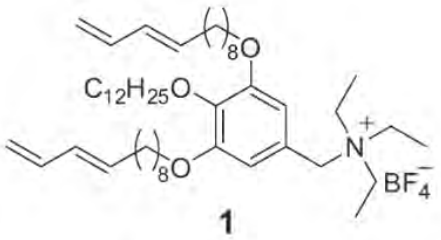 1	Thermotropic	Q_{II}	Conducting cross-linked porous material	Frise et al. (2009) [128]
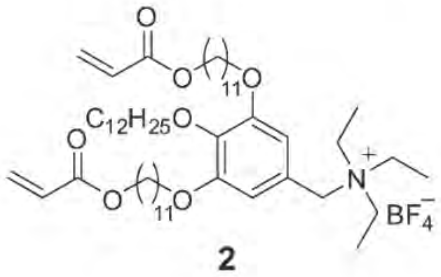 2				Ichikawa et al. (2011) [127]
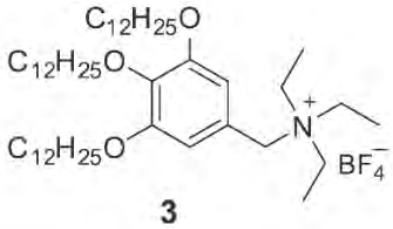 3			$NaCl$, $MgCl_2$, Na_2SO_4, $MgSO_4$ rejection	Henmi et al. (2012) [130]

	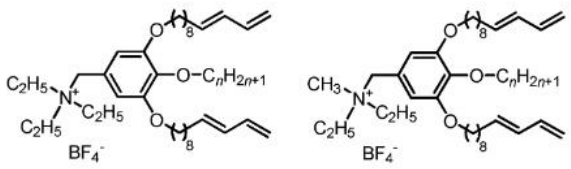 **1**(*n*): *n* = 10, 12, 14 **2**(*n*): *n* = 10, 12 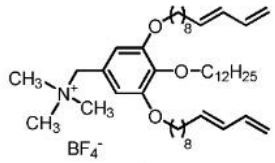 **3**(12) 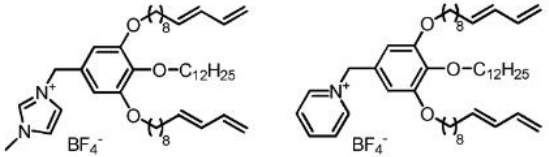 **4**(12) **5**(12)	Thermotropic	1: Q_{II} 2-5: H_{II}	NaCl, $MgSO_4$ rejection	Sakamoto et al. (2018) [133]
			H_{II}		Zhou et al. (2007) [14]
	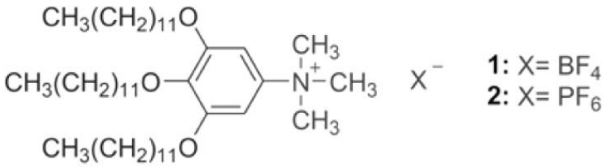 **1:** X= BF_4 **2:** X= PF_6	Thermotropic	H_{II}	Ion transport	Soberats et al. (2015) [129]

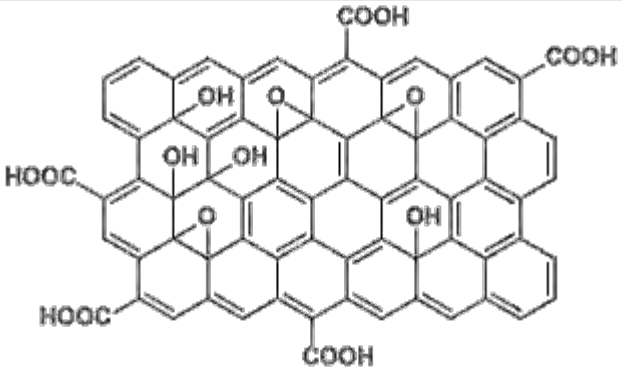 Graphene oxide	Lyotropic	L	Water filtration	Mahalingam et al. (2018) [132]
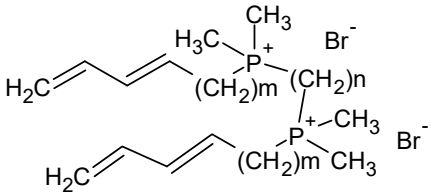 (m,n) = (10,2); (10,6); (14,6); (14,8)	Lyotropic	H_I, Q_I, L Q_I	- NaCl, $MgCl_2$, $CaCl_2$, glucose, sucrose, ethylene glycol, glycerol, PEG-600 rejection	Pindzola et al. (2002) [125] Zhou et al. (2007) [14]

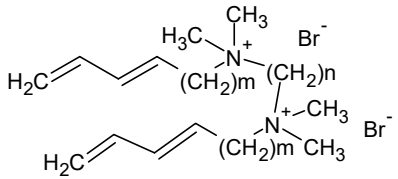 (m,n) = (10,3); (10,6)	Lyotropic	Q_I	$NaCl$, $MgCl_2$, $CaCl_2$, KCl, glucose, sucrose, ethylene glycol, glycerol rejection	Hatakeyama et al. (2010) [126]
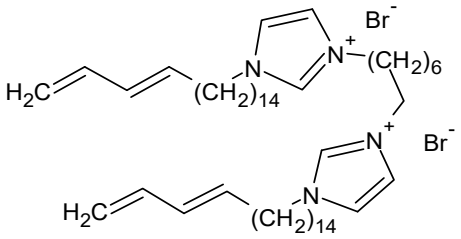	Lyotropic	Q_I	-	Bara et al. (2010) [134]
			Sucrose, glycerol, ethylene glycol, $NaCl$, $MgCl_2$ rejection	Carter et al. (2012) [131]

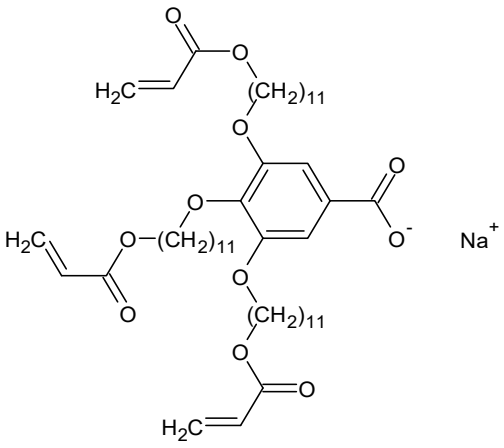	Lyotropic	H_{II}	Selective gas barrier for chemical agents	Gin et al. (2008) [123]
			Dyes filtration	Zhou et al. (2005) [135]
[N-(-4-methyoxybenzylidene)-4'-heptylaniline, 4-pentyl-4'-nitrile-biphenyl and cholesteryl oleyl carbonate]	-	-	Blood-compatible membranes	Zhou et al. (1999) [136]

1.6 Conclusion

This bibliographic study focused on the synthesis, the characterisation and the polymerisation of microemulsions and liquid crystals, and more particularly of bicontinuous nanometric structures. We discussed the specifity of each microstructure, as well as the different factors affecting more on the resulting microstructure (Section 1.1). We then detailed the various possible analytical techniques to determine the microstructure of organised surfactant-based solutions (Section 1.2). We subsequently discussed the different priming techniques to initiate the radical polymerisation in emulsion and microemulsions (Section 1.3) in order to obtain an interconnected polymeric membrane from a microemulsion template. The liquid membrane filtration process was then introduced (Section 1.4) and a literature review was carried out on the various researches conducted on the synthesis of polymeric membranes using microemulsied and liquid crystal templates (Section 1.5).

If promising syntheses of bicontinuous microstructures have been obtained the last decades, we however observe that very little extensive analyses of liquid microemulsions were conducted before the membrane thin-film syntheses. SAXS and DOSY-NMR were most of the time overlooked and only conductimetric, viscosimetric or QELS analyses were conducted. We therefore suggest in this thesis work to extensively investigate our quaternary and quinary non-ionic systems. Such a study will allow us to fully assess the possible monomer microstructures adopted by the systems, as dicussed in Chapter 3. We will also discuss, how the initial microstructure and the polymerisation process will impact on the final polymer porous material microstructure. The resulting polymer networks will be characterised and their performance on membrane filtration will be addressed in Chapter 4.

Finally, from an industrial point of view, the synthesis of hollow fibre composite membranes is highly desirable, due to the high active surface per unit volume of these membranes. However, to our knowledge only one research team [137] coated a bicontinuous microemulsion on the surface of hollow-fibre membranes. The Laboratoire de Génie Chimique de Toulouse having substantially developed research projects on the coating of hollow-fibre membranes, we propose to discuss the applicability of this coating process to microemulsion deposits. The mathematical models depicting the liquid-on-fibre deposition will be adapted to the case of microemulsions in Chapter 5.

References

[1] R. J. Stokes and D. F. Evans, *Fundamentals of interfacial engineering*. John Wiley & Sons, 1996.

[2] D. N. Karunaratne, G. Pamunuwa, and U. Ranatunga, *Introductory chapter : Microemulsions*. 2017. doi: http://dx.doi.org/10.5772/57353.

[3] D. Varade, K. Aramaki, and C. Stubenrauch, 'Phase diagrams of water–alkyltrimethylammonium bromide systems', *Colloids Surf. A Physicochem. Eng. Asp.*, vol. 315, no. 1–3, pp. 205–209, 2008, doi: 10.1016/j.colsurfa.2007.07.031.

[4] T. P. Hoar, 'Transparent Water-in-Oil Dispersions : the Oleopathic Hyro-Micelle', *Nature*, vol. 152, pp. 102–103, 1943, doi: 10.1097/01241398-198709000-00023.

[5] B. Lindman, N. Kamenka, B. Brun, and P. G. Nilsson, 'On the structure and dynamics of microemulsions self-diffusion studies', *Microemulsions*, Springer, 1982, pp. 115–129.

[6] P. A. Winsor, 'Hydrotropy, solubulisation and related emulsification porcesses. Part I', *J. Chem. Soc. Faraday Trans.*, vol. 53, no. 9, pp. 1689–1699, 1947, doi: 10.1017/CBO9781107415324.004.

[7] C. Stubenrauch, R. Tessendorf, A. Salvati, D. Topgaard, R. Strey, and I. Lynch, 'Gelled polymerizable microemulsions. 2. Microstructure', *Langmuir*, vol. 24, no. 16, pp. 8473–8482, 2008, doi: 10.1021/la800918g.

[8] P. Chatelain, 'Cristaux liquides', *Tech. Ing.,* no. 1, 1996, doi: 10.3406/bulmi.1954.4892.

[9] M. W. Tate, E. F. Eikenberry, D. C. Turner, E. Shyamsunder, and S. M. Gruner, 'Nonbilayer phases of membrane lipids', *Chem. Phys. Lipids*, vol. 57, no. 2–3, pp. 147–164, 1991, doi: 10.1016/0009-3084(91)90073-K.

[10] D. L. Gin, W. Gu, B. A. Pindzola, and W. J. Zhou, 'Polymerized lyotropic liquid crystal assemblies for materials applications', *Acc. Chem. Res.*, vol. 34, no. 12, pp. 973–980, 2001, doi: 10.1021/ar000140d.

[11] G. J. T. Tiddy, 'Surfactant-water liquid crystal phases', *Phys. Rep.*, vol. 57, no. 1, pp. 1–46, 1980, doi: 10.1016/0370-1573(80)90041-1.

[12] J. M. Seddon, 'Structure of the inverted hexagonal (HII) phase, and non-lamellar phase transitions of lipids', *Biochim. Biophys. Acta – Rev. Biomembr.*, vol. 1031, no. 1, pp. 1–69, 1990, doi: 10.1016/0304-4157(90)90002-T.

[13] K. Fontell, 'Cubic phases in surfactant and surfactant-like lipid systems', *Colloid Polym. Sci.*, vol. 268, no. 3, pp. 264–285, 1990, doi: 10.1007/BF01490251.

[14] M. Zhou, P. R. Nemade, X. Lu, X. Zeng, E. S. Hatakeyama, R. D. Noble and D. Gin, 'New type of membrane material for water desalination based on a cross-linked bicontinuous cubic lyotropic liquid crystal assembly', *J. Am. Chem. Soc.*, vol. 129, no. 31, pp. 9574–9575, 2007, doi: 10.1021/ja073067w.

[15] R. Strey, M. Brandt, B. Jakobs, and T. Sottmann, 'Efficiency boosting by amphiphilic block copolymers in microemulsions: Dependence on surfactant and oil chain length', *Stud. Surf. Sci. Catal.*, vol. 132, pp. 39–44, 2000.

[16] R. Strey, 'Microemulsion microstructure and interfacial curvature', *Colloid Polym. Sci.*, vol. 272, no. 8, pp. 1005–1019, 1994, doi: 10.1007/BF00658900.

[17] T. H. Chieng, L. M. Gan, W. K. Teo, and K. L. Pey, 'Porous polymeric membranes by bicontinuous microemulsion polymerization: Effect of anionic and cationic surfactants', *Polymer (Guildf)*, vol. 37, no. 26, pp. 5917–5925, 1996, doi: 10.1016/S0032-3861(96)00452-1.

[18] C. Peinado, P. Bosch, V. Martin, and T. Corrales, 'Photoinitiated Polymerization in Bicontinuous Microemulsions: Fluorescence Monitoring', *J. Polym. Sci. A. Polym. Chem.*, vol. 44, pp. 5291–5303, 2006, doi: 10.1002/pola.

[19] T. Cosgrove, *Colloid science: principles, methods and applications*. John Wiley & Sons, 2010.

[20] R. Aveyard, B. P. Binks, S. Clark, and J. Mead, 'Interfacial Tension Minima in Oil-Water-Surfactant Systems. Behaviour of alkane–aqueous NaCl systems containing aerosol OT', *J. Chem. Soc. Faraday trans. 1*, vol. 82, no. 1, pp. 125–142, 1986, doi: https://doi.org/10.1039/F19868200125.

[21] T. H. Chieng, L. M. Gan, C. H. Chew, S. C. Ng, and K. L. Pey, 'Microporous polymeric materials by microemulsion polymerization: Effect of the ratio of long and short alkyl chain length cationic surfactants', *Polymer (Guildf)*, vol. 37, no. 21, pp. 4823–4831, 1996, doi: 10.1016/S0032-3861(96)00316-3.

[22] R. Skurtveit, J. Sjöblom, J. Bouwstra, G. Gooris, and M. H. Selle, 'Effect of electrolyte on the phase behavior and emulsion stability in the system didodecyldimethylammonium bromide (DDAB)/dodecane/water', *J. Colloid Interface Sci.*, vol. 152, no. 1, pp. 205–217, 1992, doi: 10.1016/0021-9797(92)90020-M.

[23] A. Ceglie, K. P. Das, and B. Lindman, 'Microemulsion structure in four-component systems for different surfactants', *Colloids and surfaces*, vol. 28, pp. 29–40, 1987, doi: 10.1016/0166-6622(87)80164-6.

[24] B. Jakobs, T. Sottmann, R. Strey, J. Allgaier, L. Willner, and D. Richter, 'Amphiphilic block copolymers as efficiency boosters for microemulsions', *Langmuir*, vol. 15, no. 20, pp. 6707–6711, 1999, doi: 10.1021/la9900876.

[25] B. R. Wiesenauer and D. L. Gin, 'Nanoporous polymer materials based on self-organized, bicontinuous cubic lyotropic liquid crystal assemblies and their applications', *Polym. J.*, vol. 44, no. 6, pp. 461–468, 2012, doi: 10.1038/pj.2012.15.

[26] Y. Yamashita and K. Sakamoto, 'Hydrophilic–Lipophilic Balance (HLB): Classical Indexation and Novel Indexation of Surfactant', *Encyclopedia of Biocolloid and Biointerface Science*, H. Ohshima, Ed. Wiley, 2016, pp. 570–574.

[27] J. R. Kanicky, J.-C. Lopez-Montilla, S. Pandey, and D. O. Shah, 'Surface Chemistry in the Petroleum Industry', *Handbook of Applied Surface and Colloid Chemistry*, Wiley, 2001, pp. 251–267.

[28] W. T. Godbey, 'Gene delivery', *Biotechnology and its Applications*, 2nd ed., Academic Press, 2022, pp. 287–325. doi: 10.1016/B978-0-12-817726-6.00012-5.

[29] J. N. Israelachvili, 'Thermodynamic Principles of Self-Assembly', *Intermolecular and Surface Forces*, Academic Press, 2011, pp. 503–534. doi: 10.1016/B978-0-12-375182-9.10019-3.

[30] W. Griffin, 'Classification of surface-active agents by HLB', *J. Soc. Cosmet. Chem.*, vol. 1, pp. 311–326, 1949.

[31] W. Griffin, Calculation of HLB values of non-ionic surfactants, *J. Soc. Cosmet. Chem.*, vol. 5, pp. 249–256, 1954.

[32] J. T. Davies, *Interfacial Phenomena*, 2nd ed. 1963.

[33] I. J. Lin, J. P. Friend, and Y. Zimmels, 'The effect of structural modifications on the hydrophile–lipophile balance of ionic surfactants', *J. Colloid Interface Sci.*, vol. 45, no. 2, pp. 378–385, Nov. 1973, doi: 10.1016/0021-9797(73)90275-0.

[34] X. Guo, Z. Rong, and X. Ying, 'Calculation of hydrophile–lipophile balance for polyethoxylated surfactants by group contribution method', *J. Colloid Interface Sci.*, vol. 298, no. 1, pp. 441–450, Jun. 2006, doi: 10.1016/J.JCIS.2005.12.009.

[35] J. N. Israelachvili, D. J. Mitchell, and B. W. Ninham, 'Theory of self-assembly of hydrocarbon amphiphiles into micelles and bilayers', *J. Chem. Soc., Faraday Trans. 2*, vol. 72, pp. 1525–1568, 1976, doi: 10.1039/F29767201525.

[36] I. J. Lin and L. Marszall, 'CMC, HLB, and effective chain length of surface-active anionic and cationic substances containing oxyethylene groups', *J. Colloid Interface Sci.*, vol. 57, no. 1, pp. 85–93, 1976, doi: 10.1016/0021-9797(76)90178-8.

[37] C. Tanford, 'Micelle Shape and Size', *J. Phys. Chem.*, vol. 76, no. 21, pp. 3020–3024, 1972, doi: 10.1021/j100665a018.

[38] F. Reiss-Husson and V. Luzzati, 'The Structure of the Micellar Solutions of Some Amphiphilic Compounds in Pure Water as Determined by Absolute Small-Angle X-Ray Scattering Techniques', *J. Phys. Chem.*, vol. 68, no. 12, pp. 3504–3511, 1964, doi: 10.1021/j100794a011.

[39] D. Attwood and A. T. Florence, 'Surfactants', *FASTtrack: Physical Pharmacy*, 2nd ed., Pharmaceutical Press, Ed. 2012, pp. 55–78. Accessed: Feb. 11, 2022. [Online]. Available: www.pharmpress.com

[40] A. Lattes, I. Rico, A. de Savignac, and A. A. Z. Samii, 'Formamide, a water substitute in micelles and microemulsions structural analysis using a diels-alder reaction as a chemical probe', *Tetrahedron*, vol. 43, no. 7, pp. 1725–1735, 1987, doi: 10.1016/S0040-4020(01)90284-4.

[41] C. Noirjean, 'Microémulsions Solidifiées : une nouvelle voie vers les conducteurs protoniques ?', PhD thesis, Université de Versailles Saint-Quentin-en-Yvelines, 2014. [Online]. Available: https://tel.archives-ouvertes.fr/tel-01095096/

[42] N. M. Correa, J. J. Silber, R. E. Riter, and N. E. Levinger, 'Nonaqueous Polar Solvents in Reverse Micelle Systems', *Chem. Rev.*, vol. 112, no. 8, pp. 4569–4602, 2012, doi: 10.1021/CR200254Q.

[43] K. Shinoda and H. Saito, 'The Stability of O/W type emulsions as functions of temperature and the HLB of emulsifiers: The emulsification by PIT-method', *J. Colloid Interface Sci.*, vol. 30, no. 2, pp. 258–263, 1969, doi: 10.1016/S0021-9797(69)80012-3.

[44] M. Nilsson, O. Söderman, and I. Johansson, 'The effect of polymers on the phase behavior of balanced microemulsions: diblock-copolymer and comb-polymers', *Colloid Polym. Sci.*, vol. 284, no. 11, pp. 1229–1241, 2006.

[45] M. Fanun, *Microemulsions: properties and applications*. CRC press, 2008.

[46] Y. Talmon and S. Prager, 'Statistical thermodynamics of phase equilibria in microemulsions', *J. Chem. Phys.*, vol. 69, no. 7, pp. 2984–2991, 1978, doi: https://doi.org/10.1063/1.437016.

[47] B. Lindman and U. Olsson, 'Structure of microemulsions studied by NMR', *Berichte der Bunsengesellschaft/Physical Chemistry Chemical Physics*, vol. 100, no. 3, pp. 344–363, 1996, doi: 10.1002/bbpc.19961000321.

[48] T. Gostan, D. Tramesel, E. Brun, Y. Prigent, and M.-A. Delsuc, 'L'expérience DOSY, une puissante méthode RMN pour l'analyse de mélanges complexes et la détection de traces', *Spectra analyse*, vol. 240, no. December 2013, pp. 25–32, 2004.

[49] Brucker Biospin, 'DOSY and Diffusion by NMR'.

[50] R. Najjar, 'Microemulsions – A Brief Introduction', *Microemulsions – An introduction to Properties and Applications*, 2012, pp. 3–30.

[51] P. Kumar and K. L. Mittal, *Handbook of Microemulsion Science and Technology*. New York: Marcel Dekker, 1999.

[52] A. Kogan, D. E. Shalev, U. Raviv, A. Aserin, and N. Garti, 'Formation and characterization of ordered bicontinuous microemulsions', *J. Phys. Chem. B.*, vol. 113, no. 31, pp. 10669–10678, 2009, doi: 10.1021/jp901617g.

[53] V. Tchakalova, C. Bailly, and W. Fieber, 'Food-grade bicontinuous microemulsions', *Flavour Fragr. J.*, vol. 29, no. 1, pp. 67–74, 2014, doi: 10.1002/ffj.3181.

[54] Y. F. Zuev, A. B. Mirgorodskaya, and B. Z. Idiyatullin, 'Structural properties of microheterogeneous surfactant-based catalytic systems: Multicomponent self-diffusion NMR approach', *Appl. Magn. Reson.*, vol. 27, no. 3–4, pp. 489–500, 2004, doi: 10.1007/BF03166745.

[55] B. Lindman, K. Shinoda, U. Olsson, D. Anderson, G. Karlström, and H. Wennerström, 'On the demonstration of bicontinuous structures in microemulsions', *Colloids Surf.*, vol. 38, no. 1, pp. 205–224, 1989, doi: 10.1016/0166-6622(89)80154-4.

[56] D. P. Acharya and P. G. Hartley, 'Progress in microemulsion characterization', *Curr. Opin. Colloid Interface Sci.*, vol. 17, no. 5, pp. 274–280, 2012, doi: 10.1016/j.cocis.2012.07.002.

[57] K. Aramaki, K. Tawa, L. K. Shrestha, T. Iwanaga, and M. Karnada, 'Formation and cleansing performance of bicontinuous microemulsions in water/poly (oxyethylene) alkyl ether/ester-type oil systems', *J. Oleo Sci.*, vol. 62, no. 10, pp. 803–808, 2013, doi: 10.5650/jos.62.803.

[58] L. Guo, Y. Fang, X. Liang, Y. Xu, J. Chen, Y. Li, S. Fang, and Y. Meng, 'Influence of polysorbates (Tweens) on structural and antimicrobial properties for microemulsions', *Int. J. Pharm.*, vol. 590, no. 18, p. 119939, 2020, doi: 10.1016/j.ijpharm.2020.119939.

[59] M. Nayeri, M. Zackrisson, and J. Bergenholtz, 'Scattering functions of core-shell-struct ured hard spheres with Schulz-distributed radii', *J. Phys. Chem. B.* ,vol. 113, no. 24, pp. 8296–8302, 2009, doi: 10.1021/jp811482w.

[60] "core_shell_sphere – SasView 5.0.4 documentation." https://www.sasview.org/docs/user/models/core_shell_sphere.html (accessed Jan. 05, 2022).

[61] "hardsphere – SasView 5.0.4 documentation." https://www.sasview.org/docs/user/models/hardsphere.html (accessed Jan. 05, 2022).

[62] S. Peng, Q. Guo, T. C. Hughes, and P. G. Hartley, 'In situ synchrotron SAXS study of polymerizable microemulsions', *Macromolecules*, vol. 44, no. 8, pp. 3007–3015, 2011, doi: 10.1021/ma102978u.

[63] R. J. Hickey, T. M. Gillard, M. T. Irwin, T. P. Lodge, and F. S. Bates, 'Structure, viscoelasticity, and interfacial dynamics of a model polymeric bicontinuous microemulsion', *Soft Matter*, vol. 12, no. 1, pp. 53–66, 2015, doi: 10.1039/c5sm02009c.

[64] K. V. Schubert, R. Strey, S. R. Kline, and E. W. Kaler, 'Small angle neutron scattering near Lifshitz lines: Transition from weakly structured mixtures to microemulsions', *J. Chem. Phys.*, vol. 101, no. 6, pp. 5343–5355, 1994, doi: 10.1063/1.467387.

[65] S. H. Chen, S. L. Chang, and R. Strey, 'On the interpretation of scattering peaks from bicontinuous microemulsions', *Prog. Colloid Polym. Sci.*, vol. 81, pp. 30–35, 1990, doi: 10.1007/bfb0115519.

[66] S. Xie, D. J. Meyer, E. Wang, F. S. Bates, and T. P. Lodge, 'Structure and Properties of Bicontinuous Microemulsions from Salt-Doped Ternary Polymer Blends', *Macromolecules*, vol. 52, no. 24, pp. 9693–9702, 2019, doi: 10.1021/acs.macromol.9b01963.

[67] C. Schulreich, C. Angermann, S. Höhn, R. Neubauer, S. Seibt, R. Stehle, A. Lapp, A. Richardt, A. Diekmann and T. Hellweg, 'Bicontinuous microemulsions with extremely high temperature stability based on skin friendly oil and sugar surfactant', *Colloids Surf. A Physicochem. Eng. Asp.*, vol. 418, pp. 39–46, 2013, doi: 10.1016/j.colsurfa.2012.10.039.

[68] G. Tartaro, H. Mateos, D. Schirone, R. Angelico, and G. Palazzo, 'Microemulsion microstructure(s): A tutorial review', *Nanomaterials*, vol. 10, no. 9, pp. 1–40, 2020, doi: 10.3390/nano10091657.

[69] C. Stubenrauch, R. Tessendorf, R. Strey, I. Lynch, and K. A. Dawson, 'Gelled polymerizable microemulsions. 1. Phase behavior', *Langmuir*, vol. 23, no. 14, pp. 7730–7737, 2007, doi: 10.1021/la700685g.

[70] M. Magno, R. Tessendorf, B. Medronho, M. G. Miguel, and C. Stubenrauch, 'Gelled polymerizable microemulsions. Part 3 Rheology', *Soft Matter*, vol. 5, no. 23, pp. 4763–4772, 2009, doi: 10.1039/b914281a.

[71] A. Figoli, J. Hoinkis, A. Alsoy Sacide, and J. Bundschuh, *Application of Nanotechnology in Membranes for Water Treatment*. 2017.

[72] D. Distler, W. S. Neto, and F. Machado, 'Emulsion Polymerization', *Reference Module in Materials Science and Materials Engineering*, 2017. doi: 10.1016/B978-0-12-803581-8.03746-2.

[73] N. Kohut-Svelko, R. Pirri, J. M. Asua, and J. R. Leiza, 'Redox Initiator Systems for Emulsion Polymerization of Acrylates', *J. Polym. Sci. A. Polym. Chem.*, vol. 47, pp. 2917–2927, 2009, doi: 10.1002/pola.

[74] T. H. Chieng, L. M. Gan, C. H. Chew, S. C. Ng, and K. L. L. Pey, 'Formation of microporous polymeric materials by microemulsion polymerization of methyl methacrylate and 2-hydroxyethyl methacrylate', *J. Appl. Polym. Sci.*, vol. 60, pp. 1561–1568, 1996, doi: 10.1002/(SICI)1097-4628(19960606)60:10<1561::AID-APP6>3.0.CO;2-H.

[75] F. J. E. Sanz, J. F. Lahitte, and J. C. Remigy, 'Membrane synthesis by microemulsion polymerisation stabilised by commercial non-ionic surfactants', *Desalination*, vol. 199, no. 1–3, pp. 127–129, 2006, doi: 10.1016/j.desal.2006.03.156.

[76] C. Yagci and U. Yildiz, 'Redox polymerization of methyl methacrylate with allyl alcohol 1,2-butoxylate-block-ethoxylate initiated by Ce(IV)/HNO3 redox system', *Eur. Polym. J.*, vol. 41, no. 1, pp. 177–184, 2005, doi: 10.1016/j.eurpolymj.2004.08.008.

[77] H. Yu, Y. Fang, L. Chen, and S. Chen, 'Investigation of redox initiators for free radical frontal polymerization', *Polym. Int.*, vol. 58, no. 8, pp. 851–857, 2009, doi: 10.1002/pi.2590.

[78] J. E. Puig, V. H. Pérez-Luna, M. Pérez-González, E. R. Macías, B. E. Rodríguez, and E. W. Kaler, 'Comparison of oil-soluble and water-soluble initiation of styrene polymerization in a three-component microemulsion', *Colloid Polym. Sci.*, vol. 271, no. 2, pp. 114–123, 1993, doi: 10.1007/BF00651813.

[79] C. H. Chew, T. D. Li, L. H. Gan, C. H. Quek, and L. M. Gan, 'Bicontinuous-nanostructured polymeric materials from microemulsion polymerization', *Langmuir*, vol. 14, no. 21, pp. 6068–6076, 1998, doi: 10.1021/la970990a.

[80] M. A. Macchione, C. Biglione, and M. Strumia, 'Design, synthesis and architectures of hybrid nanomaterials for therapy and diagnosis applications', *Polymers (Basel)*, vol. 10, no. 5, pp. 1–34, 2018, doi: 10.3390/polym10050527.

[81] M. Stamm, *Polymer Surfaces and Interfaces*, no. 1. 2008.

[82] A. W. Mohammad, Y. H. Teow, W. L. Ang, Y. T. Chung, D. L. Oatley-Radcliffe, and N. Hilal, 'Nanofiltration membranes review: Recent advances and future prospects', *Desalination*, vol. 356, pp. 226–254, 2015, doi: 10.1016/j.desal.2014.10.043.

[83] J.-C. Rémigy and S. Desclaux, 'Filtration membranaire (OI, NF, UF) - Présentation des membranes et modules', *Tech. Ing.*, p. 27, 2007.

[84] F. Galiano, A. Figoli, S. A. Deowan, D. Johnson, S. A. Altinkaya, L. Veltri, G. De Luca, R. Mancuso, N. Hilal, B. Gabriele, and J. Hoinkis, 'A step forward to a more efficient wastewater treatment by membrane surface modification via polymerizable bicontinuous microemulsion', *J. Membr. Sci.*, vol. 482, pp. 103–114, 2015, doi: 10.1016/j.memsci.2015.02.019.

[85] F. Galiano, I. Friha, S. A. Deowan, J. Hoinkis, Y. Xiaoyun, D. Johnson, R. Mancuso, N. Hilal, B. Gabriele, S. Sayadi, and A. Figoli, 'Novel low-fouling membranes from lab to pilot application in textile wastewater treatment', *J. Colloid Interface Sci.*, vol. 515, pp. 208–220, 2018, doi: 10.1016/j.jcis.2018.01.009.

[86] T. H. Chieng, L. M. Gan, C. H. Chew, S. C. Ng, and K. L. Pey, 'Microstructural control of porous polymeric materials via a microemulsion pathway using mixed nonpolymerizable and polymerizable anionic surfactants', *Langmuir*, vol. 12, no. 2, pp. 319–324, 1996, doi: 10.1021/la950493z.

[87] F. Bléger, A. K. Murthy, F. Pla, and E. W. Kaler, 'Particle Nucleation during Microemulsion Polymerization of Methyl Methacrylate', *Macromolecules*, vol. 27, no. 9, pp. 2559–2565, 1994, doi: 10.1021/ma00087a026.

[88] J. Mokry, J. Karbanova, J. Lukas, V. Paleckova, and B. Dvorankova, 'Biocompatibility of HEMA Copolymers Designed for Treatment of CNS Diseases with Polymer-Encapsulated Cells', *Biotechnol. Prog.*, vol. 16, no. 5, pp. 897–904, 2000, doi: 10.1021/BP000113M.

[89] M. Sivakumar and K. P. Rao, 'Synthesis, characterization, and in vitro release of ibuprofen from poly(MMA-HEMA) copolymeric core–shell hydrogel microspheres for biomedical applications', *J. Appl. Polym. Sci.*, vol. 83, no. 14, pp. 3045–3054, 2002, doi: 10.1002/APP.10310.

[90] J. R. Hwang and M. v. Sefton, 'The effects of polymer concentration and a pore-forming agent (PVP) on HEMA-MMA microcapsule structure and permeability', *J. Membr. Sci.*, vol. 108, no. 3, pp. 257–268, 1995, doi: 10.1016/0376-7388(95)00168-9.

[91] M. v. Sefton and W. T. K. Stevenson, 'Microencapsulation of live animal cells using polyacrylates', *Adv. Polym. Sci.*, vol. 107, pp. 143–197, 1993, doi: 10.1007/BFB0027553.

[92] E. G. Campioni, J. N. Nobrega, and M. V. Sefton, 'HEMA/MMMA microcapsule implants in hemiparkinsonian rat brain: biocompatibility assessment using [3H]PK11195 as a marker for gliosis', *Biomaterials*, vol. 19, no. 7–9, pp. 829–837, 1998, doi: 10.1016/S0142-9612(97)00241-X.

[93] A. F. R. Pimenta, A. P. Serro, R. Colaço, and A. Chauhan, 'Optimization of intraocular lens hydrogels for dual drug release: Experimentation and modelling', *Eur. J. Pharm. Biopharm.*, vol. 141, pp. 51–57, 2019, doi: 10.1016/J.EJPB.2019.05.016.

[94] P. D. Dalton, L. Flynn, and M. S. Shoichet, 'Manufacture of poly(2-hydroxyethyl methacrylate-co-methyl methacrylate) hydrogel tubes for use as nerve guidance channels', *Biomaterials*, vol. 23, no. 18, pp. 3843–3851, 2002, doi: 10.1016/S0142-9612(02)00120-5.

[95] S. Sen-Britain, D. Britain, W. L. J. Hicks, and J. A. J. Gardella, 'HEMA Hydrogel Copolymer Surface Chemistry Influences Localization and Release of Single and Multiple Wound Healing Growth Factors', *SSRN*, no. Preprint, Apr. 2019, Available at SSRN: https://ssrn.com/abstract=3368801.

[96] T. Yan, R. Sun, H. Deng, B. Tan, and N. Ao, 'The morphological and biomechanical changes of keratocytes cultured on modified p(HEMA-MMA) hydrogel studied by AFM', *Scanning*, vol. 31, no. 6, pp. 246–252, 2009, doi: 10.1002/SCA.20170.

[97] P. Chhabra, R. Gupta, G. Suri, M. Tyagi, G. Seshadri, S. Sabharwal, U.K. Niyogi, and R. K. Khandal, 'Studies on development of polymeric materials using gamma irradiation for contact and intraocular lenses', *Int. J. Polym. Sci.*, vol. 2009, 2009, doi: 10.1155/2009/906904.

[98] A. Y. Sung and T. H. Kim, 'Optical application of poly(HEMA-co-MMA) containing silver nanoparticles and N,N-dimethylacrylamide', *Korean J. Chem. Eng.*, vol. 29, no. 5, pp. 686–691, 2012, doi: 10.1007/S11814-011-0231-1.

[99] F. W. Bär, F. H. van der Veen, A. Benzina, J. Habets, and L. H. Koole, 'New biocompatible polymer surface coating for stents results in a low neointimal response', *J. Biomed. Mater. Res.*, vol. 52, no. 1, pp. 193–198, 2000, doi: 10.1002/1097-4636(200010)52:1<193::AID-JBM25>3.0.CO;2-7.

[100] J.-P. Montheard, M. Chatzopoulos, and D. Chappard, '2-Hydroxyethyl Methacrylate (HEMA): Chemical Properties and Applications in Biomedical Fields', *J. Macromol. Sci. C.*, vol. 32, no. 1, pp. 1–34, 1992, doi: 10.1080/15321799208018377.

[101] "NEOPHIL® – Polymem." https://www.polymem.fr/produits/membranes/neophil/ (accessed May 13, 2022).

[102] Y. Zhang, J. L. Sargent, B. W. Boudouris, and W. A. Phillip, 'Nanoporous membranes generated from self-assembled block polymer precursors: Quo Vadis?', *J. Appl. Polym. Sci.*, vol. 132, no. 21, pp. 41683-1–17, 2015, doi: 10.1002/app.42002.

[103] T. H. Chieng, L. M. Gan, C. H. Chew, S. C. Ng, and K. L. Pey, 'Formation of Microporous Polymeric Materials By Microemulsion Polymerization of Methyl Methacrylate and 2 - H ydroxyethyl Methacrylate', *J. Appl. Polym. Sci.*, vol. 60, pp. 1561–1568, 1996.

[104] T. H. Chieng, L. M. Gan, C. H. Chew, and S. C. Ng, 'Morphology of microporous polymeric materials by polymerization of methyl methacrylate and 2-hydroxyethyl methacrylate in microemulsions', *Polymer (Guildf)*, vol. 36, no. 10, pp. 1941–1946, 1995, doi: 10.1016/0032-3861(95)91436-B.

[105] A. Figoli, *Synthesis of nanostructured mixed matrix membrane for facilitated gas separation*. 2001.

[106] T. D. Li, L. M. Gan, C. H. Chew, W. K. Teo, and L. H. Gan, 'Preparation of ultrafiltration membranes by direct microemulsion polymerization using polymerizable surfactants', *Langmuir*, vol. 12, no. 24, pp. 5863–5868, 1996, doi: 10.1021/la960284u.

[107] L. S. Wang, P. Y. Chow, T. T. Phan, I. J. Lim, and Y. Y. Yang, 'Fabrication and characterization of nanostructured and thermosensitive polymer membranes for wound healing and cell grafting', *Adv. Funct. Mater.*, vol. 16, no. 9, pp. 1171–1178, 2006, doi: 10.1002/adfm.200500408.

[108] L. M. Gan, J. Liu, L. P. Poon, C. H. Chew, and L. H. Gan, 'Microporous polymeric composites from bicontinuous microemulsion polymerization using a polymerizable nonionic surfactant', *Polymer (Guildf)*, vol. 38, no. 21, pp. 5339–5345, 1997, doi: 10.1016/S0032-3861(97)00080-3.

[109] W. R. P. Raj, M. Sasthav, and H. M. Cheung, 'Microcellular polymeric materials from microemulsions: Control of microstructure and morphology', *J. Appl. Polym. Sci.*, vol. 47, no. 3, pp. 499–511, 1993, doi: 10.1002/app.1993.070470310.

[110] W. R. Palani Raj, M. Sasthav, and H. M. Cheung, 'Polymerization of single-phase microemulsions: Dependence of polymer morphology on microemulsion structure', *Polymer (Guildf)*, vol. 36, no. 13, pp. 2637–2646, 1995, doi: 10.1016/0032-3861(95)91212-P.

[111] J. Liu, W. K. Teo, C. H. Chew, and L. M. Gan, 'Nanofiltration membranes prepared by direct microemulsion copolymerization using poly(ethylene oxide) macromonomer as a

polymerizable surfactant', *J. Appl. Polym. Sci.*, vol. 77, no. 12, pp. 2785–2794, 2000, doi: 10.1002/1097-4628(20000919)77:12<2785::AID-APP270>3.0.CO;2-9.

[112] W. R. P. Raj, M. Sasthav, and H. M. Cheung, 'Polymerization of Microstructured Aqueous Systems Formed Using Methyl Methacrylate and Potassium Undecenoate', *Langmuir*, vol. 8, no. 8, pp. 1931–1936, 1992, doi: 10.1021/la00044a009.

[113] L. M. Gan, T. H. Chieng, C. H. Chew, and S. C. Ng, 'Microporous Polymeric Materials from Microemulsion Polymerization', *Langmuir*, vol. 10, no. 11, pp. 4022–4026, 1994, doi: 10.1021/la00023a020.

[114] F. Galiano, S. A. Schmidt, X. Ye, R. Kumar, R. Mancuso, E. Curcio, B. Gabriele, J. Hoinkis, and A. Figoli, 'UV-LED induced bicontinuous microemulsions polymerisation for surface modification of commercial membranes – Enhancing the antifouling properties', *Sep. Purif. Technol.*, vol. 194, pp. 149–160, 2018, doi: 10.1016/j.seppur.2017.10.063.

[115] L. M. Gan, T. D. Li, C. H. Chew, W. K. Teo, and L. H. Gan, 'Microporous Polymeric Materials from Polymerization of Zwitterionic Microemulsions', *Langmuir*, vol. 11, no. 9, pp. 3316–3320, 1995, doi: 10.1021/la00009a009.

[116] L. M. Gan, P. Y. Chow, Z. Liu, M. Han, and C. H. Quek, 'The zwitterion effect in proton exchange membranes as synthesised by polymerisation of bicontinuous microemulsions', *Chem. Comm.*, no. 35, pp. 4459–4461, 2005, doi: 10.1039/b508035e.

[117] S. Prevost, T. Lopian, M. Pleines, O. Diat, and T. Zemb, 'Small-angle scattering and morphologies of ultraflexible microemulsions', *J. Appl. Crystallogr.*, vol. 49, no. 6, pp. 2063–2072, 2016, doi: 10.1107/S1600576716016150.

[118] S. H. Chen, S. L. Chang, R. Strey, J. Samseth, and K. Mortensen, 'Structural evolution of bicontinuous microemulsions', *J. Phys. Chem.*, vol. 95, no. 19, pp. 7427–7432, 1991, doi: 10.1021/j100172a058.

[119] F. Galiano, 'Preparation and characterisation of polymerisable bicontinuous microemulsion membranes for water treatment application', PhD thesis, Universita' della Calabria, 2012. [Online]. Available: http://hdl.handle.net/10955/995

[120] S. dos Santos, L. Piculell, O. J. Karlsson, and M. da Graa Miguel, 'Phase diagrams come alive: Understanding how to create, destroy or change ordered surfactant structures by

polymerizing the counterions', *Soft Matter*, vol. 7, no. 5, pp. 1830–1839, 2011, doi: 10.1039/c0sm00958j.

[121] S. Norvez, 'Cristaux liquides, d'un état insoupçonné de la matière aux écrans plats', *L'Act. Chim.*, no. 387-388–389, pp. 148–152, 2014.

[122] E. I. Kovshev, L. M. Biinov, and V. V. Titov, 'Thermotropic Liquid Crystals and Their Applications', *Russ. Chem. Rev.*, vol. 46, no. 5, pp. 753–798, 1977, doi: https://doi.org/10.1070/RC1977v046n05ABEH002143.

[123] D. L. Gin, J. E. Bara, R. D. Noble, and B. J. Elliott, 'Polymerized lyotropic liquid crystal assemblies for membrane applications', *Macromol. Rapid Commun.*, vol. 29, no. 5, pp. 367–389, 2008, doi: 10.1002/marc.200700707.

[124] A. Mueller and D. F. O'Brien, 'Supramolecular materials via polymerization of mesophases of hydrated amphiphiles', *Chem. Rev.*, vol. 102, no. 3, pp. 727–757, 2002, doi: 10.1021/cr000071g.

[125] B. A. Pindzola, J. Jin, and D. L. Gin, 'Cross-linked normal hexagonal and bicontinuous cubic assemblies via polymerizable gemini amphiphiles', *J. Am. Chem. Soc*, vol. 125, no. 10, pp. 2940–2949, 2003, doi: 10.1021/ja0208106.

[126] E. S. Hatakeyama, B. R. Wiesenauer, C. J. Gabriel, R. D. Noble, and D. L. Gin, 'Nanoporous, bicontinuous cubic lyotropic liquid crystal networks via polymerizable gemini ammonium surfactants', *Chemi. Mater.*, vol. 22, no. 16, pp. 4525–4527, 2010, doi: 10.1021/cm1013027.

[127] T. Ichikawa, M. Yoshio, A. Hamasaki, J. Kagimoto, H. Ohno, and T. Kato, '3D Interconnected Ionic Nano-Channels Formed in Polymer Films: Self-Organization and Polymerization of Thermotropic Bicontinuous Cubic Liquid Crystals', *J. Am. Chem. Soc.*, vol. 133, no. 7, pp. 2163–2169, 2015 2011, doi: 10.1021/JA106707Z.

[128] A. E. Frise, T. Ichikawa, M. Yoshio, H. Ohno, S. V. Dvinskikh, T. Kato, and I.Furó, 'Ion conductive behaviour in a confined nanostructure: NMR observation of self-diffusion in a liquid-crystalline bicontinuous cubic phase', *Chem. comm.*, vol. 46, no. 5, pp. 728–730, 2010, doi: 10.1039/B915931B.

[129] B. Soberats, M. Yoshio, T. Ichikawa, X. Zeng, H. Ohno, G. Ungar, and T. Kato, 'Ionic Switch Induced by a Rectangular-Hexagonal Phase Transition in Benzenammonium Columnar Liquid Crystals', *J. Am. Chem. Soc.*, vol. 137, no. 41, pp. 13212–13215, 2015, doi: 10.1021/jacs.5b09076.

[130] M. Henmi, K. Nakatsuji, T. Ichikawa, H. Tomioka, T. Sakamoto, M. Yoshio, and T. Kato, 'Self-organized liquid-crystalline nanostructured membranes for water treatment: Selective permeation of ions', *Adv. Mater.*, vol. 24, no. 17, pp. 2238–2241, 2012, doi: 10.1002/adma.201200108.

[131] B. M. Carter, B. R. Wiesenauer, E. S. Hatakeyama, J. L. Barton, R. D. Noble, and D. L. Gin, 'Glycerol-based bicontinuous cubic lyotropic liquid crystal monomer system for the fabrication of thin-film membranes with uniform nanopores', *Chem. Mater.*, vol. 24, no. 21, pp. 4005–4007, 2012, doi: 10.1021/cm302027s.

[132] D. K. Mahalingam, S. Wang, and S. P. Nunes, 'Graphene Oxide Liquid Crystal Membranes in Protic Ionic Liquid for Nanofiltration', *ACS Appl. Nano Mater.*, vol. 1, no. 9, pp. 4661–4670, Sep. 2018, doi: 10.1021/acsanm.8b00927.

[133] T. Sakamoto *et al.*, 'Development of Nanostructured Water Treatment Membranes Based on Thermotropic Liquid Crystals: Molecular Design of Sub-Nanoporous Materials', A*dv. Sci.*, vol. 5, no. 1, pp. 1–9, 2018, doi: 10.1002/advs.201700405.

[134] J. E. Bara, E. S. Hatakeyama, B. R. Wiesenauer, X. Zeng, R. D. Noble, and D. L. Gin, 'Thermotropic liquid crystal behaviour of gemini imidazolium-based ionic amphiphiles', *Liq. Cryst.*, vol. 37, no. 12, pp. 1587–1599, 2010, doi: 10.1080/02678292.2010.521859.

[135] M. Zhou, T. J. Kidd, R. D. Noble, and D. L. Gin, 'Supported lyotropic liquid-crystal polymer membranes: Promising materials for molecular-size-selective aqueous nanofiltration', *Adv. Mater.*, vol. 17, no. 15, pp. 1850–1853, 2005, doi: 10.1002/ADMA.200500444.

[136] C. Zhou and Z. Yi, 'Blood-compatibility of polyurethane/liquid crystal composite membranes', *Biomaterials*, vol. 20, pp. 2093–2099, 1999, doi: 10.1016/S0142-9612(99)00080-0.

[137] T. D. Li, L. M. Gan, C. H. Chew, W. K. Teo, and L. H. Gan, 'Hollow-fiber membranes coated with polymerizable bicontinuous microemulsions', *J. Membr. Sci.*, vol. 133, no. 2, pp. 177–187, 1997, doi: 10.1016/S0376-7388(97)00102-6.

Chapter 2 – Material and methods

CHAPTER 2 – MATERIAL AND METHODS 77

2.1 MATERIAL 81
2.1.1 Monomers 81
2.1.2 Non-ionic surfactants 82
2.1.3 Initiators 82
2.1.4 Oxygen scavengers 83
2.1.5 Organic solvents 83
2.1.6 Membranes 83
2.2 METHODS 84
2.2.1 Polymerisation of the microemulsion 84
2.2.1.1 UV polymerisation 84
2.2.1.2 RedOx polymerisation 85
2.2.2 Surfactant removal and polymer cleaning 85
2.3 ANALYSIS 86
2.3.1 Elaboration of pseudo-ternary phase diagrams 86
2.3.1.1 Visual observation of the sample 86
2.3.1.2 Conductivity 86
2.3.1.3 Nuclear magnetic resonance (NMR) 87
2.3.1.3.1 Peak attribution 87
2.3.1.3.2 Pulsed Gradient Spin Echo – Diffusion Ordered Spectroscopy 88
2.3.2 Temperature monitoring UV-light 89
2.3.3 Contact angle 89
2.3.4 Small Angle X-ray Scattering (SAXS) 89
2.3.5 Scanning Electron Microscopy (SEM) 90
2.3.6 Cryo-scanning Electron Microscopy (Cryo-SEM) 91
2.3.7 Attenuated Total Reflectance Fourier-Transform Infrared Spectroscopy (ATR-FTIR) . 91
2.3.8 Water permeability 92
REFERENCES 93

2.1 Material

2.1.1 Monomers and cross-linker

Monomers: methyl methacrylate (MMA), 2-hydroxyethyl methacrylate (HEMA).

Cross-linker: ethylene glycol dimethacrylate (EGDMA)

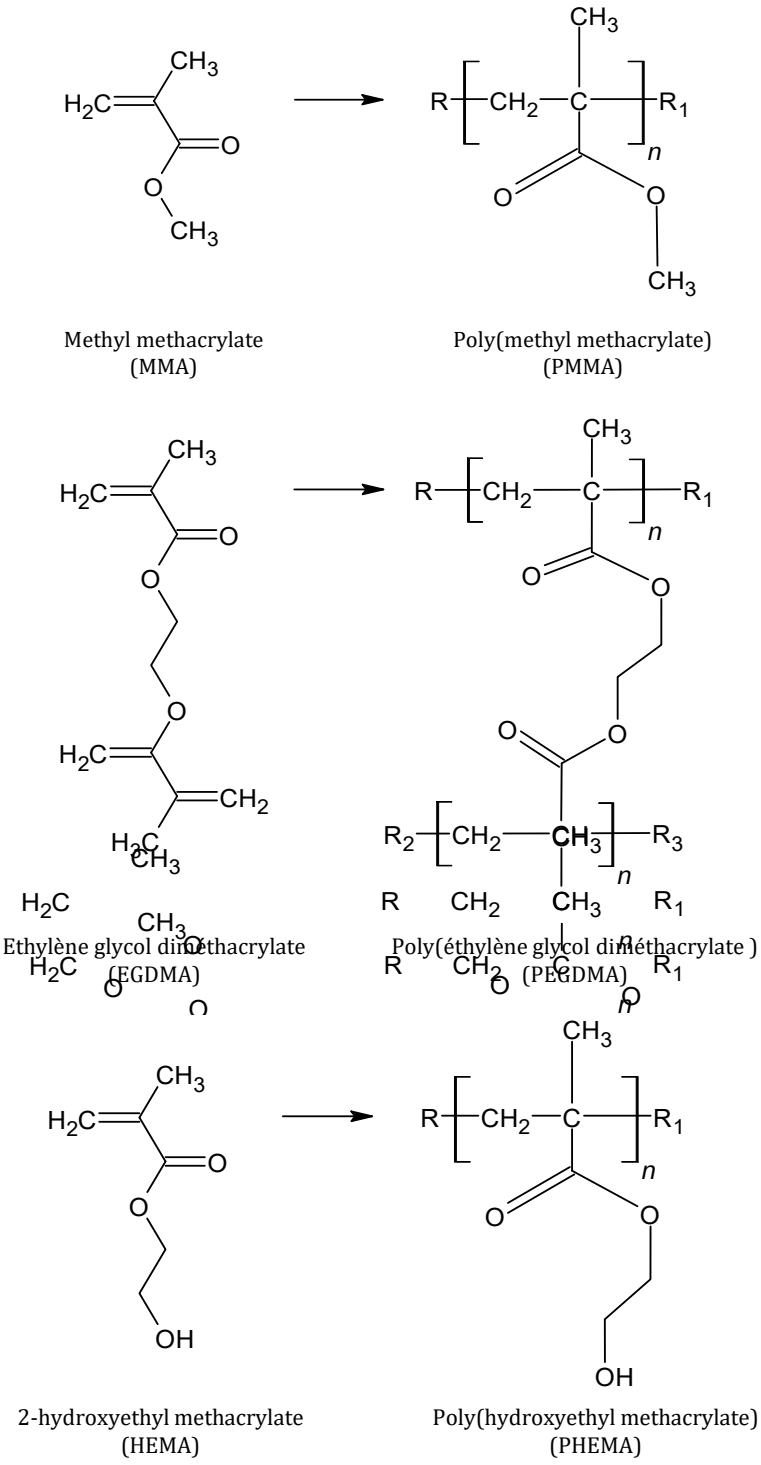

Figure 1.1 – Chemical structure of monomers and corresponding polymers.

All monomers were purchased from Sigma Aldrich (France) and purified using an alumina column prior to use.

2.1.2 Non-ionic surfactants

Synperonic™ A11 was kindly provided by Croda (France). Tergitol ™ 15-S-12 was purchased from Sigma-Aldrich (France). The surfactants were used without further purification.

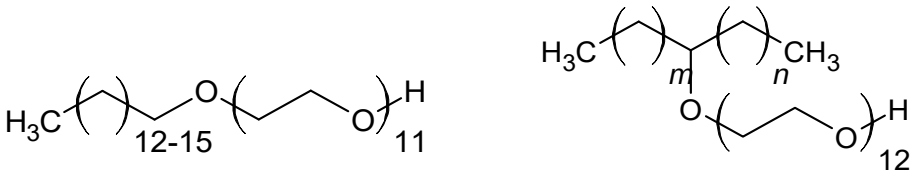

Synperonic™ A11 Tergitol™ 15-S-12

Figure 2.2 – Chemical structure of the non-ionic surfactants used.

2.1.3 Initiators

RedOx polymerisation: ammonium persulfate (APS) and tetramethylethylenediamine (TMEDA), were purchased from Sigma-Aldrich (France).

Photopolymerisation: 2,2-dimethoxy-2-phenylacetophenone (DMPA), was purchased from Sigma-Aldrich (France).

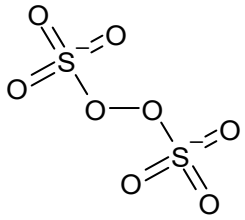

Ammonium persulfate (APS)

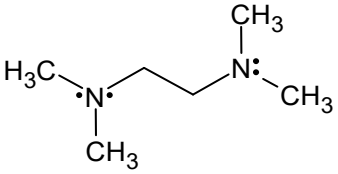

Tetramethylethylenediamine (TMEDA)

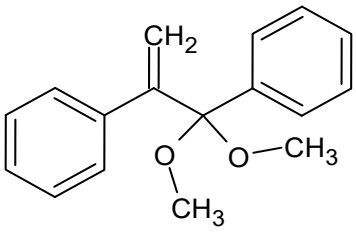

2,2-dimethoxy-2-phenylacetophenone (DMPA)

Figure 2.3 – Chemical structure of RedOx couple and the Norrish I photoinitiator used.

2.1.4 Oxygen scavengers

Triethanolamine (TEOA) and the triethylamine (TEA) were purchased from Sigma-Aldrich (France).



Triethylamine (TEA) Triethanolamine (TEOA)

Figure 2.4 - Chemical structure of the oxygen scavengers used.

2.1.5 Organic solvents

Polymer washing: acetone, ethanol, methanol purchased from VWR (France) were tested. Ultrapure water (Ω = 18.2 MΩ·cm) was used, otherwise specified.

2.1.6 Membranes

Microfiltration PES flat-sheet membranes MicroPES™ Type 2F were purchased from Membrana-3M (Germany). These membranes exhibit a nominal pore size of 0.2 µm and a thickness of 110 ± 10 µm. The technical data-sheet of the commercial membrane is reported in Appendix 1.

2.2 Methods

2.2.1 Polymerisation of the microemulsion

The surfactant-based mix was purged 2 min under Argon gas (1.5 ± 0.9 $L.min^{-1}$) before casting.

Use of a 50 µm thick mould: The mould material depends on the initiation method used: a borosilicate mould was used for RedOx and UV-LED initiations. A mixed borosilicate-quartz mould was used for the UV-TQ150 initiation to allow the full range of UV to pass through the mould upper material (quartz). The monomer solution was set between two borosilicate cover glass – 22x22 mm, thickness N°0 (VWR, France) – or between a borosilicate cover glass and a quartz glass – 2 ± 0.2 mm thickness.

Use of a casting-knife: the monomer solution was casted manually on a glass plate using a casting-knife of defined thickness (100 µm) and polymerised as is.

2.2.1.1 UV polymerisation

DMPA was added at an amount of 2 wt.% with respect to the total mass of the solution. The photopolymerisation of the microemulsion was carried out using two UV lamps. The Emissivity spectra of UV lamps is reported in Appendix 2. The irradiation duration for each sample as a function of the lamp used is summarised in Table 2.1.

Monochromatic UV lamp: the LED Cube 100 UV lamp (λ = 385 nm) (Hoenle, Germany) was set at a distance of 9 cm from the sample (out of the UV box) and irradiated for various durations (60 to 3600s) at a lamp power of 90%.

Polychromatic UV lamp: the TQ150 UV lamp (Hereaus, Germany) was set at a distance of 4 cm from the sample and irradiated for various duration (2 to 5 min).

Table 2.1 –Duration of the polymerisation process as a function of the composition for the two UV-lamps.

Lamp used	**(46:8:46)$_{33:33:33}$**	**(46:8:46)$_{62:19:19}$**	**(21:23:56)$_{62:19:19}$**
TQ150 *(+100 s warming period)*	3 min 20 s	1 min 20 s	20 s
LED	3600 s	120 s	60 s

2.2.1.2 RedOx polymerisation

APS was added to 0.3 wt.% with respect to the total mass amount of the aqueous phase. TMEDA was added in an equimolar amount with respect to APS. The sample was casted prior to the system complete gelification, cf. Table 2.2.

Table 2.2 – Gelification and deposition time for each composition polymerised using RedOx initiation.

Lamp used	**(46:8:46)$_{33:33:33}$**	**(46:8:46)$_{62:19:19}$**	**(21:23:56)$_{62:19:19}$**
Gelification time	5 min 1 s ± 41 s	6 min 20 s ± 27 s	2 min 56 s ± 14 s
Deposition time	2 min	2 min	2 min

2.2.2 Surfactant removal and polymer cleaning

The synthesised polymer network was kept under atmospheric conditions and protected from natural light for 12 h after priming, to ensure the complete conversion. The sample was then washed in magnetically stirred UP-water (at least two successive baths) at room temperature to eliminate the surfactants and unreacted monomers. The polymer was then stored in UP-water before analysis.

2.3 Analysis

2.3.1 Elaboration of pseudo-ternary phase diagrams

The pseudo-ternary phase diagrams presented in this work result from a combination of various analytical techniques, described in the following subsections.

2.3.1.1 Visual observation of the sample

The first step towards the construction of the diagrams is the visual observation: an opaque mixture indicates an unstable domain, while a transparent one indicates a microemulsion. In order to differentiate the nanoemulsion and microemulsion the stability of the mixture was studied over 3 months.

After addition of one component to the surfactant-based solution, the mixture was agitated using a stirring plate and left to equilibrate for five to fifteen minutes. The visual aspect of the sample (monophasic or polyphasic) was then reported. When specified, the birefringence of the sample was also tested using a cross-polarised analyser, kindly provided by Dr. Kevin Roger.

2.3.1.2 Conductivity measurements

Conductivity measurements were done using a Portavo 907 Multi (Knick, Germany). Samples were immersed in a 298K (25°C) thermostated bath under stirring and titrated with an aqueous solution of NaCl (0.01M) using an automated pump, as presented in Figure 2.5. The system was equilibrated for five minutes and the conductivity was measured. As the surfactants used are non-ionic, NaCl was added to the aqueous phase (water) to allow ionic displacement.

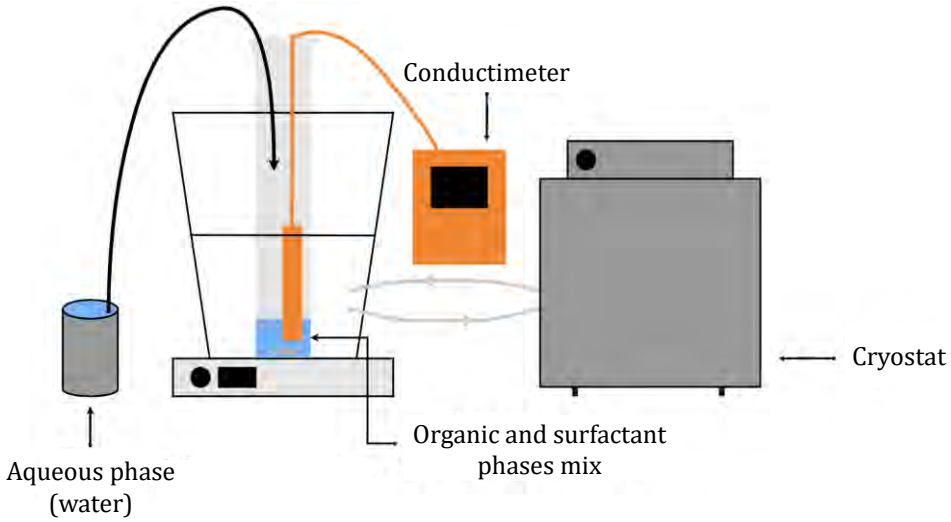

Figure 2.5 – Experimental set-up for the visual and conductimetric monitoring of mixtures of organic, surfactant and water phases at 25°C.

2.3.1.3 Nuclear magnetic resonance (NMR)

PGSE-NMR measurements were obtained using an Avance 400 MHz (Bruker, Germany) spectrometer with a Z-gradient Probe TBO 5 mm BB {1H, 31P}, at Institut de Chimie de Toulouse. As the microstructure is strongly dependent on the composition, no deuterated solvent was used as an internal reference while determining diffusion coefficient and chemical shifts. For this reason the peaks of each compounds were attributed in the surfactant-based solution, prior to analysis.

2.3.1.3.1 Peak attribution

- **Peak attribution for the MMA and HEMA monomers**

The peak attribution on the ^{1}H NMR spectra of MMA and HEMA is presented in Figure 2.6. The attribution was performed using $CDCl_3$ as internal standard.

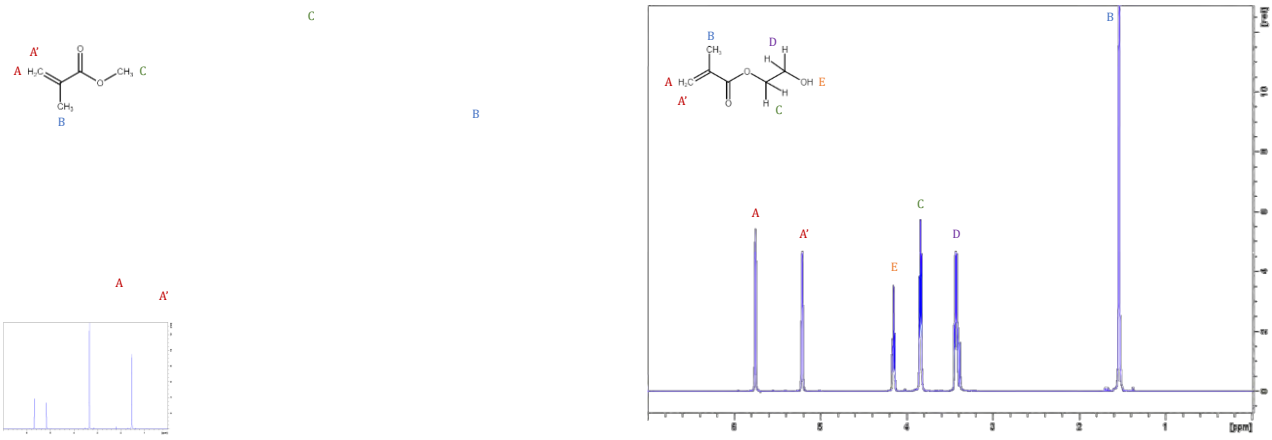

Figure 2.6 – ^{1}H NMR spectrum of (left) MMA and (right) HEMA in $CDCl_3$ and peak attribution.

- **Peak attribution for the quinary acrylate system**

The peak attribution to each compound in the ^{1}H NMR was performed by successively adding each compound into a microemulsion mix, cf. Figure 2.7. This mix was chosen in order to clearly identify each and every peak upon chemical additions. The peak attribution was based on the increase of the peak intensity and on the monomer spectra. The whole peak attribution of the microemulsion spectrum is presented in Figure 2.8

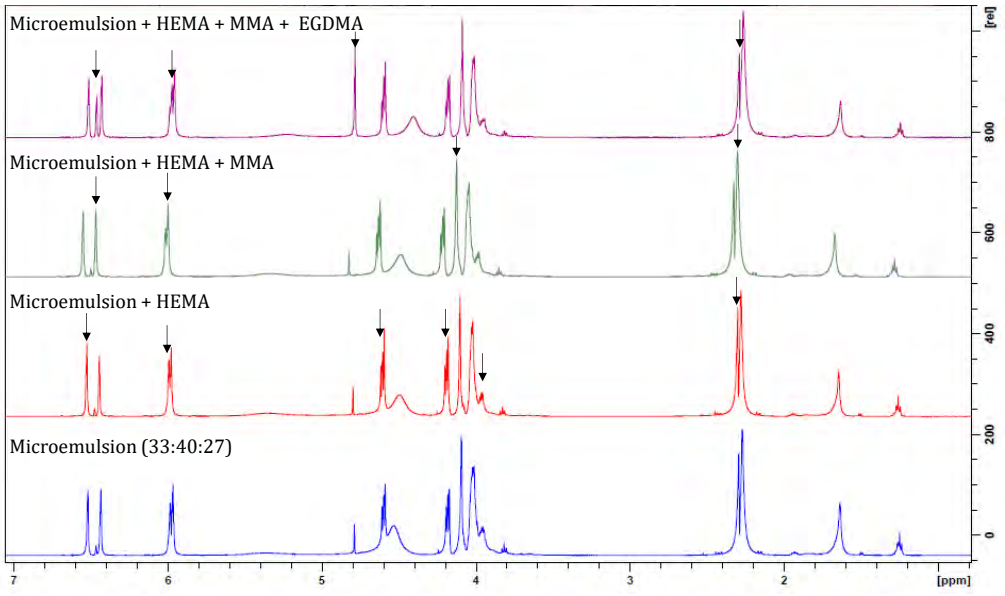

Figure 2.7 - Assignment of the ^{1}H NMR peaks by successive addition of each compound to a solution $(33:40:27)_{62:19:19}$ microemulsion.

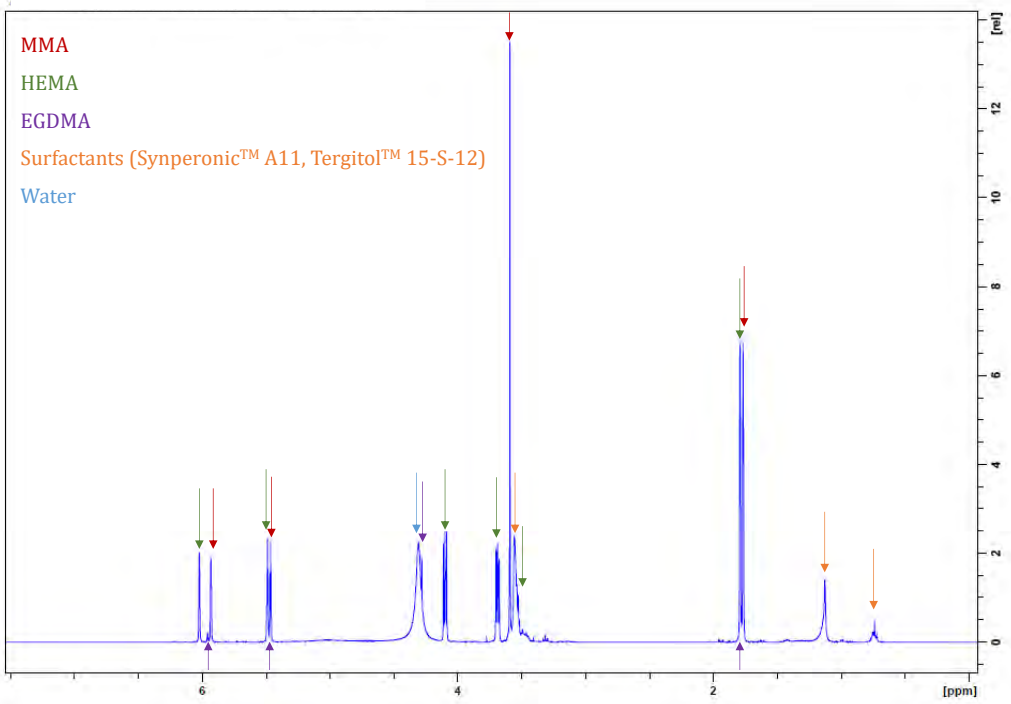

Figure 2.8 - ^{1}H NMR spectra and peak attribution of the monomers in the $(25:19:56)_{62:19:19}$ microemulsion.

2.3.1.3.2 Pulsed Gradient Spin Echo – Diffusion Ordered Spectroscopy NMR (DOSY-NMR)

PGSE-DOSY NMR measurements were obtained using a Bruker Avance 400 MHz spectrometer with a Z-gradient Probe TBO 5 mm BB {^{1}H, ^{31}P}, at the Institut de Chimie de Toulouse (ICT). All diffusion measurements were performed using the stimulated echo pulse sequence (stebpgp1s) at a temperature of 298 K. The recycle delay was adjusted to 3 s to allow full relaxation. The shape of the gradient was Sine with a length adjusted between 0.8 ms at 2.6 ms,

while the gradient strength was varied in 16 increments (5–95%) of the gradient ramp created by the Bruker software, DOSY. The diffusion time was set between 100 ms and 150 ms depending on the water concentration. The diffusion coefficients were determined using the Bruker TopSpin software by linear least-squares fits to the Stejskal–Tanner plots using the Simfit algorithm of Bruker software package T1/T2.

2.3.2 Temperature monitoring UV-light

The temperature of the sample when exposed to UV-light was monitored using a flat PT100 sensor (Prosensor, France).

2.3.3 Contact angle determination

The static contact angle was determined from a drop of water deposited in air on flattened non-porous polymer and glass surfaces at 22°C by a DSA30 drop shape analyser (Krüss, Germany) equipped with an image-processing software. A micro-syringe deposited a 2 µL water drop on the surface of the investigated material. The measurement of the contact angle was made 30 s after the drop contacted the surface to allow for the liquid stabilisation. The water contact angle for material was averaged over four to seven measurements.

2.3.4 Small Angle X-ray Scattering (SAXS)

SAXS measurements were performed on a XEUSS 2.0 bench (Xenocs, France) and a copper internal source Genix3D (λ=1.542 Å) (Xenocs, France) at Laboratoire de Génie Chimique, Toulouse. A (800x800) μm^2 X-ray beam was produced with an energy of 8 keV and a flow of 98.10^6 $ph.mm^2.s^{-1}$. The scattered X-rays were collected on a 150x150 mm Pilatus 1M detector (DECTRIS, Japan) located at a distance of 1216 mm from the sample, so that scattering curves cover a scattering vector (q) range of 0.009 – 0.510 $Å^{-1}$. The samples were equilibrated for 24 h at room temperature (23-25°C) prior to analysis. Samples were loaded in a vacuum chamber and exposed to the X-ray beam once each for 600 s (monomer samples) or 6x 1200 s (polymer samples). All experiments were repeated at least twice (otherwise specified).

Monomer samples preparation: the samples were injected into borosilicate capillaries before being flame-sealed. The samples were investigated in a thermoregulated cell at 25°C, otherwise specified. The scattering curves were then subtracted by a borosilicate reference capillary containing UP water (acquisition: 6 x 1200 s).

It should be noted that some authors ([1–4] among others) proposed to use an empty capillary as a reference for subtraction. We however decided to do otherwise, because the scattering length density of air is highly different than the one of the liquid compounds used, cf. Table 2.3. Such a difference can then lead to a convolution of air with the X-ray beam. In this project, we decided to use a borosilicate with UP water as reference, to decrease the difference of SLD between the reference and the sample. Such a buffer is however not ideal and a mix of MMA, water and HEMA would be more representative of the contrast in the system. However, such a monophasic mix is not achievable for most of the compositions investigated. To avoid the impact of the contrast of the liquid-capillary interfaces (below ca. 0.02 $Å^{-1}$) [4], the curves presented in this work will be investigated in the range 0.02 – 0.5 $Å^{-1}$.

Table 2.3 – Scattering length densities (SLD) of air, water and the three acrylate monomers used in this project. Calculation carried out with the "SLD Calculator" tool of the SASView software.

Compound	**Air**	**Water**	**MMA**	**HEMA**	**EGDMA**
SLD ($Å^{-2}$)	1.01E-8	9.44E-6	8.60E-6	9.83E-6	9.57E-6

Polymer samples preparation: the samples were loaded in a five position (Ø: 5mm) solid sample holder. This sample holder can be used in atmospheric condition or filled with a liquid buffer to allow for an investigation of hydrated samples. When investigating hydrated polymers, the sample holder was filled with UP water. The polymer scattering curves were then subtracted by a water reference (acquisition: 6 x 1200 s).

The resulting scattering curves were fit with various models on the SASView software. When several curves are presented in the same graph, a multiplicative factor was applied to the intensity to present an exploded view of the curves (otherwise specified).

2.3.5 Scanning Electron Microscopy (SEM)

All samples were cryo-fractured in liquid nitrogen and coated with a nanometric metal layer. The deposited metal depends on the device used for observation.

Pristine polymer network: Observation done at the Laboratoire de Génie Chimique using the JSM 7100F FEG-SEM (JEOL, Japan). A platinum coating was deposited using the EM ACE600 sputter coater (Leica Microsystems, Germany).

Pristine and coated membrane MicroPES™ membranes: Observation done at the Laboratoire de Génie Chimique using the Phenom World XL SEM (Thermo Fischer, Netherlands) and the TM3000 SEM (HITACHI, Japan). A gold coating was deposited using the Emitech K500X sputter coater (Quorum Technologies Limited, United-Kingdom).

2.3.6 Cryo-scanning Electron Microscopy (Cryo-SEM)

- Sample manipulation

The sample was inserted between two high-pressure freezing (HPF) specimen carriers dedicated for cryofracture (Leica Microsystems, Germany) and immediately loaded into an ICE HPF machine (Leica Microsystems, Germany). The sample was fixated and frozen within 5 ms at 2050 bar, and then transferred to cryovials under liquid nitrogen. Then HPF specimen carrier with the frozen sample was then inserted in a PP3000T preparation chamber (Quorum Technologies Limited, United-Kingdom). More information regarding the preparation of the samples can be found in the article from Payre and al. [5]. After a quick transfer under vacuum in the preparation chamber, the samples were fractured at -140°C, sublimed at -95°C during 30 min and then coated by platinum sputtering. They were at last transferred in the Quanta 250 FEG-SEM (FEI, USA) chamber and kept at -140°C for observation at an accelerating voltage of 10 kV at Centre de Microscopie Électronique Appliquée à la Biologie (CMEAB).

- Data analysis

All cryo-SEM images used for the pore size determination were subjected to the same data treatment, using the ImageJ software. First, the scale of the image was adjusted based on the scale from the cryo-SEM analysis. The image was then converted to an 8-bit image. Because the image is required to be a binary (i.e. black and white) image, it was converted to an 8-bit format and a threshold range was set to identify the pores from the polymer matrix. Each pore was then isolated and analysed using the "Analyze Particles" function. A minimum size was identified as a pixel default size in each picture, to exclude anything different from a pore in the image. The area of each pore was then reported and the pore size calculated assuming circular pores.

2.3.7 Attenuated Total Reflectance Fourier-Transform Infrared Spectroscopy (ATR-FTIR)

Infrared spectra were obtained with a Nicolet Nexus 670 (Thermo Fisher Scientific, USA) spectrophotometer. The analyses were performed at the Institut de Chimie de Toulouse (ICT).

The samples were deposited on a diamond crystal substrate and at least three spectra were recorded in the 400-4000 cm^{-1} domain.

2.3.8 Water permeability

Water permeability at 20°C L_{P20} ($m^3.m^{-2}.s^{-1}.bar^{-1}$) is defined as the ratio of the inflow volume J_{20} to the applied transmembrane pressure ΔP for the measured membrane thickness h_m (µm), cf. Eq. 2.1.

$$L_{P20} = \frac{J_{20}}{\Delta P} \qquad \text{Eq. 2.1}$$

The flux measurements were carried out in 2.5 cm diameter Amicon® Stirred Cell Reservoirs (Merck, Germany) at room temperature, as presented in Figure 2.9.

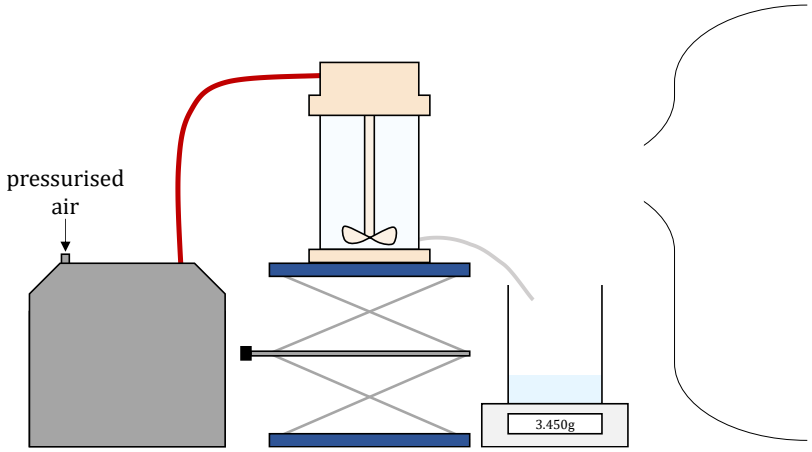

Figure 2.9 – Schematic representation of a front filtration system with an Amicon® cell [6].

The fluxes were obtained by recording the weight of the water permeate for various duration (between 5 – 30 min) and for various ranges of pressure (from 0.2 to 6 bars). All samples were studied for at least one pressure increase/decrease cycle. To avoid a temperature dependence, the ratio of the inflow volume for a temperature T is corrected to 20°C using Eq. 2.2, so that the permeability is normalised to 20°C.

$$J_{20} = \frac{J_T}{\exp\left(6.435 - \frac{1885}{T}\right)} \qquad \text{Eq. 2.2}$$

References

[1] O. Regev, S. Ezrahi, A. Aserin, N. Garti, E. Wachtel, E.W. Kaler, A. Khan, Y. Talmon, A Study of the microstructure of a four-component nonionic microemulsion by cryo-TEM, NMR, SAXS, and SANS, Langmuir. 12 (1996) 668–674. https://doi.org/10.1021/la950505g.

[2] S. Ezrahi, E. Wachtel, A. Aserin, N. Garti, Structural polymorphism in a four-component nonionic microemulsion, J. Colloid Interface Sci. 191 (1997) 277–290. https://doi.org/10.1006/jcis.1997.4962.

[3] A. Kogan, D.E. Shalev, U. Raviv, A. Aserin, N. Garti, Formation and characterization of ordered bicontinuous microemulsions, J. Phys. Chem. B. 113 (2009) 10669–10678. https://doi.org/10.1021/jp901617g.

[4] S. Prevost, T. Lopian, M. Pleines, O. Diat, T. Zemb, Small-angle scattering and morphologies of ultraflexible microemulsions, J. Appl. Crystallogr. 49 (2016) 2063–2072. https://doi.org/10.1107/S1600576716016150.

[5] B. Payre, E. Gontier, A. Jarray, Y. Martinez, J.P. Laugier, A. Delalleau, B.M. Gaillard, I. Anselme, D. Goudounèche, I. Fourquaux, M. Hemati, V. Gerbaud, M.B. Delisle, C. Guilbeau-Frugier, A new HPF specimen carrier adapter for the use of high-pressure freezing with cryoscanning electron microscope: two applications: stearic acid organization in a hydroxypropyl methylcellulose matrix and mice myocardium, J. Microsc. 271 (2018) 255–265. https://doi.org/10.1111/JMI.12713.

[6] Sigma-Aldrich, User Guide: Amicon® Stirred CellsUser Guide: Amicon® Stirred Cells, (n.d.). https://www.sigmaaldrich.com/technical-documents/articles/biology/amicon-stirred-cells.html.

Chapter 3

Chapter 3 – Elaboration of pseudo-ternary phase-diagrams of the monomer systems by SAXS and DOSY-NMR analyses

CHAPTER 3 – ELABORATION OF PSEUDO-TERNARY PHASE-DIAGRAMS OF THE MONOMER SYSTEMS BY SAXS AND DOSY-NMR ANALYSES 95

3.1 INTRODUCTION 99
3.2 SYSTEM COMPOSITION 100
3.3 NON-IONIC QUATERNARY SYSTEM 102
3.3.1 Elaboration of the pseudo-ternary phase diagrams 102
3.3.2 Impact of the co-surfactant on the microstructure of the system 107
3.4 NON-IONIC QUINARY SYSTEM 110
3.3.1 Elaboration of the pseudo-ternary phase diagrams 110
3.4.2 Evolution of the microstructure upon water dilution 113
3.4.2.1 DOSY-NMR analysis 113
3.4.2.1.1 Self-diffusion coefficients D_0 of the pure compounds 113
3.4.2.1.2 Self-diffusion coefficients D of the quinary solutions the (15:85) water dilution line 114
3.4.2.2 SAXS analysis 118
3.4.2.3 On the microstructure adopted by the systems upon water dilution 119
3.5 CONCLUSION 125
REFERENCES 129

3.1 Introduction

To our knowledge, when synthesising polymer membranes from a self-assembled MMA:water:HEMA:surfactant(s) system, the microstructure of the systems has only been studied using conductivity and viscosity measurements. These measurements allow for the determination of W/O and O/W microstructures surrounding an intermediate region – which is usually considered as bicontinuous. Those three ranges of conductivity values are delimited by two slope discontinuities – called percolation threshold – indicating a significant change in the microstructure. In the microemulsion field, other techniques have been used to identify the microstructure of the monomer solutions, namely SAXS [1]–[5] and DOSY-NMR [2], [5]–[7] analyses, among others [8].

To that end we will discuss the microstructure of an acrylate quinary (or 5-compounds) non-ionic system water:MMA:(HEMA:Synperonic™ A11:Tergitol™ 15-S-12). This system was chosen based on previous work carried out by our research team at the Laboratoire de Génie Chimique. Both surfactants used are commercial, non-ionic and non-polymerisable. The Synperonic™ A11 is a linear C12-C15 ethoxylated alcohol, while the Tergitol™ 15-S-12 is a secondary C12-C14 ethoxylated alcohol. The composition of the surfactant phase will be listed as follows in the remaining of this thesis (HEMA: Synperonic™ A11: Tergitol™ 15-S-12). We will investigate three compositions of this surfactant phase, to provide information regarding the impact of HEMA on the acrylate system.

All systems will be described using a pseudo-ternary diagram based on various techniques such as conductivity, birefringence, DOSY-NMR and SAXS analyses. The results will allow us to discuss whether a bicontinuous interconnected network can be achieved before the system polymerisation. This prior determination will allow us to discuss the conservation of the microstructure of the template microemulsion upon its polymerisation in Chapter 4.

This chapter will address the following questions:

- *What is the microstructure of the monomer acrylate system prior to polymerisation?*
- *How does the addition of HEMA impact the microstructure of the monomer mixture, as we confirmed that this compound acts as a co-surfactant and co-solvent in the investigated system?*

3.2 System composition

The system composition governs the microstructure of the resulting microemulsion. Non-ionic surfactants will not be impacted by the ionicity of the aqueous phase, which therefore will not be investigated in the following sub-sections. In this chapter, we will investigate three different mass compositions of the surfactant phase (HEMA: Synperonic™ A11: Tergitol™ 15-S-12): (0:50:50), (33:33:33) and (62:19:19). The microstructure of the systems was examined at 25°C.

The choice and the weight ratio of the two commercial non-ionic non-polymerisable surfactants – i.e. Synperonic™ A11 and Tergitol™ 15-S-12 – was based on previous research work carried out in our research team in the Laboratoire de Génie Chimique. Twenty-two commercial surfactants were initially considered. The surfactants allowing the greatest intake of water into the system – and thus potentially the greatest membrane porosity – were isolated. It was then observed that the combination of these identified surfactants could further increase the water input into the system, Synperonic™ A11 and Tergitol™ 15-S-12 providing the highest possible water input. For this reason, the present work will be carried out with an equimassic ratio of these two commercial surfactants.

The HLB values of these surfactants are respectively 13.9 and 14.7. The HEMA HLB has been estimated to 9.4 using the Griffin empirical formula for non-ionic surfactants [9], [10], cf. Eq. 3.2, considering O-CH_2-CH_2-OH as the hydrophilic group. Based on the previous work from our research group, we calculated the HLB of our surfactant mixes using the Griffin formula [9], cf. Eq. 3.1 and Table 3.1.

$$\mathrm{HLB_{mix}} = \sum_{i} w_i . \mathrm{HLB_i} \qquad \text{Eq. 3.1}$$

$$\mathrm{HLB_i} = 20 \frac{\mathrm{M_{hydrophilic\ group}}}{\mathrm{M_{molecule\ i}}} \qquad \text{Eq. 3.2}$$

Table 3.1– Surfactant phase composition and for various HLB values.

Composition name	**(62:19:19)**	**(33:33:33)**	**(0:50:50)**
HLB	**11.2**	**12.7**	**14.3**
HEMA	62.0 wt.%	33.3 wt.%	0 wt.%
Synperonic™ A11	19.0 wt.%	33.3 wt.%	50 wt.%
Tergitol™ 15-S-12	19.0 wt.%	33.3 wt.%	50 wt.%

The HLB presented are given as indication only. Indeed, to obtain more specific information on the prediction of the mean-curvature of the surfactant interface, the assessment of the CPP or HLD (Hydrophilic Lipophilic Deviation) are necessary.

In the following of this manuscript, the three investigated systems will be referred as the composition of their surfactant phase, namely: (62:19:19), (33:33:33) and (0:50:50). The compositions presented will be named as followed (water mass content:MMA mass content:Surfactant phase mass content)$_{\text{composition of the surfactant phase}}$. For example, a solution from the (62:19:19) system which contains 25 wt.% water, 30 wt.% MMA and 45 wt.% of surfactant phase will be named: $(25:30:45)_{62:19:19}$.

3.3 Non-ionic quaternary system investigation

We will first investigate a quaternary system made of water as the aqueous phase, MMA as the oil phase and an equimassic mix of the Synperonic™ A11 and Tergitol™ 15-S-12 non-ionic surfactants – the (0:50:50) system. We will then discuss the impact of the addition of the HEMA co-surfactant on the microstructure of the system.

3.3.1 Elaboration of the pseudo-ternary phase diagrams

The first step for the microstructure characterisation of the acrylate systems is the delimitation of the microemulsified domain. For this purpose, a visual investigation of the various compositions was carried out at 25°C. A mix is classified as a microemulsion if it is a monophasic, transparent and non-birefringent solution. On the contrary, a surfactant-based mix is identified as a liquid crystal if it is a monophasic, transparent and birefringent solution – except for cubic liquid crystals which are not birefringent. If the viscosity of the solution is a powerful criterion to identify cubic liquid crystals [11], SAXS analyses can confirm and specify the microcrystalline arrangement adopted by the molecules in liquid crystals.

The pseudo-ternary diagram presented in Figure 3.1 below has been achieved through the investigation of eight water dilution lines, two surfactants dilution lines and one organic MMA dilution line at 25°C. The birefringence of the system and its single-phase nature was tested for all tested compositions in these dilution lines.

First, we highlighted the existence of a large polyphasic domain (**blue**) for low surfactant contents, including the binary MMA:water domain. Above this unstable zone, we evidenced two non-birefringent zones. The **yellow** largest area is assumed to be a microemulsified domain, based on the low viscosity of the solutions, as well as the two SAXS scattering curves carried out in this domain (N°5 and N°6). The second non-birefringent, low viscous domain (**grey**), located right above the unstable zone were unfortunately not be investigated by SAXS due to a lack of time. It is therefore not possible to conclude whether microemulsions or cubic structures occur in this narrow domain. We finally demonstrated the occurrence of four birefringent zones – and thus liquid crystals zones – separated by various tie-lines (dashed zones). This thermodynamically unstable domain usually consists of a polyphasic, partially birefringent unstable mixture.

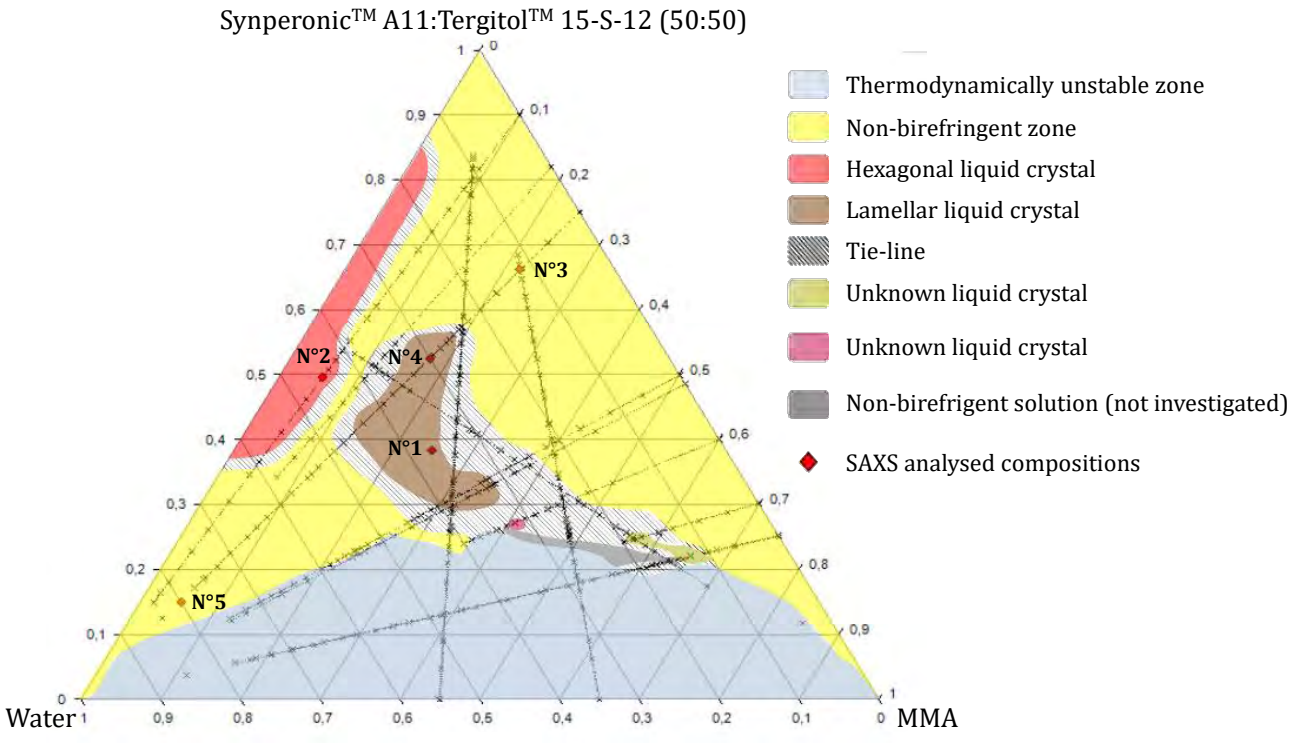

Figure 3.1 – Pseudo-ternary phase diagram of the (0:50:50) acrylate system at 25°C.

We then analysed several compositions from the brown (N°1, N°2 and N°3) and red (N°4) LC domains using X-ray scattering. The following sub-sections will discuss the structure occurring in both birefringent **red** and **brown** liquid crystal (LC) domains. The composition of the samples analysed using the SAXS techniques are detailed in Table 3.2. It should be noted that the structure of the **grey** and **pink** LC domains was however not determined due to lack of time.

Table 3.2 – Composition (in wt.%) of the samples investigates using SAXS analysis.

Sample	Water	MMA	Synperonic™ A11:Tergitol™ 15-S-12
N°1	36.8%	24.8%	38.3%
N°2	44.9%	5.5%	49.7%
N°3	11.9%	21.9%	66.2%
N°4	30.0%	17.5%	52.4%
N°5	79.9%	5.0%	15.0%

- **Identification of the hexagonal and lamellar domains**

The SAXS scattering curves of the composition N°1 (**brown** LC domain) and N°2 (**red** LC domain) are presented in Figure 3.2 below. The N°1 scattering curve exhibits two peaks with a characteristic d-spacing ratio of $1:\frac{1}{2}$, indicating the occurrence of a lamellar phase. As for sample N°2, three peaks distant from the first one with a characteristic d-spacing ratio of $1:\frac{1}{\sqrt{3}}:\frac{1}{2}$ are observed, indicating the existence of a hexagonal liquid crystal phase.

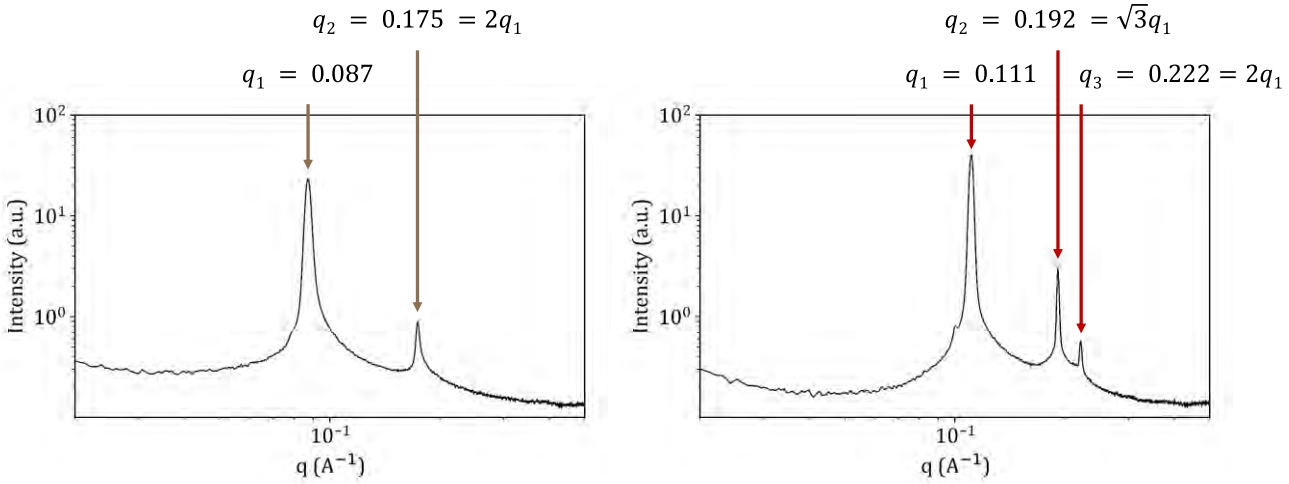

Figure 3.2 – SAXS scattering curves of a (left) lamellar (N°1) and (right) hexagonal (N°2) liquid crystal structures at 25°C. One exposition per sample.

Considering that the internal structure will not change within a same liquid crystal zone, we can therefore conclude that the red LC domain consists of hexagonal liquid crystals, and the brown LC zone of lamellar liquid crystals. We then determined the lattice parameter of each structure, as depicted in Figure 3.3, using and Eq. 3.3 for lamellar structures d_L and Eq. 3.4 for hexagonal structures d_H [12]. Considering the low MMA composition of the hexagonal domain compared to water, we therefore assume that this structure is a hexagonal direct H_I structure, as presented in Figure 3.3.

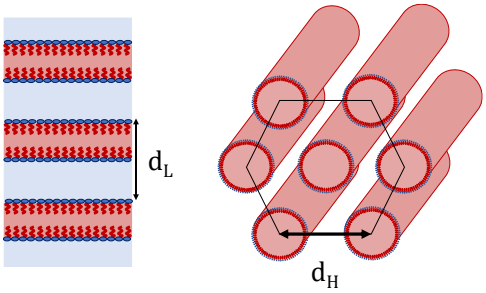

Figure 3.3 – Schematic representation of the lattice parameter in (left) lamellar and (right) hexagonal liquid crystal structures.

$$d_L = \frac{2\pi}{q_1} \quad \text{Eq. 3.3}$$

$$d_H = \frac{4\pi}{q_1\sqrt{3}} \quad \text{Eq. 3.4}$$

The lattice parameters extracted from the scattering curves of both samples are presented in Table 3.3. We determined that the centres of each cylinder constituting the hexagonal lattice are 65.4 nm apart, while the lamellae constituting the lamellar lattice are 5.7 nm apart. We can then conclude that the red and brown zones are respectively nanometric hexagonal and lamellar liquid crystal structures.

Table 3.3 – Scattering peak positions and associated lattice parameter in the lamellar (N°1) and (N°2) samples.

Sample	q_1 (Å^{-1})	q_2 (Å^{-1})	q_3 (Å^{-1})	Lattice parameter (Å)
N°1	1.10E-1	2.18E-1	-	57
N°2	1.11E-1	1.92E-1	2.22E-1	654

- **Identification of the non-birefringent domain**

The **yellow** non-birefringent domain shown in the (0:50:50) pseudo-ternary diagram in Figure 3.1 was partially investigated using SAXS analyses. To that end, three compositions of the $(75:25)_{MMA:Surfactants}$ water dilution line were investigated: two samples belong to the non-birefringent domain (N°3 and N°5) and one sample belongs to the lamellar domain (N°4). The associated SAXS scattering curves of these two samples are presented in Figure 3.4 below.

No defined thin peak is observed in the scattering curves of both N°3 and N°5 samples, indicating that no cubic phase is occurring in our systems. The scattering curve of the sample N°3 shows the existence of a broad peak for low-water contents. Such a scattering curve indicates the occurrence of a characteristic distance between inhomogeneities and can be attributed either to a micellar or a L_3 sponge structure [2], [13]–[16].

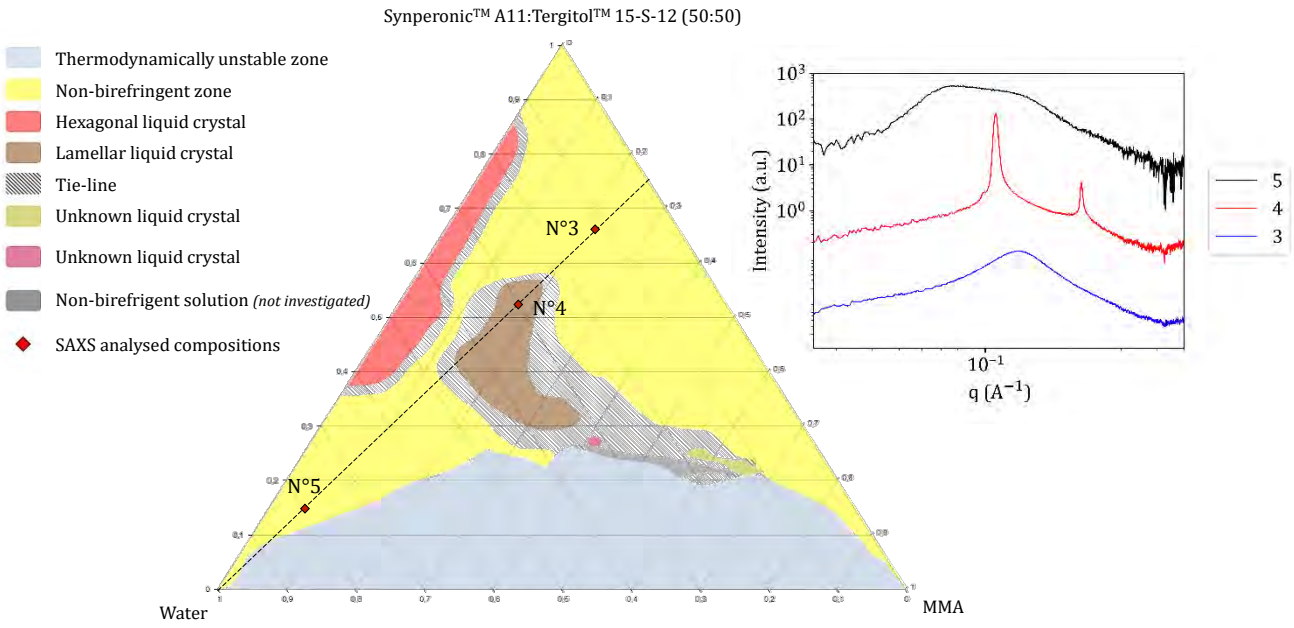

Figure 3.4 – SAXS scattering curves of the N°3, N°4 and N°5 samples at 25°C, along the (75:25)$_{MMA:Surfactants}$ water dilution line. One exposition per sample.

Sample N°5, with high water content, exhibits two overlapping broad peaks, as well as a rise in intensity at small scattering vectors. Such a pattern of scattering curves have been attributed to micellar structures by some authors [2], [13]–[15]. Obtaining micellar structures would be consistent with the general pattern of the mean-curvature evolution upon water dilution (c.f. Figure 3.5), the lamellar structure being characterised by a zero-mean curvature. However, to confirm these observations, DOSY-NMR and conductivity would have to be carried out on these samples.

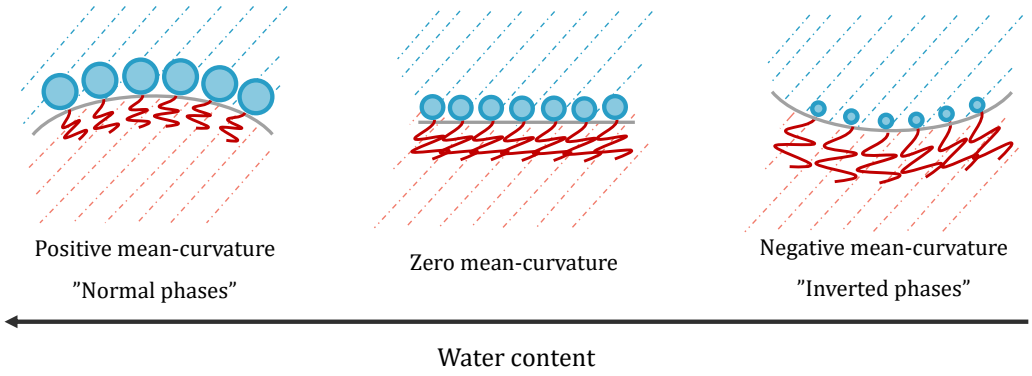

Figure 3.5 – General evolution of the mean-curvature of surfactant interfaces upon water addition [17].

Intermediate conclusions:

In this section, we evidenced the possibility to formulate non-ionic liquid crystals based on a water:MMA:Synperonic™ A11:Tergitol™ 15-S-12. We identified the existence of a lamellar and a hexagonal structures, as well as two other unidentified liquid crystal zones. We also evidenced

the occurrence of a non-birefringent and non-cubic zone. Even if the analysis we performed on the few selected samples did not evidence the occurrence of a bicontinuous structure, such structures may exist in the vicinity of the lamellar domain, as suggested by Kogan et al. (2009) [2]. Further SAXS analyses, combined to complementary techniques such as conductivity measurements and DOSY-NMR, will necessary to fully assess the microstructure adopted by this non-birefringent and non-cubic zone in the (0:50:50) acrylate system.

3.3.2 Impact of the co-surfactant on the microstructure of the system

It is common practice to use a co-surfactant in surfactant-based systems to further decrease the surface tension of the interface. 2-hydroxyethyl methacrylate (HEMA) has been widely used as a co-surfactant in various research projects aimed at the synthesis of membranes from microemulsion templates, as detailed in Chapter 1. As this compound is also a monomer, its use has proven to modify the pore size of the resulting polymer network, which might be useful to tune the properties of the polymer membrane. In the following section, we will discuss the behaviour of the system upon HEMA addition, to better understand its impact on the system. Previous research work carried out by our research team in the Laboratoire de Génie Chimique, developed a specific composition to be polymerised in order to obtain a nanometric porous material to be used in membrane filtration, as discussed in Chapter 4. We then diluted a $(38:29:33)_{0:50:50}$ composition with HEMA so that the composition of interest when reaching 34.7 wt.% HEMA in the system. This initial composition is located into the lamellar domain of the (0:50:50) acrylate pseudo-ternary system. After the addition of 4.6 ± 0.2 wt.% HEMA, no birefringence was observed indicating a disappearance of the lamellar liquid crystal phase. We then investigated the evolution of the microstructure of the system for several HEMA contents using SAXS analysis, as presented in Figure 3.6.

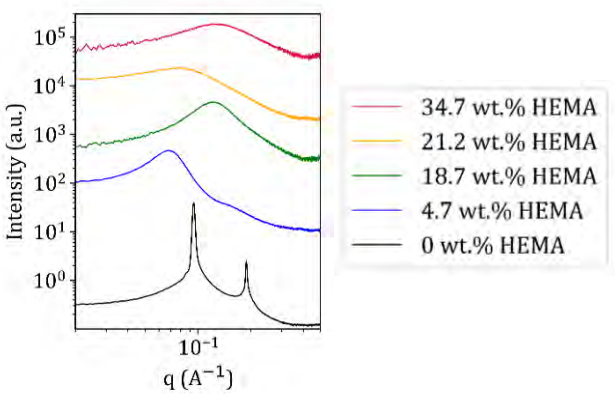

Figure 3.6 – SAXS scattering curves representing the evolution of microstructure of the $(38:29:33)_{0:50:50}$ composition upon HEMA addition, at 25°C. One exposition per sample.

The SAXS scattering curves presented above show the disappearance of the thin and well-defined peaks indicating a lamellar structure, when adding 4.7 wt.% HEMA. Two broad peaks are found instead and indicate the absence of a long-range order but the preservation of a short-range order. We then observe that further increasing the amount of HEMA in the system modifies both the position of the maxima of the broad peaks and the general shape of the curves.

At the birefringence disappearance limit (4.7 wt.% HEMA), two broad scattering peaks are observed. Compared to the lamellar structure (0 wt.% HEMA), these two broad peaks are shifted towards smaller values of scattering vector, indicating an increase of the size of the structure. Plus, we note a d-spacing ratio of 0.438 between these two broad peaks, while a lamellar structure exhibits a spacing ratio of ½. Such a result seems to indicate that the initial lamellar structure (0 wt.% HEMA) is being distorted upon addition of 4.7 wt.% of HEMA. This distortion will cause the loss of the long-range structuration of the liquid crystal while maintain a short-range order highlighted by the occurrence of the broad peaks. Because the characteristic distance between the lamellae increases from 6.5 nm to 9.1 nm (cf. Eq. 3.3) after addition of HEMA, we conclude that these molecules will swell the structure and be into one or both of the antagonist phases. When further diluting the system 4.7 wt.% system with HEMA, a gradual decrease in the intensity of the scattering curves is observed. Such a behaviour can result from a decrease from the interface stiffness and thus indicating a decrease of the order in the microstructure [1], [3], [18], [19].

Kogan et al. (2009) [2] reported the use of short amphiphilic organic co-surfactants, that altered the surfactant lamellar interface and led to bicontinuous structures with short-range order. Maldonado et al. [20] and Oberdisse et al. [21] also specified that non-ionic surfactant systems usually evolve from a lamellar to an L_3 sponge structure upon co-surfactant addition, visually characterised by a loss of birefringence and of viscosity, which we observed when diluting the $(38:29:33)_{0:50:50}$ composition with 4.6 ± 0.2 wt.% of HEMA. These visual observations combined to the analysis of the SAXS scattering curves presented in Figure 3.6 could indicate the existence of a bicontinuous or L_3 sponge phase upon HEMA addition. In order to determine whether a L3 sponge phase is obtained, the flow birefringence of the sample is to be analysed: a L3 structure will appear birefringent when undergoing a shear constraint that will align the surfactant interface and create a temporary lamellar structure [22].

However, because HEMA is also a co-solvent of the system and is able to co-solubilise MMA and water, one can question if an interconnected structure is obtained when diluting the system

with high amounts of HEMA. Indeed, the co-solubilisation of the organic and aqueous phases can give rise to nanostructured aggregates [23]. Such a hypothesis was however not further investigated as part of this project due to lack of time.

Intermediate conclusions:

After the addition of 4.6 ± 0.2 wt.% HEMA, the acrylate non-ionic monomer system becomes fluid and loss its birefringent nature under cross-polarised light, indicating a disappearance of the lamellar liquid crystal. Based from the scattering curves in Figure 3.6, we concluded that when 4.7 wt.% HEMA is added in the system, the lamellar liquid crystal structure undergoes a distortion and a growth of its lamella(e). Such a modification of the structure results in a loss of the characteristic long-ranged structuration of the liquid crystal.

Based on the experiments we carried out, we were however not able to definitely conclude on the structure of the systems when increasing the amount of HEMA. The microstructure of the systems containing 18.7 wt.% and 34.7 wt.% HEMA will be further discussed in Section 3.4.

3.4 Non-ionic quinary systems investigation

Based on the results presented in Section 3.3, we evidenced that addition of HEMA will destabilise the lamellar liquid crystalline domains and give rise to bicontinuous microstructures. However, we did not investigate the evolution of other (dis)ordered structures upon addition of the co-surfactant. We propose to address this issue by analysing two quinary systems containing different HEMA to surfactants mass ratios (HEMA:Synperonic™ A11:Tergitol™ 15-S-12): the (62:19:19) and (33:33:33) systems. To that end, a global conductimetric approach will be combined with specific SAXS and DOSY-NMR analyses.

3.4.1 Elaboration of the pseudo-ternary phase diagrams

The first step for the characterisation of the microstructure of the two acrylate systems is the delimitation of the microemulsified (or cubic) domains. For this purpose, a visual investigation of the various compositions was carried out at 25°C. A mix is classified as a microemulsion if it is monophasic, transparent and non-birefringent. The stability of the transparent solutions was proved over three months. The system also needs to be established as non-cubic to be fully assessed as a microemulsion, which we will later discuss in Sections 3.4.2 and Appendix 4. The resulting pseudo-ternary phase diagrams are presented in Figure 3.7. It should be noted that the biphasic structure along the axes of the ternary diagrams was not probed, except for the MMA:water axis. We reported the behaviour of the quinary system as soon as a drop of the third phase was added into the liquid system.

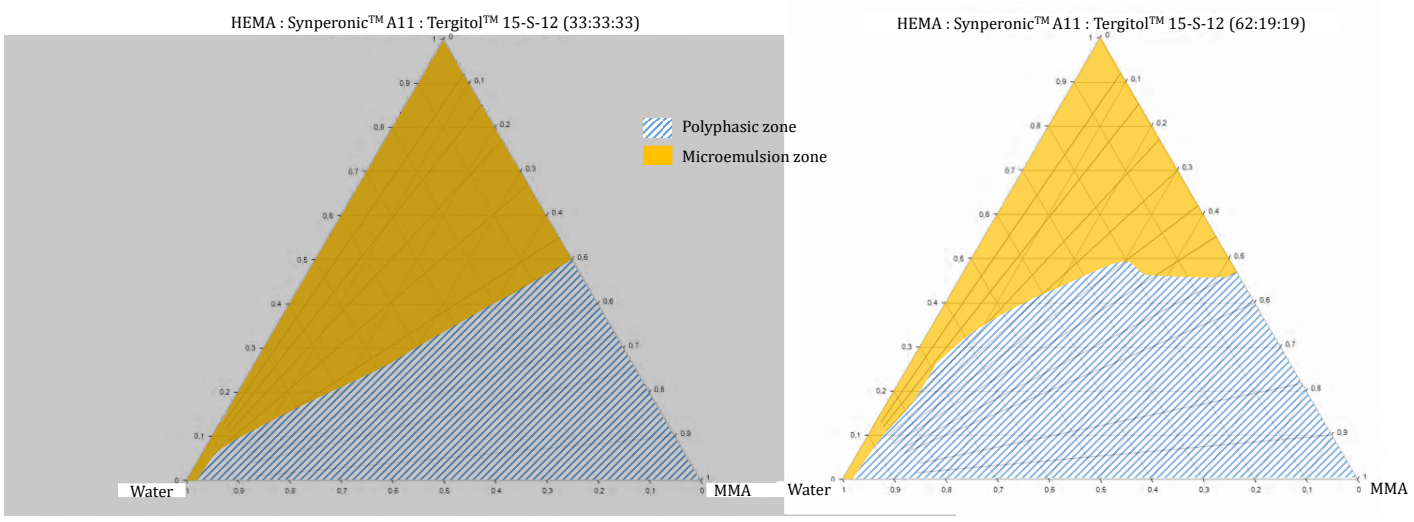

Figure 3.7 – Pseudo-ternary diagrams of thermodynamically stable and unstable zones for the (left) (62:19:19) and (right) (33:33:33) acrylate systems at 25°C. Monophasic (water:surfactants) and (MMA:surfactants) binary systems, biphasic (water:MMA) system up to ca. 99 wt.% water.

When comparing both pseudo-ternary diagrams, we observe that the size of the microemulsified zone is increased in the (33:33:33) compared to the (62:19:19) system. Plus, the high MMA to surfactant domain at low water content (< 10 wt.%) are polyphasic in the quinary systems, whereas such domains are monophasic in the quaternary (0:50:50) system. These observations are consistent with the impact of the amphiphilic HEMA on the (0:50:50) quaternary system. Indeed, we demonstrated in the previous section that increasing the quantity of HEMA in the system leads to a more disordered structure and a looser surfactant interface. Adding an increasing amount of HEMA in the quaternary system decreases the strength of the interface and thus its ability to stabilise the system. Plus, HEMA can also act as a co-solvent, thus further increasing the amount of the phases to be stabilised by the interface.

Conductivity measurements were then carried out to better characterise the microstructure of the transparent domains. In order to monitor the conductivity of non-ionic systems, the addition of an electrolyte in the system is necessary. As polyethoxylated non-ionic surfactants are not impacted by the salinity of the solution, such a modification will not impact on the microstructure of the investigated mix. Two conductimetric methods have been discussed in the literature [24]–[26]: adding the salt in the initial MMA-surfactant mix (the salt being dissolved due to the hydrated nature of the surfactants) or in the aqueous solution – here water. Both methods are valid but provide slightly different boundaries, cf. Figure 3.8.

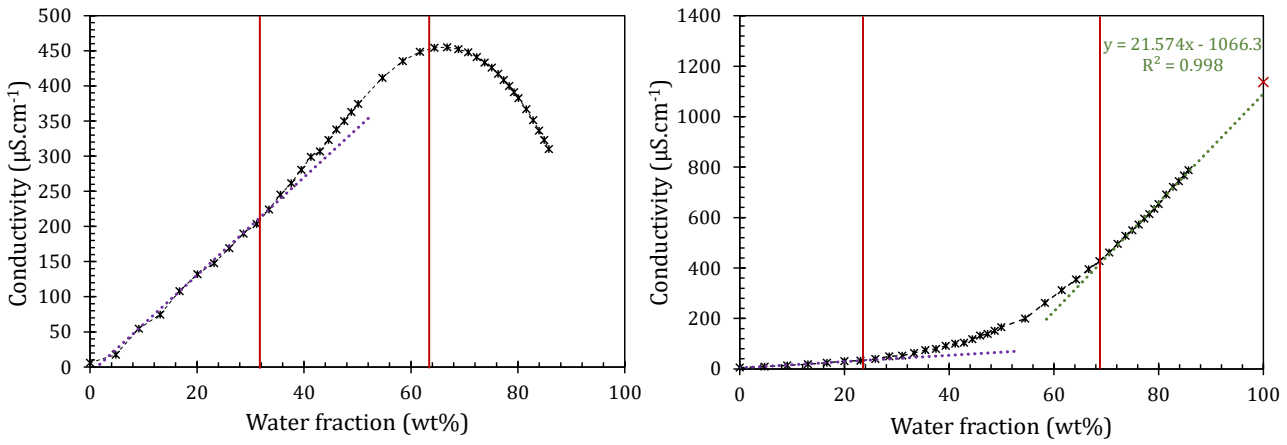

*Figure 3.8 – Conductivity curves of the (15:85)$_{62:19:19}$ water dilution line as function of the water content at 25°C. The ionic compound (NaCl) is contained in the (**left**) organic and (**right**) aqueous solution.*

We decided to dilute the system with a NaCl aqueous solution (0.01M), indeed this choice allows for an easier delimitation of the micellar zone by the determination of the slope discontinuities. The delimitation of both percolation boundaries was then determined when a slope discontinuity was observed. As expected, three zones are identified based on the

evolution of the conductivity. In the example presented in the right of Figure 3.8, a hydrophobic zone presenting low conductivity is observed up to 24 wt.% water. Upon further water addition the conductivity increases non-linearly until 67 wt.%. Finally, above 67 wt.%, a highly hydrophilic zone is observed where the conductivity increases linearly. When extrapolating this linear increase, the value of pure water is also reached (1137 $\mu S.cm^{-1}$ ± 4 %). The delimitation of the micellar-intermediate structures based on the conductimetric measurements for all the water dilution lines in both (33:33:33) and (62:19:19) system is reported in the pseudo-ternary diagram, cf. Figure 3.9.

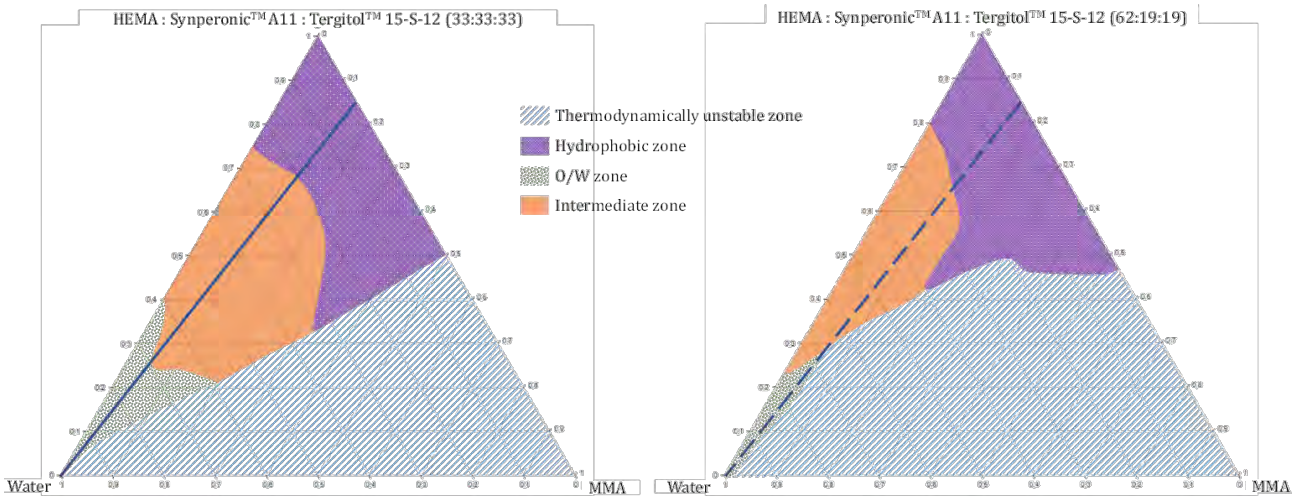

Figure 3.9 – Pseudo-ternary phase diagrams from conductivity measurements and the (15:85) water dilution line for the (left) (33:33:33) and (right) (62:19:19) acrylate systems at 25°C. Binary systems not investigated.

Intermediate conclusions:

Based on the literature, we could expect a W/O system up to 24 wt.% water, an O/W system above 67 wt.% and an intermediate bicontinuous structure. However, such information cannot be drawn from conductimetric measurement only, as other hydrophobic and hydrophilic non-birefringent microstructures may occur (e.g. cubic LC). Hence for the time being, we will refer to these three domains as the hydrophobic, intermediate and hydrophilic zones with respect to the water increase. Other analyses, such as DOSY-NMR and SAXS, are required to fully investigate the microstructure of the mixture and to conclude whether the transparent, non-birefringent domain is a cubic or a microemulsified domain. Such analyses cannot be carried out for the entire monophasic area. Thus, we will focus on the investigation of specific dilution lines in the following sub-sections.

3.4.2 Evolution of the microstructure upon water dilution

In order to follow the evolution of the thermodynamically stable microstructures upon water addition, we will investigate the (15:85) water dilution line in both (33:33:33) and (62:19:19) systems, as presented in Figure 3.9. SAXS and DOSY-NMR analyses will allow to determine the structural transitions induced by a water increase.

3.4.2.1 DOSY-NMR analysis

The (15:85) water dilution line for both (33:33:33) and (62:19:19) systems were investigated using DOSY-NMR analyses. Before proceeding with the examination of the system, it is important to note self-diffusion coefficients determined by DOSY-NMR are average coefficients: if a constituent is found in two distinct phases, its self-diffusion coefficient will be an average value of its coefficient in both phases.

3.4.2.1.1 Self-diffusion coefficients D_0 of the pure compounds

As a rule of thumb, regardless of intermolecular interactions, the diffusion coefficient of molecules in pure solution decreases with the increase of their molecular mass. The self-diffusion coefficients of water, MMA and HEMA are thus expected to be ranked as follows: $D_0^{H_2O} \gg D_0^{MMA} > D_0^{HEMA}$. The results in Table 3.4 however indicate that the MMA and water self-diffusion coefficients are quite similar, while the HEMA diffusion coefficient is very low – ten times lower – compared to those of water and MMA. The experimental data presented as part of this work are in good agreement with the coefficients reported in the literature.

Table 3.4 – Self-diffusion coefficient at 25°C of pure water, HEMA and MMA using DOSY-NMR.

Self-diffusion coefficient (10^{-9} $m^2.s^{-1}$)	**HEMA**	**Water**	**MMA**
Determined as part of this project	0.204 ± 0.006	2.32 ± 0.04	2.40 ± 0.05
From the literature	0.312 [27]	2.299 [28]	3.06 [29]

This observation is however not surprising, because water and HEMA are both hydrophilic molecules that can create H-bonds between themselves. The occurrence of interactions between molecules will decrease their mobility, and thus their diffusion coefficient. As a result, water molecules will diffuse at about the same velocity as MMA molecules because the acrylate compound does not exhibit any interaction with itself, unlike water. For the same reason, HEMA

and MMA – having a fairly similar molecular weight – will diffuse at very different rates due to the intermolecular interactions occurring between HEMA molecules.

3.4.2.1.2 Self-diffusion coefficients D of the quinary solutions the (15:85) water dilution line

The self-diffusion coefficients of water, MMA and HEMA for various compositions along the (15:85) water dilution line are summarised in Figure 3.9. Due to the overlap of the hydroxyl peaks of water and HEMA, the water self-diffusion coefficient for a 5 wt.% water content was not determined. The associated relative diffusion coefficients $\frac{D}{D_0}$ are reported in Figure 3.11. These relative coefficients represent the ability of the molecule to move through the mix compared to the pure liquid and is thus calculated as a ratio of the diffusion coefficient in the mix to the pure liquid (see Table 3.4).

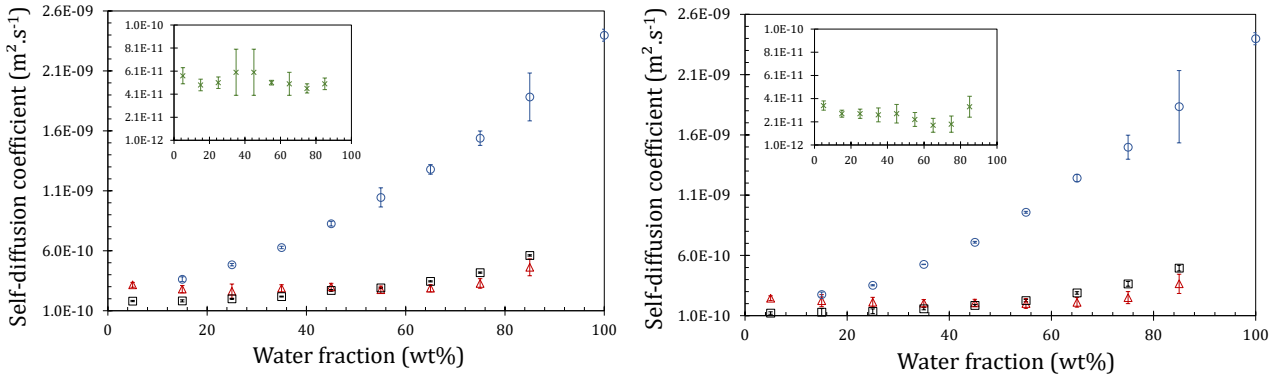

Figure 3.10 – Evolution of the diffusion coefficient of (△) MMA, (□) HEMA, (○) water and (×) non-ionic surfactants at 25°C, as a function of the water content along the (15:85) water dilution line in the (left) (62:19:19) and (right) (33:33:33) acrylate systems.

In both (33:33:33) and (62:19:19) systems, the MMA and HEMA self-diffusion coefficients remain stable respectively up to 65 wt.%. In the (33:33:33) system, the MMA and HEMA self-diffusion coefficients are respectively about 3E-10 and 2E-10 $m^2.s^{-1}$, while they both are about 2E-10 in the (62:19:19) system. Above 65 wt.% of water, their self-diffusion coefficients slightly increase: MMA coefficients reaches 3.6E-10 and 4.6E-10 $m^2.s^{-1}$, while HEMA coefficients reaches 4.9E-10 and 5.6E-10 $m^2.s^{-1}$ for 85 wt.% water in the (33:33:33) and (62:19:19) systems respectively. The relative diffusion coefficients of MMA remain between 0.11 and 0.16 $m^2.s^{-1}$ for the whole range of water content for both systems. HEMA relative diffusion coefficient, in turn, increases sharply and non-linearly upon water dilution from 0.6 and 0.9 to 2.4 and 2.7, for the (33:33:33) and (62:19:19) systems respectively.

Such an evolution originates from the creation of hydrogen bonds, as detailed for pure HEMA molecules. Bellaire et al. [30] reported that the dilution of the pure alcohol solution decreases the hydrogen bond (H-bond) prevalence and thus increases the mobility of the alcohol – and in our case of HEMA. We must however note that this result does not imply that the HEMA molecules do not longer form H-bonds, as they can still form H-bonds with smaller molecules such as water. However, the hindrance will be reduced and the mobility enhanced compared to identical molecules binding with each other.

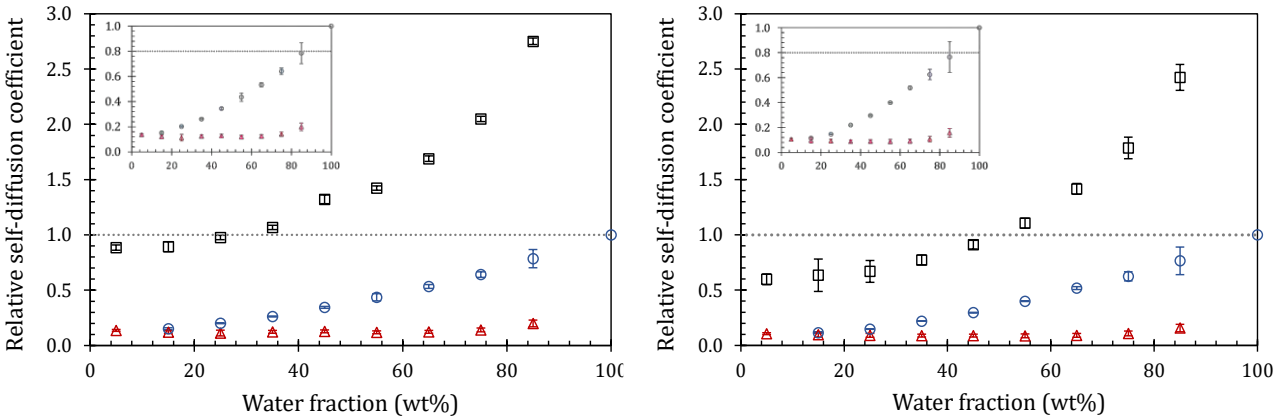

Figure 3.11 – Evolution of the relative self-diffusion coefficient of (△) MMA, (□) HEMA and (○) water at 25°C, as a function of the water content along the (15:85) water dilution line in the (left) (62:19:19) and (right) (33:33:33) acrylate systems.

We then observe that the diffusion coefficient of MMA and HEMA is not significantly modified upon water dilution for both surfactant phase compositions. These results indicate that the surface area available for the movement of MMA and HEMA molecules remains highly restricted up to 65 wt.%, but then slightly increases until 85 wt.% water dilution for both investigated acrylate systems. We also can note that the value of these coefficients is quite similar for HEMA and MMA, which implies that both molecules will be free to move across a similar surface per second – and thus tend to indicate that they belong to a single phase. This result is reinforced by the fact that HEMA average self-diffusion coefficients are always at least an order above the ones of the surfactant mix. From these results, we conclude that HEMA molecules are not strictly restricted to the surfactant interface and will mostly be found in the organic phase as a co-solvent of MMA.

No evolution of the self-diffusion coefficients of the non-ionic surfactants mix (Synperonic™ A11 and Tergitol™ 15-S-12) was observed throughout the dilution process, as they remained around 4-6E-11 and 2-4E-11 in the (33:33:33) and (62:19:19) systems respectively. This result

indicates that the surfactant molecules' mobility remained almost unchanged during water dilution.

Water self-diffusion coefficients, in turn, increase from 2.8E-10 or 3.6E-10 to 2.4E-9 $m^2.s^{-1}$ when raising the water content from 5 to 85 wt.%, for the (33:33:33) and (62:19:19) systems respectively. The water relative self-diffusion coefficient increases from 0.12 and 0.15 to 1, for the (33:33:33) and (62:19:19) system respectively. This increase indicates an expansion of the surface area available for the movement of water molecules upon water dilution. Above 85 wt.% of water, the relative self-diffusion coefficient of water is equal or higher than 0.8, indicating that the aqueous phase is becoming a continuous phase in the system.

It should be noted that the self-diffusion coefficients of water behave non-linearly when considering the full dilution range of water, for both (33:33:33) and (62:19:19) systems. However, if only high-water contents are considered, a linear evolution of the coefficient is observed – above 45 wt.% in both systems – and the diffusion coefficient of pure water (2.4E-9 $m^2.s^{-1}$) is successfully obtained when extrapolated to a dilution of 100 wt.%. We hypothesise this non-linear evolution of relative self-diffusion coefficient of water to result from the nature of the head-groups of the non-ionic polyethoxylated (PEO) surfactants. It has been reported that the water-EO interaction lowers the solvent mobility near the surfactant interface (cf. Figure 3.12), leading to lower self-diffusion coefficients [6], [31].

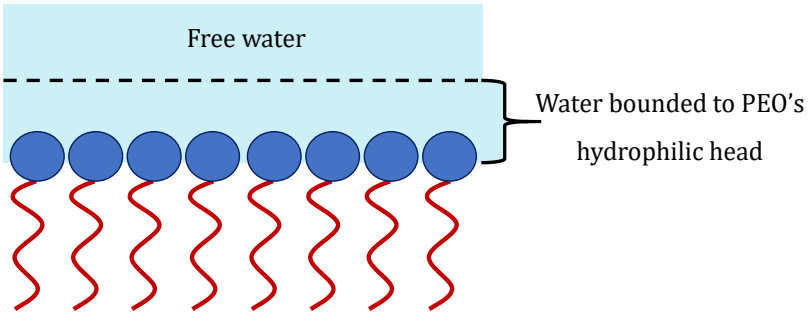

Figure 3.12 – Schematic representation of the hydration phenomenon occurring when using polyethoxylated surfactants.

An empirical correction can be applied to compensate this hydration effect. However, this correction factor must be determined beforehand on the basis of the diffusion of micellar microstructures, which is outside our scope. We can nevertheless note that, as the diffusion coefficients are average coefficients the hydration impact will decrease upon system dilution. Indeed, the freer water the less the impact of the bounded water on the average self-diffusion coefficient. We therefore conclude that for low water contents, the average self-diffusion

coefficient will be lowered by the hydration effect, but when increasing the water content in the system, the hydration effect will be less impacting until a linear increase is achieved.

Intermediate conclusions:

As detailed in the Bibliographic study (Chapter 1), the self-diffusion coefficient of a compound indicates how restricted the molecules are in the solution and thus whether these molecules are found in a restricted or open medium. Classical microemulsified systems (W/O → bicontinuous → O/W structures), exhibit a decrease in the self-diffusion coefficient of the organic compounds, combined to an increase of the water self-diffusion coefficient upon water dilution. However, the present (33:33:33) and (62:19:19) systems behave differently, as neither MMA nor HEMA coefficients are strictly higher than the self-diffusion of water. This information tends to indicate that the organic phase cannot be a continuous medium, even at low water contents. Indeed, in order to be considered as a continuous phase, self-diffusion coefficients in the following range are expected:

$$D^{continuous} \approx 10E\text{-}9\ m^2.s^{-1};\ D^{dispersed} \approx 10E\text{-}11\ m^2.s^{-1} \quad \text{and} \quad \left(\frac{D}{D_0}\right)_{continuous} > 0.8;\ \left(\frac{D}{D_0}\right)_{dispersed} \approx 0.3$$

Such values are never reached for the organic phase (maximum 4-5 E-10 $m^2.s^{-1}$). Plus, up to 65 wt.% of water, MMA and HEMA coefficients do not significantly vary, which indicates that the organic structure does not evolve upon water dilution, which is highly uncommon and seems to be in contradiction with the common behaviour of microemulsions upon water dilution.

The aqueous phase in turns, slowly grows in this dilution range, as expected when diluting the system with water. Above 85 wt.% of water, the relative self-diffusion coefficient of water is equal or higher than 0.8, indicating that the aqueous phase is becoming a continuous phase in the system. We would therefore expect the oil phase to form discrete droplets, but this phenomenon seems to be contradicted by the increase of both MMA and HEMA self-diffusion coefficients.

Finally, we evidenced a similar behaviour of the self-diffusion coefficients of water, MMA and HEMA regarding their evolution and their value upon water dilution for the two (33:33:33) and (62:19:19) acrylate systems. We therefore assume that the ratio HEMA to non-ionic surfactant does not have a significant impact on the size of both hydrophilic and hydrophobic phases in the two investigated systems.

Based on the mere DOSY-NMR results, it is not possible to conclude on the microstructure adopted by the (62:19:19) and (33:33:33) systems. SAXS analyses of the two investigated dilution lines were then performed in order to obtain more information on the microstructure adopted by the two systems.

3.4.2.2 SAXS analysis

The SAXS scattering curves of the (15:85) dilution lines for both (62:19:19) and (33:33:33) systems are presented in Figure 3.13. The X-ray source used for these analyses was less powerful than the one presented in Chapter 2 and produced a flow of 18.10^6 ph.mm^2.s^{-1}. Each sample was exposed to the X-ray beam 6 x 1200 s at room temperature (23°C).

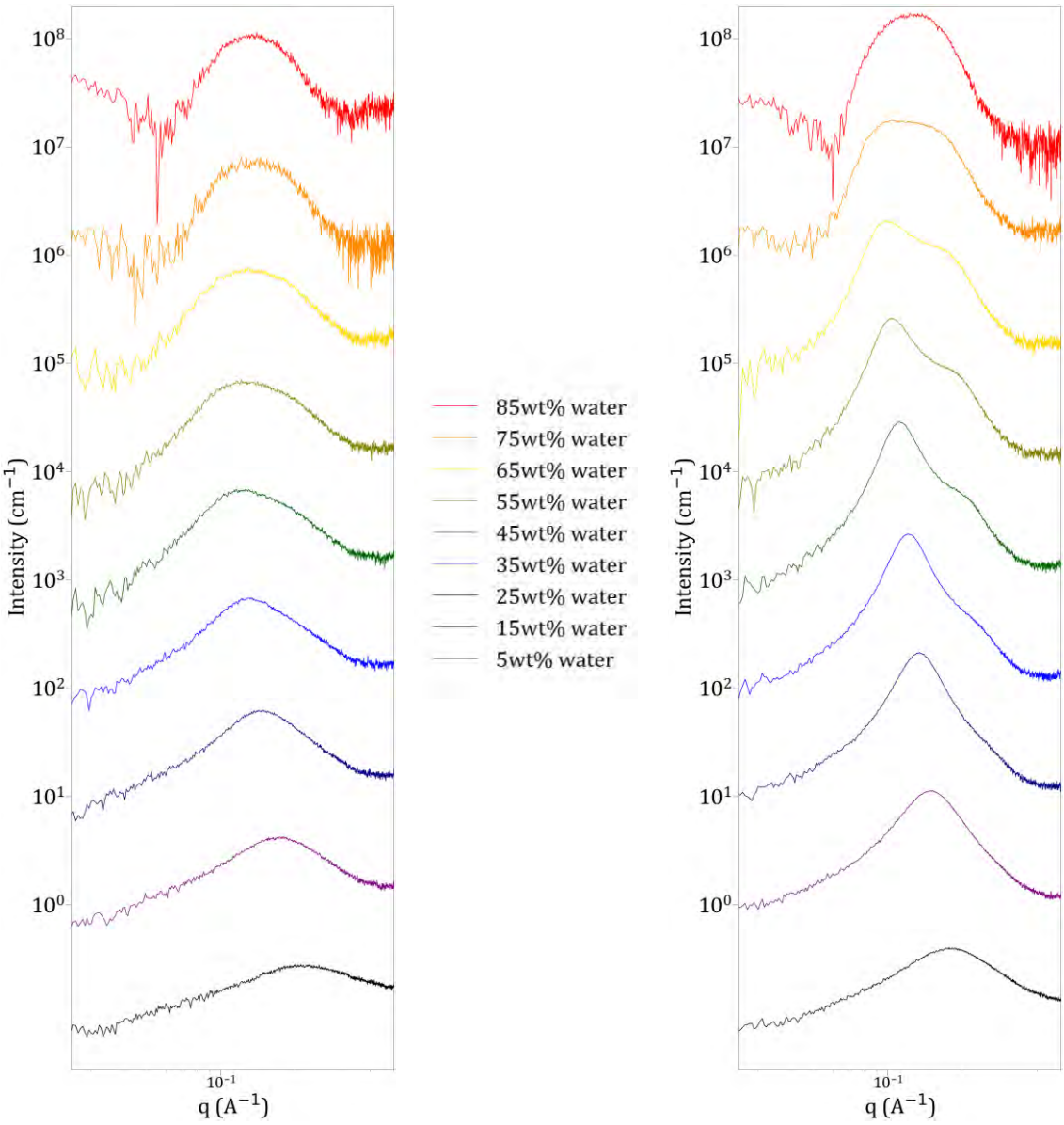

Figure 3.13 – SAXS scattering curves of the (15:85) water dilution line at 25°C, for the (left) (62:19:19) and (right) (33:33:33) acrylate systems.

First, we observe no thin, well-defined peaks characteristic of liquid crystal structures. We can therefore conclude that the solution is not a cubic liquid crystal. We then note that two dilution lines exhibit a common pattern: a single peak is observed for low water contents, a second (more or less well-defined) peak then appears above 35 wt.% and 25 wt.% water and these two peaks will finally merge for ca. 75 wt.% and 85 wt.% water, for the (62:19:19) and (33:33:33) systems respectively. Finally, we note that the intensity of the peaks decreased between the (33:33:33) and the (62:19:19) systems.

We also observe that the maximum of both peaks of each shift towards smaller values of scattering vector upon water dilution up to 65 wt.% and 75 wt., for the (62:19:19) and (33:33:33) systems respectively. This behaviour indicates the occurrence of a nanometric microstructure, growing upon water addition. Above such an amount of water, the peaks start to merge into one peak and an increase of the signal intensity for low scattering vectors is observed, which indicates the appearance of a structure factor and thus interactions between objects constituting the solution. Such a pattern is typical micellar scattering curves [2], [13]–[15] for water content above 75 wt.% in the (62:19:19) system and 85 wt.% in the (33:33:33) system.

3.4.2.3 On the microstructure adopted by the systems upon water dilution

In order to conclude on the microstructure of the (33:33:33) and (62:19:19) monomer self-assemblies, we tried to perform a cryo-TEM analysis of some samples along the (15:85) water dilution line. We were however unable to analyse the samples below 75 wt.% water due to the impossibility of instantaneously freezing the monomer sample in liquid ethane at -185°C. Such a behaviour of the sample was attributed to the presence of high concentrations of surfactants in the system. At high water dilution, we were able to freeze the sample, although we were still unsure of the possible modification of its microstructure due to the temperature change in the sample prior to freezing. A cryo-TEM analysis would have allow us to visualise the sample and to unequivocally conclude on the microstructure of the sample.

Based on the **conductivity**, **DOSY-NMR** and **SAXS** analysis we concluded that:

- The system remained quite hydrophobic up to 25 wt.% water. A sharp linear increase of conductivity was then observed after 65 wt.% water, which tends to indicate the occurrence of a continuous aqueous phase. See **Figure 3.8**.

- The self-diffusion coefficients of both MMA and HEMA remain stable up to ca. 65 wt.% water, after which they both slightly increase. The self-diffusion coefficients of water, in turn, increases throughout all the investigated range. Above 85 wt.% the self-diffusion coefficient of water is greater than 0.8 indicating that water has become a continuous medium. However, it seems inconsistent for MMA and HEMA to be a continuous medium, even for extremely low water content due to their low diffusion coefficients. See **Figure 3.10** and **Figure 3.11**.

- No characteristic scattering peaks of liquid crystal phases are observed. Two scattering broad peaks are observed in X-Ray scattering above ca. 15-25 wt.% water. Two peaks are observed when diluting the system with water, but the second peak is less defined in the system containing more HEMA (i.e. the (62:19:19) system). As the amount of water is increased, the maximum of both peaks shifts towards lower scattering vectors, indicating a growth of the structure up to 65 wt.% of water. When further increasing the water content above 75-85 wt.%, the two peaks are merging to give rise to a single broad peak of higher scattered intensity. An increase in the intensity of the signal is observed for low scattering vectors, indicating the occurrence of a structure factor. See **Figure 3.13**.

Based on the mere conductivity, DOSY-NMR and SAXS analyses carried out as part of this research project, it seems uncertain to definitively conclude on the microstructure adopted by the two quinary systems investigated. However, we can identify a similar pattern in all analyses:

- **Below 25-35 wt.% water:** Occurrence of a hydrophobic solution where neither the organic nor the aqueous phase can form a continuous medium. A single scattering peak of low intensity is observed. Increasing the amount of water increases the intensity of the broad scattering peak and increases the self-diffusion coefficient – and thus the size – of the aqueous domain.
  - **Small organic domains and aqueous domains co-existing. Slight increase in the size of the aqueous domain.**

- **Between 25-35 wt.% and 75-85 wt.% water:** The conductivity of the solution increases slightly and non-linearly. The self-diffusion coefficients of MMA and HEMA do not evolve remain as low as ca. 10^{-10} $m^2.s^{-1}$. The self-diffusion of water continues to increase upon water addition. Occurrence of two scattering peaks shifting towards lower scattering vectors when increasing the amount of water in the system: increase in the "object" size.

- **Swelling of the nanometric structure upon water addition, associated to a growth of the aqueous phase, but not of the organic phase. Still no continuous medium found in the solution.**

- **Above 75-85 wt.% water:** The conductivity of the solution increases dramatically and linearly. The self-diffusion coefficient of water increases and reaches 0.8, indicating water has become a continuous medium. The self-diffusion coefficients of MMA and HEMA slightly increases. The two observed scattering peaks are merging into one peak of higher intensity. The system exhibits an increase of intensity for low values of scattering vector indicating the occurrence of a structure factor. The scattering pattern observed for 85 wt.% water are typical of micellar structures [2], [13]–[15].
  - **Growth of the aqueous domain until it becomes a continuous phase. MMA and HEMA become a dispersed phase stabilised by the non-ionic surfactants. The increase in the self-diffusion coefficients of MMA and HEMA is, however, uncommon when obtaining O/W structures.**

These results are to be combined to the microstructures identified in the (0:50:50) quaternary system, which did not contain any HEMA co-surfactant. In order to apprehend the modification of the structure upon HEMA addition, we will assimilate the two (15:85) water dilution lines discussed in Section 3.4.2, as two water dilution lines in the (0:50:50) system, which are then diluted with HEMA to reach the compositions of the (62:19:19) and (33:33:33) quinary systems. We will refer to these dilution lines as the $(32:68)^{33:33:33}$ and the $(21:79)^{62:19:19}$ water dilution lines in the (0:50:50), cf. Figure 3.14.

We note that both $(32:68)^{33:33:33}$ and the $(21:79)^{62:19:19}$ water dilution lines cross the lamellar domain and its associated tie-line. However, when diluting these two dilution lines with HEMA both lamellar structures disappear. This disappearance is consistent with the co-surfactant and co-solvent role of HEMA: increasing the HEMA content in the system loosens the surfactant interface and decrease its capacity to create an organised structure, which is also observed when comparing the definition and the intensity of the peaks in both (62:19:19) and (33:33:33) systems. Indeed, the (33:33:33) system – which contains the lower amount of HEMA – exhibits broad peaks better defined than the (62:19:19) system, whose peaks are so weakly defined they create a broad asymmetrical shoulder. Plus, the scattered intensity of the (33:33:33) curves is higher than the (62:19:19) curves, indicating a decrease of the stiffness of the surfactant interface, and thus a decrease of the internal order.

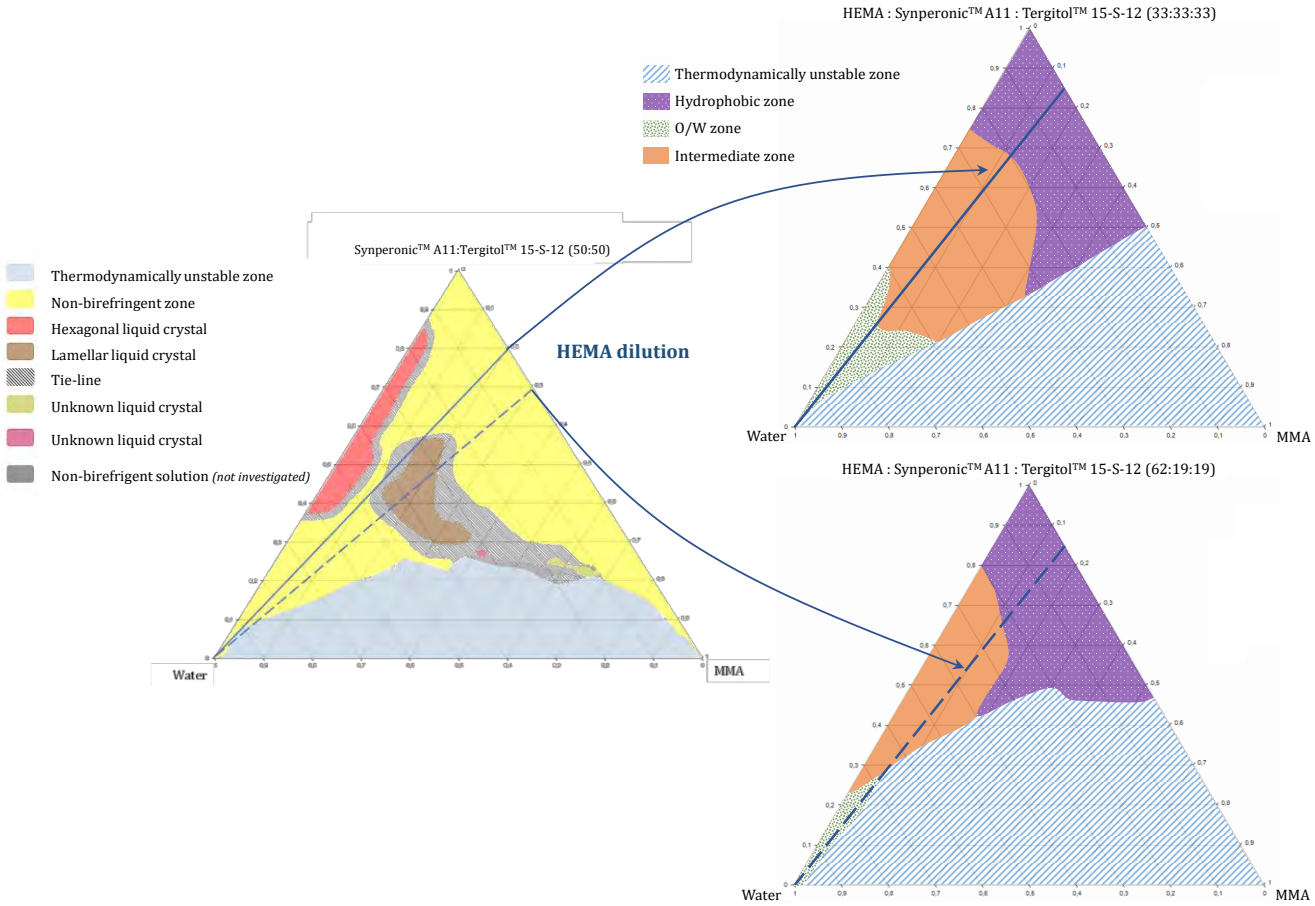

*Figure 3.14 – (**plain**) $(32:68)^{33:33:33}$ and (**dashed**) $(21:79)^{62:19:19}$ water dilution lines in the (0:50:50) system and the associated dilution lines in the (**bottom**) (62:19:19) and (**top**) (33:33:33) systems.*

Based on the results presented in Section 3.3, we therefore conclude that the zone crossed by the $(32:68)^{33:33:33}$ and the $(21:79)^{62:19:19}$ dilution lines exhibit low curvature of the surfactant interface between ca. 25 wt.% and 55 wt.%. Diluting lamellar structures with a co-surfactant can affect the Gaussian elastic modulus of the interface and modify its topology [21], [32]. If this modulus is positive a saddle-like topology is favoured (sponge phase), while a negative modulus will favour closed aggregates (vesicles) [33]. However, because neither the organic nor the aqueous phase can form a continuous medium based on the DOSY-NMR analyses, the occurrence of a vesicular structure in the quinary systems seems quite unlikely. The occurrence of a bicontinuous microemulsions originating from a lamellar structure was also discussed by Kogan et al. (2009) [2] and Nakamura et al. (1997) [34]. Kogan et al. (2009) reported the achievement of a bicontinuous structure when diluting a mix of triacetin/D-R- tocopherol acetate/ethanol (3/1/4) and Tween 60 with water. This author reported similar order of magnitude in the diffusion coefficients using DOSY-NMR as well as similar SAXS scattering patterns. They concluded on the occurrence of an "ordered bicontinuous structure" originating from the distortion of a lamellar structure upon heating at an intermediate regime of 25-65

wt.% water. We therefore hypothesise here the occurrence of an interconnected structure between ca. 25 wt.% and 55 wt.% water in the quinary systems. We further assume that the aqueous channels swell when increasing the water content from 25 to 55 wt.%, but not the organic channels. Nakamure et al. (1997) [34] diluted a hexanol/sucrose monododecanoate system with a (50:50 wt.%) mix of water:decane solution. They reported the swelling of both organic and aqueous lamellae, causing the hexanol co-surfactant to be distributed in the oil and in the palisade layer of the surfactant interface. This surfactant bilayer is then assumed to become more flexible during the system dilution, leading to the appearance of a bicontinuous structure.

Above 55 wt.% water, we observe a sharper increase of both conductivity and water self-diffusion coefficients. Based on these observations, we therefore assume that the aqueous channels of this interconnected structure are not able to swell anymore upon water addition and undergo breakage to give rise to a continuous aqueous medium above 85 wt.% of water. This assumption is also consistent with the SAXS scattering curves, which display the transition from two broad peaks to a single peak and a signal pattern characteristic of micellar structure.

However, we note an increase of the self-diffusion coefficients of both MMA and HEMA, which is quite uncommon when obtaining O/W micelles. Kogan et al. (2009) [2] also reported such an increase in the self-diffusion of the co-solvent/co-surfactant compounds and justified this behaviour as the displacement of these molecules into the aqueous continuous medium, as they were no longer needed in the surfactant interface to create oil micelles. Such a justification is also in good agreement for the present system, as HEMA can co-solubilise MMA and water. It is therefore possible for HEMA to be partially located in the aqueous phase, where it can co-solubilise a small amount of MMA. Such a phenomenon could then explain the increase in the self-diffusion coefficients of both MMA and HEMA when the aqueous phase becomes continuous.

Below 25 wt.% of water, it seems unlikely for a micellar structure to occur based on the self-diffusion coefficients obtained for the organic and aqueous phases. As no characteristic scattering pattern was observed and because we were not able to conclude on the structure adopted by the quaternary (0:50:50) system for such a water content, we can only conclude on the co-existence of confined aqueous and organic domains stabilised by a large quantity of surfactants.

Intermediate conclusions:

We discussed the possible microstructure adopted by the (33:33:33) and (62:19:19) systems based on DOSY-NMR, conductivity and SAXS analysis. Even if we were not able to definitely conclude, we suggest the occurrence of an interconnected structure (bicontinuous microemulsion or sponge phase – i.e. surfactant monolayer or bilayer) originating from the dilution of the lamellar structures with HEMA molecules. Such an assumption is in good agreement with the analyses presented in this manuscript and the literature. However, the discussed microstructure could also result from the system co-solubilisation with HEMA and the occurrence of dynamic nanostructures, as briefly discussed in Section 3.3.2. We therefore advise, as an example, to further investigate the hypothesis of a transition from a flexible system to ultraflexible system upon addition of HEMA in future work [23].

To assess the whole transparent non-birefringent zones of the (62:19:19) and (33:33:33) systems, we also investigated the microstructure of the acrylate systems through two additional MMA:surfactant phase dilution lines, while maintaining a constant water content in Appendix 4. Through SAXS and DOSY-NMR analyses, we obtained a similar conclusion to the one presented for the (15:85) water dilution line above. We however notice an increase in the organic and aqueous structures when decreasing the ratio of surfactant phase to MMA.

In order to conclude on the microstructure, we propose to carry out two analyses. The first one is a Small-Angle Neutron Scattering (SANS). Indeed, using contrast extinction, it is possible to investigate the microstructure adopted by each compound. Such an analysis could be combined with a visualisation of the global microstructure using a liquid cell transmission electron microscopy, i.e. observation of the liquid in a closed environmental cell that is transparent to the electron beam [35]. This method allows the liquid to be observed without being frozen, while still preventing its evaporation. The development of 3D tomography on liquid cell TEM seems also a promising technique to visualise the microstructure and conclude on the microstructure of the self-assembled monomer system [36].

3.5 Conclusion

We investigated the microstructure adopted by systems of various surfactant phase (HEMA:Synperonic™ A11: Tergitol™ 15-S-12) compositions, namely the (0:50:50), (33:33:33) and (62:19:19) systems. The elaboration of the three pseudo-ternary phase diagrams (see Figure 3.15) was carried out using cross-polarised light observation, conductivity measurements as well as DOSY-NMR and SAXS analyses. The purpose of our investigation was twofold and aimed to answer two questions:

- **How does the addition of the HEMA co-surfactant and co-solvent impact the microstructure of the monomer mix?**

HEMA is an amphiphilic monomer, miscible in both water and MMA phases. Its weak amphiphilic nature allows it to alter the surfactant interface mean-curvature, which we evidenced in this Chapter. We demonstrated that HEMA addition led to a disorganisation of the liquid crystal structures and gave rise to transparent non-birefringent domains. We also evidenced that further increasing the HEMA content in the system led to a decrease of the scattered intensity of the SAXS curves, thus indicating a decrease in the interface stiffness. If some authors reported the achievement of a sponge-phase upon dilution of a lamellar structure with a co-surfactant solution, we were however not able to unequivocally conclude on the achievement of such a structure when diluting the present system with HEMA. Such a behaviour however tends to confirm the role of HEMA as a co-surfactant, as stated by other authors [24], [37]–[45].

Depending on the authors, HEMA has been located in the organic [24], [40], [42], [45], surfactant [39], [44] and aqueous [41] phase. Because we considered HEMA as a co-surfactant, we chose to incorporate this compound in the surfactant phase. However, using DOSY-NMR analyses we concluded that MMA and HEMA most probably belong to a single organic phase, indicating a significant proportion of HEMA is also located on the organic phase. One might therefore question the choice we made to consider HEMA as a co-surfactant in the pseudo-ternary phase diagram. In order to conclude where the HEMA molecules are located, SANS analyses using deuterated HEMA can be considered. Such an analysis would allow for the determination of the location and proportion of HEMA molecules are located in the mix. Depending on the results obtained, further composite phases could be considered to create additional pseudo-ternary phase diagram(s), e.g. a composite HEMA and MMA organic phase.

Such additional information would allow for a better description of the systems presented in this manuscript.

- **What is the microstructure adopted by the system as a function of the HEMA to the non-ionic commercial surfactants?**

We identified two main behaviours in our systems, depending on their HEMA content. The system was named after their composite surfactant phase ratio: (HEMA:Synperonic™ A11:Tergitol™ 15-S-12). The quaternary (0:50:50) system – which does not contain any co-surfactant – presents three identified main domains: thermodynamic unstable polyphasic, liquid crystal and transparent and non-birefringent domains. A partial investigation of the liquid crystal domains allowed for the identification of lamellar and hexagonal domains. However, at least two other liquid crystal domains were left unidentified due to lack of time. Their identification would allow for a better understanding of the system.

We then investigated two other systems, characterised by a composite surfactant phase containing HEMA as co-surfactant. The (62:19:19) and (33:33:33) systems exhibit a restricted monophasic domain compared to their analogous domains (0:50:50) system. This phenomenon was attributed to the decrease of the surfactant content in the system, to the benefit of HEMA co-surfactant. We also demonstrated the disappearance of the liquid crystal domains upon co-surfactant addition, which also results from the weak amphiphilic behaviour of HEMA. These organised domains are progressively disorganised to give rise to a transparent non-birefringent structure. Based on DOSY-NMR, we concluded that no continuous organic nor aqueous medium could occur below ca. 55 wt.% water, indicating the absence of W/O structure. Combining conductivity, DOSY-NMR and SAXS analyses, we then assumed that the organised structures of the (0:50:50) system are distorted upon HEMA addition, to create a bicontinuous structure. We further hypothesised that these aqueous channels swell upon water addition, until water molecules cannot be further absorbed by the channels. The structure would then undergo breakage and give rise to an O/W micellar structure. Based on the results presented in this thesis, we were however unable to conclude on the microstructure adopted by the (62:19:19) and (33:33:33) systems below 25 wt.% of water. We advise further work to investigate the hypothesis of the occurrence of dynamic nanostructures resulting from the co-solubilisation of the aqueous and organic phases with HEMA, to conclude on the hypotheses here discussed. SANS and liquid TEM associated to 3D tomography could give some more insight on the microstructure adopted by the system.

In this work, we investigated the impact of the composition of the system for a fixed temperature. However, we know that the temperature factor has a dramatic impact on the structure adopted by the quaternary and quinary systems, due to the polyethoxylated nature of both Synpernonic™ A11 and Tergitol™ 15-S-12. Their ethoxylated functions will reversibly dehydrate upon heating, which promote their oil solubilisation and thus increase the interface mean-curvature. The construction of fishtail diagrams would then allow for a better overall understanding of the system, which is highly dependent on both temperature and composition.

Because commercial surfactants consist of a mix of amphiphilic molecules of various hydrocarbon lengths, using a mix of commercial surfactants complicates the determination of the microstructure adopted in the system. In order to fully elucidate the structure of the system, we therefore advise to simplify its composition by using only one pure non-ionic non-polymerisable surfactant.

In the next chapter, we will discuss the polymerisation of several self-assembled structures located in both the (62:19:19) and (33:33:33) systems to determine their suitability as a polymer material for liquid membrane filtration.

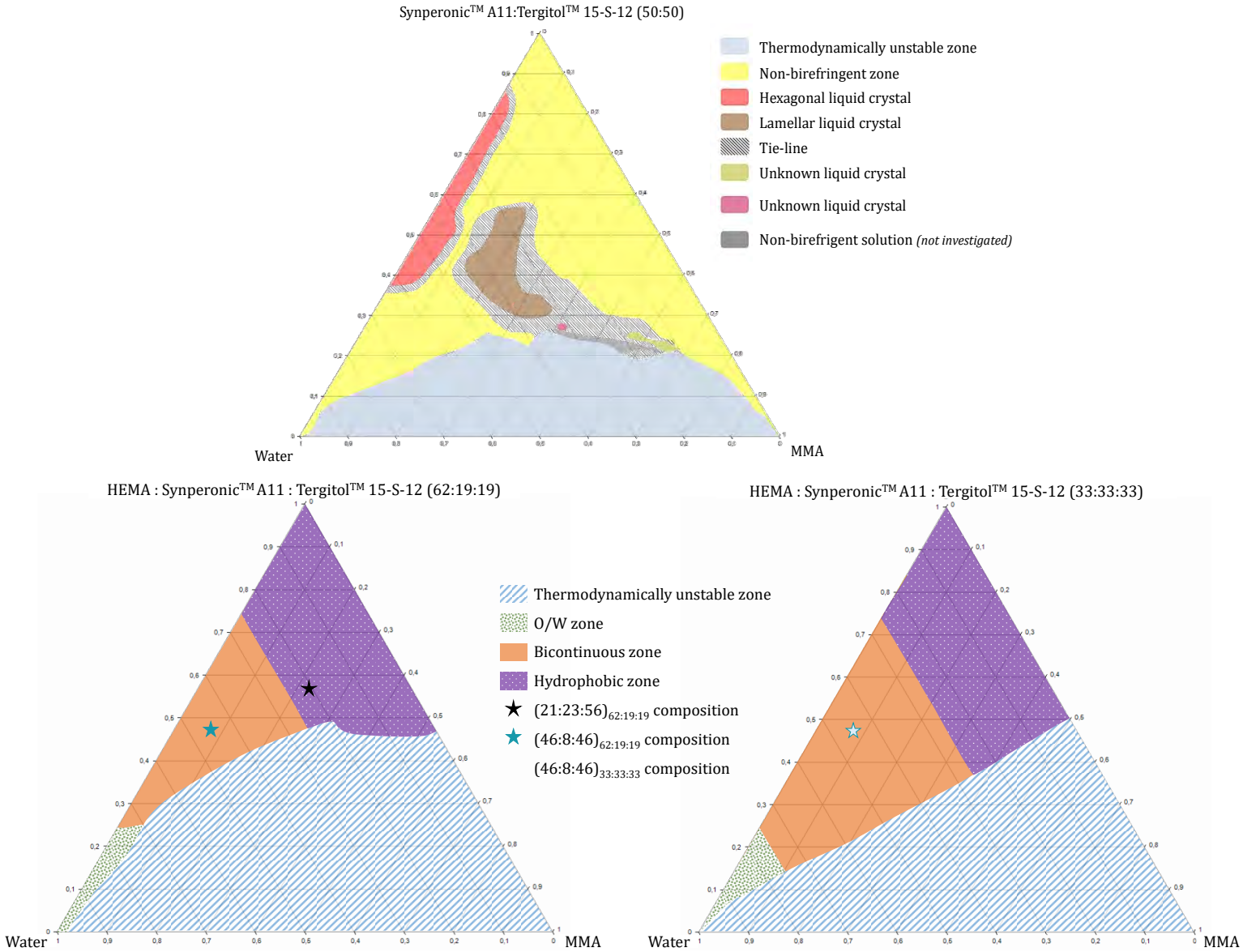

Figure 3.15 – Pseudo-ternary phase diagrams of the (top) (0:50:50), (middle) (62:19:19) and (bottom) (33:33:33) acrylate non-ionic systems

References

[1] R. J. Hickey, T. M. Gillard, M. T. Irwin, T. P. Lodge, and F. S. Bates, 'Structure, viscoelasticity, and interfacial dynamics of a model polymeric bicontinuous microemulsion', *Soft Matter*, vol. 12, no. 1, pp. 53–66, 2015, doi: 10.1039/c5sm02009c.

[2] A. Kogan, D. E. Shalev, U. Raviv, A. Aserin, and N. Garti, 'Formation and characterization of ordered bicontinuous microemulsions', *J. Phys. Chem. B*, vol. 113, no. 31, pp. 10669–10678, 2009, doi: 10.1021/jp901617g.

[3] S. Prevost, T. Lopian, M. Pleines, O. Diat, and T. Zemb, 'Small-angle scattering and morphologies of ultraflexible microemulsions', *J. Appl. Crystallogr.*, vol. 49, no. 6, pp. 2063–2072, 2016, doi: 10.1107/S1600576716016150.

[4] S. H. Chen, S. L. Chang, R. Strey, J. Samseth, and K. Mortensen, 'Structural evolution of bicontinuous microemulsions', *J. Phys. Chem.*, vol. 95, no. 19, pp. 7427–7432, 1991, doi: 10.1021/j100172a058.

[5] B. Lindman, K. Shinoda, U. Olsson, D. Anderson, G. Karlström, and H. Wennerström, 'On the demonstration of bicontinuous structures in microemulsions', *Colloids and Surfaces*, vol. 38, no. 1, pp. 205–224, 1989, doi: 10.1016/0166-6622(89)80154-4.

[6] B. Lindman and U. Olsson, 'Structure of microemulsions studied by NMR', *Berichte der Bunsengesellschaft/Physical Chem. Chem. Phys.*, vol. 100, no. 3, pp. 344–363, 1996, doi: 10.1002/bbpc.19961000321.

[7] V. Tchakalova, C. Bailly, and W. Fieber, 'Food-grade bicontinuous microemulsions', *Flavour Fragr. J.*, vol. 29, no. 1, pp. 67–74, 2014, doi: 10.1002/ffj.3181.

[8] G. Tartaro, H. Mateos, D. Schirone, R. Angelico, and G. Palazzo, 'Microemulsion microstructure(s): A tutorial review', *Nanomaterials*, vol. 10, no. 9, pp. 1–40, 2020, doi: 10.3390/nano10091657.

[9] J.-L. J. Salager, R. Anton, J.-M. Aubry, and R. Antón, 'Formulation des microémulsions par la méthode HLD', *Tech. l'Ingénieur, …*, vol. JC1, no. J2157, pp. 1–21, 2001, [Online]. Available: http://www.firp.ula.ve/archivos/cuadernos/01_TechIng_Salager_HLD.pdf%5Cnhttp://cat.inist.fr/?aModele=afficheN&cpsidt=21724954.

[10] J. Ontiveros, 'Classification des tensioactifs et huiles biocompatibles par mesure de la température d'inversion de phase (PIT) et comparaison des diagrammes de phases', pp. 1–232, 2014, [Online]. Available: https://ori-nuxeo.univ-lille1.fr/nuxeo/site/esupversions/d6ec8a23-39ee-4fe5-8d11-602f819e7a3c.

[11] G. Montalvo, M. Valiente, and E. Rodenas, 'Rheological Properties of the L Phase and the Hexagonal, Lamellar, and Cubic Liquid Crystals of the CTAB/Benzyl Alcohol/Water System', 1996, Accessed: Jul. 26, 2022. [Online]. Available: https://pubs.acs.org/sharingguidelines.

[12] H. Li, L. Dang, S. Yang, J. Li, and H. Wei, 'The study of phase behavior and rheological properties of lyotropic liquid crystals in the LAS/AES/H2O system', *Colloids Surfaces A Physicochem. Eng. Asp.*, vol. 495, pp. 221–228, Apr. 2016, doi: 10.1016/J.COLSURFA.2016.01.055.

[13] O. Regev *et al.*, 'A Study of the microstructure of a four-component nonionic microemulsion by cryo-TEM, NMR, SAXS, and SANS', *Langmuir*, vol. 12, no. 3, pp. 668–674, 1996, doi: 10.1021/la950505g.

[14] C. Noirjean, 'Microémulsions Solidifiées : une nouvelle voie vers les conducteurs protoniques ?', PhD thesis, Université de Versailles Saint-Quentin-en-Yvelines, 2014.

[15] A. Kogan, A. Aserin, and N. Garti, 'Improved solubilization of carbamazepine and structural transitions in nonionic microemulsions upon aqueous phase dilution', *J. Colloid Interface Sci.*, vol. 315, no. 2, pp. 637–647, Nov. 2007, doi: 10.1016/J.JCIS.2007.06.087.

[16] B. Angelov *et al.*, 'SAXS investigation of a cubic to a sponge (L3) phase transition in self-assembled lipid nanocarriers', *Phys. Chem. Chem. Phys.*, vol. 13, no. 8, pp. 3073–3081, Feb. 2011, doi: 10.1039/C0CP01029D.

[17] M. Zhou *et al.*, 'New type of membrane material for water desalination based on a cross-linked bicontinuous cubic lyotropic liquid crystal assembly', *J. Am. Chem. Soc.*, vol. 129, no. 31, pp. 9574–9575, 2007, doi: 10.1021/ja073067w.

[18] S. Peng, Q. Guo, T. C. Hughes, and P. G. Hartley, 'In situ synchrotron SAXS study of polymerizable microemulsions', *Macromolecules*, vol. 44, no. 8, pp. 3007–3015, 2011, doi: 10.1021/ma102978u.

[19] S. Engelskirchen, N. Elsner, T. Sottmann, and R. Strey, 'Triacylglycerol microemulsions stabilized by alkyl ethoxylate surfactants-A basic study. Phase behavior, interfacial tension and microstructure', *J. Colloid Interface Sci.*, vol. 312, no. 1, pp. 114–121, 2007, doi: 10.1016/j.jcis.2006.09.022.

[20] A. Maldonado, R. Ober, T. Gulik-Krzywicki, W. Urbach, and D. Langevin, 'The sponge phase of a mixed surfactant system', *J. Colloid Interface Sci.*, vol. 308, no. 2, pp. 485–490, Apr. 2007, doi: 10.1016/J.JCIS.2007.01.012.

[21] J. Oberdisse, 'Introduction to soft matter and neutron scattering', *EPJ Web Conf.*, vol. 188, p. 01001, Sep. 2018, doi: 10.1051/EPJCONF/201818801001.

[22] M. S. Leaver, U. Olsson, H. Wennerström, R. Strey, and U. Würz, 'Phase behaviour and structure in a non-ionic surfactant–oil–water mixture', *J. Chem. Soc. Faraday Trans.*, vol. 91, no. 23, pp. 4269–4274, Jan. 1995, doi: 10.1039/FT9959104269.

[23] M. Gradzielski, M. Duvail, P. M. De Molina, M. Simon, Y. Talmon, and T. Zemb, 'Using Microemulsions: Formulation Based on Knowledge of Their Mesostructure', *Chem. Rev.*, vol. 121, no. 10, pp. 5671–5740, May 2021, doi: 10.1021/ACS.CHEMREV.0C00812/ASSET/IMAGES/LARGE/CR0C00812_0032.JPEG.

[24] L. M. Gan, J. Liu, L. P. Poon, C. H. Chew, and L. H. Gan, 'Microporous polymeric composites from bicontinuous microemulsion polymerization using a polymerizable nonionic surfactant', *Polymer (Guildf).*, vol. 38, no. 21, pp. 5339–5345, 1997, doi: 10.1016/S0032-3861(97)00080-3.

[25] T. H. Chieng, L. M. Gan, C. H. Chew, S. C. Ng, and K. . L. Pey, 'Formation of microporous polymeric materials by microemulsion polymerization of methyl methacrylate and 2-hydroxyethyl methacrylate', *J. Appl. Polym. Sci.*, vol. 60, pp. 1561–1568, 1996.

[26] M. Laguës and C. Sauterey, 'Percolation transition in water in oil microemulsions. Electrical conductivity measurements', *J. Phys. Chem.*, vol. 84, no. 26, pp. 3503–3508, 1980, doi: 10.1021/j100463a003.

[27] J. Strauch *et al.*, 'Diffusion coefficients of the monomer and oligomers in hydroxyethyl methacrylate', *J. Polym. Sci. Part A Polym. Chem.*, vol. 41, no. 16, pp. 2491–2501, Aug. 2003, doi: 10.1002/POLA.10789.

[28] M. Holz, S. R. Heil, and A. Sacco, 'Temperature-dependent self-diffusion coefficients of water and six selected molecular liquids for calibration in accurate 1H NMR PFG measurements', *Phys. Chem. Chem. Phys.*, vol. 2, no. 20, pp. 4740–4742, Jan. 2000, doi: 10.1039/B005319H.

[29] M. C. Griffiths, J. Strauch, M. J. Monteiro, and R. G. Gilbert, 'Measurement of diffusion coefficients of oligomeric penetrants in rubbery polymer matrixes', *Macromolecules*, vol. 31, no. 22, pp. 7835–7844, Nov. 1998, doi: 10.1021/MA980169L/ASSET/IMAGES/LARGE/MA980169LF00013.JPEG.

[30] D. Bellaire, H. Kiepfer, K. Münnemann, and H. Hasse, 'PFG-NMR and MD Simulation Study of Self-Diffusion Coefficients of Binary and Ternary Mixtures Containing Cyclohexane, Ethanol, Acetone, and Toluene', *J. Chem. Eng. Data*, vol. 65, no. 2, pp. 793–803, Feb. 2020, doi: 10.1021/ACS.JCED.9B01016/ASSET/IMAGES/ACS.JCED.9B01016.SOCIAL.JPEG_V03.

[31] B. Balinov, U. Olsson, and O. Söderman, 'Structural Similarities between the L3 and Bicontinuous Cubic Phases in the AOT-Brlne System', *J. Phys. Chem.*, vol. 95, pp. 5931–5936, 1991, Accessed: Jul. 21, 2022. [Online]. Available: https://pubs.acs.org/doi/pdf/10.1021/j100168a041.

[32] R. Íñiguez-Palomares and A. Maldonado, 'Topology change by screening the electrostatic interactions in a polymer-surfactant system', *Colloid Polym. Sci.*, vol. 287, no. 12, pp. 1475–1479, Dec. 2009, doi: 10.1007/S00396-009-2118-9/FIGURES/4.

[33] W. Helfrich, 'Elastic Properties of Lipid Bilayers: Theory and Possible Experiments', *Zeitschrift fur Naturforsch. - Sect. C J. Biosci.*, vol. 28, no. 11–12, pp. 693–703, Dec. 1973, doi: 10.1515/ZNC-1973-11-1209/MACHINEREADABLECITATION/RIS.

[34] N. Nakamura, T. Tagawa, K. Kihara, I. Tobita, and H. Kunieda, 'Phase transition between microemulsion and lamellar liquid crystal', *Langmuir*, vol. 13, no. 7, pp. 2001–2006, Apr. 1997, doi: 10.1021/LA960606U/ASSET/IMAGES/LARGE/LA960606UF00008.JPEG.

[35] S. Pu, C. Gong, and A. W. Robertson, 'Liquid cell transmission electron microscopy and its applications', *R. Soc. Open Sci.*, vol. 7, no. 1, Jan. 2020, doi: 10.1098/RSOS.191204.

[36] W. J. Dearnaley *et al.*, 'Liquid-Cell Electron Tomography of Biological Systems', *Nano Lett.*, vol. 19, no. 10, pp. 6734–6741, Oct. 2019, doi:

10.1021/ACS.NANOLETT.9B01309/SUPPL_FILE/NL9B01309_SI_006.MOV.

[37] T. D. Li, L. M. Gan, C. H. Chew, W. K. Teo, and L. H. Gan, 'Preparation of ultrafiltration membranes by direct microemulsion polymerization using polymerizable surfactants', *Langmuir*, vol. 12, no. 24, pp. 5863–5868, 1996, doi: 10.1021/la960284u.

[38] F. Galiano, 'Preparation and characterisation of polymerisable bicontinuous microemulsion membranes for water treatment application', PhD thesis, Universita' della Calabria, 2012.

[39] F. Galiano *et al.*, 'Novel low-fouling membranes from lab to pilot application in textile wastewater treatment', *J. Colloid Interface Sci.*, vol. 515, pp. 208–220, 2018, doi: 10.1016/j.jcis.2018.01.009.

[40] F. Galiano *et al.*, 'A step forward to a more efficient wastewater treatment by membrane surface modification via polymerizable bicontinuous microemulsion', *J. Memb. Sci.*, vol. 482, pp. 103–114, 2015, doi: 10.1016/j.memsci.2015.02.019.

[41] F. J. E. Sanz, J. F. Lahitte, and J. C. Remigy, 'Membrane synthesis by microemulsion polymerisation stabilised by commercial non-ionic surfactants', *Desalination*, vol. 199, no. 1–3, pp. 127–129, 2006, doi: 10.1016/j.desal.2006.03.156.

[42] C. H. Chew, T. D. Li, L. H. Gan, C. H. Quek, and L. M. Gan, 'Bicontinuous-nanostructured polymeric materials from microemulsion polymerization', *Langmuir*, vol. 14, no. 21, pp. 6068–6076, 1998, doi: 10.1021/la970990a.

[43] L. Pisani, 'Simple Expression for the Tortuosity of Porous Media', *Transp. Porous Media 2011 882*, vol. 88, no. 2, pp. 193–203, Feb. 2011, doi: 10.1007/S11242-011-9734-9.

[44] L. M. Gan, T. H. Chieng, C. H. Chew, and S. C. Ng, 'Microporous Polymeric Materials from Microemulsion Polymerization', *Langmuir*, vol. 10, no. 11, pp. 4022–4026, 1994, doi: 10.1021/la00023a020.

[45] C. H. Chew *et al.*, 'Bicontinuous structures of polymerized microemulsions: 1H NMR self-diffusion and conductivity studies', *Langmuir*, vol. 13, no. 11, pp. 2917–2921, 1997, doi: 10.1021/la9607971.

Chapter 4

Chapter 4 – Polymerisation and characterisation of self-assembled systems stabilised by non-polymerisable surfactants

CHAPTER 4 – POLYMERISATION AND CHARACTERISATION OF SELF-ASSEMBLED SYSTEMS STABILISED BY NON-POLYMERISABLE SURFACTANTS 135

3.1 INTRODUCTION 139

4.2 COMPLETE CASE STUDY: $(21:23:56)_{62:19:19}$ COMPOSITION 140

4.2.1 Polymer microstructure characterisation 141

4.2.1.1 Microstructure of the polymer depending on the initiation method 141

4.2.1.2 Evolution of the microstructure during the polymerisation process 149

4.2.1.3 Evolution of the microstructure upon removal of non-polymerisable surfactants 153

4.2.2 Membrane performances 157

4.2.2.1 Selectivity of the $(21:23:56)_{62:19:19}$ membrane 157

4.2.2.2 Water permeability 159

4.2.2.3 Experimental determination of the water permeability of the $(21:23:56)_{62:19:19}$ UV-TQ150 membrane 165

4.3 INVESTIGATION OF $(46:8:46)_{62:19:19}$ AND $(46:8:46)_{33:33:33}$ COMPOSITIONS 174

4.3.1 Microstructure of the polymer depending on the initiation method 174

4.3.2 Analysis of the $(46:8:46)_{62:19:19}$ UV-TQ150 sample 178

4.4 CONCLUSION 182

REFERENCES 186

4.1 Introduction

In the previous Chapter, we demonstrated that the use of Synperonic™ A11 and Tergitol™ 15-S-12 allows for the occurrence of both organised and quite disorganised structures, as a function of the composition and the co-surfactant quantity. For the purpose of our study, we decided to focus only on the previously discussed quinary systems. Therefore, the polymerisation of liquid crystal structures will not be addressed as part of this work.

In this Chapter, we will discuss how the monomer microstructure evolves upon polymerisation. To that end, we will present a comprehensive case study based on the formulation developed in our research team prior to this work. We will investigate whether the polymerisation process is a critical factor to consider. We will also identify the microstructure of the resulting cross-linked polymer network and estimate to what extent this polymer is a good candidate to enhance the performance of porous membranes. Finally, we will examine whether other formulations and polymerisation inititation processes can be considered to further improve the membrane performance of the cross-linked polymer network. **All the compositions investigated in this Chapter will be listed according to the following notation:**

(Water wt.%: MMA wt.%: Surfactant phase wt.%)(HEMA wt.% in surfactant phase: Synperonic™ A11 wt.% in surfactant phase: Tergitol™ 15-S-12 wt.% in surfactant phase)

This chapter will address the following questions:

- *How is the monomer microemulsified structure affected by the polymerisation process: is the nanoscaled microstructure maintained throughout the polymerisation process when using non-polymerisable surfactants?*
- *How do the system composition and the polymerisation initiation method impact on the final microstructure of polymer when polymerising a monomer self-assembled system stabilised using a mix of non-ionic and non-polymerisable surfactants?*
- *Are any investigated polymerised monomer self-assemblies of significant interest for membrane filtration?*

4.2 Complete case study: $(21:23:56)_{62:19:19}$ composition

The $(21:23:56)_{62:19:19}$ composition was developed in our research team by Sanz et al. [1]. This formulation belongs to the bicontinuous domain of the (62:19:19) system, as presented in Figure 4.1. The high amount of HEMA in this composition (34.97 wt.%) causes the monomer structure to be highly disorganised, as previously discussed in Chapter 3.

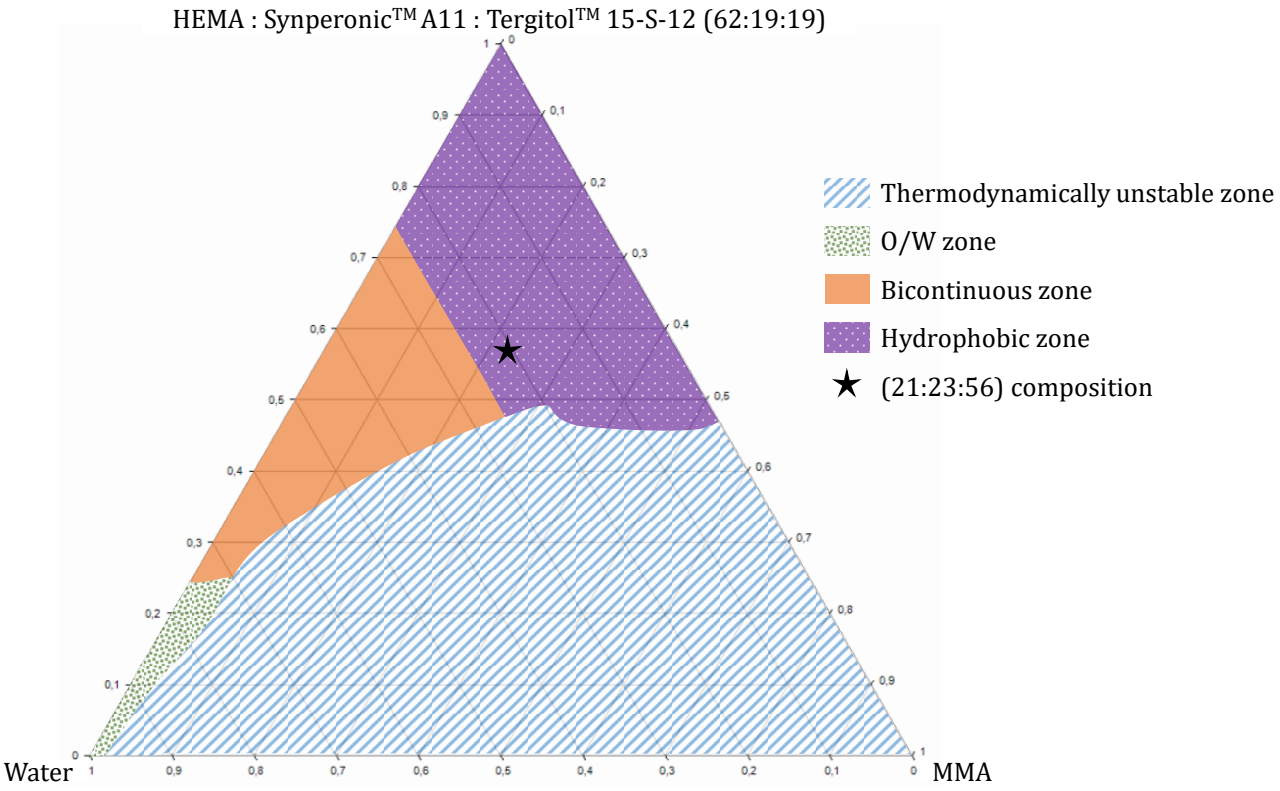

Figure 4.1 – Location of the $(21:23:56)_{62:19:19}$ composition considered in our comprehensive case study.

Two compounds will be added to the mixtures represented in the pseudo-ternary phase diagrams presented in the previous Chapter: a cross-linker and an initiator. Indeed, using a cross-linker – ethylene glycol dimethacrylate (EGDMA) – allows to achieve a strong interconnected polymer network. Some authors [2–10] also reported the use of such a compound to reach the system gel point quicker, and thus to shorten the period during which the microstructure can evolve. As part of our work, the amount of cross-linker added in the system was set to 4 wt.% (or 2.4 mol.%) of all the monomers in the system, i.e. MMA and HEMA.

Adding an initiator in the system allows to trigger the polymerisation process, either by exposing the sample to UV light (photopolymerisation) or by adding the second element of the couple oxidant-reductor. The type of initiator and its quantity used in the system are addressed in the Appendix 3. We will first discuss the evolution of the microstructure of this specific composition upon polymerisation. Three initiation paths will be discussed as part of this work:

RedOx initiation, UV polymerisation under a monochromatic LED lamp and UV polymerisation under polychromatic TQ150 mercury lamp. We will discuss how this initiation step affects the resulting polymer structure. Finally, the performances of the polymer membranes will be estimated based on the statistical analysis of the cryo-SEM images of each sample.

4.2.1 Polymer microstructure characterisation

The polymerisation process has been investigated and optimised, as described in Appendix 3. In the following, we will consider the parameters presented in Chapter 2. In order to avoid any modification of the composition due to evaporation, we polymerised the microemulsified sample between two borosilicate lamella (RedOx and UV-LED initiations) or between a borosilicate and a quartz lamella (UV-TQ150 initiation). Indeed, quartz allows UVC and UVB rays to penetrate the monomer sample, which borosilicate prevents.

4.2.1.1 Microstructure of the polymer depending on the initiation method

The $(21{:}23{:}56)_{62:19:19}$ polymers cured using RedOx, UV-LED and UV-TQ150 polymerisation methods were investigated using classic SEM analyses, cf. Figure 4.2. In each case, we observe no porosity in the polymer cross-section. We therefore suspect a collapse of the nanopores during the dehydration following the washing step and/or the application of a secondary void in the SEM chamber. This collapse could be due to the shrinking of the nanometric pores and the formation of weak bonds between the polymer chains, which can create H-bonds (e.g. with the hydrophilic ester function on the PHEMA units).

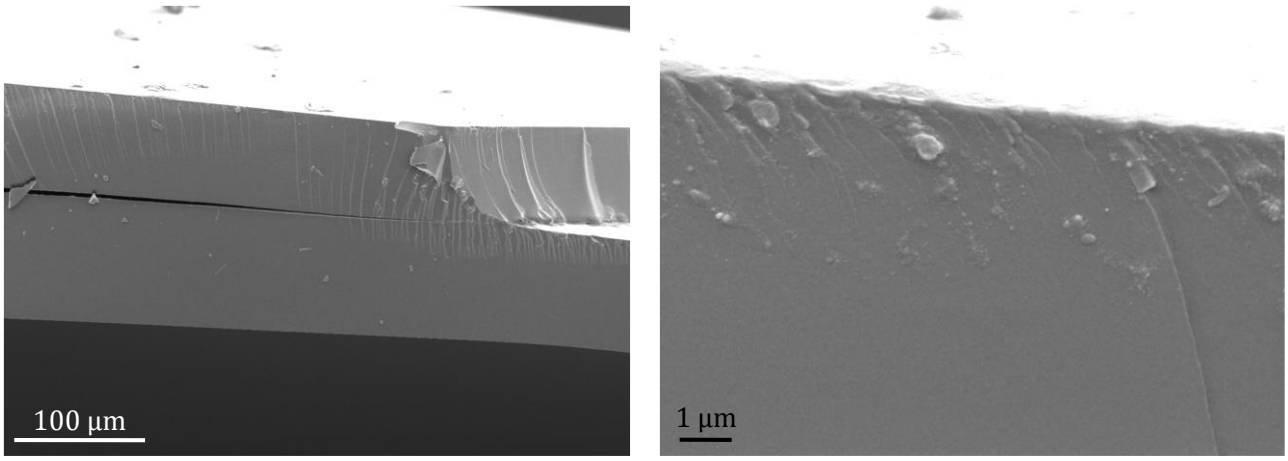

Figure 4.2 – SEM images of a dehydrated UV-LED polymerised $(21{:}23{:}56)_{62:19:19}$ cross-section.

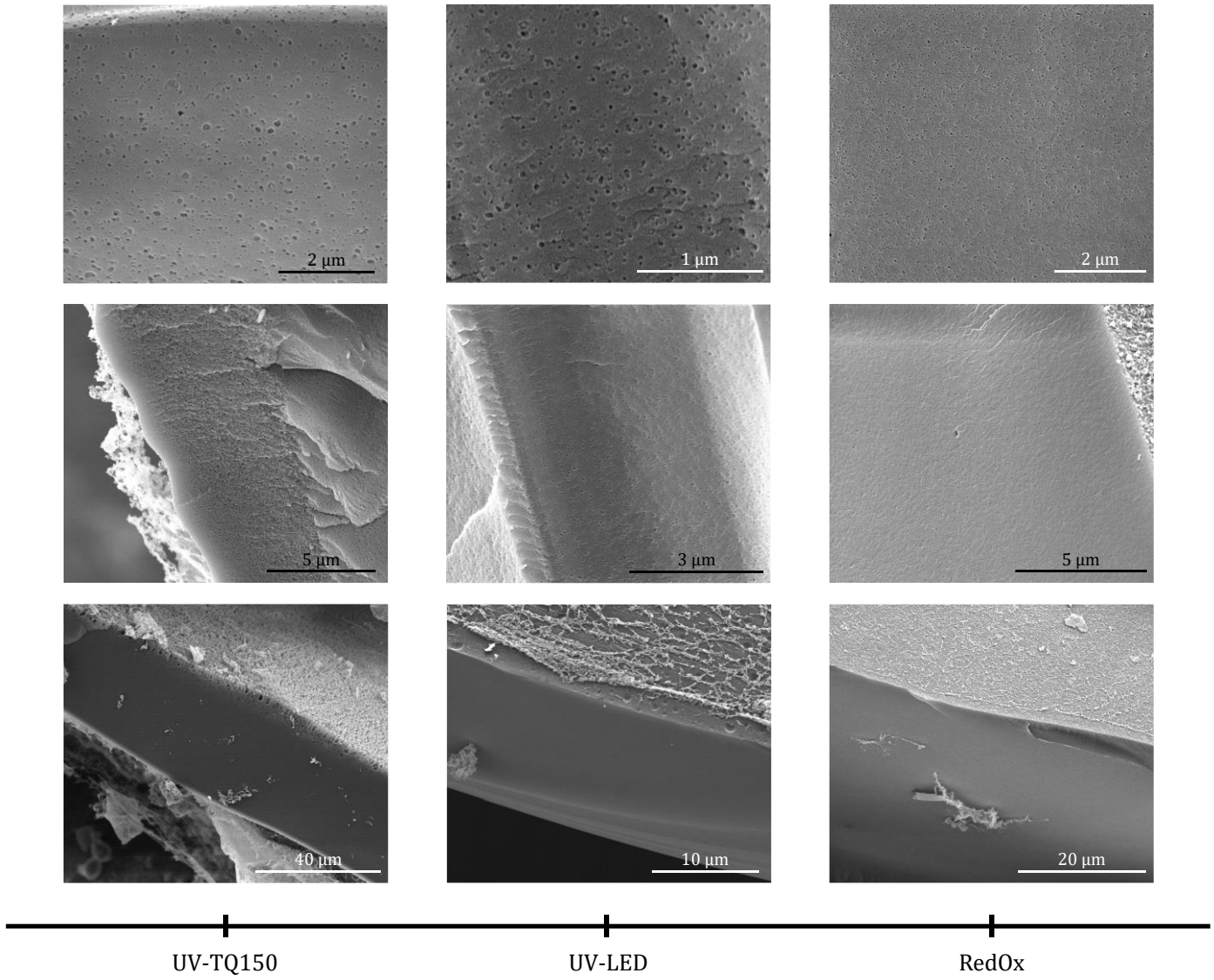

Figure 4.3 – Cryo-SEM cross-sections images of the $(21:23:56)_{62:19:19}$ composition, cured with RedOx and UV (under the LED or the TQ150 lamp) initiations.

To prove this last hypothesis, we carried out a cryo-SEM analysis on hydrated $(21{:}23{:}56)_{62:19:19}$ polymer samples. We first note that the images presented in Figure 4.3 prove the occurrence of a nanometric porosity in the sample cross-sections, regardless of the initiation of the polymerisation process. This observation confirms our assumptions regarding the structure collapse under dehydration and/or application of the void on a dehydrated sample.

We then observe that the photopolymerised samples exhibit asymmetrical structure. The UV-TQ150 sample displays three different zones: a dense surface layer of ca. 500 nm, an intermediate porous structure and finally a highly porous second surface layer of about 5 µm. This porous layer consists of about 3 µm of highly porous interconnected structure and ca. 2 µm of polymer agglomerates forming macroporosities on top. The intermediate porous structure displays a decreasing porosity through the thickness of the dense layer from 500 nm to the highly porous layer. A similar phenomenon is observed along the UV-LED cross-section: two surfaces of different porosity are framing a central nanoporous presenting a porosity gradient, but to a lesser extent as no macroporosities are observed. The RedOx initiated sample in turn does not exhibit any porosity gradient as such, but both surfaces are denser than the sample central thickness. Because no porosity gradient was observed in the RedOx sample, we conclude that the occurrence of a modification of the pore size along the membrane thickness is, at least partly, due to the UV penetration gradient into the monomer sample thickness due to the Beer-Lambert law behaviour of the UV intensity.

The difference of microstructure between the surfaces and the polymer bulk is due to the difference in interactions between the polymer and the borosilicate glass compared to the polymer against itself. Such a phenomenon has already been reported by other researchers [7,11–13] when synthesising polymer membranes, but no explanation was discussed. More generally, the modification of the surfactant-based solution interfaces has been attributed to a Gibbs-Marangoni effect [14–17]. This effect occurs when a pure liquid is being evaporated, when surfactants are present in the system or when both phenomena occur simultaneously, as discussed by Van Gaalen et al. (2021) [17]. When the solution in contact with an interface undergoes a gradient of surface tension – caused by the interaction of the surfactants with the interface and/or by the evaporation of the liquid – a so-called Marangoni flux occurs to restore the system thermodynamic balance, as described in Figure 4.14.

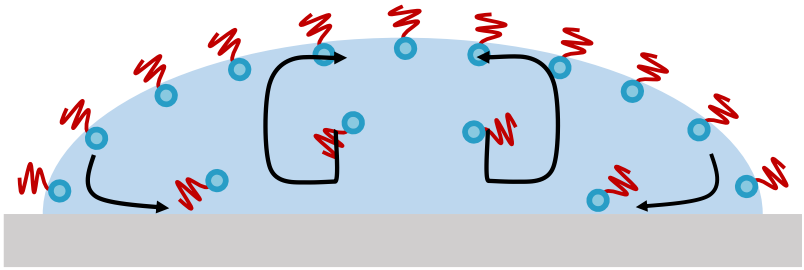

Figure 4.4 – Schematic representation of the Marangoni circulation occurring in a drop of surfactant-based solution.

The surfactant from the liquid-vapour interface is displaced to the solid-liquid interface, leading to a depletion of the former interface. The surfactant present in the bulk will then move towards this air-liquid interface to restore an equilibrated system, as described by Von Bahr et al. (1999) [16]. We thus assume that because the borosilicate behaves as a hydrophilic substrate with the microemulsion ($\theta = 25 \pm 3°$), the microemulsion may rearrange its structure to better accommodate to this hydrophilic surface. Plus, we observe some rugosity above the dense layer on the polymer surfaces, which we attribute to the occurrence of polymer aggregates at the interfaces. We therefore conclude that the polymer interfaces in contact with the borosilicate, or quartz, glass will bear more hydrophilic particles and more surfactant molecules than the polymer bulk. As a result, the oil displaced from the interface towards the bulk will give rise to a subsequent dense polymer layer in the vicinity of the solid-liquid interface.

No difference between the upper and lower surface are observed for the RedOx sample, indicating an isotropic polymerisation process. The UV-cured samples however present two different surface structures, one surface being much denser than the other. As detailed above, the presence of a glass plate above the sample modifies the affinity in the vicinity of the interface, but also prevents water and MMA evaporation. Indeed, UV-lamps heat the sample up, especially polychromatic lamps such as the TQ150 which emits IR for 100 s before emitting UV light. Hence, some easily vaporisable compounds (i.e. MMA and water) may vaporise before and/or during the UV-irradiation and unsuccessfully try to escape the solution because of the upper glass plate. Such an evaporation gives rise to a more complex Marangoni effect on the upper liquid-solid interface, which now combines a surface tension gradient caused by two phenomena: a surfactant displacement due to solid-liquid interface contact and a solvent evaporation. This combination gives rise to some macroporosities under the polychromatic UV-TQ lamp, cf. Figure 4.5.

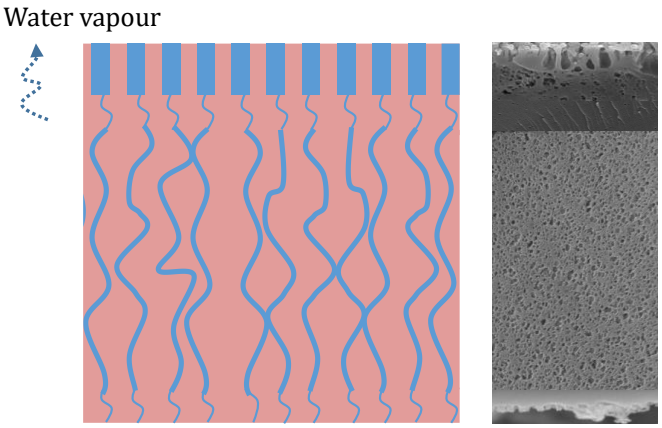

Figure 4.5 – Schematic representation of the membrane structure as a function of the water evaporation during UV polymerisation.

We also observe that when using a low-heating UV-device (i.e. the LED lamp), no macroporosities occur but large pores are observed on the upper surface. This observation directly results from the lower temperature increase – and thus to a lower evaporation phenomenon – caused by the LED compared to the polychromatic lamp. Finally, we conclude that because the opposite bottom interface of the cured polymer is less affected by sample heating of the lamps, it rearranges in a similar way to the RedOx sample.

We will now further discuss the polymer bulk. We observe that, depending on the initiation method, the bulk pore size and distribution are modified. In order to quantify the pore size and the pore size distribution of the three samples, we carried out a statistical analysis of the cryo-SEM images, for each sample as presented in Figure 4.6. Because the photoinitiated polymer samples exhibit an anisotropic behaviour in the bulk polymer, we differentiated the low (selective) and high (porous) porosity domains of the polymer bulk.

The statistical distribution of the pore radius for each sample – high and low porosity domains distinguished – is presented in Figure 4.7. We first note that the RedOx sample displays a narrower distribution of pore radius (2-20 nm) than the UV-LED sample (5-35 nm), which in turn is narrower than the pore radius distribution in the UV-TQ150 sample (2-115 nm). To better describe each porous polymer, we then determined the mean pore radius of each sample, using a lognormal distribution model – which is widely used for membrane pore size distribution [18] – as presented in Table 4.1. For the two anisotropic photopolymerised samples, only the least porous – and most selective – part of the sample was considered (i.e. dashed distributions in Figure 4.7). To avoid the impact of the mould material, the interfaces were not investigated and only the polymer bulk is assessed.

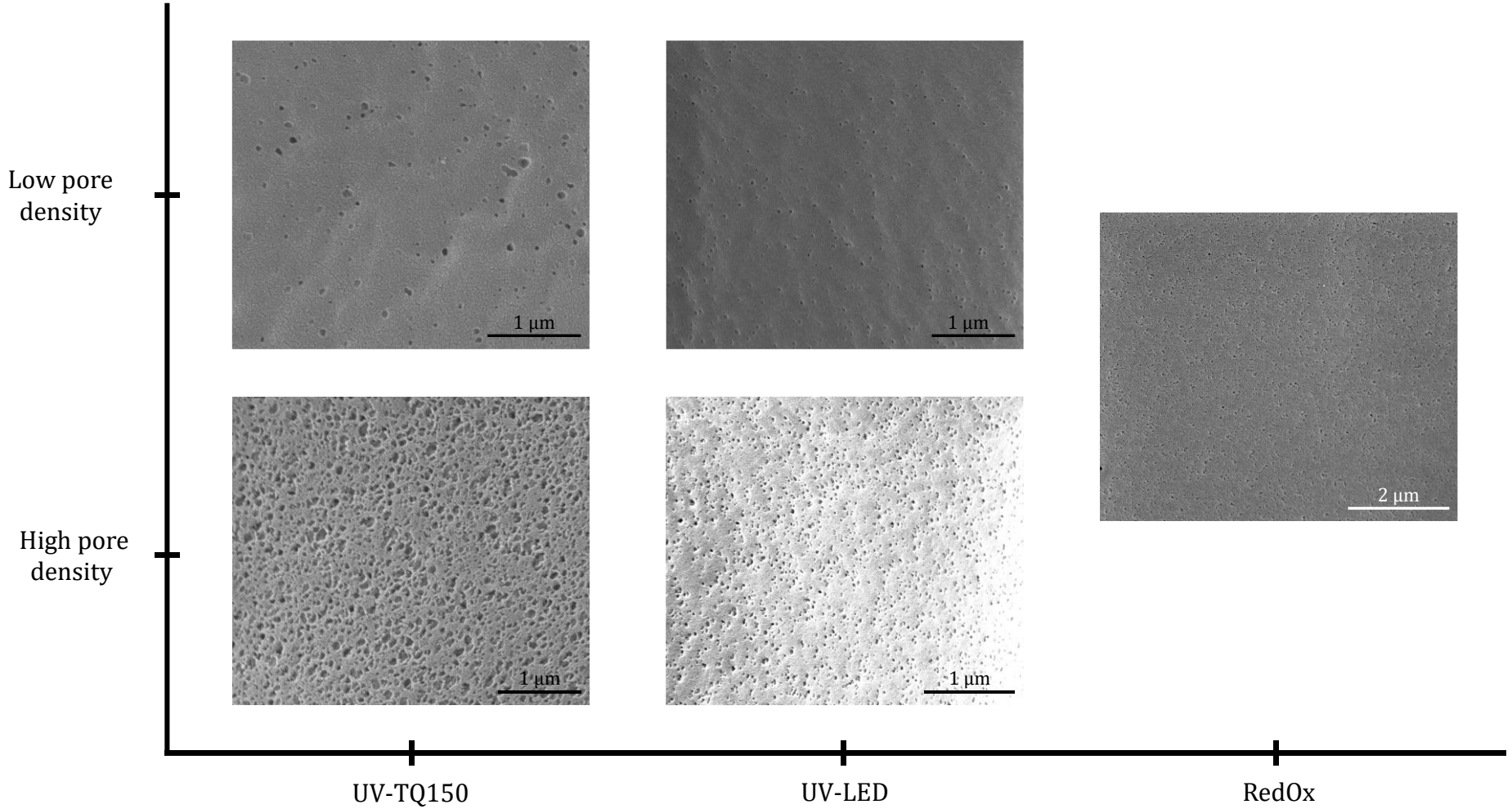

Figure 4.6 – Cryo-SEM images of the cross-sections used for the statistical analysis of the pore size and pore size distribution, using ImageJ software.

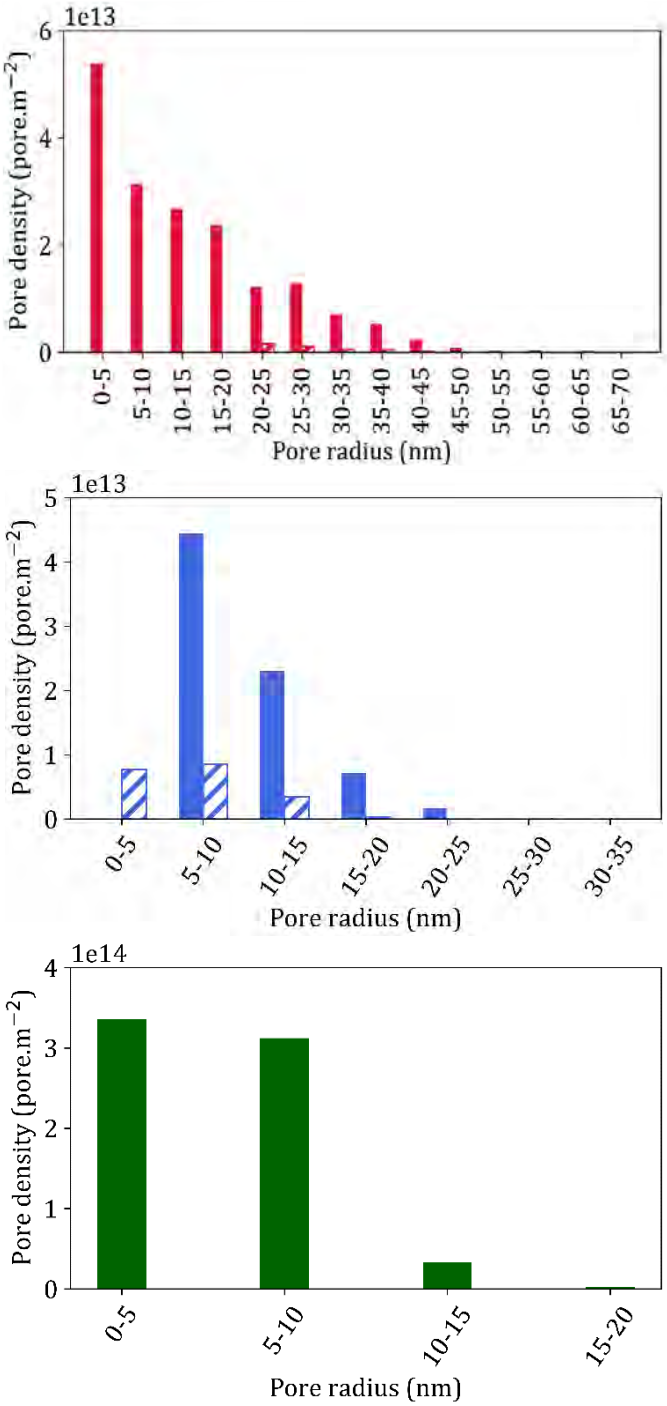

*Figure 4.7 – Distribution of pore radius in the polymer bulk from the numerical analysis from the cryo-SEM images. (**red**) UV-TQ150, (**blue**) UV-LED and (**green**) RedOx sample, (**plain**) porous and (**dashed**) selective domains of the anisotropic samples.*

Overall, we observe that the pore size distribution seems to follow a lognormal distribution for all the three samples. However when assessing the distributions with the X^2 test, we note that these distributions of the UV samples follow a lognormal distribution with a confidence level of about 10%. We attribute this issue to the occurrence of pore junctions, which are observed in the cryo-SEM images, cf. Figure 4.6. Such a behaviour would therefore decrease the

representativeness of small pores to the benefit of large pores in the distribution presented in Figure 4.7.

Table 4.1 – Statistical analysis of the pore distribution of the selective domain of (21:23:56)$_{62:19:19}$ asymmetric polymer membrane as a function of the initiation method.

Initiation method	Mean radius (nm)	Pore radius range (nm)
UV-TQ150	14 ± 11	4.5 – 63.1
UV-LED	7 ± 4	3.9 – 17.0
RedOx	7 ± 4	1.5 – 15.5

We notice that the pore radius ranges and mean radius of the UV-LED and RedOx samples are about 3 times narrower than the one of the UV-TQ150 sample. We also experimentally observe that the polymerisation duration is longer for the RedOx (ca. 15 min) than for the UV-LED (ca. 60 s) initiation method, which is in turn longer than the UV-TQ150 method (<1 s, lamp warm-up period excluded). We can therefore conclude that for the (21:23:56)$_{62:19:19}$ sample, the pore size increases when the polymerisation kinetics decreases.

We therefore conclude that using an isotropic initiation method (RedOx) logically leads to a narrower pore size distribution, compared to anisotropic initiation methods (UV). Plus, for anisotropic photopolymerisations, we observed that the longer the polymerisation duration, the smaller the pore size and the narrower the distribution. We therefore conclude that, in this specific case, the decrease of the polymerisation kinetics induces a better homogenisation of the pore structure during the process and thus a narrower pore size distribution. This homogenisation also led to smaller pore radii for our system.

Intermediate conclusions:

The cryo-SEM images evidenced the occurrence of a porous and, at least partially, interconnected network for all investigated samples, regardless of their initiation method. We however concluded that the polymerisation kinetics and the isotropic behaviour of the initiation method affect the pore size and the interface structure, the latter being modified by the Marangoni effect due to the interaction of surfactants with the solid surface, and in the case of cured samples the evaporation of the solvent. For the (21:23:56)$_{62:19:19}$ system, a longer

isotropic polymerisation process leads to a narrower pore size distribution, associated to smaller pore radii.

As a conclusion, we evidenced based on the experimental results that the initiation method is a critical factor to be considered, due to the non-polymerisable nature of the surfactants used. Indeed, the surfactant to polymer affinity being different from that to monomer, the interface curvature will evolve during the polymerisation, and so will the system microstructure. Because the initiation step impacts greatly the propagation of the polymerisation, the quantity of monomer to polymer at a given moment – and thus the interface curvature – will vary depending on the initiation method applied. Further work focused on understanding each initiation mechanism and kinetic will be needed to identify the origin of the observed differences.

We highlighted the occurrence of a bicontinuous structure before and after polymerisation of the $(21{:}23{:}56)_{62:19:19}$ system. We will now discuss how the polymerisation and the washing processes affected the initial monomer microstructure.

4.2.1.2 Evolution of the microstructure during the polymerisation process

In Chapter 3, we discussed the $(21{:}23{:}56)_{62:19:19}$ monomer sample microstructure. In the last paragraphs, we then highlighted that the associated polymer obtained by UV (LED and polychromatic lamps) and RedOx initiation methods is nanoporous. Some authors argued that polymerising a monomer system structured by non-polymerisable surfactants may result in the conservation of the microstructure [5,6]. We propose to verify this affirmation for the Synperonic™ A11 and Tergitol™ 15-S-12 non-polymerisable surfactant system.

Figure 4.8 below represents the scattering curves of the $(21{:}23{:}56)_{62:19:19}$ monomer and UV-LED polymer samples. As detailed in the previous Chapter 3, the curve of the monomer sample consists of a broad peak, whose scattering vector associated to the peak of maximum intensity can be used to determine the characteristic distance between the scattering inhomogeneities – i.e. the interconnected monomer channels, cf. Eq. 4.1. We determined this characteristic distance to be 4.8 nm (q_{max} = 1.3E-1 $Å^{-1}$) in the monomer system.

$$d = \frac{2.\pi}{q_{max}} \qquad \text{Eq. 4.1}$$

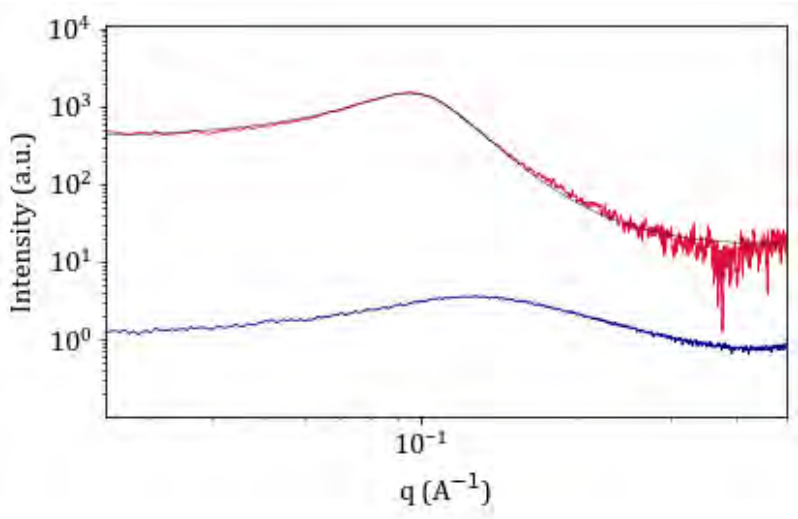

*Figure 4.8 – SAXS scattering curves of the (21:23:56)$_{62:19:19}$ UV-LED sample (**blue**) before and (**red**) after water polymerisation. (**black**) Teubner-Strey associated fit.*

Then, we note that the red scattering curve associated to the (21:23:56)$_{62:19:19}$ polymer sample is different from the monomer sample, which indicates a modification of the microstructure during polymerisation. Such an evolution of a monomer structure stabilised by other non-polymerisable surfactants has already been discussed as by Dos Santos et al. (2011) [19]. The polymer scattering curve presents an intensity plateau up to 0.10 Å^{-1}, followed by a decrease in intensity up to 0.20 Å. Such a scattering pattern is usually associated to the Teubner-Strey fit (cf. Eq. 1.16), which describes bicontinuous interconnected structures [20–22]. A_2, C_1, C_2 and B are constant, I(q) and q are the intensity of the signal and the scattering vector respectively.

$$I(q) \propto \frac{1}{A_2 + C_1.q^2 + C_2.q^4} + B \qquad \text{Eq. 1.16}$$

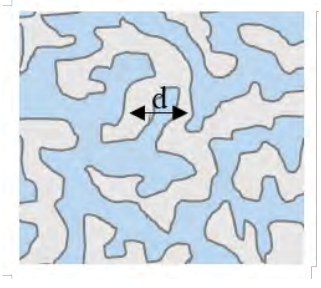

Figure 4.9 – Representative scheme of the periodicity and the correlation length in a bicontinuous system. Adapted from Jones and Lodge [23].

The Teubner-Strey fit allows to determine the periodicity d of the sample (cf. Eq. 1.17) – i.e. the channel repeat distance – as well as the system correlation length ξ (cf. Eq. 1.18)– i.e. the distance over which the system remains locally ordered – as presented in Figure 4.9.

$$d = 2.\pi.\left[\frac{1}{2}.\left(\frac{A_2}{C_2}\right)^{\frac{1}{2}} - \frac{1}{4}.\frac{C_1}{C_2}\right]^{-\frac{1}{2}} \quad \text{Eq. 1.17}$$

$$\xi = \left[\frac{1}{2}.\left(\frac{A_2}{C_2}\right)^{\frac{1}{2}} + \frac{1}{4}.\frac{C_1}{C_2}\right]^{-\frac{1}{2}} \quad \text{Eq. 1.18}$$

Based on these two parameters, it is then possible to calculate the amphiphilicity f_a and the polydispersity $k_p.\xi$ factors, cf. Eq. 1.19 and Eq. 1.20. These two factors allow for the qualification of the order in the system microstructure [24–28].

$$f_a = \frac{C_1}{\sqrt{4.C_1.C_2}} = \frac{1 - \left(\frac{2.\pi.\xi}{d}\right)^2}{1 + \left(\frac{2.\pi.\xi}{d}\right)^2} \quad \text{Eq. 1.19}$$

$$k_p.\xi = \frac{2.\pi}{d}.\xi \quad \text{Eq. 1.20}$$

The amphiphilicity factor ranges from -1 to 1. If $f_a \cong -1$, the structure is highly ordered and considered as lamellar. The more this factor tends towards 1, the more the system loses a quasi-periodic order. A system is then considered as an isotropic bicontinuous structure if $-0.9 < f_a < -0.7$. When the amphiphilic factor increases and tends towards 0, the structure crosses the Lifshitz line and the resulting structure is then inhomogeneous, alternating between ordered and disordered structures. When the microemulsion is completely disordered, then the factor reaches 1. Above this value, the structure loses its quasi-periodic order and the remaining interfaces become independent of each other.

Similarly, the polydispersity factor $k_p.\xi$ qualifies the ordination of the bicontinuous structure: the higher the factor, the more ordered the structure. If $k_p.\xi < 2$, then the bicontinuous structure is qualified as disordered gyroid. As soon as the factor is above 2, the structure can be qualified as ordered gyroid, i.e. as an interplay of organic and aqueous layers separated by a surfactant layer, according to Ezrahi et al (1997) [29].

The parameters extracted from this mathematical modelisation of the experimental data are reported in Table 4.2 below. We can note that the amphiphilic factor is comprised between -0.7 and -0.9, and the polydispersity factor is also above 2. These values indicate that, before the washing step, the gyroid structure is quite ordered and maintains a local order over 3.6 nm, as highlighted by the correlation length value. Finally, we calculated the channel repeat distance

to be 6.3 nm, which indicates that the size of the monomer bicontinuous structure size – of initially 4.8 nm – is increased during the polymerisation process.

Table 4.2 – Teubner-Strey parameters extracted from the $(21:23:56)_{62:19:19}$ UV-LED polymer before its washing.

Periodicity d (Å)	Correlation length ξ (Å)	Amphiphilicity factor f_a	Polydispersity factor $k_p.\xi$
63.5	36.5	-0.86	3.61

Intermediate conclusions:

Because the Teubner-Strey model seems to fit our experimental data well, we conclude that a bicontinuous nanostructure is obtained after the polymerisation under the UV-LED lamp. However, because the scattering curves of the monomer and polymer systems are different, their microstructures are also different. Therefore, we conclude that the present system undergoes some structural changes during the polymerisation due to the non-polymerisable nature of the Synperonic™ A11 and Tergitol™ 15-S-12 surfactants.

It should be noted that the Teubner-Strey fit accounts for a decrease in intensity with a slope of q^{-4} after the intensity plateau. In our case, this slope is $q^{-4.18}$ (R^2=0.984) in the range 0.105-0.275 $Å^{-1}$. Such a range was chosen to consider the linear decrease of the intensity without being impacted by the convolution of Kapton™. Having a slope different from q^{-4} indicates that the polymer interface is not well defined and might be a limitation to the application of the Teubner-Strey fit, which we however considered to be applicable due to the close value of the experimental slope compared to the theoretical value.

After completion of the polymerisation process, these surfactants will not be incorporated into the polymer matrix and will be located into the aqueous channels of the polymer network before being eliminated by successive water washing baths. We will now discuss the impact of the surfactant removal on the porous interconnected polymer network.

4.2.1.3 Evolution of the microstructure upon removal of non-polymerisable surfactants

In order to determine the impact of the non-polymerisable surfactant removal on the microstructure, we studied the microstructure of a $(21{:}23{:}56)_{62:19:19}$ UV-LED polymer, before and after water the washing step, using SAXS analyses, as presented in Figure 4.10. The washed sample was studied under hydrated conditions to avoid the structure from collapsing due to dehydration.

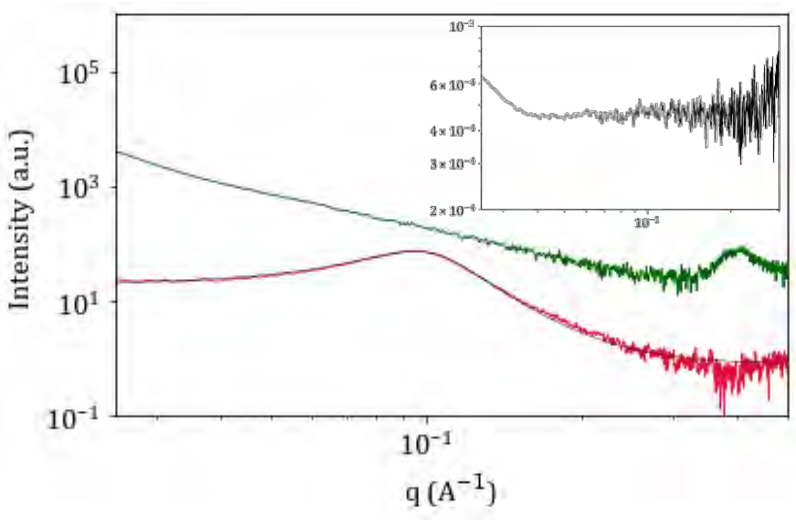

*Figure 4.10 – SAXS scattering curves of the $(21{:}23{:}56)_{62:19:19}$ UV-LED polymer (**red**) before and (**green**) after water washing. (**black**) Teubner-Strey associated fit. Inset: $f(q) = I(q)q^2$.*

We first observe a wide peak due the 0.3-0.5 $Å^{-1}$ range, which is an artefact of the numerical treatment of the scattering curve. As a reminder, each SAXS curve presented in this work has been obtained by subtracting a buffer solution, in our case water. However, the carrier being a watertight Kapton™ cell, the addition of the hydrated sample in the water reference cell led to an increase of the water content in the sample and thus to a convolution of the Kapton™ peak. This phenomenon led to an impossibility to perfectly subtract the Kapton™ reference peak to the Kapton™ peak of the polymer in the 0.3-0.5 $Å^{-1}$ range and thus to an artefact, which does not impact on the information obtained from this scattering curve.

We then observe a loss of signal after water washing and surfactant removal from the polymer and the occurrence of a decay of the scattered intensity in q^{-2} from 0.0375 to 0.3 $Å^{-1}$, cf. Inset Figure 4.10. We therefore conclude that the structuration of the sample observed before washing was caused by the presence of the surfactants in the aqueous channels. As the nanostructuration observed on the polymer containing the surfactants appears undetectable after the non-polymerisable surfactants removal, we can however immediately refute the

hypothesis of the structural collapse of the porous channels upon the removal of surfactants due to the cryo-SEM images which indicate the occurrence of nanometric pores. We then hypothesise that the q^{-2} decay of the intensity to represent the PMMA-PHEMA cross-linked polymer chains constituting the polymer matrix. We can first conclude that the polymer washing of the sample was effective and actively removed the non-polymerisable surfactants from the nanoporous channels. This information confirms the visual observation that when agitating the water used for the polymer washing, foam was formed due to the presence of surfactants. This result also confirms the open-ended porous behaviour of the polymer synthesised. Indeed, the modification of the scattering signal proves that the surfactants were removed from the polymer porosity, and thus that the pores constituting the polymer are effectively open and unclogged. A closed porosity would have prevented the elimination of the surfactants otherwise.

This last conclusion is also consistent with the cryo-SEM and SAXS analyses performed on the polymer before and after the surfactant removal. Indeed, we evidenced in Section 4.2.1.2 that the bicontinuous polymer structure exhibits a periodicity of 6.3 nm in the unwashed system (cf. Table 4.2). Upon the polymer water washing – and surfactant removal – we observed pores with a diameter of about 14 nm using cryo-SEM analysis in Section 4.2.1.1. We also know that the $(21{:}23{:}56)_{62:19:19}$ investigated composition contains 59.7 wt.% of monomer, 19 wt.% of water and 21.3 wt.% of non-polymerisable non-ionic commercial surfactants. Upon polymerisation – and assuming a full conversion of the monomers – the polymer matrix and the aqueous channels containing the surfactants then respectively represent 59.7 wt.% and 40.3 wt.% of the overall material.

Based on the technical data sheet provided by the manufacturers, both Synperonic™ A11 and Tergitol™ 15-S-12 have a density around the unity. Right after polymerisation, the porous channels are then composed of 19 vol.% of water and 21.3 vol.% of non-polymerisable surfactants. Assuming a homogeneous distribution of the molecules of surfactant in the porous channels, we therefore conclude that the aqueous channel volume appears almost twice wider after the removal of the surfactants. The effective mean diameter of the water channel is then increased from 6.4 nm to 13.4 nm after the removal of the surfactants, which is consistent with the cryo-SEM observations of the pore mean radius (7 ± 4 nm).

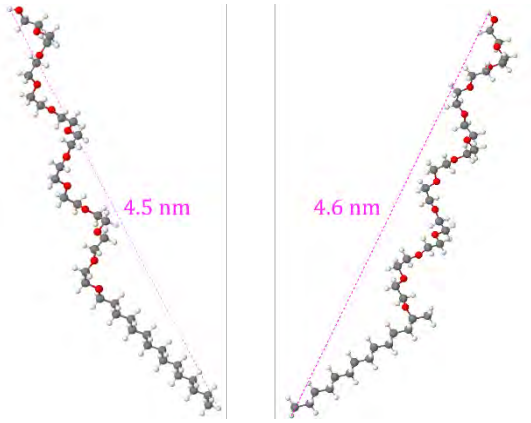

*Figure 4.11 – Non-ionic surfactant structure and dimension obtained from the MolView software: (**left**) Synperonic™ A11 and (**right**) Tergitol™ 15-S-12.*

Plus, we estimated the length of both commercial non-polymerisable surfactants using MolView software to be around 4.5-4.6 nm, cf. Figure 4.11. Assuming the surfactant molecules will expand as much as possible in the aqueous channel, as presented in Figure 4.12, we would expect the effective porous channel diameter to be twice the length of a surfactant molecule ($2 \times 4.5 = 9$ nm) plus the mean pore diameter determined using the Teubner-Strey fit for the polymer before surfactant removal (6.3 nm). The total mean pore diameter would then be around 15.3 nm, which is once again consistent with the observations of the cryo-SEM images.

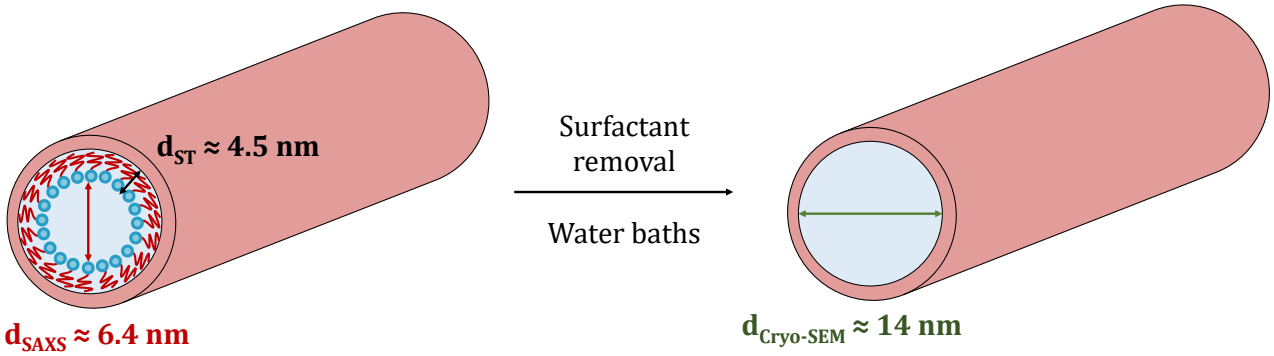

Figure 4.12 – Schematic representation of the aqueous channel before and after non-polymerisable surfactant removal.

Finally, we note a modification of the slope of the scattered intensity below 0.0375 $Å^{-1}$, cf. Inset Figure 4.10. Such a discontinuity occurs for a characteristic distance d = 16.7 nm, which is quite similar to the mean pore size observed using the cryo-SEM technique (14 ± 6 nm). We here suggest that upon the removal of the surfactants, the pores of the organic matrix appear wider in SAXS analysis and their signal is shifted towards the edge of the detection window, thus causing a modification of the slope of the scattered intensity.

Intermediate conclusions:

All the arguments presented in the previous sections indicate that the monomer system evolves during the polymerisation process, even if we concluded on the achievement of an interconnected nanoporous polymer. Upon washing however, we observe the disappearance of the broad scattering peak associated to the Teubner-Strey fit. We concluded that this "loss" of signal is due to the removal of the surfactant interface in the aqueous channels and the increase of the effective aqueous pore size. We conclude that using non-polymerisable surfactants does not only impact on the maintenance of the monomer structure upon polymerisation, but also on the size of the resulting polymer network. For a similar open porous structure, the use of non-polymerisable surfactants will lead to larger pores than in cases where polymerisable surfactants are used.

We therefore confirmed the open nature of the porosity in the polymer network, which allowed for the washing of the non-polymerisable surfactants molecules. We then estimated that twice of the aqueous channels was constituted of the non-ionic surfactants and that their actual size was twice the value determined before the water washing of the polymer sample, i.e. 13.4 nm. This result is consistent with the observation cryo-SEM detailed above, where we determined the mean aqueous channel radius of the UV-LED sample to be 7 ± 3 nm. We then conclude that such a pore size range is difficult to completely analyse with the SAXS instrument used as part of this study: only the smallest pore sizes of our sample were determined using the SAXS technique. In order to clearly evidence the bigger porosity of our structure, a USAXS or USANS synchrotron analysis could be considered.

In the previous sub-sections, we focused on the evolution of the UV-LED sample from a monomer to a polymer, and finally to a surfactant-free polymer structure. As we observed quite similar polymer structures when investigating the RedOx, the UV-LED and the UV-TQ150 samples with the cryo-SEM technique, we assume that the conclusions drawn for the UV-LED sample will be similar for the RedOx and UV-TQ150 samples. We however note that because the polymerisation kinetics – and thus the resulting pore size – are different from a polymerisation initiation to another, so will the associated scattering curves. For example, we expect the RedOx sample to exhibit a (more or less defined) broad peak for lower scattering vector values than the UV-LED sample. In essence, the nanoporous interconnected structures we identified in the $(21{:}23{:}56)_{62:19:19}$ system seem to meet the criteria to be an interesting

candidate as an ultrafiltration material. For this reason, we will now investigate the potential of these polymer networks for applications in the field of separative membrane filtration.

4.2.2 Membrane performances

In the following sub-sections, we will discuss the theoretical performances – i.e. water permeability at 20°C and selectivity – of the three $(21{:}23{:}56)_{62:19:19}$ polymer networks discussed in Section 4.2.1.

4.2.2.1 Selectivity of the $(21{:}23{:}56)_{62:19:19}$ membrane

The selectivity of the three investigated polymer membranes was estimated using Ferry's law (cf. Eq. 4.2), considering steric retention only. We estimated the retention coefficient of each polymer membrane as a function of the hydrodynamic radius r_{hydro} of the particles retained by the membrane.

$$R_m = \left(1 - \left(1 - \frac{r_{hydro}}{r_m}\right)^2\right)^2 \qquad \text{Eq. 4.2}$$

For each sample, we considered the membrane radius r_m to be the mean pore radius obtained from the statistical analysis of the pore size distribution of the selective area of each polymer sample cf. Table 4.1.

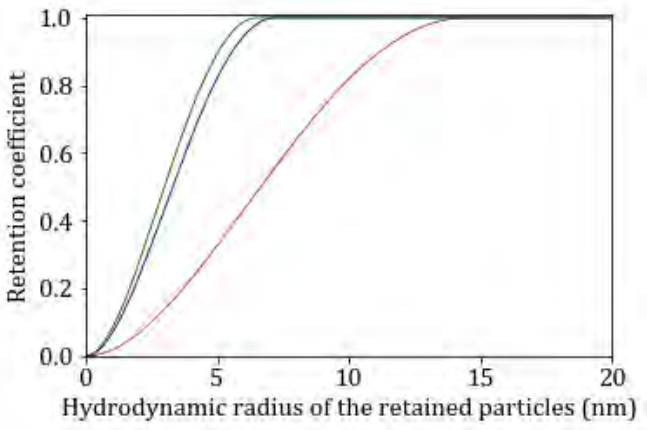

*Figure 4.13 – Estimated evolution of the retention coefficient of the $(21{:}23{:}56)_{62:19:19}$ polymer membrane as a function of the hydrodynamic radius of the particles retained, based on the statistical analysis of the cryo-SEM cross-sections images. (**red**) UV-TQ150, (**blue**) UV-LED and (**green**) RedOx samples.*

The calculated retention coefficient of each $(21{:}23{:}56)_{62:19:19}$ polymer membrane as a function of the hydrodynamic radius of the pollutant is displayed in Figure 4.13. We note that the RedOx and UV-LED samples exhibit a quite similar evolution of the retention coefficient, due to their

similar mean pore radius (7 ± 3 nm for both polymers). The UV-TQ150 sample in turn can only retain larger molecules due to its larger mean pore size (14 ± 11 nm).

We then estimated the selectivity of these three membranes towards neutral polyethylene glycol molecules (PEG). The PEG molecular weight cut-off (MWCO) of each $(21{:}23{:}56)_{62:19:19}$ polymer membranes was determined for $R_m = 0.9$, using the formula proposed by Gassara et al. (2013) [30]), cf. Eq. 4.3 and Eq. 4.4. The hydrodynamic radius of the pollutant retained by the membrane and the associated PEG MWCO for $R_m = 0.9$ are reported in Table 4.3. r_{hydro} is expressed in nm and M_w is the PEG molecular weight (g.mol^{-1} or Da).

$$r_{hydro} = 0.01673 M_w{}^{0.57777} \ (750\ \text{Da} < M_w < 35\ \text{kDa}) \qquad \text{Eq. 4.3}$$

$$r_{hydro} = 0.01044 M_w{}^{0.587} \ (M_w > 35\ \text{kDa}) \qquad \text{Eq. 4.4}$$

Table 4.3 – Minimum hydrodynamic radius of the particles retained by the $(21{:}23{:}56)_{62:19:19}$ polymer membranes and the MWCO associated for $R_m = 0.9$, as a function of the initiation method.

Initiation method	Hydrodynamic radius of retained particles (nm)	PEG MWCO (kDa)
UV-TQ150	11.2	145
UV-LED	5.4	22
RedOx	5.0	20

We conclude that the selective area of the three polymer samples allows for the retention of nanometric compounds. Once again, we observe a lower selectivity of the UV-TQ150 sample compared to the two other samples, due to its larger pore size. Based of the estimated radius of the pollutants retained by the polymer, we concluded that the UV-TQ150 sample belongs to the high-ultrafiltration (UF) range, while the UV-LED and RedOx samples both belong to the UF range in term of selectivity (MWCO between 500-500,000 Da [31,32] and pore size between 2 – 500 nm [33]).

4.2.2.2 Water permeability of the $(21:23:56)_{62:19:19}$ membrane

Based on the cryo-SEM analysis, we were able to determine the pore size range of the $(21:23:56)_{62:19:19}$ samples, for the three types of polymerisation initiations considered. We now propose to calculate the expected permeability for the membranes made of each studied polymer, using Poiseuille's law for pore flow, cf. Eq. 4.5 below. To that end, we will consider the following hypotheses:

- The membrane is isotropic in the cross-section thickness: we will then overlook the structure modification in the vicinity of the material interfaces. The calculated permeability is therefore to be adapted as a function of the interface microstructure.
- The pores are cylindrical, perpendicular to the membrane surface and through-going in the total membrane thickness. In order to account for the tortuosity of the gyroid structure, the ideal Poiseuille's equation will be modified to incorporate a tortuosity factor (cf. Figure 4.14).
- The pore radii of the porous membrane are assumed small compared to the average path length of the fluid $\langle\lambda\rangle$, i.e. $\langle\lambda\rangle \gg r_m \rightarrow h_m > 1 - 2\ \mu m$.

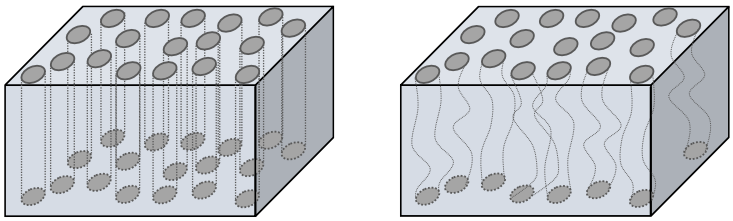

Figure 4.14 – Schematic representation of the porous model considered for the calculation of the permeability using Poiseuille's law: (left) for an ideal system ($\tau = 1$) and (right) for a tortuous gyroid system ($\tau = 1.06 - 1.35$) [34].

The resulting Poiseuille's law allows for the determination of the volumetric flow rate of liquid (Q) in pores. Here, η_{20} is the viscosity of the liquid (water) at 20°C, r_m is the pore radius, $\langle\lambda\rangle$ the average path length of the fluid and ΔP is the pressure applied on the fluid for it to cross the porous material. The average path length of the fluid into the membrane is related to the membrane thickness h_m and tortuosity factor τ using Eq. 4.6 [35]. It should be noted that in the ideal case – i.e. pores considered as cylinders perpendicular to the membrane surface – the tortuosity factor is equal to the unity ($\tau = 1$). Luo et al. (2020) [34] reported a tortuosity factor between 1.06 and 1.35 for gyroid structures, which we will use in our theoretical approach.

$$Q = \frac{\pi {r_m}^4 \Delta P}{8\eta_{20}\langle\lambda\rangle} = \sum_{r_m} \frac{\pi {r_m}^4 \Delta P}{8\eta_{20}\tau h_m} \quad \text{Eq. 4.5}$$

$$\tau = \frac{\langle\lambda\rangle}{h_m} \quad \text{Eq. 4.6}$$

It is then possible to determine the liquid flow in the pores at 20°C (J_{20}), S being the membrane surface (cf. Eq. 4.7). To access to the water permeability at 20°C (L_{P20}), we consider the pore size distribution of a membrane established in Section 4.2.1.1. We therefore have to consider a sum of pore radius and the equation simplifies to Eq. 4.8, where $n(r_m)$ is the pore density of each pore radius considered.

$$J_{20} = \frac{Q}{S} \quad \text{Eq. 4.7}$$

$$L_{P20} = \sum_{r_m} \frac{J_{20}(r)}{\Delta P} = \sum_{r_m} n(r_m) \frac{\pi {r_m}^4}{8\eta_{20}\tau h_m} \quad \text{Eq. 4.8}$$

- **$(21:23:56)_{62:19:19}$ polymer membranes**

In order to apply Poiseuille's law, we mentioned that the polymer membrane must be considered as isotropic. However, we evidenced that the UV samples are asymmetric due to the UV-penetration gradient they undergo. We therefore distinguished two extreme cases for the UV-LED and UV-TQ150 samples: the least and the most permeable. The least permeable case will consider the highest tortuosity factor for a gyroid network ($\tau = 1.35$) associated to the selective cross-section domain identified in cryo-SEM images. On the contrary, the most permeable case will consist of the lower factor ($\tau = 1.06$) associated to the porous cross-section domain of the cryo-SEM images. In the case of the isotropic RedOx polymer, the extreme cases consider mean permeability extracted from the cryo-SEM statistical analysis associated to the extreme gyroid tortuosity factors. Such an analysis will give us a realistic permeability range where the experimental value is expected to be found.

Figure 4.10 presents the evolution of the permeability of the polymer membrane, calculated using Eq. 4.8, as a function of the membrane thickness, for the three $(21:23:56)_{62:19:19}$ polymers investigated in Section 4.2.1.1 (UV-LED, UV-TQ150 and Redox). We note that both the maximum and minimum permeabilities of the UV-LED and the RedOx samples dramatically drop below 25 $L.m^{-2}.h^{-1}.bar^{-1}$ when the membrane thickness is thicker than 10 µm. The UV-TQ150 sample in turn allows for higher permeabilities, which ranges between 46 and 776

$L.m^{-2}.h^{-1}.bar^{-1}$ for a 10 µm-thick membrane. These calculated permeabilities do not account for the structure of the interfaces. Therefore, the higher permeability estimated for the UV-TQ150 polymer compared to the other two samples is not a consequence of the macroporosities found in the UV-TQ150 upper surface. This result is directly linked to the broader pore size distribution associated to bigger pore size of the sample (cf. Section 4.2.1.1) compared to the UV-LED and RedOx samples. Indeed, the pore size distribution and the pore radius are the two most impacting factors in Eq. 4.8 and will cause the increase of the membrane permeability compared to the two other samples investigated.

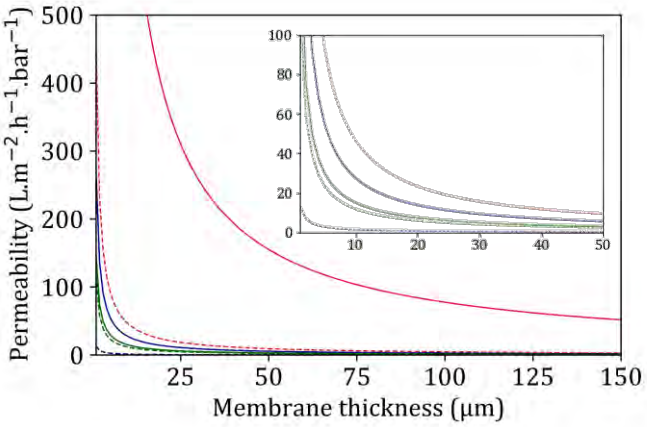

*Figure 4.15 – Evolution of the water permeability at 20°C of the $(21:23:56)_{62:19:19}$ polymer membrane as a function of the membrane thickness. (**red**) UV-TQ, (**blue**) UV-LED and (**green**) RedOx samples; (**plain**) maximum and (**dashed**) minimum permeability.*

We demonstrate here that the permeability is expected to dramatically drop up to a polymer thickness of 25 µm for all the polymers investigated. This numerical analysis emphasises the need to achieve extremely thin polymer coatings in order to maintain a high permeability. Plus, at first sight it seems that the UV-TQ150 sample exhibits the highest permeability of the three samples. However, such permeabilities were established while considering the UV-samples isotropic, in the least and most permeable cases. In the next paragraphs, we will account for the anisotropic behaviour of the cured polymer samples.

- **$(21:23:56)_{62:19:19}$ asymmetrical cured membranes**

We observe that the permeability associated to the so-called selective area of the photopolymerised samples are heavily impacting on the permeability of the overall membrane. The thickness of this selective area must be controlled during polymerisation in order not to dramatically decrease the permeability. Indeed, asymmetric membranes can be considered as composite samples, which permeability behave as a series resistance, cf. Eq. 4.9. Therefore, if

the selective area is predominant in the sample cross-section, the polymer overall permeability will be dictated by the permeability and the thickness of this selective domain.

$$\frac{1}{\mathrm{Lp}_{\mathrm{composite}}} = \frac{1}{\mathrm{Lp}_{\mathrm{porous\ substrate}}} + \frac{1}{\mathrm{Lp}_{\mathrm{thin-film}}} \qquad \text{Eq. 4.9}$$

In order to highlight the critical impact of the so-called selective area, we numerically investigated the evolution of the permeability of a $(21{:}23{:}56)_{62:19:19}$ asymmetrical sample of constant thickness as a function of the proportion of the selective thin-film thickness in the cross-section, the remaining of the polymer thickness being considered to be the porous layer. We then simulated the evolution of the permeability of an overall 10 µm membrane, as presented in Figure 4.16. The results presented evidence that the permeability of the UV-TQ150 sample is divided by 2.5 – from 390 to 151 $L.m^{-2}.h^{-1}.bar^{-1}$ – when the thickness of the selective thin-film is increased from 0 to 2 µm. In turn, the UV-LED sample exhibits a drop of its water permeability from 27 to 1 $L.m^{-2}.h^{-1}.bar^{-1}$, as soon as a selective thickness of 1 µm is obtained. We therefore evidenced the crucial need to control the proportion of the selective thin-film in the cross-section of the asymmetric polymer to achieve the highest permeability possible.

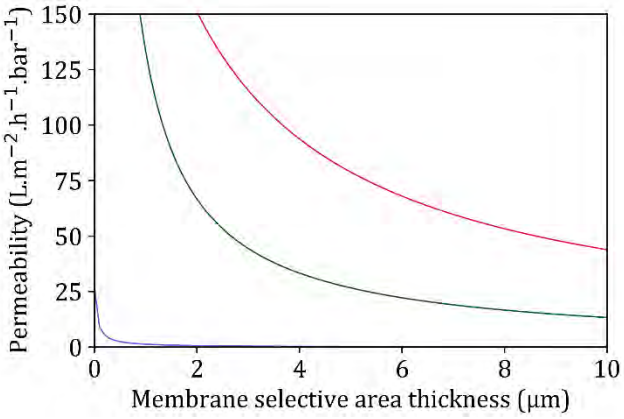

*Figure 4.16 – Evolution of the water permeability at 20°C of a 10 µm thick asymmetrical $(21{:}23{:}56)_{62:19:19}$ polymer as a function of the thickness of the selective domain. (**red**) UV-TQ150 and (**blue**) UV-LED. The permeability of an isotropic RedOx sample ($\tau_{mean} = 1.06$) (**green**) is presented for comparison.*

We also demonstrated that the use of a RedOx polymerisation process might be an interesting alternative to avoid a permeability decrease caused by the anisotropy of the cured samples. Indeed, we presented the calculated permeability of the RedOx sample in Figure 4.16 above for comparison. We notice that the thin-film permeability of this isotropic sample will always be higher than the permeability of the UV-LED polymer regardless of the selective area thickness. Plus, we discussed the selectivity of each polymer membrane in the previous Section and

evidenced that the RedOx sample is the one exhibiting the highest selectivity of the three samples. It therefore seems that the RedOx sample is a good compromise to achieve high permeability and high selectivity. In the last paragraphs, we will discuss the impact of this coating on a commercial microfiltration (MF) membrane.

- **Example of a $(21:23:56)_{62:19:19}$ RedOx composite membrane**

In these paragraphs, we will discuss the manufacture of composite membranes based on the deposition of the $(21:23:56)_{62:19:19}$ RedOx polymer thin-film on a commercial MicroPES™ flat-sheet MF membrane. This commercial membrane is 110 ± 10 µm thick and we evidenced its permeability to be 111 ± 18 $L.h^{-1}.m^{-2}.bar^{-1}$ after compacting. Based on the previous paragraphs, we can predict the permeability of a MicroPES™ membrane coated with an increasing coating thickness h_m using Eq. 4.9, as presented in Figure 4.17. We considered the mean tortuosity factor in the range of gyroid structures ($\tau = 1.21$).

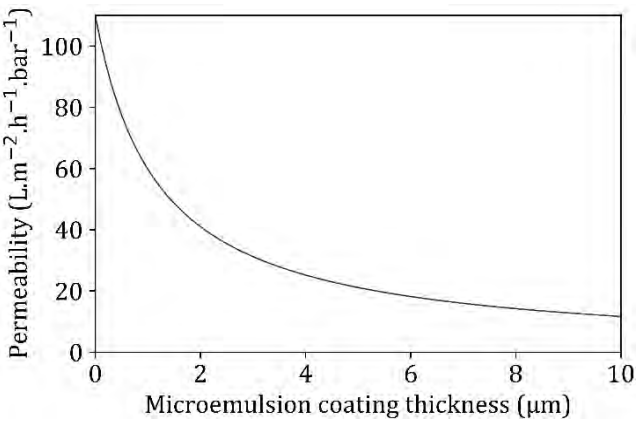

Figure 4.17 – Evolution of the water permeability at 20°C of the composite MicroPES™ flat-sheet membrane coated with $(21:23:56)_{62:19:19}$ RedOx polymer as a function of the coating thickness.

As expected from Eq. 4.9, the coating of a thin $(21:23:56)_{62:19:19}$ RedOx polymer film lowers the composite MF membrane permeability. Indeed, we observe a decrease of the permeability from 110 to 60 $L.m^{-2}.h^{-1}.bar^{-1}$ when depositing a 1 µm polymer coating. When increasing the coating thickness to 10 µm, the composite permeability then drops to 12 $L.m^{-2}.h^{-1}.bar^{-1}$. Such an estimation is consistent with the experimental results reported by Galiano et al. (2018) [4]. This research team synthesised a nanostructured polymer thin-film from microemulsion templating and then coated a UF PES membrane (L_p = 350 $L.m^{-2}.h^{-1}.bar^{-1}$). They evidenced that a thin-film coating of 4 µm allowed for a permeability of 76 $L.m^{-2}.h^{-1}.bar^{-1}$, while a 10 µm thick coating decreased the composite permeability below 20 $L.m^{-2}.h^{-1}.bar^{-1}$.

Intermediate conclusions:

We first estimated the selectivity of the $(21{:}23{:}56)_{62:19:19}$ RedOx, UV-LED and UV-TQ150 polymers, based on Ferry's law and assuming only steric hindrance of the pores. We estimated the MWCO of these three polymer membranes to be about 19.5, 22.3 and 145.4 kDa respectively. We therefore concluded that all three samples belong to the UF selectivity range (MWCO: 500–500,000 Da). However, one must note that the UV-LED and RedOx samples are more selective than the UV-TQ150 sample.

We then predicted the maximum water permeability at 20°C of these three samples based on the cryo-SEM images of each polymer. To that end, we adapted Poiseuille's law for an ideal porous material to a gyroid network. We assumed that all the pores observed on the SEM images are cylindrical, perpendicular to the membrane surface and through-going in the total membrane thickness. To avoid the impact of the interfaces, we only investigated the polymer bulk, which we considered isotropic. Because the photopolymerised samples undergo a UV-penetration gradient and thus a pore size gradient, this last assumption is false. We therefore considered two extreme cases that should frame the experimental value: the least and most permeable isotropic polymer membranes. We then considered the asymmetric membranes as composite membranes made of a selective and porous domain of various thickness.

We evidenced that the anisotropic nature of the sample can be highly detrimental to the permeability if the least porous domain dictates the permeable behaviour of the sample. Our simulation highlighted that a 10 µm asymmetric UV-LED polymer membranes presented a lower permeability than a 10 µm isotropic RedOx sample, regardless of the selective thickness in the overall cross-section. The UV-TQ150 sample exhibits higher permeability than the RedOx sample but also lower selectivity. Therefore, a compromise must be found, and because the highest selectivity is sought, the RedOx sample seems to be a good candidate. However, we also evidenced that such a compromise has a significant and negative impact on on the membrane permeability as we estimated a decrease below 75 $L.m^{-2}.h^{-1}.bar^{-1}$ for a coating thicker than 2 µm. We then investigated the permeability of a composite membrane constituted from the $(21{:}23{:}56)_{62:19:19}$ RedOx coating on a commercial compacted MF membrane. We estimated that depositing a 1 µm coating divided by 1.8 the permeability of the pristine supporting membrane, from 110 to 60 $L.m^{-2}.h^{-1}.bar^{-1}$. These estimations are however consistent with some experimental results reported by some authors [4].

Overall, our theoretical estimation of the performance of the $(21:23:56)_{62:19:19}$ polymer membranes highlighted the potential in ultrafiltration of our polymer materials. However, coating thickness as low as a few micrometres has to be achieved in order to reach acceptable permeabilities for separative applications. We evidenced that for a 10 µm sample, a maximum permeability of 13 $L.m^{-2}.h^{-1}.bar^{-1}$ was achieved for an isotropic membrane (i.e. RedOx sample). Unfortunately, such low coating thicknesses cannot be achieved for flat-sheet membrane modification, using the technologies available in the Laboratoire de Génie Chimique. The polymerisation of 100 µm $(21:23:56)_{62:19:19}$ monomer solutions will be now discussed.

4.2.2.3 Experimental determination of the water permeability of the $(21:23:56)_{62:19:19}$ UV-TQ150 membrane

The experimental analysis of the polymerised $(21:23:56)_{62:19:19}$ samples was only carried out for the UV-TQ150 samples only. We investigated the behaviour of both asymmetric $(21:23:56)_{62:19:19}$ and PES-$(21:23:56)_{62:19:19}$ composite membranes. The samples presented were casted on a glass plate (asymmetric membrane) or on a supporting membrane (PES composite membrane) and no upper glass plate was used. Indeed, due to technical limitations we were unable to increase the size of the mould without impacting the homogeneity of the polymer.

- **Asymmetric $(21:23:56)_{62:19:19}$ UV-TQ150 membrane**

The behaviour of two ~ 100 µm thick $(21:23:56)_{62:19:19}$ UV-TQ150 asymmetric membranes were investigated by performing two successive cycles of increase/decrease of the applied pressure, between 0.2-1 bar as presented in Figure 4.18. Each measurement was performed for 5 minutes.

The M112 membrane is a 112 ± 7 µm thick $(21:23:56)_{62:19:19}$ UV-TQ150 asymmetric membrane, while the M82 is an 82 ± 8 µm thick membrane. The estimated flux (cf. Section 4.2.2.2) associated to both membranes is presented in plain line in the inset and will compared to the experimental data in the next paragraphs.

We see that the flux increased up to 630 $L.m^{-2}.h^{-1}$ for the M112 sample when applying a pressure of 1 bar, while only up to 200 $L.m^{-2}.h^{-1}$ for the M82 sample. We note that the water flux does not evolve linearly with pressure, neither in increase nor in decrease of applied pressure. We also observe that the measured flux is similar for the two pressure cycles, indicating no damage and breakage of the sample during the filtration process.

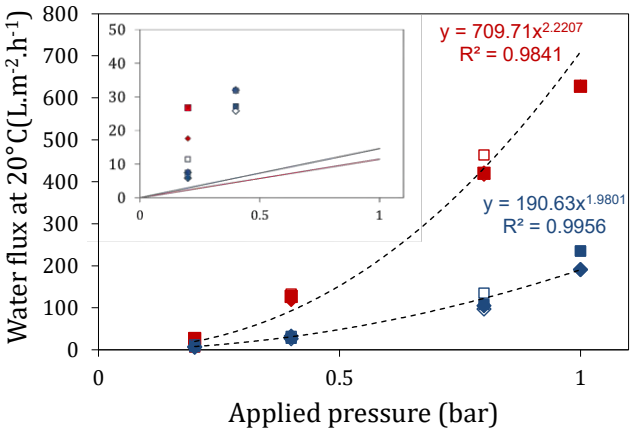

*Figure 4.18 – Experimental evolution of the water flux at 20°C through the (**red**) M112 and the (**blue**) M82 membrane. (□) First and (◊) second pressure cycle, (**plain**) increase and (**hollow**) decrease of the applied pressure. Inset: (**plain lines**) flux estimated from images of cryo-SEM analysis.*

In the limited time of this project, we were not able to experimentally determine the cause of the increase in the flux as a function of the applied pressure. However, based on Poiseuille's law (cf. Eq. 4.5) we identified that only the pore size and the effective pore length ⟨λ⟩ – i.e. the tortuosity over the membrane thickness – are dependent on the material structure. However, when applying compressive or tensile stress, the effective length of the pore will not be impacted, the tortuosity factor compensating the modification of the material thickness. Hence, we estimated that only the modification of the pore size could cause the non-linear behaviour of the flux as a function of the pressure applied on the membrane, cf. Eq. 4.10.

$$R_{J20} = \frac{J_{20}(P)}{J_{20}(0.2\ \text{bar})} = \left(\frac{r_m(P)}{r_m(0.2\ \text{bar})}\right)^4 \frac{P}{P(0.2\ \text{bar})} = \Delta r_m{}^4 \Delta P \qquad \text{Eq. 4.10}$$

The results presented in Table 4.4 depict the evolution of the pore size $\left(\Delta r_m = \frac{r_m(P)}{r_m(0.2\ \text{bar})}\right)$ of the two membranes as a function of the increase of pressure. The results presented were obtained by considering the water flux obtained at 0.2 bar as a reference. We note that when increasing the applied pressure to 1 bar, the average pore radius should increase by 51-65% compared to that obtained at a pressure of 0.2 bar. Such a modification corresponds to an increase from ca. 29 nm to 44 – 48 nm of the pore radius. In order to confirm the hypothesis of an increase in the pore size, we suggest to trace the retention of a PEO of ca. 500 kDa as a function of the applied pressure. Indeed, based on the estimation of selectivity of the polymer membrane (cf. Section 4.2.2.1) we concluded that such 480 kDa PEO with would be retained at 90% by the membrane. If the pores are actually dilating when increasing the pressure applied on the membrane, we

expect the PEO initially retained for low pressure (e.g. 0.2 bar) to pass through the membrane when increasing the applied pressure.

Table 4.4 – Determination of the pore size r_m upon modification of the applied pressure during water filtration from 0.2 to P bar.

$\Delta P = \frac{P}{0.2\ bar}$	$J_{20}(P)$ ($m^3.m^{-2}.h^{-1}$)	R_{J20}	Δr_m
	M112		
1	16.9	1	1.00
2	124.1	7.4	1.38
4	430.5	25.5	1.59
5	628.3	37.3	1.65
	M82		
1	8.3	1	1.00
2	29.2	3.5	1.15
4	111.1	13.5	1.35
5	212.9	25.8	1.51

We first hypothesised the occurrence of a large defect in the membrane. Such a membrane with a defect can be represented as a diaphragm. The defect in the membrane would cause a constriction of the preferential flow path, which would widen when exiting the material. However, such a modification of the water path would induce an evolution of the flow rate as a function of the applied pressure according to the form: $Q = f\left(\Delta P^{\frac{1}{2}}\right)$ and thus $J_{20} = f\left(\Delta P^{\frac{1}{2}}\right)$ [36]. In our case, we observe an evolution of the type: $Q = f(\Delta P^{2.22})$ and $Q = f(\Delta P^{1.98})$ for the M112 and M82 membrane respectively. We therefore believe that a defect could not explain the non-linear evolution of the water flux as function of the applied pressure.

Our second hypothesis consists of the atypical deformation of the polymer network upon compressive stress. This assumption is consistent with the behaviour of the hydrated polymer network when cut in circular shape for the determination of the water flux through the membrane as a function of the applied pressure. Indeed, we observed a modification in the size of the hydrated membrane sample after the circular cutting of the membranes (i.e. compressive stress). The initial diameter of the polymer (4.6 cm) shrank by about 2 mm, resulting in a loss of surface of about 4.35%. We therefore hypothesise an anisotropic behaviour of the sample under external stress. Such a behaviour resembles the one of auxetic structures: when compressed in one direction, it becomes thinner in the perpendicular directions [36], cf. Figure 4.28.

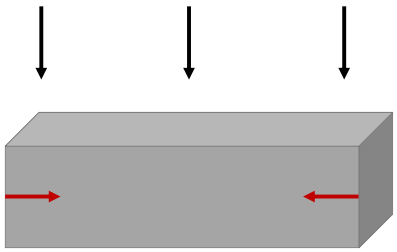

Figure 4.19 – Schematic representation of the deformation of an auxetic material under compressive stress.

Such a behaviour would be consistent with the experimental determination of the flux. Indeed, when applying a compressive stress (i.e. pressure) on the membrane surface, we can suppose that the pores will undergo a perpendicular thinning, resulting in larger pores as presented in Figure 4.20.

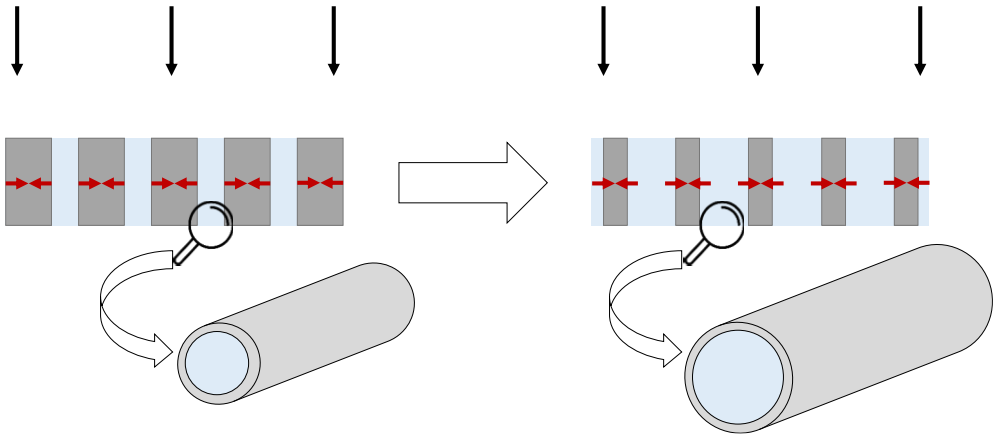

Figure 4.20 – Schematic representation of the hypothesised deformation the polymer membrane under compressive stress.

Such materials are characterised by a negative Poisson's ratio, defined in Eq. 4.11. In order to confirm this hypothesis, we suggest to monitor the relative transverse shrinkage and the

relative elongation under compressive or tensile stress using a strain measuring device on a uniform cross-section of the sample.

$$\nu = \frac{\text{relative transverse shrinkage}}{\text{relative elongation}} \qquad \text{Eq. 4.11}$$

Intermediate conclusions:

Based on the monitoring of the water flux as a function of the applied pressure, we concluded that the $(21{:}23{:}56)_{62:19:19}$ asymmetric polymer membrane displays an elastic behaviour. This assumption is consistent with the repeatability of the experimental fluxes over the pressure cycles (no defect or breakage of the polymer) and the fact that the experimental flux at 0.2 bar is quite similar to the flux calculated from the pore size distribution at atmospheric pressure. We therefore believe that applying a pressure up to 1 bar can result in an elastic dilatation of the pore size due to the mechanical properties of the investigated polymer network. Further analyses are required to confirm such assumptions, for example the investigation of the mechanical properties and the determination of Poisson's ratio, as well as the monitoring of the retention as a function of the applied pressure.

As part of this work, we decided to investigate the behaviour of the polymer network when trapped into a porous polymer matrix, in the present case a commercial MF PES membrane.

- **$(21{:}23{:}56)_{62:19:19}$ UV-TQ150 coating on a MF supporting membrane**

We photografted a coating of the $(21{:}23{:}56)_{62:19:19}$ on a deconditioned and uncompacted MicroPES™ MF-PES commercial membrane. The coating was deposited on the commercial membrane using a 100 µm casting-knife. After washing and drying, we analysed the PES-$(21{:}23{:}56)_{62:19:19}$ composite membrane using SEM analysis, cf. Figure 4.21 and Figure 4.22.

We observed that the monomer solution completely penetrated the supporting membrane prior to polymerisation and that no polymer coating is obtained on the surface of the MicroPES™. Plus, we see that the $(21{:}23{:}56)_{62:19:19}$ polymer coating mostly polymerised in the small pore size domain of the asymmetric MicroPES™ membrane. We conclude that the monomer liquid penetrated the PES matrix and was subsequently trapped in its small pores due to the occurrence of a low Laplace pressure, i.e. a highly negative Laplace pressure. The phenomenon of capillary penetration of the liquid monomer coating inside the membrane will be further addressed in Chapter 5, Section 5.4.3.2.

The water permeability of the PES composite membrane was then experimentally determined. As no water flux was obtained up to 2 bar, a preliminary wetting step with a water:isopropanol solution (50:50 vol.%) was carried out for 1 h. The water permeability of the samples was then investigated for various ranges of applied pressure, cf. Table 4.5 and Figure 4.23.

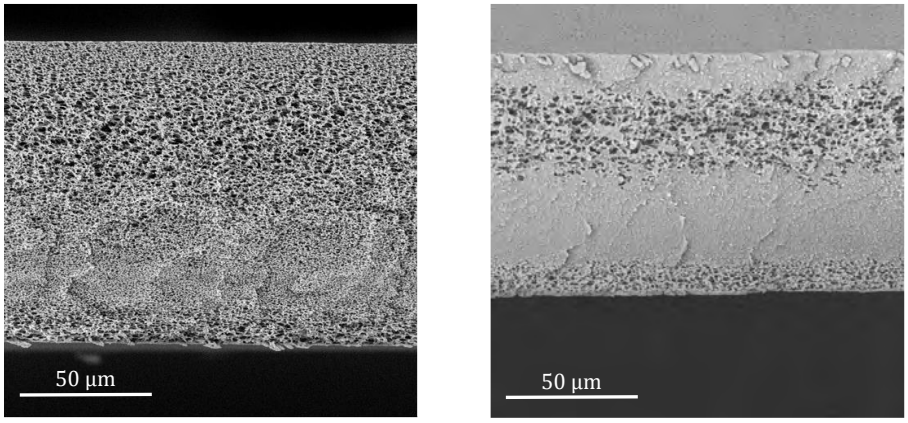

*Figure 4.21 – SEM images of cross-sections of (**left**) a pristine MicroPES™ flat-sheet membrane and (**right**) a coated MicroPES™ membrane coated with the (21:23:56)$_{62:19:19}$ monomer solution.*

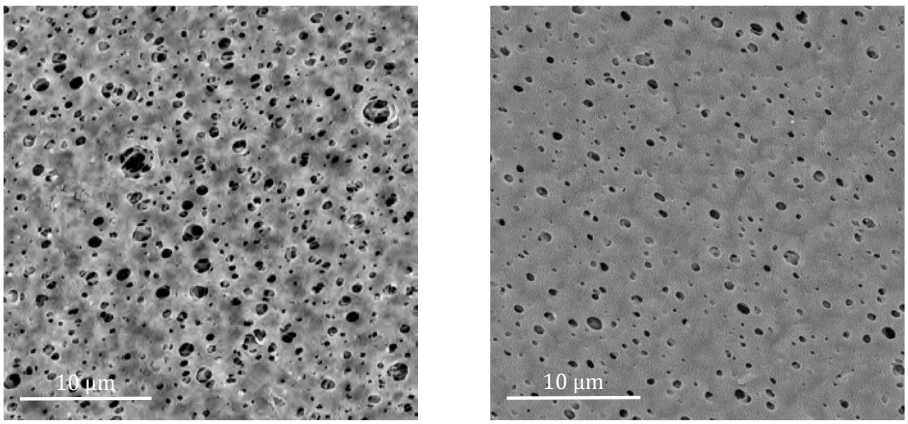

*Figure 4.22 – SEM images of the selective surface of (**left**) a pristine MicroPES™ flat-sheet membrane and (**right**) a coated MicroPES™ membrane coated with the (21:23:56)$_{62:19:19}$ monomer solution.*

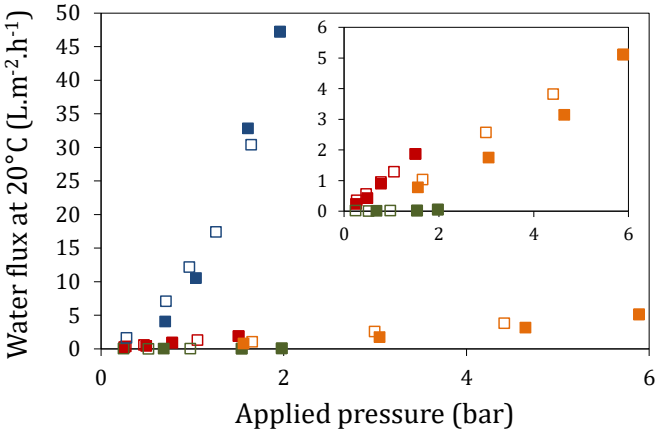

*Figure 4.23 – Experimental evolution of the water flux at 20°C through MicroPES™ flat-sheet membranes coated with 100 µm (21:23:56)$_{62:19:19}$ monomer solution and cured under the TQ150 lamp. (**plain**) increase and (**hollow**) decrease of the applied pressure. Color legend in Table 4.5.*

We first note, that no hysteresis of the measured fluxes is observed for the four PES-(21:23:56)62:19:19 composite membranes, contrary to the pristine deconditioned MicroPES™ membrane ($Lp_{pristine\ MicroPES}$ = 111 ± 18 L.m^{-2}.h^{-1}.bar^{-1}, after compacting the membrane for 20 min at 2 bar). We then observe that the water flux through the composite membrane are at least 5 times lower than the flux obtained when filtrating through the asymmetric (21:23:56)62:19:19 UV-TQ150 membrane.

Table 4.5 – Experimental coating thickness obtained from SEM observation and permeability associated to the investigated ranges of applied pressure.

Sample	Coating thickness (µm)	Investigated pressure domain (bar)	Water permeability (L.m^{-2}.h^{-1}.bar^{-1})	
			Pressure increase	Pressure decrease
PES-(21:23:56)$_{62:19:19}$_1	75 ± 13	0.2 – 2.0	*No linear behaviour*	
PES-(21:23:56)$_{62:19:19}$_2	29 ± 2	0.3 – 2.0	*No linear behaviour*	
PES-(21:23:56)$_{62:19:19}$_3	60 ± 6	0.3 – 1.5	1.24	1.19
PES-(21:23:56)$_{62:19:19}$_4	52 ± 4	1.5 – 5.9	0.86	0.75

We also observe that the flux does not evolve linearly over the 0.2 – 2.0 bar range, similarly to the asymmetric (21:23:56)$_{62:19:19}$ membrane discussed above. The PES-(21:23:56)$_{62:19:19}$_1 and

PES-$(21:23:56)_{62:19:19}$_2 membranes both display a sharper increase in their flux when increasing the pressure above 1.5 bar. To confirm this observation, we investigated the behaviour of our samples PES-$(21:23:56)_{62:19:19}$_3 and the PES-$(21:23:56)_{62:19:19}$_4 membranes in the range of applied pressure of 0.3 – 1.5 and 1.5 – 5.9 respectively. In both ranges, we observe a linear evolution of the water flow as a function of the applied pressure, both in increasing and decreasing pressure. We therefore conclude that a non-linear behaviour as a function of the applied pressure may occur similarly to the asymmetric $(21:23:56)_{62:19:19}$ membrane, but for a higher applied pressure of ca. 1.5 bar.

Intermediate conclusions:

When comparing the asymmetric and composite $(21:23:56)_{62:19:19}$ membranes, we note that the fluxes obtained when filtrating through the composite membranes are less important than for the asymmetric membranes. Plus, the non-linear evolution of the fluxes as a function of the applied water pressure clearly appears for higher pressure compared to the asymmetric membrane. Combining these observations with those of the asymmetric $(21:23:56)_{62:19:19}$ sample, we suggest that a deformation of the polyacrylate network still occurs when trapped into the PES support. However, as the polyacrylate network is trapped within small pores (5 – 10 µm), the cross-sectional area exposed to pressure is smaller than that of the asymmetric membrane. Therefore, for a similar applied pressure, the compressive stress experienced by the polyacrylate network in the MicroPES™ is also lower than in the asymmetric membrane. This statement is also in good agreement with the previous paragraphs: an increased applied pressure is needed to deform the polyacrylate network compared to the asymmetric membrane. The origin of the assumed atypical mechanical behaviour of the polymer network is however not well understood at the moment and needs to be further investigated.

To our knowledge, no mention of the elasticity of the membrane under water pressure has been reported in the literature. Only Galiano (2012) [5] mentioned an elastic and flexible behaviour of the polymer sample when it is wet, while a brittle and fragile behaviour when it is dried, behaviour that we also observed for the pristine $(21:23:56)_{62:19:19}$ polymer. In addition, few authors determined the permeability of similar polymer membranes. However, the determination of the water permeability has been performed either on a thin-film composite polymer membrane [4,37] and/or for a single applied pressure [3,5,37], which may explain why no elastic behaviour has been reported.

It should be noted that the impact of alcohols on the PHEMA and PMMA structure (discussed in Appendix 3) is considered not to damage the system because of the cross-linked nature of the polymer network. This assumption is also strengthened by the diluted nature of the alcohol used and the short period of exposure of the cross-linked network to this solution. Another limitation we noted is the ratio Synperonic™ A11 to Tergitol™ 15-S-12 used for the PES-$(21{:}23{:}56)_{62:19:19}$ synthesis. The ratio used in this specific case is different from the one investigated in the remainder of Chapter 4: 20:80 instead of 50:50. We believe that such a difference does not have a significant impact on the system due to the similar nature of the two surfactants and because commercial surfactants already consist of a mixture of molecules with different chain lengths. However, we strongly recommend the present results to be confirmed in the future.

Finally, we assumed in the last paragraphs, that the microstructure of the polyacrylate structure trapped into the pore of the PES membrane is similar to that of the asymmetric $(21{:}23{:}56)_{62:19:19}$ membranes. However, a modification of the microstructure of the monomer self-assembly trapped into the small pores of the supporting membrane may occur prior to polymerisation, due to Marangoni effect along the interfaces. In order to fully understand the behaviour of the $(21{:}23{:}56)_{26:19:19}$ membrane, the microstructure of the coating trapped into the pores should be further assessed.

Overall, we conclude that the $(21{:}23{:}56)_{62:19:19}$ polymer is effectively porous and through-going with open pores. The experimental flux obtained for low applied pressure is consistent with the numerical simulation performed using the pore size distribution under atmospheric pressure. However, we observed a non-linear evolution of water flux as a function of the applied pressure, which we attributed to an anisotropic behaviour of our polyacrylate network under compressive stress. Further analyses are however needed to fully understand the origin of such a non-linear behaviour.

4.3 Investigation of $(46{:}8{:}46)_{62:19:19}$ and $(46{:}8{:}46)_{33:33:33}$ compositions

In Section 4.2, we carried out a comprehensive investigation of the $(21{:}23{:}56)_{62:19:19}$ sample. We will now discuss two different non-ionic compositions, formulated using the same non-ionic surfactant mix (i.e. equimassic mix of Synperonic™ A11 and Tergitol™ 15-S-12): the $(46{:}8{:}46)_{62:19:19}$ and $(46{:}8{:}46)_{33:33:33}$ compositions. These two compositions both contain the same amount of water, MMA and surfactant phase, but the composition of the latter will vary from one composition to another. As a reminder, the surfactant phase composition is described as follows (HEMA:Synperonic™ A11:Tergitol™ 15-S-12).

The $(46{:}8{:}46)_{62:19:19}$ composition will contain more HEMA than the $(46{:}8{:}46)_{33:33:33}$ formulation, and thus will lead to a higher polymer percentage compared to the $(46{:}8{:}46)_{33:33:33}$. Both monomer samples belong to the systems discussed in Chapter 1.

4.3.1 Microstructure of the polymer depending on the initiation method

Similarly to what have been presented for the $(21{:}23{:}56)_{62:19:19}$ sample, a cross-linker (EGDMA) and an initiator (UV or RedOx) have been added to the (46:8:46) monomers solutions before beginning the polymerisation process. The same three initiation methods will be investigated in the following: RedOx and UV initiations (under a LED or a polychromatic TQ150 lamp). The resulting polymer networks underwent a water washing process, as described in Chapter 2, and subsequently observed using the cryo-SEM technique, cf. Figure 4.25.

For the two investigated monomer compositions, both UV-LED and RedOx initiation methods lead to highly heterogeneous samples, which present an alternation of dense and micrometric porous domains. It should be noted that no nanometric pore was observed in these polymers. The RedOx and UV-LED samples all present an alternation of dense and micrometric aggregate structure, both on surface and in the bulk. These inhomogeneities are caused by the destabilisation of the system during the polymerisation. Because these inhomogeneities not only occur on the surface but also in the polymer bulk, we conclude that the specific affinities with the substrate interface are not the only difficulty to overcome in order to access a homogeneous structure.

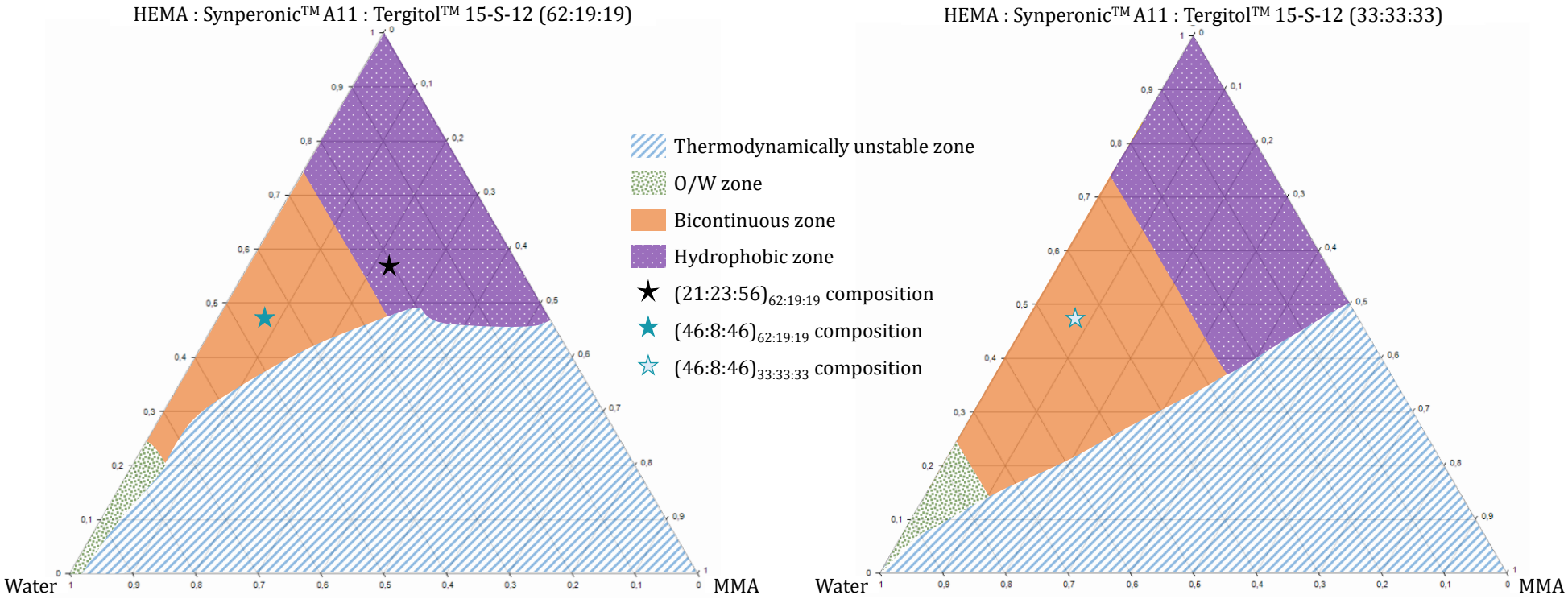

Figure 4.24 – Ternary-phase diagrams of the investigated system for the (top) (62:19:19) and (bottom) (33:33:33) surfactant ratios, and the associated polymerised compositions.

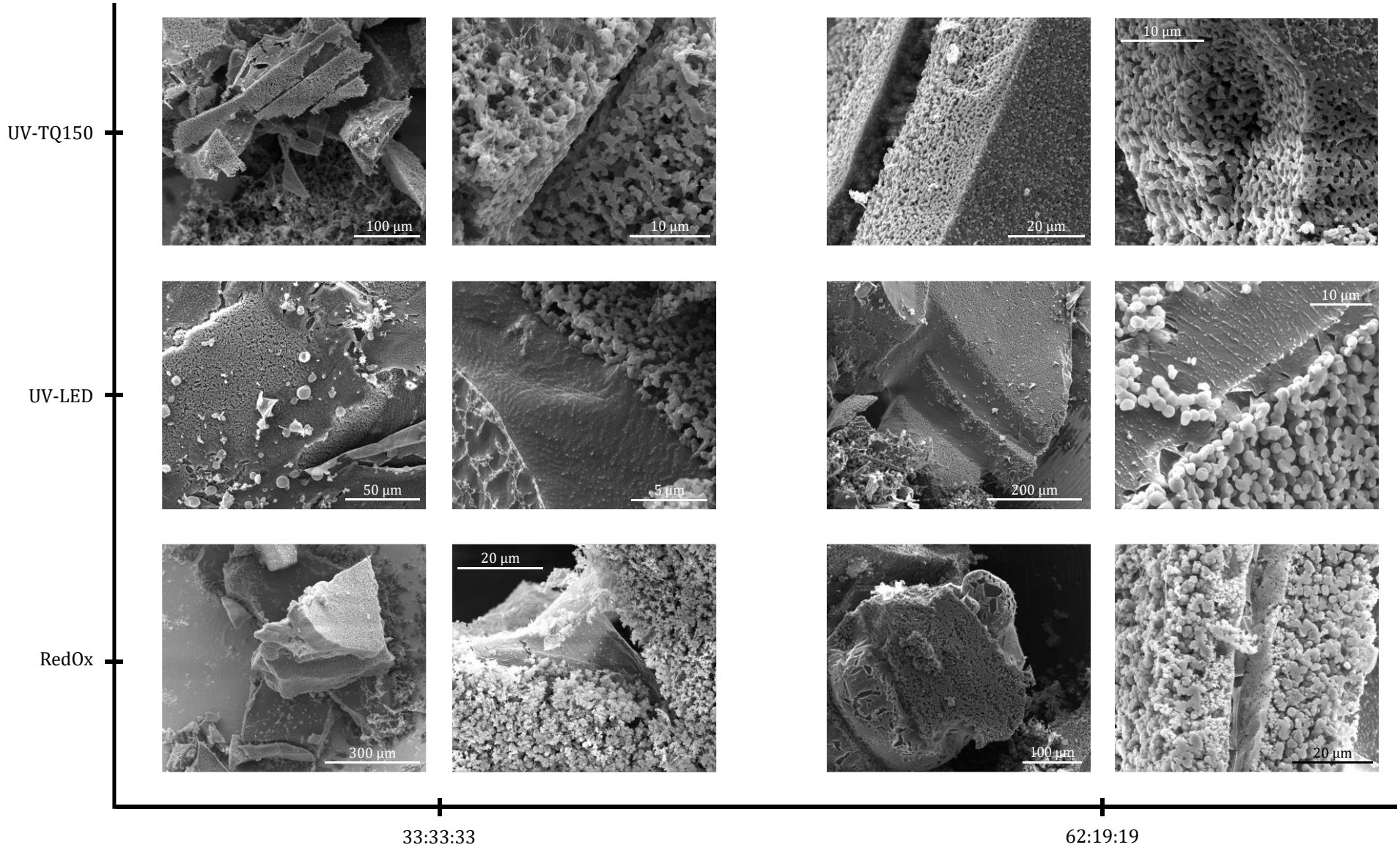

Figure 4.25 – Cryo-SEM cross-sections images of the two (46:8:46) compositions, cured with RedOx and UV (under the LED or the TQ150 lamp) initiations.

The UV-TQ150 samples, in turn, present a highly structured bicontinuous micrometric structure. The (62:19:19) sample is uniform and does not present any dense domain, which is not the case of the (33:33:33) sample, which is heterogeneous in the bulk polymer. Hence, the $(46{:}8{:}46)_{66:66:66}$ UV-TQ150 sample is the only one of these six investigated polymers to display a uniform, micrometric bicontinuous structure, with porous channels of 550-850 nm. Finally, we observe that the UV-TQ150 samples also exhibit a porosity gradient, which is inherent to the photopolymerisation process, as discussed in Section 4.2.1.1.

Table 4.6 – (46:8:46) systems polymerisation duration, as a function of the initiation method.

Initiation method	**$(46{:}8{:}46)_{33:33:33}$**	**$(46{:}8{:}46)_{62:19:19}$**
UV-TQ150	3 min 20 s *(+100 s warming period)*	1 min 20 s *(+100 s warming period)*
UV-LED	1 h	2 min
RedOx	> 5 min	> 6 min

Compared to the other five samples, the $(46{:}8{:}46)_{62:19:19}$ UV- TQ150 sample is quickest to be polymerised, cf. Table 4.6. We therefore conclude that in this specific case, the faster the polymerisation kinetics, the more homogeneous the structure. We, along other researchers [19], proved in Section 4.2.1.2 that, using non-polymerisable surfactants leads to an evolution of the system microstructure. We therefore remind that the two (46:8:46) systems will evolve during polymerisation, regardless of the initiation method.

Plus, compared to the $(21{:}23{:}56)_{62:19:19}$ previously discussed, the (46:8:46) systems exhibit a high-water to monomers ratio. We assume that such a low monomer content leads to thinner interconnected domains, which will undergo breakage more quickly upon destabilisation of the surfactant interface, leading to a less homogeneous and continuous network. It is therefore critical to form a large number of radicals before the cleavage of the interconnected structure. Using the TQ150 polychromatic lamp increases the number of radicals created in the system compared to the LED monochromatic lamp. The more the radicals formed before the system evolution, the better the formation of an interconnected structure. Regarding the RedOx sample, we also observed the formation of polymer beads in water when investing the polymerisation process of both (46:8:46) compositions in a test tube. We therefore conclude that a slower polymer conversion leads to the disappearance of a bicontinuous structure.

Intermediate conclusions:

The polymerisation of the $(46{:}8{:}46)_{33:33:33}$ and $(46{:}8{:}46)_{62:19:19}$ compositions using the UV-LED, UV-TQ150 and RedOx initiation methods confirmed the evolution of the microstructure during the polymerisation process, due to the non-polymerisable nature of the surfactants used, as discussed in Section 4.2.1.1. However, unlike the $(21{:}23{:}56)_{62:19:19}$ composition the water to monomer ratio of the $(46{:}8{:}46)_{33:33:33}$ and $(46{:}8{:}46)_{62:19:19}$ are respectively 2.6 and 1.6 times lower than for the previous case study. We therefore hypothesised that decreasing to monomer content decreases the ability of the system to withstand the structural change for longer, resulting in a less homogeneous and a less continuous polymer network. We therefore concluded that the fastest initiation method made it possible to initiate the maximum radicals before the bicontinuous structure cleavage and to maintain a uniform porous structure.

Such a behaviour is in good agreement with the occurrence of a spinodal decomposition phenomenon during polymerisation. Indeed, the appearance of a radical monomer associated with the growth of the polymer chains will subsequently lead to the coalescence of the organic monomer domains. When blocking the destabilisation of the system by increasing the viscosity (i.e. increasing the conversion rate), the destabilisation of the system is then stopped and the final microstructure is obtained. Therefore, the polymerisation kinetics and the gel point onset time govern the polymer microstructure. Modifying the composition and/or the initiation method will modify these two parameters and thus impact on the resulting polymer structure.

In the following, we will discuss the $(46{:}8{:}46)_{62:19:19}$ UV-TQ150 sample, which we identified as the only sample of the previous batch of interest for the manufacture of nanoporous polymer membranes.

4.3.2 Analysis of the $(46{:}8{:}46)_{62:19:19}$ UV-TQ150 sample

The only uniform polymer structure obtained upon polymerisation is the $(46{:}8{:}46)_{62:19:19}$ UV-TQ150 sample. We identified a pore size gradient in the sample, due to the photopolymerisation the sample underwent. Similarly to what have been done for the $(21{:}23{:}56)_{62:19:19}$ polymers, we investigated the theoretical membrane performance of the $(46{:}8{:}46)_{62:19:19}$ UV-TQ150 polymer. Based on the cryo-SEM images, we conclude that the membrane is asymmetrical. In order to assess the performances of such a membrane, we will consider this polymer as a composite membrane made of a porous substrate overlaid by a thin-film, cf. Figure 4.26.

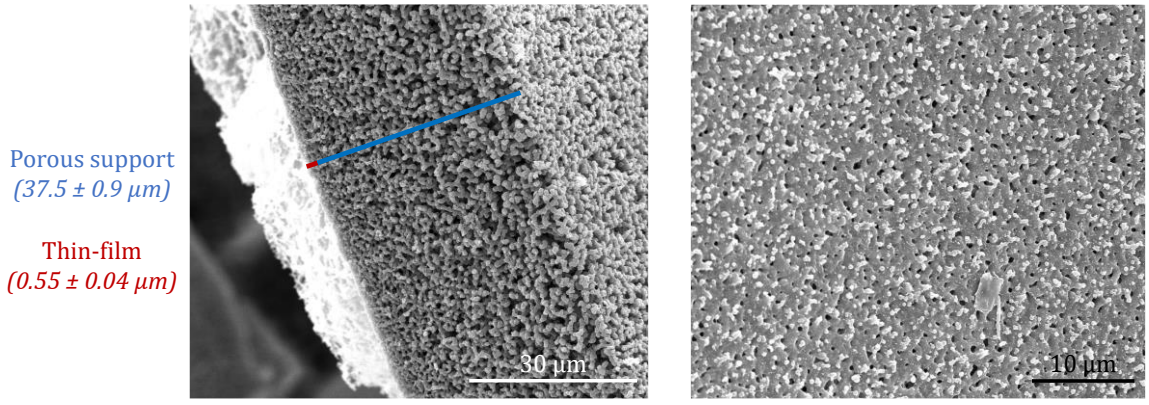

*Figure 4.26 – Cryo-SEM images of (**left**) the (46:8:46)$_{62:19:19}$ UV-TQ150 asymmetric polymer and the delimitation of the so-called thin-film and of the porous domain and (**right**) the selective surface.*

Using the ImageJ software, we carried out a statistical analysis of the pore radius and the pore size distribution in both porous and selective areas identified in Figure 4.26 above. The results are presented in Figure 4.27 below.

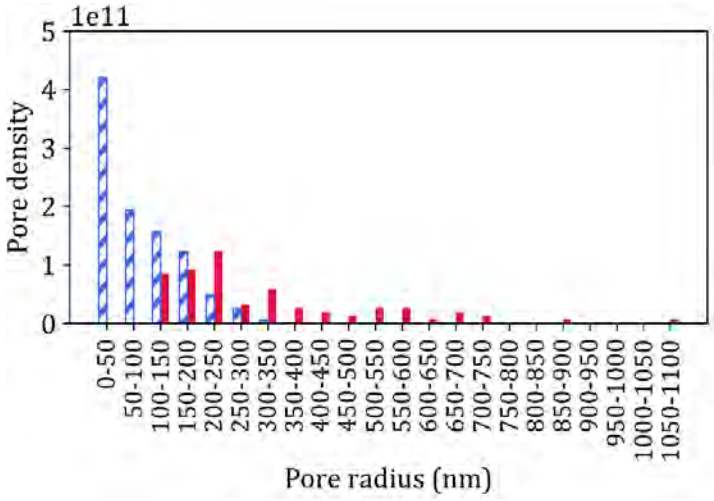

*Figure 4.27 – Distribution of pore radius of the (46:8:46)$_{62:19:19}$ UV-TQ150 sample from the numerical analysis from the cryo-SEM images. (**blue, dashed**) Selective thin-film and (**red, plain**) porous cross-section areas.*

We first note that the pore density on the polymer is narrower and localised on smaller pore radii (25-370 nm) than the porous domain (110-1060 nm). Plus, the porous domain exhibits large pores but a very low pore density compared to the so-called thin-film. These observations are consistent with what is usually observed for composite membranes: the thin-film displays a high pore density narrowed around small sizes, while the porous area shows bigger pore sizes associated to a broad pore size distribution. Considering a lognormal pore radius distribution, which is usual in the case of porous membranes, we determined the mean pore radius of the selective area of the (46:8:46)$_{62:19:19}$ UV-TQ150 polymer membrane to be 90 ± 91 nm. Similarly

to what has been discussed in Section 4.2.1.1 for the $(21:23:56)_{62:19:19}$ membrane, a lognormal distribution fits well the selective thin-film pore distribution, but not so well the pore distribution in the porous domain. Such a behaviour is attributed to the increase of the channel size throughout the entire membrane thickness: the porous domain being asymmetric, we obtain a large distribution of pore size.

We then estimated the selectivity of this membrane using Ferry's law (cf. Eq. 4.2), similarly to what has been presented in Section 4.2.2.1. The retention of the polymer membrane as a function of the hydrodynamic radius r_{hydro} of the particles retained is presented in Figure 4.28. We calculated that in order to have an intrinsic retention coefficient of $R_m = 0.9$, the particles filtrated must have a hydrodynamic radius bigger than 68.4 nm. When considering the retention of PEGs, we estimated the MWCO of this membrane was estimated to be 3,200 kDa. Such a selectivity would allow the membrane to be considered as a low-MF membrane.

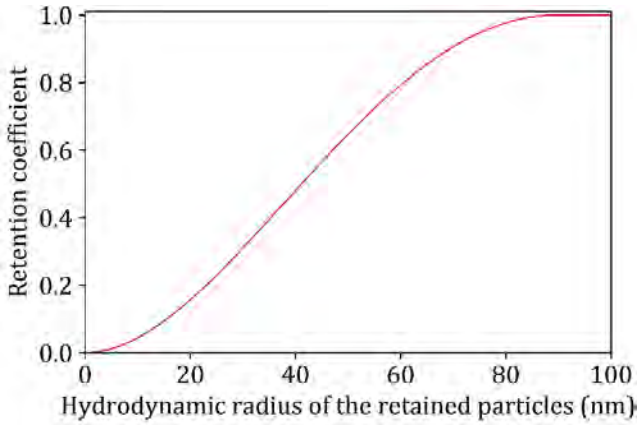

Figure 4.28 – Estimated evolution of the retention coefficient of the $(46:8:46)_{62:19:19}$ UV-TQ150 polymer membrane as a function of the hydrodynamic radius of the particles retained, based on the statistical analysis of the cryo-SEM cross-sections images.

We also estimated the water permeability at 20°C using Poiseuille's law for a tortuous gyroid structure (cf. Eq. 4.8), assuming the same hypotheses as in Section 4.2.2.2. To that end, we considered the composite membrane permeability as a series resistance, cf. Eq. 4.9. The results obtained as a function of the tortuosity factor are presented in Table 4.7.

The resulting theoretical water of the $(46:8:46)_{62:19:19}$ polymer membrane was estimated to lay between 44,000 and 59,000 L. $m^{-2}.h^{-1}.bar^{-1}$. As we determined above the pore radius, we conclude that this membrane would allow the retention of particles with a size about 50-740 nm. We therefore have evidenced the possibility to combine the selectivity of a low MF membrane with a high permeability of a MF membrane [38].

Table 4.7 – Theoretical water permeability at 20°C of the $(46:8:46)_{62:19:19}$ UV-TQ150 polymer membrane, as a function of the tortuosity factor τ.

Sample	Permeability ($L.m^{-2}.h^{-1}.bar^{-1}$) for τ = 1.06	Permeability ($L.m^{-2}.h^{-1}.bar^{-1}$) for τ = 1.35
Thin-film area ($h_{thin\text{-}film}$ = 0.55 ± 0.04 µm)	120,000	94,000
Porous area ($h_{porous\ area}$ = 37.5 ± 0.9 µm)	104,000	82,000
$(46:8:46)_{62:19:19}$ asymmetric membrane	**44,000**	**56,000**

Intermediate conclusions:

We evidenced that the $(46:8:46)_{62:19:19}$ UV-TQ150 polymer membrane allowed for a low-MF selectivity combined to a high permeability, usually obtained for MF membranes. One specificity of the present polyacrylate systems is the cross-linked nature of the polymer network. Such a characteristic is interesting regarding solvent resistance of the membrane. Indeed, common MF membranes (PSF, PEEK, PVDF, etc.) are sensitive to organic solvents and will dissolve in their contact. Using cross-linked polymer networks allows for better chemical resistance of the membrane [39,40]. The $(46:8:46)_{62:19:19}$ UV-TQ150 polymer membrane could therefore be of high interest for solvent filtration. However, one of the main drawbacks of such cross-linked materials is their brittle nature [41]. In our case, the $(46:8:46)_{62:19:19}$ UV-TQ150 polymer membrane was carefully handled to avoid breakage. In order to confirm the potential of this polymer network for solvent filtration, its mechanical resistance and its resistance to common solvent have to be assessed. Moreover, based on the conclusion drawn from the experimental results presented in Section 4.2.2.3 for the $(21:23:56)_{62:19:19}$ membrane, we can expect a deformation of the polymer network under pressure, which would lead to a higher water permeability but also a lower retention under water pressure. The present simulation therefore needs to be experimentally investigated.

4.4 Conclusion

This fourth chapter aimed at the study of the microstructure adopted by several polymer systems upon polymerisation of bicontinuous microemulsified monomer templates. To that end, we investigated three initial monomer self-assembled systems and three polymerisation processes: chemical (RedOx) and photochemical (UV-LED and UV-TQ150). Our investigation addressed the following questions:

- **How is the monomer microemulsified structure affected by the polymerisation process: is the nanoscaled microstructure maintained throughout the polymerisation process when using non-polymerisable surfactants?**
  How do the system composition and the polymerisation initiation method impact on the final microstructure of polymer when polymerising a monomer self-assembled system stabilised using a mix of non-ionic and non-polymerisable surfactants?

Using SAXS and cryo-SEM analyses, we concluded that the $(21{:}23{:}56)_{62:19:19}$ polymers display a porous interconnected network. The polymer structure identified is however different from the one of the monomer system. We evidenced that the polymer systems have a larger structure (5-120 nm) than the monomer system (4.8 nm) regardless of the polymerisation method. Plus, depending on the initiation method applied, we observed a variation of the resulting polymer structure. Indeed, because the polymerisation kinetics vary from an initiation method to another, the mean-curvature of the surfactant interface evolves differently during the polymerisation process, and so does the microstructure. Further work is however needed to fully apprehend the impact of the polymerisation kinetics on the polymer microstructure.

We also noted that the photopolymerisation process leads to an anisotropic polymer structure and to the occurrence of a pore gradient in the membrane thickness caused by the UV-penetration gradient into the polymer bulk. The RedOx initiation method, in turn, leads to an isotropic porous bulk material. Finally, we observed that the interfaces of the samples differ from the polymer bulk. We imputed this phenomenon to the occurrence of a Marangoni flow in our solution, caused by the interaction of the surfactants with the solid interface, combined to the evaporation of the solvent in the case of cured samples. The investigated samples exhibit a rough dense interface in contact with borosilicate glass, but we assume that their structure may vary if polymerised in contact of other substrates. Such a parameter has to be controlled in

order to avoid the occurrence of non-porous structures, which will dramatically decrease the polymer water permeability.

We also demonstrated an increase of the nanoscale of the polymer structure after the removal of the non-polymerisable surfactants located in the aqueous porous channels. We can therefore conclude that for equivalent surfactant molecules, a non-polymerisable surfactant will lead to larger pore sizes than its polymerisable analogue.

We then investigated the polymerisation of two other self-assembled monomer compositions: the $(46{:}8{:}46)_{62:19:19}$ and the $(46{:}8{:}46)_{33:33:33}$. The $(46{:}8{:}46)_{33:33:33}$ polymer exhibit non-uniform heterogeneous structures, that randomly alternated between porous micrometric structure formed by polymer aggregates and dense non-porous structures, for all three polymerisation initiations investigated. The $(46{:}8{:}46)_{62:19:19}$ polymer also exhibits non-uniform heterogeneous structure for the RedOx and UV-LED initiations. The $(46{:}8{:}46)_{62:19:19}$ UV-TQ150, in turn, displays a uniform micrometric bicontinuous structure. This behaviour has been linked to the blocking of a spinodal decomposition mechanism occurring in the system during the polymerisation process. The final microstructure of the polymer therefore depends on the polymerisation kinetics and on the onset of the gel point. We therefore highlighted that both the composition and the polymerisation method are of the utmost importance when polymerising a monomer self-assembly stabilised by non-polymerisable surfactants. Out of the nine investigated samples, only four were porous and uniform: the $(21{:}23{:}56)_{62:19:19}$ RedOx, the $(21{:}23{:}56)_{62:19:19}$ UV-LED, the $(21{:}23{:}56)_{62:19:19}$ UV-TQ150 and the $(46{:}8{:}46)_{62:19:19}$ UV-TQ150. Only these four samples have been investigated to be used as membrane materials for liquid filtration.

- **Are the $(21{:}23{:}56)_{62:19:19}$ and the $(46{:}8{:}46)_{62:19:19}$ compositions of significant interest for membrane filtration?**

Based on a statistical analysis of the sample pore density using cryo-SEM images, we investigated the selectivity and the water permeability of the four identified samples. We highlighted that the all three $(21{:}23{:}56)_{62:19:19}$ samples (RedOx, UV-LED, UV-TQ150) display a pore size distribution compatible with the retention of nanometric compounds (<250 nm). Based on Ferry's law, we concluded that these three polymer membranes can be considered as UF membranes, considering steric retention alone.

We however evidenced that the UV-TQ150 sample belongs to the high-UF selectivity range, while the RedOx and UV-LED samples display lower pore sizes and thus a better selectivity. Using Poiseuille's law and including a tortuosity factor typical of gyroid structures ($\tau = 1.06 - 1.35$), we then estimated the theoretical permeability of the three $(21{:}23{:}56)_{62:19:19}$ polymer samples. We therefore evidenced that if the RedOx sample allowed for the smallest pore size, it also displays the highest permeability of the three polymer samples, considering the anisotropic (and thus limiting) nature of the UV-samples. We concluded, based on the numerical analysis carried out using the cryo-SEM cross-section images, that the RedOx initiation method is the most interesting one to access the most selective and most permeable $(21{:}23{:}56)_{62:19:19}$ polymer membranes. We further concluded that, in order to reach the permeability range of UF membranes (50-500 $L.m^{-2}.h^{-1}.bar^{-1}$), the polymer coating thickness has to be as low as a few micrometres, which is consistent with some results previously reported [4]. However, technologies for the deposition of coatings with a thickness of a few micrometres on flat-sheet membranes were not available in the Laboratoire de Génie Chimique. We therefore focused on the synthesis and analysis of 100 µm thick asymmetric and composite PES membranes. In both cases, we observed a non-linear and repeatable evolution of the water flow as a function of the applied pressure up to 1 bar. We therefore hypothesise that the cross-linked acrylate polymer network deforms under pressure. We further hypothesised that this deformation leads to an expansion of the pore size of the polymer membrane. To confirm this assumption, we suggest two further analyses. The first is to confirm - or deny - the anisotropic behaviour of the polymer network by determining the Poisson's ratio of the material, which should be negative in the case of an auxetic material. The second analysis we suggest is to monitor the retention PEOs as a function of the pressure: if the pores effectively expand when increasing the pressure on the system, a drop of retention is expected at some point. If such an expansion of the pore size is confirmed, we do not expect the synthesised system to be of high interest for separative applications. In that case, we however suggest its use for catalytic applications: such an elastic network could trap the active particles during a pressure increase-decrease cycle on the polymer network.

The $(46{:}8{:}46)_{62:19:19}$ UV-TQ150 cross-linked polymer network, in turn, exhibited a high theoretical permeability, typical of MF membranes. Plus, from statistical analysis of cryo-SEM images the membrane pore size was estimated to range between 50-740 nm. We then determined that particles with a hydrodynamic radius higher or equal to 68.4 nm could be retained with a retention coefficient of at least 0.9, which is typical of low-MF membranes. Such

dual behaviour is linked to the asymmetric nature of the sample. Indeed, the membrane selective part of the cross-section is really thin compared to the total thickness of the membrane. Hence, this cross-linked polymer allows for the combination of a high selectivity and a high permeability. Due to its cross-linked nature, such a polymer membrane could be of high interest for solvent filtration, provided its mechanical resistance is high enough to withstand pressure.

Overall, we evidenced that the self-assembled acrylate systems stabilised by a mix of the non-ionic non-polymerisable Synperonic™ A11 and Tergitol™ 15-S-12 surfactants can be considered for the manufacture of polymers of various porosity and structure, as a function of the system composition and the polymerisation initiation method applied.

References

[1] F. J. E. Sanz, J. F. Lahitte, and J. C. Remigy, 'Membrane synthesis by microemulsion polymerisation stabilised by commercial non-ionic surfactants', *Desalination*, vol. 199, no. 1–3, pp. 127–129, 2006, doi: 10.1016/j.desal.2006.03.156.

[2] F. Galian, I. Friha, S. A. Deowan, J. Hoinkis, Y. Xiaoyun, D. Johnson, R. Mancuso, N. Hilal, B. Gabriele, S. Sayadi, and A. Figoli, 'Novel low-fouling membranes from lab to pilot application in textile wastewater treatment', *J. Colloid Interface Sci.*, vol. 515, pp. 208–220, 2018, doi: 10.1016/j.jcis.2018.01.009.

[3] F. Galiano, A. Figoli, S. A. Deowan, D. Johnson, S. A. Altinkaya, L. Veltri, G. De Luca, R. Mancuso, N. Hilal, B. Gabriele, and J. Hoinkis, 'A step forward to a more efficient wastewater treatment by membrane surface modification via polymerizable bicontinuous microemulsion', *J. Memb. Sci.*, vol. 482, pp. 103–114, 2015, doi: 10.1016/j.memsci.2015.02.019.

[4] F. Galiano, S. A. Schmidt, X. Ye, R. Kumar, R. Mancuso, E. Curcio, B. Gabriele, J. Hoinis, and A. Figoli, 'UV-LED induced bicontinuous microemulsions polymerisation for surface modification of commercial membranes – Enhancing the antifouling properties', *Sep. Purif. Technol.*, vol. 194, pp. 149–160, 2018, doi: 10.1016/j.seppur.2017.10.063.

[5] F. Galiano, 'Preparation and characterisation of polymerisable bicontinuous microemulsion membranes for water treatment application', PhD thesis, Universita' della Calabria, 2012.

[6] G. Leong-Ming and C. H. Chew, 'Microporous polymer composites from microemulsion polymerization', *Colloids Surfaces A Physicochem. Eng. Asp.*, vol. 123–124, pp. 681–693, 1997, doi: 10.1016/S0927-7757(96)03812-5.

[7] T. H. Chieng, L.M. Gan, C. H. Chew, S. C. Ng, and K. L. Pey, 'Microporous Polymeric Materials by Microemulsion Polymerization: Effect of Surfactant Concentration of Singapore', *Langmuir*, vol. 11, pp. 3321–3326, 1995, doi: 10.1016/S0032-3861(96)00316-3.

[8] L. M. Gan, T. H. Chieng, C. H. Chew, and S. C. Ng, 'Microporous Polymeric Materials from Microemulsion Polymerization', *Langmuir*, vol. 10, no. 11, pp. 4022–4026, 1994, doi: 10.1021/la00023a020.

[9] C. H. Chew, L. M. Gan, L. H. Ong, K. Zhang, T. D. Li, T. P. Loh, and P. M. MacDonald, 'Bicontinuous structures of polymerized microemulsions: 1H NMR self-diffusion and conductivity studies', *Langmuir*, vol. 13, no. 11, pp. 2917–2921, 1997, doi: 10.1021/la9607971.

[10] L. M. Gan, J. Liu, L. P. Poon, C. H. Chew, and L. H. Gan, 'Microporous polymeric composites from bicontinuous microemulsion polymerization using a polymerizable nonionic surfactant', *Polymer (Guildf).*, vol. 38, no. 21, pp. 5339–5345, 1997, doi: 10.1016/S0032-3861(97)00080-3.

[11] T. H. Chieng, L. M. Gan, W. K. Teo, and K. L. Pey, 'Porous polymeric membranes by bicontinuous microemulsion polymerization: Effect of anionic and cationic surfactants', *Polymer (Guildf).*, vol. 37, no. 26, pp. 5917–5925, 1996, doi: 10.1016/S0032-3861(96)00452-1.

[12] T. H. Chieng, L. M. Gan, C. H. Chew, S. C. Ng, and K. . L. Pey, 'Formation of microporous polymeric materials by microemulsion polymerization of methyl methacrylate and 2-hydroxyethyl methacrylate', *J. Appl. Polym. Sci.*, vol. 60, pp. 1561–1568, 1996, doi: https://doi.org/10.1002/(SICI)1097-4628(19960606)60:10<1561::AID-APP6>3.0.CO;2-H.

[13] T. H. Chieng, L. M. Gan, C. H. Chew, S. C. Ng, and K. L. Pey, 'Microporous polymeric materials by polymerization of microemulsions containing different alkyl chain lengths of cationic surfactants', *Polymer (Guildf).*, vol. 37, no. 21, pp. 4823–4831, 1996, doi: 10.1016/S0032-3861(96)00316-3.

[14] W. Wang, H. Wei, Z. Du, X. Tai, and G. Wang, 'Formation and characterization of fully dilutable microemulsion with fatty acid methyl esters as oil phase', *ACS Sustain. Chem. Eng.*, vol. 3, no. 3, pp. 443–450, 2015, doi: 10.1021/SC500667N.

[15] E. Golabi, F. S. Azad, S. S. Ayatollahi, S. N. Hosseini, and N. Akhlaghi, 'Experimental study of wettability alteration of limestone rock from oil-wet to water-wet using various surfactants', *Soc. Pet. Eng. - SPE Heavy Oil Conf. Canada 2012*, vol. 1, pp. 746–761, 2012, doi: 10.2118/157801-MS.

[16] M. Von Bahr, F. Tiberg, and B. V. Zhmud, 'Spreading dynamics of surfactant solutions', *Langmuir*, vol. 15, no. 20, pp. 7069–7075, 1999, doi: 10.1021/LA9902760.

[17] R. T. van Gaalen, C. Diddens, H. M. A. Wijshoff, and J. G. M. Kuerten, 'Marangoni circulation in evaporating droplets in the presence of soluble surfactants', *J. Colloid Interface Sci.*, vol. 584, pp. 622–633, 2021, doi: 10.1016/J.JCIS.2020.10.057.

[18] M. L. Quezada Jiménez, 'Photo-greffage de membranes et distributuion initiale de taille des pores : Mise en évidence des limitations', PhD thesis, Université Toulouse 3 Paul Sabatier, 2007.

[19] S. dos Santos, L. Piculell, O. J. Karlsson, and M. Da Graa Miguel, 'Phase diagrams come alive: Understanding how to create, destroy or change ordered surfactant structures by polymerizing the counterions', *Soft Matter*, vol. 7, no. 5, pp. 1830–1839, 2011, doi: 10.1039/c0sm00958j.

[20] S. H. Chen, S. L. Chang, R. Strey, J. Samseth, and K. Mortensen, 'Structural evolution of bicontinuous microemulsions', *J. Phys. Chem.*, vol. 95, no. 19, pp. 7427–7432, 1991, doi: 10.1021/j100172a058.

[21] N. Zhou, F. S. Bates, and T. P. Lodge, 'Mesoporous membrane templated by a polymeric bicontinuous microemulsion', *Nano Lett.*, vol. 6, no. 10, pp. 2354–2357, 2006, doi: 10.1021/nl061765t.

[22] V. Castellino, E. Acosta, and Y. L. Cheng, 'Interpenetrating polymer networks templated on bicontinuous microemulsions containing silicone oil, methacrylic acid, and hydroxyethyl methacrylate', *Colloid Polym. Sci.*, vol. 291, no. 3, pp. 527–539, 2013, doi: 10.1007/s00396-012-2741-8.

[23] B. H. Jones and T. P. Lodge, 'Nanocasting nanoporous inorganic and organic materials from polymeric bicontinuous microemulsion templates', *Polym. J. 2012 442*, vol. 44, no. 2, pp. 131–146, 2012, doi: 10.1038/pj.2011.136.

[24] S. Peng, Q. Guo, T. C. Hughes, and P. G. Hartley, 'In situ synchrotron SAXS study of polymerizable microemulsions', *Macromolecules*, vol. 44, no. 8, pp. 3007–3015, 2011, doi: 10.1021/ma102978u.

[25] R. J. Hickey, T. M. Gillard, M. T. Irwin, T. P. Lodge, and F. S. Bates, 'Structure, viscoelasticity, and interfacial dynamics of a model polymeric bicontinuous microemulsion', *Soft Matter*, vol. 12, no. 1, pp. 53–66, 2015, doi: 10.1039/c5sm02009c.

[26] T. Kang, S. Qian, G. S. Smith, C. Do, and W. T. Heller, 'Small-angle neutron scattering study of a dense microemulsion system formed with an ionic liquid', *Soft Matter*, vol. 13, no. 39, pp. 7154–7160, 2017, doi: 10.1039/c7sm01516j.

[27] K. V. Schubert, R. Strey, S. R. Kline, and E. W. Kaler, 'Small angle neutron scattering near Lifshitz lines: Transition from weakly structured mixtures to microemulsions', *J. Chem. Phys.*, vol. 101, no. 6, pp. 5343–5355, 1994, doi: 10.1063/1.467387.

[28] S. H. Chen, S. L. Chang, and R. Strey, 'On the interpretation of scattering peaks from bicontinuous microemulsions', *Prog. Colloid Polym. Sci.*, vol. 81, pp. 30–35, 1990, doi: 10.1007/bfb0115519.

[29] S. Ezrahi, E. Wachtel, A. Aserin, and N. Garti, 'Structural polymorphism in a four-component nonionic microemulsion', *J. Colloid Interface Sci.*, vol. 191, no. 2, pp. 277–290, 1997, doi: 10.1006/jcis.1997.4962.

[30] I. Baudin, 'Interactions polymères hydrosolubles/particules : rôle dans le phénomène de colmatage de membranes d'ultrafiltration utilisées pour la production d'eau potable', PhD thesis, Université Pierre et Marie Curie, 1991.

[31] American Membrane Technology Association, 'Ultrafiltration Membrane Filtration'. https://www.amtaorg.com (accessed Aug. 23, 2022).

[32] Lenntech, 'Molecular weight cutoff (MWCO)'. https://www.lenntech.fr/services/mwco.htm (accessed Aug. 23, 2022).

[33] B. Spivakov and V. Shkinev, 'MEMBRANE TECHNIQUES | Ultrafiltration', in *Encyclopedia of Analytical Science: Second Edition*, P. Worsfold, A. Townshend, and C. Poole, Eds. Elsevier, 2005, pp. 524–530.

[34] J. W. Luo, L. Chen, T. Min, F. Shan, Q. Kang, and W. Q. Tao, 'Macroscopic transport properties of Gyroid structures based on pore-scale studies: Permeability, diffusivity and thermal conductivity', *Int. J. Heat Mass Transf.*, vol. 146, p. 118837, 2020, doi: 10.1016/J.IJHEATMASSTRANSFER.2019.118837.

[35] J.-P. Montheard, M. Chatzopoulos, and D. Chappard, '2-Hydroxyethyl Methacrylate (HEMA): Chemical Properties and Applications in Biomedical Fields', *J. Macromol. Sci. Part C*, vol. 32, no. 1, pp. 1–34, 1992, doi: 10.1080/15321799208018377.

[36] Y. Wang *et al.*, 'Mechanically robust, biocompatible, and durable PHEMA-based hydrogels enabled by the synergic effect of strong intermolecular interaction and suppressed phase separation', *Polymer (Guildf).*, vol. 254, p. 125083, 2022, doi: 10.1016/J.POLYMER.2022.125083.

[37] P. D. Dalton, L. Flynn, and M. S. Shoichet, 'Manufacture of poly(2-hydroxyethyl methacrylate-co-methyl methacrylate) hydrogel tubes for use as nerve guidance channels', *Biomaterials*, vol. 23, no. 18, pp. 3843–3851, 2002, doi: 10.1016/S0142-9612(02)00120-5.

[38] T. Yan, R. Sun, H. Deng, B. Tan, and N. Ao, 'The morphological and biomechanical changes of keratocytes cultured on modified p (HEMA-MMA) hydrogel studied by AFM', *Scanning*, vol. 31, no. 6, pp. 246–252, 2009, doi: 10.1002/SCA.20170.

[39] P. Chhabra *et al.*, 'Studies on development of polymeric materials using gamma irradiation for contact and intraocular lenses', *Int. J. Polym. Sci.*, vol. 2009, 2009, doi: 10.1155/2009/906904.

[40] A. Y. Sung and T. H. Kim, 'Optical application of poly(HEMA-co-MMA) containing silver nanoparticles and N,N-dimethylacrylamide', *Korean J. Chem. Eng.*, vol. 29, no. 5, pp. 686–691, 2012, doi: 10.1007/S11814-011-0231-1.

[41] A. Kogan, D. E. Shalev, U. Raviv, A. Aserin, and N. Garti, 'Formation and characterization of ordered bicontinuous microemulsions', *J. Phys. Chem. B*, vol. 113, no. 31, pp. 10669–10678, 2009, doi: 10.1021/jp901617g.

[42] P. Aimar, P. Bacchin, and A. Maurel, 'Filtration membranaire (OI, NF, MFT) - Aspects théoriques : perméabilité et sélectivité', *Tech. Ing.*, pp. 1–25, 2010, [Online]. Available: https://books.google.com/books?id=2bL_CNorgdsC&pgis=1.

[43] C. S. Ong, H. T. Lay, N. R. Tamilselvam, and J. W. Chew, 'Cross-Linked Polycarbonate Microfiltration Membranes with Improved Solvent Resistance', *Langmuir*, vol. 37, no. 13, pp. 4025–4032, 2021, doi: 10.1021/ACS.LANGMUIR.1C00383.

[44] K. Vanherck, G. Koeckelberghs, and I. F. J. Vankelecom, 'Crosslinking polyimides for membrane applications: A review', *Prog. Polym. Sci.*, vol. 38, no. 6, pp. 874–896, 2013, doi: 10.1016/J.PROGPOLYMSCI.2012.11.001.

[45] K. S. Goh, J. Y. Chong, Y. Chen, W. Fang, T. H. Bae, and R. Wang, 'Thin-film composite hollow fibre membrane for low pressure organic solvent nanofiltration', *J. Memb. Sci.*, vol. 597, p. 117760, 2020, doi: 10.1016/J.MEMSCI.2019.117760.

Chapter 5

Chapter 5 – Microemulsion dip-coating on hollow-fibre membrane: an industrial prospect?

CHAPTER 5 – MICROEMULSION DIP-COATING ON HOLLOW-FIBRE MEMBRANE: AN INDUSTRIAL PROSPECT? 193

3.1 INTRODUCTION 197
5.2 DESCRIPTION OF THE DIP-COATING PROCESS FOR HOLLOW-FIBRE 198
5.3 MODELS OF FLUID DEPOSITION ON FIBRES 200
5.3.1 Newtonians fluids coating 200
5.3.2 Complex surfactant-based solutions 203
5.3.2.1 Surfactant solutions 204
5.3.2.2 Colloidal suspensions 206
5.3.2.3 Emulsions 208
5.4 SIMULATION OF HOLLOW FIBRE COATING - APPLICATIONS TO MICROEMULSIONS ON MF-PES (MICROPESTM) AND UF-PS (ZEEWEEDTM) 210
5.4.1 Operating conditions for the control of the deposited coating 211
5.4.1.1 Applicability of the LLD-law to the studied systems 211
5.4.1.2 System resolution for the determination of the deposited thickness 212
5.4.3 Coating perturbation after deposition on the fibre 219
5.4.3.1 Plateau-Rayleigh instability 219
5.4.3.1.1 Plateau-Rayleigh instability domain - Upper boundary 219
5.4.3.1.2 Plateau-Rayleigh instability domain - Lower boundary 220
5.4.3.2 Coating dynamic instability 223
5.4.3.2.1 Contact angle determination 223
5.4.3.2.2 Coating capillary penetration into the hollow-fibre 225
5.4.3.2.3 Coating dewetting 230
5.4.4 Efficiency of the dip-coating process for microemulsions 233
4.4 CONCLUSION 236
REFERENCES 240

5.1 Introduction

As stated in Chapter 1, hollow-fibres are of great industrial interest because of their high active surface per unit volume. In order to investigate the industrial application of coating bicontinuous microemulsions on the surface of supporting membranes, we will now discuss the dip coating process of commercial hollow-fibre membranes with microemulsions.

The dip-coating process has been developed for a wide variety of applications such as the production of perovskite solar cells [1], or graphene-based composite [2]. This process is most generally used to deposit a thin-film coating on a plane or cylindrical substrate. The following paragraphs will describe the process of continuous dip-coating of hollow-fibre membranes and its governing equations, depending on various factors such as the properties of the fluid deposited, the substrate – here a fibre – speed and geometrical properties.

We will then perform a numerical simulation aiming to predict the coating behaviour of a microemulsion on the surface of two commercial hollow-fibre membranes, assuming the microemulsions behave as linear simple fluids. We will focus on the impact of the reservoir radius on the dynamic meniscus shape and the resulting deposition regimes. Finally, based on the presented results we will discuss the industrial prospects of microemulsion dip-coating on hollow-fibres for the manufacturing of composite hollow-fibre membranes.

This chapter will answer the following questions:

- *To what extent does the width of the tank impact a linear liquid deposit?*
- *Assuming the microemulsion behaves as a linear simple fluid, is the fibre coating a viable industrial solution for composite membranes manufacturing?*
- *What are the prospects for the microemulsion deposition on hollow-fibre membranes?*

5.2 Description of the dip-coating process for hollow-fibre membranes

There is a wide variety of processes used for the surface modification of hollow-fibres such as Initiated Chemical Vapor Deposition (iCVD) [3], interfacial polymerisation [3], [4] or spray-coating [5]. In our work we focus on the dip-coating process, a technology that allows the deposition of uniform liquid thin-film on a substrate. This process is of high interest due to its low costs compared to other processes and is widely used in strategic industrial sectors such as lubrication and fibre optics [6].

Over the last decades our lab has also made some significant contributions to the development of dip-coated hollow-fibre membranes [7]–[9]. The dip-coating process is adapted to an industrial use for the continuous deposition of liquids on cylindrical substrates. The liquid properties (viscosity, density, surface tension, and composition/concentration) as well as the fibre geometry and the fibre speed can be tuned to reach an aimed coating thickness.

The fibre dip-coating entails the motion of the cylindrical substrate through a coil and then through a liquid solution bath. This solution is drawn by the fibre and forms a thin liquid layer on the surface of the fibre. The set-up used in the LGC allows either for a UV-polymerisation [7] or a drying step when using the lamps as ovens [8], [9] as presented in the Figure 5.1.

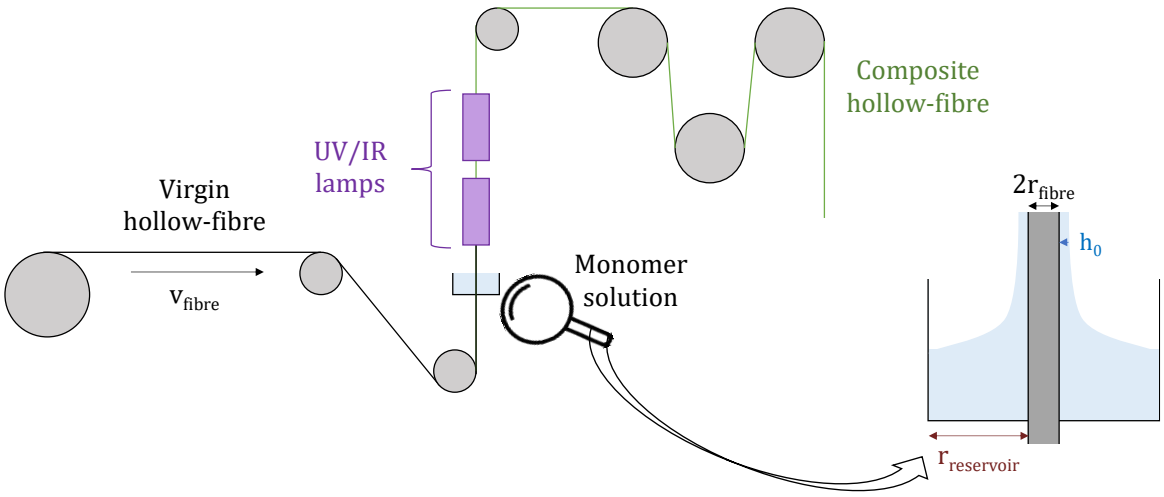

Figure 5.1 – Hollow-fibre membrane dip-coating module (a) with UV lamps for coating photografting and (b) IR lamp for coating drying.

Upon removal of the fibre from the liquid solution, a meniscus is formed and 3 domains can be identified, as presented in Figure 5.2. The first region consists of the static meniscus and is located immediately in contact with the liquid bath, where surface tension effects dominate. The second region consists of the dynamic meniscus, where the film is starting to be drawn by

the fibre. The meniscus thickness h(x) is driven by the forces applied on the liquid and governs the final film thickness deposited onto the substrate. These forces are dependent on the liquid properties, on the geometry and speed of the substrate – which will impact on the viscous and inertia forces. The last region consists of the final and flat deposited film, which thickness is constant as only the viscous and gravitational forces are exerted on the deposited liquid.

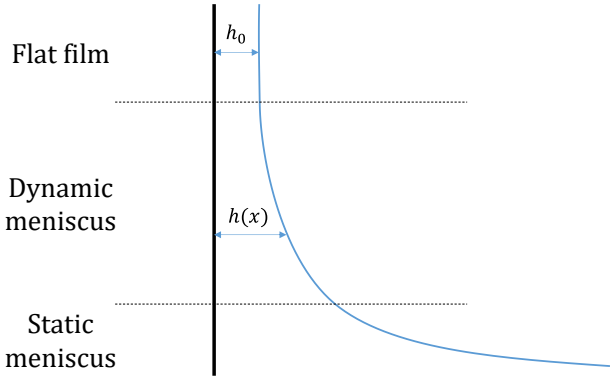

Figure 5.2 – Liquid meniscus representation for vertical fibre wiring.

5.3 Models of fluid deposition on fibres

Several models have been developed over the last decades in order to describe and predict the behaviour of the liquid when being coated using a dip-coating process. Two geometries have been studied for the substrate: a plane and a cylindrical geometry. Our following work focuses only on the state of art of cylindrical substrates. If the experimental behaviour of viscous linear Newtonians fluids meets the theoretical models, the non-linear fluids are more complex and their behaviour might vary greatly from those predictive models.

5.3.1 Newtonians fluids coating

Dip-coating of linear Newtonians fluids has been widely studied in the literature. As detailed in the previous section, the coated film thickness is determined by the forces applied on its dynamic meniscus. Thus, the physico-chemical properties of the coated liquid, the geometry of the fibre and its speed – which will impact on the inertia and viscous forces – are to be considered.

The laws describing the behaviour of the coating are governed by three dimensionless numbers which compare the forces applied on the fluid. The capillary number Ca compares the viscous forces to the capillary ones, the Weber number We compares inertia to capillary forces and the Bond number Bo the gravity to capillary forces, cf. Eq. 5.1 to Eq. 5.3.

$$Ca = \frac{v_{fibre} \cdot \eta}{\gamma} \qquad \text{Eq. 5.1}$$

$$We = \frac{{v_{fibre}}^2 \cdot \rho \cdot r_{fibre}}{\gamma} \qquad \text{Eq. 5.2}$$

$$Bo = \frac{{r_{fibre}}^2 \cdot \rho \cdot g}{\gamma} = \left(\frac{r_{fibre}}{l_c}\right)^2 \qquad \text{Eq. 5.3}$$

Where γ, η and ρ are respectively the surface tension, the viscosity and the density of the coated liquid; v_{fibre} and r_{fibre} the wiring speed and the fibre outer radius, g the acceleration of gravity and l_c the capillary length of the deposited liquid.

The homogeneity and the thickness h_0 of the deposited coating are governed by these three adimentional numbers and are essential for the numerical prediction of the coating behaviour. To that end, predictive laws were developed based on Landau [6], Levich [10] and Derjaguin [11] models, as presented in Table 5.1.

Table 5.1 – Dip-coating deposition regimes as a function of the liquid properties [9]–[11].

Regime description	Conditions	Predictive thickness equation	
Visco-capillary	• $Ca, We << 1$ • $h_0 \ll l_c$ Gravity neglected	$h_0^{LLD} = 1{,}34.\, l_c.\, Ca^{\frac{2}{3}}$ Landau-Levich-Derjaguin equation (LLD)	Eq. 5.4
Visco-capillary and visco-inertial	• $Ca, We < 1$ • $h_0 \ll l_c$ Gravity neglected • $\sqrt{\gamma.\rho.r} > \eta$	$h_0 = \frac{1{,}34.\, r_{fibre}.\, Ca^{\frac{2}{3}}}{1 - \beta(h_0)We}$ $\beta(h_0) = \frac{1}{5}.\left(\ln\left(\frac{r_{reservoir}}{h_0}\right) - 3\right)$	Eq. 5.5
Saturation and initial divergence	• $\beta(h_0) \to 0$ • $h_0 > r_{fibre}$ • $h_0 > \frac{r_{reservoir}}{\exp(3)}$	$h_0 = \frac{r_{reservoir}}{\exp(3)}$	Eq. 5.6
Viscous boundary – Lower fibre speed	• We~1 Layer enclosing the dynamic meniscus Neglected capillary suction • $h_0 < \sqrt{\frac{\eta.h_{reservoir}}{\rho.v_{fibre}}}$	$h_0 \sim \sqrt{\frac{\eta.\, h_{reservoir}}{\rho.\, v_{fibre}}}$	Eq. 5.7
Viscous boundary – Higher fibre speed	• $We \gg 1$ No more capillary action: dragging of the layer set in motion by the fibre • $h_0 \geq \sqrt{\frac{\eta.h_{reservoir}}{\rho.v_{fibre}}}$	$h_0 = \alpha.\sqrt{\frac{\eta.\, h_{reservoir}}{\rho.\, v_{fibre}}}$ α a constant	Eq. 5.8
Expulsion droplets	• $L > L^* = \frac{r_{reservoir}}{Ca}$	Irregular and uncontrolled coating	

It should be noted that the equations presented in Table 5.1 are valid only if the Eq. 5.9 and Eq. 5.10 are satisfied. In practice, these two equations indicate that the fibre outer radius must be strictly lower to the capillary length l_c (Eq. 5.9) and that the inertia is negligible compared to

the capillary forces (Eq. 5.10). If the last condition is satisfied 5 regimes are expected, otherwise only three, as detailed in Figure 5.3.

$$\mathrm{Bo} = \left(\frac{r_{\mathrm{fibre}}}{l_c}\right)^2 \ll 1 \qquad \text{Eq. 5.9}$$

$$\eta \ll \sqrt{\gamma . \rho . r_{\mathrm{fibre}}} \qquad \text{Eq. 5.10}$$

$$l_c = \sqrt{\frac{\gamma}{\rho . g}} \qquad \text{Eq. 5.11}$$

The capillary length l_c is a length scaling factor that compares gravity to the surface tension forces, cf. Eq. 5.11. This parameter is one of the key factors impacting on the behaviour of the liquid meniscus and the different regimes described above. In order to reach a homogeneous uniform liquid coating, the divergence and expulsion droplets domains are to be avoided.

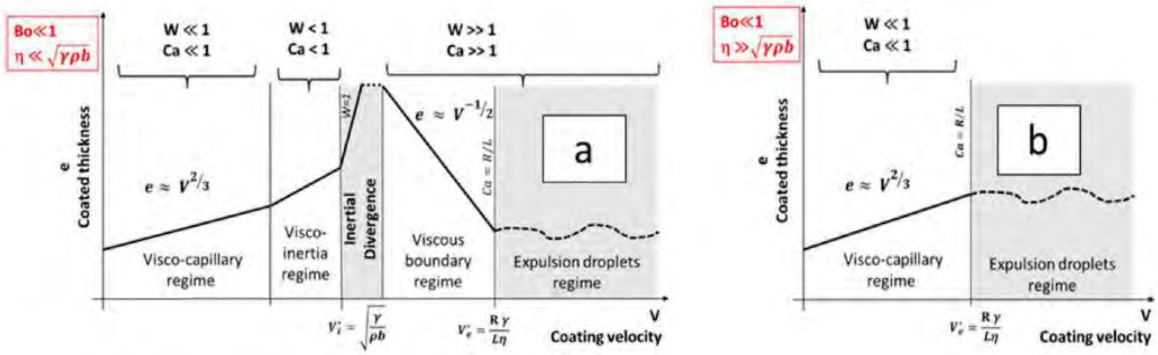

Figure 5.3 – Schematic representation of the two possible coating regimes depending on the direction of the Eq. 5.10 inequality. Reprinted with permission from Lasseugette et al. [12]*. Copyright 2013 American Chemical Society.*

The five regimes described in Table 5.1 highlight the evolution of the forces exerted on the dynamic meniscus as it grows due to the increase in fibre velocity. Initially for thin meniscus thicknesses it is possible to neglect the impact of gravity on the meniscus – for visco-capillary and visco-inertial domains – which latter has to be considered when the meniscus thickens – for saturation, initial divergence, viscous boundary and expulsion droplets domains. The viscous boundary domain appears when the dynamic meniscus thickens and is still thicker than the deposited coating. When there is no more capillary recall (We ≫ 1), only the layer of liquid that the solid has been able to set in motion leaves with the fibre. Finally, the expulsion droplet regime occurs when the meniscus at the reservoir exit gives way and drops are regularly expelled, leading to heterogeneous coatings.

Critical velocities can be determined (cf. Eq. 5.12, Eq. 5.13) to delimit the visco-inertial from the divergence regimes (V_i^*) as well as the viscous boundary from the expulsion droplets regimes (V_e^*) [10]–[12].

$$V_i^* = \sqrt{\frac{\gamma}{\rho . r_{fibre}}} \qquad \text{Eq. 5.12}$$

$$V_e^* = \frac{r_{reservoir} . \gamma}{L_{reservoir} . \eta} \qquad \text{Eq. 5.13}$$

Quéré and De Ryck [11] also proposed a single equation to relate the visco-capillary, the visco-inertial, the divergence and the saturation regimes (Eq. 5.5). This equation is based on the mathematical connection of dynamic and static menisci. The dynamic meniscus profile is limited by the flow geometry as the meniscus width cannot exceed the reservoir radius. Their development stands as long as the coating is strictly lower than $\frac{r_{reservoir}}{\exp(3)}$ – value for which $\beta(h_0) \to 0$. This last limitation is based on the appearance of the divergence when the Weber number is increased and that $\beta(h_0)We \to 1$. When the saturation is reached, the deposited thickness only depends on the reservoir aperture. The Eq. 5.6 describing the thickness deposited in the saturation regime is however a rough approximation of the reality, as the initial hypotheses – existence of a static meniscus and $h_0 < r_{fibre}$ – are no longer verified.

If the visco-capillary and visco-inertial domains are mostly studied in order to achieve a thin coating on fibres, the viscous boundary regime (cf. Eq. 5.8) may lead to thin and controlled coatings. The only additional constraint is the need to monitor and to control the liquid bath height, to avoid any depletion of the reservoir and thus a modification of the coating thickness.

5.3.2 Complex surfactant-based solutions

The various laws presented in Section 5.3.1 are only applicable for linear and homogeneous solutions. However, the fluids used in the industry are rarely similar to such simple liquids and the previous ideal models must be modified according to the specific properties of the complex fluids considered. An emphasis will be made on surfactant and colloidal solutions, as well as emulsions, in the following section.

5.3.2.1 Surfactant solutions

In presence of surfactants, the LLD law previously described undergoes some deviations, as reviewed by Rio et al. (2017) [6]. Such a modification of the LLD is caused by the incorporation of additional terms in the no-stress boundary condition at the air liquid-air interface, cf. Eq. 5.14. Where u_z is the vertical speed field, x the horizontal direction perpendicular to the fibre, h(z) the interface profile, μ* the surface viscosity, E and G the dilatational and shear elasticities.

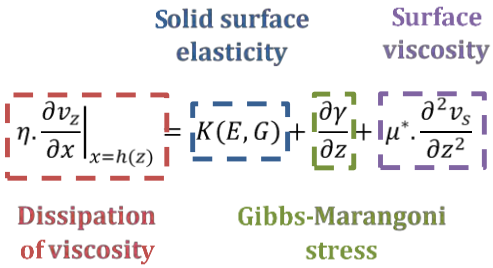

Eq. 5.14

The **solid surface elasticity** depends on both the dilatational and shear surface elasticities. Such a stress is reported for complex objects (e.g. polymers) at the interface. The **Gibbs-Marangoni stress** for its part occurs due to a surface tension gradient in the surfactant solution, caused for example by surface diffusion, exchanges between the surface and the bulk or temperature gradient leading to evaporation. Soluble and insoluble surfactants have to be distinguished because an additional term is to be considered for the determination of the surface concentration of active objects, which incorporates the flow of soluble surfactants between the bath volume and its interface with the air. Experimentally, both types of surfactant follow the LLD law, within a thickness factor α, ranging between 1 à $4^{\frac{2}{3}}$ [10]. This thickening factor is dependent of the surfactant concentration in the solution, cf. Eq. 5.15. Where Ma is the Marangoni number (cf. Eq. 5.16), c is the surfactant volume concentration, v^* an intrinsic velocity depending on the surfactant, Γ_{max} the surface excess concentration, γ and η the solution surface tension and viscosity of the solution.

$$\alpha \approx \left(\frac{4\frac{Ma\Gamma_{max}\gamma}{v^*\eta c} + 2r_{fibre}}{\frac{Ma\Gamma_{max}\gamma}{v^*\eta c} + 2r_{fibre}} \right)^{\frac{2}{3}} \qquad \text{Eq. 5.15}$$

$$Ma = -\frac{\Gamma_{max}}{\gamma}\left(\frac{\partial \gamma}{\partial \Gamma_{max}}\right) \qquad \text{Eq. 5.16}$$

Finally, **surface viscosity stress** can be caused by exchanges between the surface and the volume or because of molecular friction. The viscosity of the film drawn varies from that of the liquid bath, as described by Boussinesq number Bqs, d_{Bqs} being a characteristic length of the system. This stress is usually negligible compared to the Gibbs-Marangoni stress, but may become significant for high surfactant concentrations. The contribution of each of these additional stresses on the modification of the LLD is reported in Table 5.2.

Table 5.2 – Summary table of interface conditions and their impact on the thickness of a coating on a fibre [6], [10]*.*

Description	Conditions	Predicted thickness
Linear fluids	• $\eta.\frac{\partial v_z}{\partial x}\Big\|_{x=h(z)} = 0$	See Table 5.1
Rigid limit	• $\eta.\frac{\partial v_z}{\partial x}\Big\|_{x=h(z)} < \left(K(E,G), \frac{\partial \gamma}{\partial z}, \mu^*.\frac{\partial^2 v_s}{\partial z^2}\right)$	$h_0 \sim 4^{\frac{2}{3}}.h_0^{LLD}$ $h_0 \sim l_e.El^{\frac{4}{7}}$
Effect of the solid surface elasticity	• $K(E,G)$ not neglected	$l_e = \sqrt{\frac{k_B}{\rho.g}}$ and $El = \frac{\eta.v_f.{l_e}^2}{k_B}$
Effect of the Gibbs-Marangoni elasticity	• Insoluble surfactants *No diffusion* *High Marangoni number and/or low fibre speed* • Soluble surfactants	$h_0 \sim Ca^{\frac{2}{3}} > h_0^{LLD}$
Effect of the surface viscosity	• Non-negligible Marangoni effect • $Bqs = \frac{\eta_{surface}}{\eta.d_{Bq}}$	$h_0 \sim l_c.\alpha.Ca^{\frac{2}{3}}$

Quéré and de Ryck (1998) [10], [11] reported that solutions with a low surfactant concentration ($C_{ST} < 0.1CMC$) followed the classic LLD law, because the surface active molecules were too few

to significantly impact on the overall volume of the solution. When the surfactant concentration is increased above 0.1CMC, an increasing thickening factor α is observed. This factor increases with the surfactant concentration until it becomes constant. The authors indicated that further increasing the surfactant concentration (C_{ST}~37.5CMC) of the liquid bath led back to about the predicted LLD thickness ($\alpha \rightarrow 1$), as surfactant molecules are sufficiently numerous to avoid a concentration gradient during fibre coating.

5.3.2.2 Colloidal suspensions

Colosqui et al. (2013) [13] developed a numerical and analytical model that proved that the fibre winding determines the thickness of a colloidal coating, as well as its dependence of the particle entrainment in the coating. As a matter of fact, they evidenced that the colloidal particle can be drawn into the liquid coating only if the thickness of the film is greater than the diameter of the suspended particle.

Gans et al. (2018) [13] subsequently proved experimentally the existence of different coating regimes on a flat substrate as a function of the fibre velocity – usually described by the capillary number Ca – and the number and size of the colloidal particles, cf. Figure 5.4. This work was based on the assumptions that:

- The colloidal particles are big enough to overlook both the Brownian motion and the colloidal forces ($d_{colloid} < 100$ µm).
- The colloidal solution does not undergo any evaporation and is of neutral buoyancy to consider the density of the solution identical to the one of both the continuous and dispersed phases.
- The coating is strictly thinner than the substrate width.

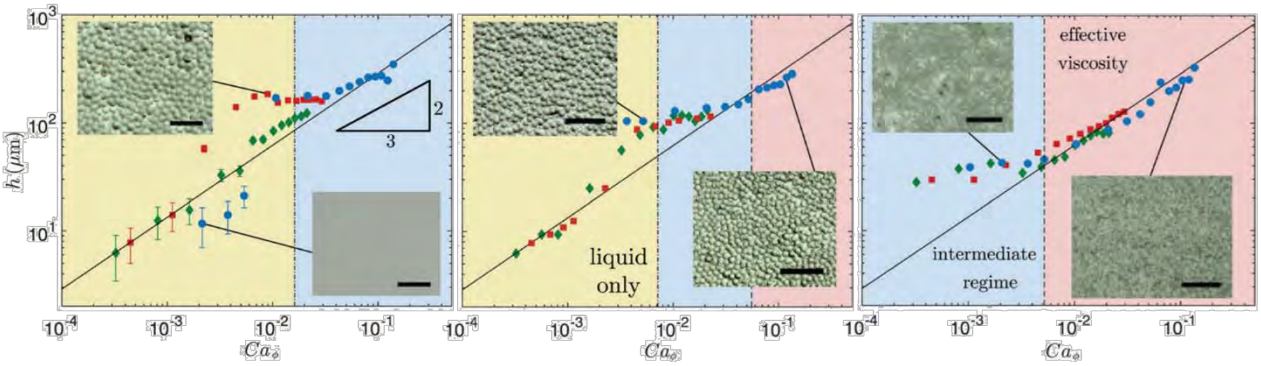

$d_{colloid}$ = 250 µm $d_{colloid}$ = 140 µm $d_{colloid}$ = 40 µm

Figure 5.4 – Thickness of colloidal coating as a function of the capillary number for 10% (♦), 18% (■) and 41% (●) volume fraction of particles. Adapted with permission from Gans et al. (2019) [13].

The first observed regime (**yellow** – left) consists of a homogeneous and uniform deposition of the interstitial liquid only, for low fibre speed ranges. Indeed, the thickness of the coating is not sufficient to allow the suspended particles to exit the meniscus, as predicted by Colosqui et al. (2013) [13]. This behaviour is observed up to a critical capillary number where the viscous force applied to the particle clusters neutralises the capillary forces constraining the particles in the bath, cf. Eq. 5.17.

$$\mathrm{Ca} < 0.6\mathrm{Bo}^{\frac{3}{4}} \qquad \text{Eq. 5.17}$$

The second regime (**blue** – middle) is a deposition on the substrate of the interstitial liquid containing heterogeneous particle clusters. The number of clusters increases with the substrate withdrawal speed. The transition with the third regime (**red** – right) occurs for a second capillary number threshold (cf. Eq. 5.18), which considers the viscosity of the whole suspension and no longer the interstitial liquid alone according to the Zarraga model, cf. Eq. 5.19. The colloidal suspension is then fully and homogeneously dragged into the coating. Its thicknesses experimentally follow the Landau-Levich-Derjaguin (LLD) equations described in Eq. 5.4 for pure liquids. It should be noted that, for dense suspensions, the second capillary threshold usually is experimentally higher than theoretically predicted, due to the ability of particles to deform the interface in the meniscus when the volume fraction of the suspension is large.

$$\mathrm{Ca}_{\phi} > 3.1\mathrm{Bo}^{\frac{3}{4}} \qquad \text{Eq. 5.18}$$

$$\mathrm{Ca}_{\phi} = \frac{\eta v_{\mathrm{fibre}} \exp(-2.34\phi)}{\gamma\left(1 - \frac{\phi}{\phi_m}\right)^3} \qquad \text{Eq. 5.19}$$

Where ϕ and ϕ_m are respectively the volume fraction and the maximum filling ratio of the particle stack in the suspension. The Bond number used by Gans et al. to determine both Eq. 5.17 and Eq. 5.18 is slightly different than defined in Eq. 5.3. Indeed, fibre radius was replaced by the particle radius in the equation, to incorporate the condition that the liquid film must be thicker than the particle radius to be drawn into the film, cf. Eq. 5.20.

$$Bo = \sqrt{\frac{d_{colloid}}{2l_c}} \qquad \text{Eq. 5.20}$$

Additional work have been carried out on the evaporation of interstitial fluid from the dynamic meniscus when coating colloidal suspensions [14], [15], [16]. This evaporation from colloidal suspensions may lead to some further variations from the classic LLD presented in Table 5.1. Berteloot et al. (2013) [14] evidenced two regimes: a low-speed regime has been evidenced where an evaporation at the solid-liquid contact line takes place, leading to a thinner coating than predicted by the LLD. The second regime of higher speeds allows to find the values foreseen by the LLD. It should be noted that the particle diffusion was not considered in this work as the minimum particle diffusion distance (ca. 250 nm) was strictly higher than the film thickness, the colloid dimensions and the capillary length l_c considered in their work.

Berteloot et al. (2013) [14] suggested the equations Eq. 5.21 and Eq. 5.22 to describe the thickness of a coating subject to evaporation of its interstitial liquid, depending on the speed regimes. For higher velocities the LLD equation is modified in order to include the influence of concentration effects of colloid particles during film deposition.

$$h_{LV} \propto \frac{\phi_{colloid}}{\phi_c} . \frac{{J_0}^2}{4.\theta_s . {v_{substrate}}^2} \qquad \text{Eq. 5.21}$$

$$h_{HV} \propto \frac{\phi_0}{\phi_c} . \frac{J_0}{\sqrt{x_\infty}} . \frac{x_\infty}{v_{substrate}} \qquad \text{Eq. 5.22}$$

$\phi_{colloid}$, ϕ_c and ϕ_0 are respectively the colloid at the stagnation surface, in the deposited film and in the liquid bath, J_0 the evaporative flux, θ_s the static meniscus angle and $x_\infty \sim 2.l_c$ its size.

5.3.2.3 Emulsions

As a reminder an emulsion is an amphiphilic colloidal system formed by two immiscible phases – aqueous and organic – randomly dispersed in suspension. Such a mixture is thermodynamically unstable and is supplemented by a surfactant which stabilises the two antagonistic phases and slows down their separation kinetics.

To our knowledge the dip-coating of emulsions on a fibre has only been studied by Quéré and De Ryck [10], [11]. These authors hypothesise two phenomena may occur when coating a cylindrical substrate with an emulsion by dip-coating, as presented in Figure 5.5. The coating

can either be of identical composition to the liquid reservoir or depleted in the discontinuous phase, as discussed for the colloid suspensions in Section 5.3.2.2.

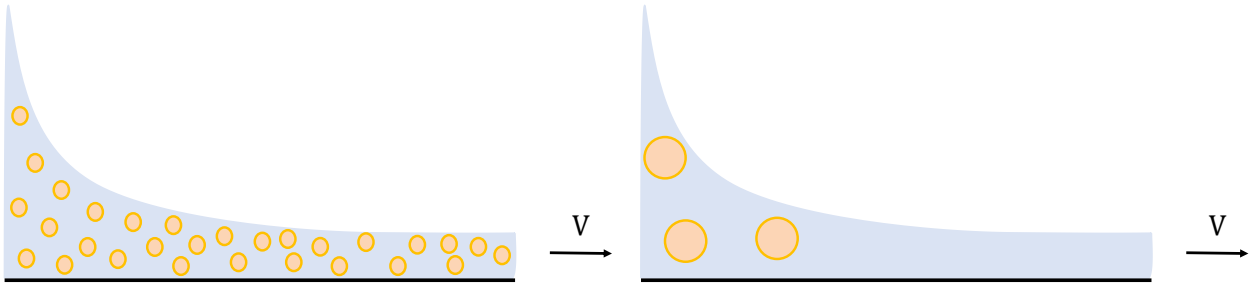

Figure 5.5 – Schematic representation of the possible situations when coating a substrate with an emulsion: entrainment of a film (left) of identical composition to the bath and (right) depleted in discontinuous phase.

Experiments evidenced that the O/W emulsion deposited on the fibre did not follow the LLD for various tested oil compositions. Indeed, at low oil concentrations the actual thickness is less than that predicted by the LLD and is independent of the fibre speed. For higher oil concentrations, the results follow the LLD which might indicate a demixing of the emulsion. The authors confirmed an oil enrichment has taken place during the coating of concentrated emulsions, confirming the last statement.

Quéré and de Ryck developed a capture model to describe the atypical behaviour of the coated emulsions, cf. Eq. 5.23. This law assumes that the deposited thickness is dependent on the volume fraction ϕ and the radius $\frac{d_{colloid}}{2}$ of the droplets of the dispersed phase.

$$h_0 = 2.\phi.\frac{d_{colloid}}{2} = \phi.d_{colloid} \qquad \text{Eq. 5.23}$$

The authors however pointed out that this model assumes that the adhesion of the oil droplets can be ensured by the Van der Waals forces between the oil and the fibre. Indeed, these forces have range (ca. 100 nm) smaller than the particle diameter, which allows the oil capture to occur by contact with the fibre. Plus, this captured oil droplet can be easily deformed inducing a good adhesion and a good resistance to the viscous force in the dynamic meniscus, allowing the particle to remain in the thin-film. The authors also neglected the time dependence to establish the Eq. 5.23. If the time spent by the emulsion on the surface of the fibre is long enough for the particles to move through Brownian motion over a distance greater than the particle diameter, then the latter equation must be corrected to incorporate a time dependence.

5.4 Simulation of hollow fibre coating - applications to microemulsions on MF-PES (MicroPES™) and UF-PS (Zeeweed™) hollow-fibres

The previous state of art regarding fibre coating is, in our work, adapted to the simulation of a microemulsion. The important properties of the microemulsion to be considered in the numerical simulation are described in Table 5.3.

Table 5.3– Physico-chemical parameters of the microemulsion considered in this simulation.

Density ($kg.m^{-3}$)	Viscosity (mPa.s)	Surface tension ($mN.m^{-1}$)	Capillary length (mm)
1024 ± 2	7 ± 2	30.1 ± 0.2	1.76

In the following simulation, two commercial hollow-fibre membranes have been considered: the Type TF10 MicroPES™ (3M – previously Membrana) and the Zeeweed™ 500S (General Electrics – previously Suez) fibres. The membrane data sheets are available in Appendix 5. The geometrical properties used for all the analytical determination are reported in Table 5.4.

Table 5.4– Geometric parameters of the fibres considered in this simulation.

Hollow fibre	Membrane type	Outer radius (µm)	Inner radius (µm)	Pore radius (µm)
MicroPES™	MF	250	150	0.25
Zeeweed™	UF	800	450	0.036

The MicroPES™ is a microfiltration polyethersulfone (PES) membrane, while the Zeeweed™ is an ultrafiltration hydrophilic polyvinylidene fluoride (PVDF) membrane. These two membranes were chosen to compare the coating behaviour based on the initial porosity of the substrate, but also due to their composition. Indeed, on the one hand PES allows for a photografting which is of high interest to create a permanent and strong coating on the substrate surface. On the other hand, PVDF is one of the most used polymers for the synthesis of membranes for water treatment and is of high interest in the scope of our study [17].

5.4.1 Operating conditions for the control of the deposited coating

The following sections will describe the critical conditions to be considered when dip-coating a fibre with a microemulsion in order to obtain a homogeneous controlled thin-film. A particular attention will be given to the modification of the well-known equations described in the state of art in order to be applied to our simulation.

5.4.1.1 Applicability of the LLD-law to the studied systems

As detailed in Section 5.3.1, two main coating behaviours are detailed in the literature. In order to precisely define the laws governing our system, the Bond number must be compared to the unity on one hand (Eq. 5.9), while the viscosity of the coating must be compared to the square root of the fibre radius multiplied by the surface tension and density of the coated liquid on the other hand (Eq. 5.10) . The results presented in Table 5.5 indicate that for both fibres our system exhibits a Bond number lower than the unity and a viscosity lower than the square-root of the fibre radius multiplied by the surface tension and density of the coated microemulsion.

Therefore, five different coating behaviours will be encountered when increasing the fibre speed, cf. Figure 5.3. Out of those five different domains only the visco-capillary and the visco-inertial regimes will be discussed in this present work. Although the viscous boundary regime may allow for a thin, controlled and homogeneous deposit, it is however not possible to predict the coating thickness due to the failure to predict the α-constant. An experimental determination of this constant would overcome this limitation, but could not be achieved during this thesis work.

Table 5.5 – Bond number and critical value for the determination of the dip-coating domains for the two hollow fibre studied.

Hollow fibre	Bond number	$\sqrt{\gamma . \rho . r_{fibre}}$ (Pa.s)
MicroPES™	0.020 << 1	$\eta << 8.1\ 10^{-2}$
Zeeweed™	0.207 << 1	$\eta << 15.9\ 10^{-2}$

In order to reach the visco-capillary and the visco-inertial regimes, the capillary and Weber numbers must both be strictly lower than unity. For our simulation, we will consider the visco-capillary and visco-inertial governing equation (cf. Eq. 5.5) to be valid as long as the capillary and Weber numbers are below 0.9, to avoid any disruption due to the inertial

divergence regime appearing when approaching We~1. Using the physico-chemical parameters of the microemulsion listed in Table 5.3, the maximum fibre speed to remain in the visco-capillary domain ($We < 0.9$) has been established to 19.8 m.min^{-1}.

To our knowledge, no work has been carried out to the dip-coating of microemulsions: only a few theoretical researches have been performed on the study of emulsions by Quéré, as presented before. Therefore, to predict the behaviour of our coating, some assumptions have to be made to apply the models presented in the previous sections.

Our main assumption is that this fibre speed limitations for emulsions, detailed in Eq. 5.17 and in Eq. 5.18, do not apply to microemulsions, and more specifically to bicontinuous microemulsions. Indeed, all the phenomena and models describing the colloidal and emulsified systems include the size of the suspension as a critical factor for the homogeneity of the system. The reason is that those systems involve the entrainment of micrometric objects in a micrometric thin-film. If the coating is thinner than the suspension size, a segregation is observed for both cases. The dip-coating of emulsions also proved – for a concentrated enough system – a modification of the composition as a function of the fibre velocity, probably resulting from a shearing of the droplets in the liquid meniscus. Because microemulsions are of nanometric size, we hypothesise that the previous behaviour regarding the thickness and the composition will not occur due to the small size of the dispersed objects compared to the coating. For this reason, we will therefore consider the microemulsions to follow the laws described in Table 5.1 for simple and linear liquids. Finally, because the Synperonic™ A11 (CMC = 72 ppm) and the Tergitol™ 15-S-12 (CMC = 104 ppm) each represents 10.64 wt.% of the system composition, we do not expect a thickening factor to impact on the laws described in Table 5.1, their quantity being too important (cf. Section 5.3.2.1).

5.4.1.2 System resolution for the determination of the deposited thickness

Based on Eq. 5.5 and on the definition of the capillary and Weber numbers (cf. Eq. 5.1 and Eq. 5.2) a second order equation is obtained. Using the system in Eq. 5.24 to Eq. 5.26, the deposited thickness can be calculated as a function of the fibre velocity and the liquid reservoir radius.

$$A.\,v_{fibre}{}^{2} + B.\,v_{fibre}{}^{\frac{2}{3}} - h_0 = 0 \qquad \text{Eq. 5.24}$$

$$A = \frac{h_0}{5}\left[\ln\left(\frac{r_{reservoir}}{h_0}\right) - 3\right] \qquad \text{Eq. 5.25}$$

$$B = 1{,}34.(r_{fibre} + h_0).\left(\frac{\eta}{\gamma}\right)^{\frac{2}{3}} \qquad \text{Eq. 5.26}$$

The importance of the reservoir radius is linked to the achievable height and width of the meniscus formed during the passing of the fibre. This radius is the limiting factor to the growth of the meniscus when increasing the fibre speed. For this reason, in the present document we will refer to the wall distance between the outer surface of the fibre to the tank wall as the reservoir radius. The effective tank radius to be considered when designing the installation will have to include the external diameter of the hollow-fibre to accommodate the present numerical simulation. When the liquid reservoir is increased, the meniscus grows and so does the deposited thickness [11]. We however do not expect the meniscus to increase indefinitely with the reservoir radius. We will therefore consider that once the maximum meniscus height is achieved, so is its maximum width. Above an upper reservoir radius boundary, a maximum $r_{reservoir}$ will be reached in Eq. 5.25. Tang and Cheng [18] determined this upper bound to be $r_{reservoir} \approx 1.85 l_c$. For the investigated microemulsion coating, the upper boundary was estimated to 3.3 mm.

Our work focuses on the determination of the microemulsion thickness deposited on the MicroPES™ and Zeeweed™ hollow-fibres. The specificity of our work lies in the parameters considered in order to carry out our simulations : if most of the work presented in the literature focus on the fibre speed none presented the reservoir radius impact, even though its impact has been proved by Quéré et al. [9], [11]. We therefore propose to study both the fibre speed and the reservoir radius for the determination of the coating thickness for the operating conditions determined previously namely a fibre speed range of [0-19.8] $m.min^{-1}$ and a reservoir radius (excluding the fibre radius) from 0.1 to 3.3 mm, as detailed in section 5.4.1.1.

Based on the equations Eq. 5.24 to Eq. 5.26 and to the physico-chemical and geometrical parameters presented in Table 5.3 and Table 5.4, the thickness of the coating has been simulated and is presented in Figure 5.6. These graphs highlight the huge impact of the reservoir radius, even though this factor is usually overlooked in simulations. Decreasing the reservoir radius below the capillary length – and thus the meniscus width – leads to the apparition of a divergence and saturation regimes, which are independent of the fibre speed (cf. Eq. 5.6).

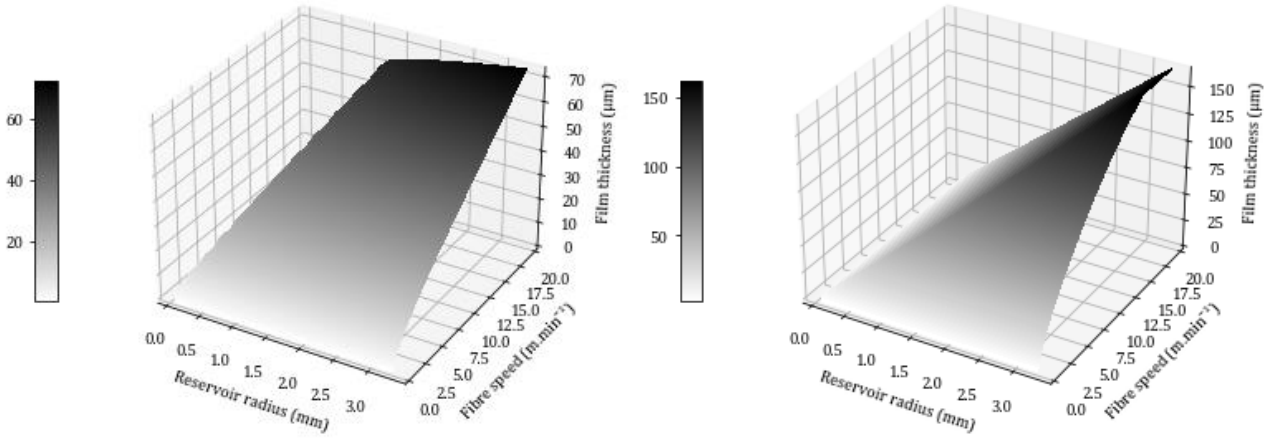

Figure 5.6 – Evolution of the coating thickness based on the fibre speed and the reservoir radius for the MicroPES™ (left) and the Zeeweed™ (right) hollow-fibres. The reservoir radius does not include the fibre radius.

Increasing the reservoir radius towards $1.85l_c = 3.3$ mm leads to the visco-capillary and visco-inertial classical equations, which are dependent on the fibre velocity (Eq. 5.4 and Eq. 5.5). The saturation regime also appears earlier for bigger fibre radii (Zeeweed™) as the deposited thickness is thicker and becomes thicker than the dynamic meniscus, leading to the divergence regime. One must keep in mind that the thicknesses presented in the previous figure for the saturation regime is based on the equation Eq. 5.6, which only approximates the real coating thickness.

This reservoir radius will impact the deposited thickness up to a value of $1.85l_c$ – in our case 3.3 mm – as the meniscus will increase with the tank radius. Above such a value, the meniscus will not thicken anymore and the tank radius considered in the calculation will cap at $1.85l_c$, no matter the actual tank radius. For these reasons we performed our numerical simulation in the visco-inertial domain: $\mathrm{We}, \mathrm{Ca} < 0.9 \leftrightarrow v \in [0; 19.8]$ m. min^{-1} and $r_{reservoir} \in [0.1; 3.3]$ mm. For these operating conditions, the coating thickness on the MicroPES™ and Zeeweed™ fibres varies respectively from 5 to 72 µm and from 58 to 164 µm, as a function of the fibre speed and of the reservoir radius. In order to reach the lowest thicknesses, we must work with the smallest fibre and reservoir radii. It therefore seems more challenging to coat thin-films ($h_0 < 50$ µm) on thicker supporting fibres. In our case, to achieve such thicknesses, we have to operate with a fibre speed of less than 2.6 m.min^{-1}, whereas fibre speeds up to 13.4 m.min^{-1} can be used with the MicroPES™ fibre.

Intermediate conclusions:

We evidenced that in fact, two factors delimit the visco-capillary and visco-inertial regimes from the divergence and saturation regimes: the meniscus radius – which can be impacted by the reservoir radius up to a certain radius – and the Weber number – which compares the impact of the inertia compared to the capillarity forces. Both factors should be considered when predicting the deposited coating thickness on the surface of a fibre. If the Weber number will always be impacting and will vary with the fibre speed, it is not the case for the reservoir radius.

This factor will impact up to a value of $1.85l_c$ – in our case 3.3 mm – until the meniscus does not thicken with the tank radius anymore. Our numerical simulation focused on the visco-inertial domain and we identified an operating fibre speed and reservoir radius range: $We, Ca < 0.9 \leftrightarrow v \in [0; 19.8]$ m. min^{-1} and $r_{reservoir} \in [0.1; 3.3]$ mm. These fibre speeds are however not optimal for industrial application. In order to be able to work at higher speeds while maintaining a homogeneous, controlled coating of low thickness, one might consider working in the viscous boundary regime where the coating thickness is only dependent on the reservoir liquid height and the fibre speed. This regime was not simulated in this work as the constant α in Eq. 5.8 is to be determined experimentally, but could not be performed during this thesis.

5.4.2 Photopolymerisation of the monomer microemulsified coating

After being coated on the fibre, the monomer solution undergoes UV-irradiation in order to initiate the polymerisation and to give rise to a solid coating. The coating module consists of two UVA-PRINT LE lamps (Hoenle – Germany) arranged at 90° to each other to ensure an even distribution of the UV radiation. Indeed, the elliptical mirrors in the lamp surrounding the fibre possess a “dead zone” where only 70% of the emitted intensity is actually perceived, near the module door and the aperture shutter. This occurrence of such a zone prevents an equivalent UV coverage around the entire circumference of the hollow-fibre.

In order to estimate the photopolymerisation process duration in our dip-coating module, we investigated the behaviour of a 100 µm-thick flat film irradiated by a similar polychromatic UV TQ150 lamp (Hoenle – Germany). The UV-spectra of both polychromatic lamps is presented in Appendix 2.

- **Photopolymerisation of the model microemulsified system under the TQ150 lamp**

First, the UV doses received by the monomer system – 4 cm from the lamp – depending on the exposure time under the TQ150 lamp has been determined using 3 UV sensors (Hoenle – Germany): UVA, UVB and UVC. We evidenced that, for all UV types, the lamp first undergoes a warm-up period of 100 ± 25 s – during which only IR radiations are emitted – and then releases a constant UV intensity. The following equations Eq. 5.27 and Eq. 5.28 depict the measured UV doses q received by the sensors depending on the exposition time Δt_{UV}, including the warm-up period. It should be noted that based on the UV-spectrum of the microemulsion, the solution does not absorb the UV radiations above 310 nm and 390 nm, respectively without and with the photoinitiator, cf. Appendix 3. Therefore, we conclude that the UVA do not participate in the formation of radicals and thus will be overlooked for the remaining study.

$$q_{UVB}^{TQ} = 35{,}48.\,\Delta t_{UV} - 2567{,}63 \qquad \text{Eq. 5.27}$$

$$q_{UVC}^{TQ} = 19{,}50.\,\Delta t_{UV} - 1606{,}18 \qquad \text{Eq. 5.28}$$

We then simulated the irradiation of the liquid coating deposited on the fibre using the UVA-Print LE by irradiating a 100 µm-thick flat film located 4 cm away from the TQ150 lamp. It is important to note that varying the film thickness will most probably impact on the polymerisation duration. Indeed, the UV radiations will penetrate more into the depth of the film, as indicated by the Beer-Lambert equation Eq. 5.29. A thinner film may allow for a quicker initiation of the most distant radicals from the lamp, and *vice versa* for thicker films. Due to technical limitations, we only tested the 100 µm thickness. Because thin-film are wanted for membrane coating, we considered the 100 µm-thin film polymerisation duration to be the longest possible: the worst polymerisation conversion.

$$\text{Absorbance} = \varepsilon[C]l_{cuve} = \varepsilon' l_{cuve} \qquad \text{Eq. 5.29}$$

The conversion of this 100 µm-thin polymer for different polymerisation duration was studied using an ATR-IRTF analysis. The conversion of the acrylate monomer was achieved by monitoring the decrease of the –C=C- peak at 817 cm^{-1}, cf. Figure 5.7.

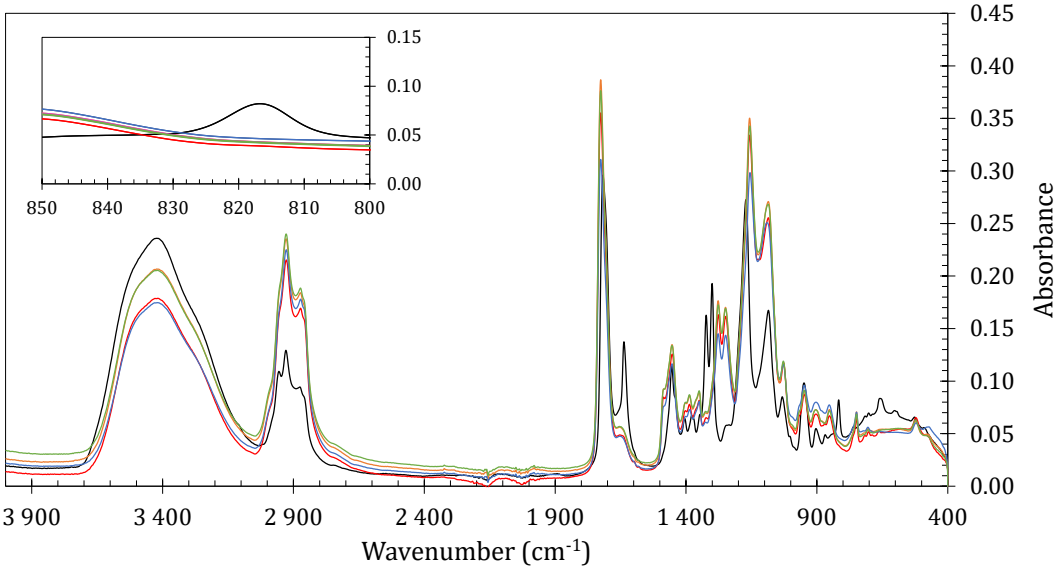

*Figure 5.7 – ATR-FTIR spectra of the (21:23:56)$_{62:19:19}$ microemulsion (**black**) before irradiation and after (**red**) 2 min, (**orange**) 4 min, (**blue**) 5 min and (**green**) 6 min under the TQ150 polychromatic lamp.*

We observe no further decrease of this peak after 2 minutes of exposure under the TQ150 polychromatic lamp and thus concluded that the polymer film is completely polymerised for a UV-exposure of 2 min under the TQ150 UV lamp (including the lamp warm-up period).

- **Extrapolation to the photopolymerisation on fibres using the coating module**

The UVA-PRINT LE irradiance I_{UV} (W.m^{-2}) as a function of the lamp power percentage P(%) has been determined by our research team beforehand [7], cf. Eq. 5.30 and Eq. 5.31. The Eq. 5.32 allows us to determine the doses q_{UV} (J.m^{-2}) received by the sample depending on the irradiation time Δt (s).

$$I_{UVB}^{LE} = 1561{,}1.\,P(\%) + 331{,}8 \qquad \text{Eq. 5.30}$$

$$I_{UVC}^{LE} = 2558{,}0.\,P(\%) + 92{,}0 \qquad \text{Eq. 5.31}$$

$$q_{UV} = \int_{t=0}^{\Delta t} I_{UV}\,dt = I_{UV}\Delta t \qquad \text{Eq. 5.32}$$

Combining these three equations allows us to determine the duration of the polymerisation of a 100 µm thick microemulsion film under the UVA-PRINT LE lamp, as a function of the lamp power P(%), cf. Eq. 5.33 and Eq. 5.34.

$$\Delta t_{UVB}^{LE} = \frac{q_{UVB}^{TQ}}{I_{UVB}^{LE}} = \frac{35{,}48.\,\Delta t_{UV} - 2567{,}63}{1561{,}1.\,P(\%) + 331{,}8} \qquad \text{Eq. 5.33}$$

$$\Delta t_{UVC}^{LE} = \frac{q_{UVC}^{TQ}}{I_{UVC}^{LE}} = \frac{19{,}50.\,\Delta t_{UV} - 1606{,}18}{2558{,}0.\,P(\%) + 92{,}0} \qquad \text{Eq. 5.34}$$

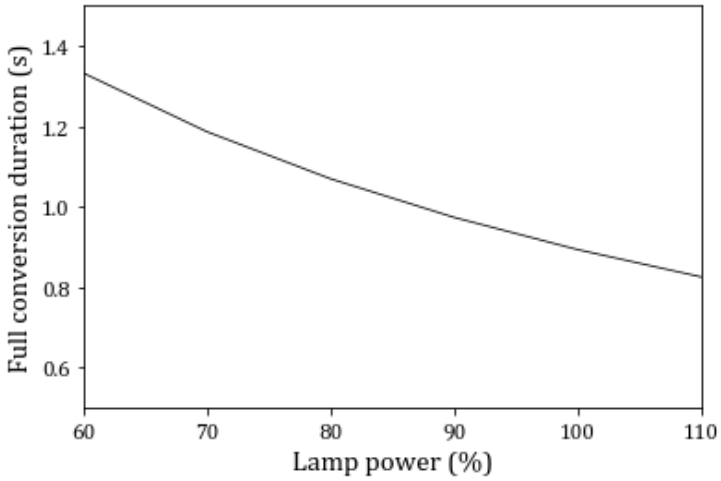

Figure 5.8 – Evolution of the full conversion time depending on the UVA-PRINT LE power.

The UVA-PRINT LE lamp power can be varied from 60 to 110% on the laboratory module. For each lamp power, we considered the full conversion of the microemulsion reached when both Δt_{UV}^{LE} where achieved. To determine the full conversion duration for each lamp power in Figure 5.8, we therefore decided to consider the longest duration, i.e. Δt_{UVB}^{LE} in Eq. 5.33.

Intermediate conclusions:

This sub-section allowed us to simulate the maximum polymerisation time achievable when coating hollow-fibre with the laboratory module. It should be noted that this duration is an estimated maximum value for a 100 µm-thick flat coating. When dip-coating the fibres, this full conversion time might be even shorter, due to the decrease of the deposit thickness allowing a better UV penetration through the monomer liquid.

To avoid a fibre melting while ensuring a short polymerisation process, we decided to consider a lamp power of 80% for the remainder of this numerical simulation. The following simulation will be carried out for a lamp power of 80%, for which the maximum time required for the total polymerisation of the 100 µm-thick microemulsion has been estimated to be 1.1 s.

5.4.3 Coating perturbation after deposition on the fibre

Once the fibre out of the liquid bath, the deposited coating may undergo different destabilisation phenomena before its polymerisation, such as dewetting or liquid penetration in the fibre pores. To experimentally ensure the continuity and the homogeneity of the coating, these phenomena domains will be identified beforehand, for various fibre speeds and various reservoir radii. For this project, we decided to set the liquid bath right below the lamp so that the polymerisation would take place right after the fibre coating. This choice was made in order to limit the occurrence of instabilities as much as possible, as detailed in the next sub-sections.

5.4.3.1 Plateau-Rayleigh instability

The Plateau-Rayleigh instability, due to the fibre geometry, is one of the main problems resulting in the coating heterogeneity after the fibre coating. Under the effect of the surface tension at the air-liquid interface, the film surface will create some undulations in order to decrease its surface energy. This will lead to a breakdown of the uniform into a succession of droplets forming fluid droplets on the fibre, as presented in Figure 5.9 [9], [10], [19].

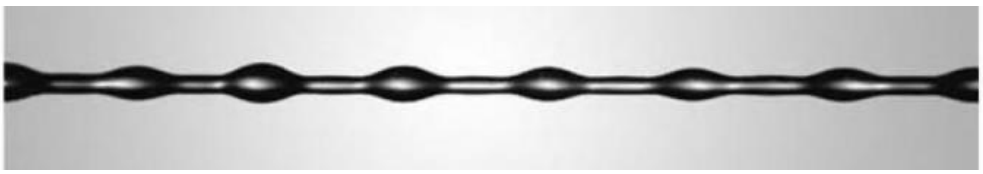

Figure 5.9 – Plateau-Rayleigh instability on a fibre surface. Reproduced with permission from Springer Nature from Lorenceau et al. [19].

5.4.3.1.1 Plateau-Rayleigh instability domain - Upper boundary

The upper boundary of the Plateau-Rayleigh instability domain can be determined so as to avoid the coating dewetting (cf. Eq. 5.35) while remaining in the visco-capillary domain. For a cylindrical fibre, the instability appears as soon as the distance between the droplets is higher than the coating perimeter on the fibre. Hence, the deposition of a minimum coating thickness h_0^* (cf. Eq. 5.25) will prevent the Plateau-Rayleigh instability.

$$h_0^* \geq r_{fibre}.(\sqrt{2}-1) \qquad \text{Eq. 5.35}$$

Based on the formula Eq. 5.35, the minimum coating thickness to be deposited on the MicroPES™ and on the Zeeweed™ hollow-fibres to avoid the Plateau-Rayleigh instability are respectively 104 µm and 331 µm. However, the deposited thickness we predicted assuming

linear fluids never reached such high thicknesses, for the considered operating conditions regarding the radius of the reservoir and the fibre speed. If the liquid is not solidified quickly enough, the Plateau-Rayleigh instability could therefore appear on both fibres in our investigated ranges: fibre speed range of [0-19.8] $m.min^{-1}$ and a reservoir radius (excluding the fibre radius) from 0.1 to 3.3 mm.

5.4.3.1.2 Plateau-Rayleigh instability domain - Lower boundary

We highlighted that our microemulsion coatings are subjected to the occurrence of Plateau-Rayleigh instability, due to their low thickness, across the whole range of operating conditions considered. This instability will occur after the coating has been deposited on the fibre for a characteristic duration τ_{PR}, cf. Eq. 5.36. In order to obtain thin and homogeneous films, the occurrence of the Plateau-Rayleigh instability has to be dynamically avoided and the coating must therefore solidify before the instability development.

$$\tau_{PR} = 12.\frac{\eta.{r_{fibre}}^4}{\gamma.{h_0}^3} \qquad \text{Eq. 5.36}$$

Based on the coating thickness determined for each fibre velocity and reservoir radius, using the equation system Eq. 5.24 to Eq. 5.26, it is possible to determine the characteristic time related to the occurrence of the Plateau-Rayleigh instability of each fibre speed and reservoir radius. If the thin film deposited on the surface of the fibre is able to polymerise before reaching this critical time τ_{PR}, then the Plateau-Rayleigh instability can be avoided. As a reminder, the full conversion of a 100 µm-thick coating has been estimated to 1.1 s at 80% in section 5.4.2.

In order to maintain a homogeneous coating, the duration for the instability development τ_{PR} must always remain longer than the coating polymerisation duration, which is 1.1s in our case. Based on Eq. 5.36, we then determined the maximum coating thickness h_0 to be deposited on the fibre, so that the characteristic duration τ_{PR} will always remain lower to 1.1s, for both fibres. Coatings thinner than 22 µm on the MicroPES™ and 102 µm on the Zeeweed™ will exhibit an instability development longer than 1.1s and will therefore not undergo Plateau-Rayleigh instability.

It is then possible to determine the general operating conditions allowing to avoid the Plateau-Rayleigh instability domain before achieving a full system polymerisation in 1.1s. To that end, we combined the critical thicknesses determined right above for both fibres to the Eq. 5.24 to

Eq. 5.26 that govern the thickness of the liquid coating on the fibre as a function of the speed and radius of the fibre. Figure 5.10 presents the minimum fibre speed as a function of the reservoir radius to be considered to avoid the Plateau-Rayleigh instability on both MF and UF fibres.

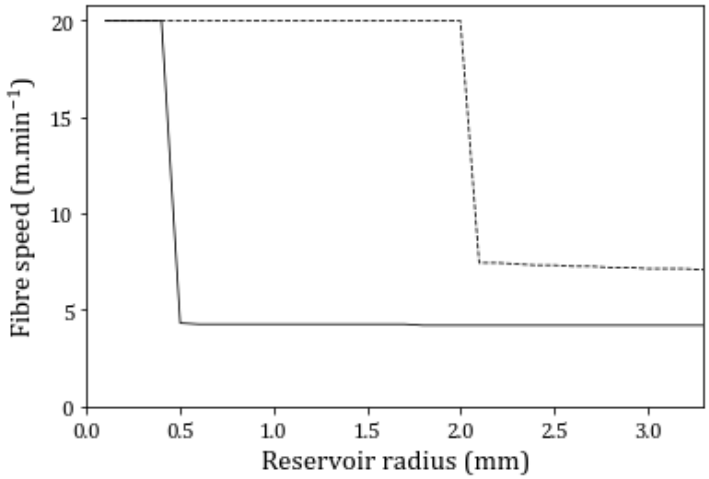

Figure 5.10 – Minimum fibre speed to be applied as a function of the reservoir radius to avoid the occurrence of the Plateau-Rayleigh instability on the (plain) MicroPES™ and the (dash) Zeeweed™ fibres.

As a first approximation, for a lamp power of 80% and thus a complete curing of the system of 1.1 s, the Plateau-Rayleigh instability cannot be avoided over the entire velocity range of the Zeeweed™ fibre – i.e. [0.1;19.8] $m.min^{-1}$ – up to a reservoir radius of 2.0 mm. The use tank radiigreater than this critical value results in an increase of the operable fibre speed range to [7.0;19.8] $m.min^{-1}$. Similarly, the coating of the MicroPES™ will be impacted by Plateau-Rayleigh instability below a reservoir radius of 0.5 mm for the entire fibre speed considered.However, for tank radii greater than 0.5 mm, Plateau-Rayleigh instability will no more occur for fibre velocities above 4.8 $m.min^{-1}$.

Plus, it is important to note that working with a reservoir radius below the critical value 1.85lc causes the meniscus to be unable to form completely. This results in a quicker occurrence of the saturation regime, and thus limit the operating range. Indeed, we stressed that the saturation regime does not allow for an exact prediction of the deposited thickness. In order to perform fibre coating with such low tank radii ranges, preliminary tests are needed to ensure a homogenous liquid coating, as well as the avoidance of the Plateau-Rayleigh instability.

Intermediate conclusions:

- Occurrence of Plateau-Rayleigh instability

In order to avoid the occurrence of Plateau-Rayleigh instability, a minimum coating thickness must be deposited on the fibre. We therefore estimated that the deposited coating must be thicker than 22 and 102 µm on the MicroPES™ and the Zeeweed™ hollow-fibres respectively. These thicknesses are quite thick to consider the deposited coating as a thin-film. To reach thinner thicknesses, Plateau-Rayleigh instability will need to be prevented by gelling the liner before its characteristic development time τ_{PR}.

- Preventing Plateau-Rayleigh instability by photopolymerisation

In order to maintain a homogeneous coating, it is possible to polymerise the microemulsion, before the occurrence of Plateau-Rayleigh instability. In Section 5.4.2, we determined that the microemulsified coating will be fully polymerised in 1.1 s maximum for a lamp power of 80%. The deposited liquid must therefore remain stable at least 1.1 s after being deposited on the fibre, in order to achieve a fully solid homogeneous coating.

We then investigated the operating conditions allowing to avoid the Plateau-Rayleigh instability and concluded that using a reservoir radius too restricted – i.e. 0.5 and 2.0 mm, for the MicroPES™ and the Zeeweed™ fibres respectively – leads to the occurrence of the instability for the entire fibre velocity range considered, i.e. [0.1;19.8]. In Figure 5.12, we demonstrated that above these critical reservoir radii, a minimum fibre speed of 4.8 $m.min^{-1}$ and 7.0 $m.min^{-1}$ is needed to avoid this instability for the MicroPESTM and the ZeeweedTM fibres respectively. Such fibre speeds lead to coating thicknesses of about 24 and 98 µm, respectively. If a deposited coating of 24 µm can be interesting, a 98 µm film will highly impact on the composite membrane permeability and limit its industrial interest, as discussed in Section 5.4.4.

It should be noted it is possible to work with higher fibre velocities to reach the viscous boundary regime, but the same investigation would have to be performed in order to avoid the occurrence of Plateau-Rayleigh instability. Plus, the dynamic evolution of the viscosity during polymerisation may decrease the minimum fibre speed calculated above, allowing for thinner coated films.

5.4.3.2 Coating dynamic instability

Two dynamic instabilities will be investigated in the following sub-sections: coating penetration into the pores and dewetting. Both phenomena are related to the affinity of the deposited liquid and the substrate, quantified by the solid-liquid contact angle.

5.4.3.2.1 Contact angle determination

Contact angles between various non-porous polymer substrates and three liquids were measured using a goniometer. The polymers chosen are common membrane materials: polyvinylidene fluoride (PVDF), polysulfone (PSU), cellulose acetate and polypropylene (PP). The deposited liquids are water and the $(21{:}23{:}56)_{62:19:19}$ monomer microemulsion discussed in Chapter 4.

The investigated microemulsion demonstrated a different behaviour from that of water when deposited on the surface of the polymeric substrates. The $(21{:}23{:}56)_{62:19:19}$ droplets exhibit a dynamic contact angle before reaching the equilibrium. This behaviour was observed mostly on PSU and PVDF substrates, as presented in Figure 5.11 and Figure 5.12.

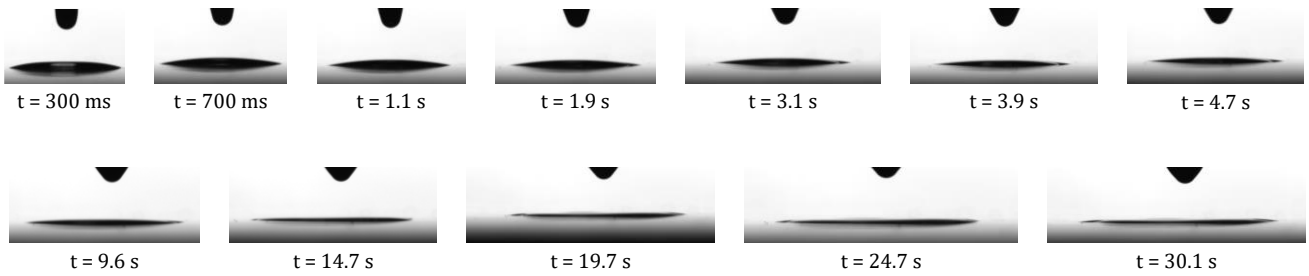

Figure 5.11 – Evolution of the $(21{:}23{:}56)_{62:19:19}$ microemulsion drop after deposition on PSU.

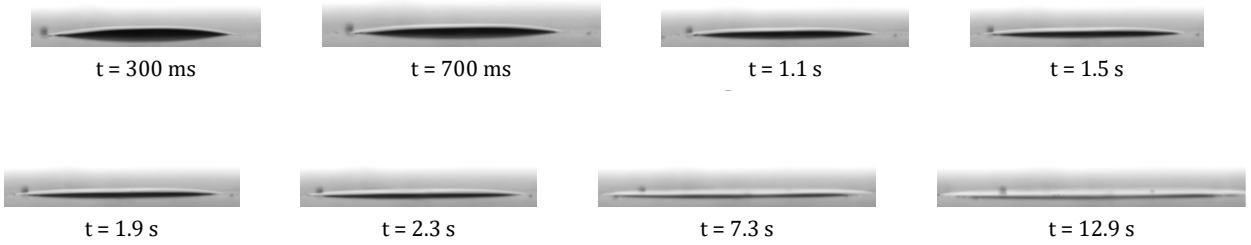

Figure 5.12 – Evolution of the $(21{:}23{:}56)_{62:19:19}$ microemulsion drop after deposition on PVDF.

The results presented in Figure 5.13, present the evolution of the contact angle between the solutions and the substrates investigated. We reported the initial contact angle – 300 ms after its deposition – and at equilibrium. To ensure the equilibrium for all the tested cases, we determined the contact angle after 30 s.

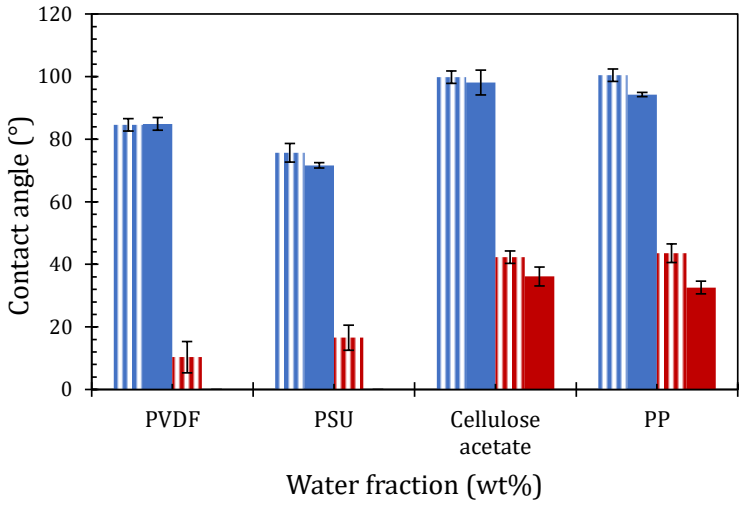

Figure 5.13 – Contact angles between various non-porous polymer substrates and (■) water and (■) the $(21:23:56)_{62:19:19}$ microemulsion. Measurement done (**dashed**) 300 ms and (**plain**) 30 s after the drop deposition.

After deposition of the $(21:23:56)_{62:19:19}$ microemulsion, we observe a decrease of the contact angle value, no matter the initial hydrophilicity of the polymer substrate. Such a behaviour has already been observed by other authors [20]–[22] and was attributed to the dynamic diffusion and adsorption of the surfactant molecules. Von Bahr et al. (1999) [22] reported that, for hydrophobic solid substrates, surfactant molecules are being displaced from the liquid-vapour to the liquid-solid interface, thus modifying the thermodynamic equilibrium of the system. The liquid-vapour interface being depleted from surfactant molecules, a diffusion flux occurs from the solution bulk to supply new surfactant molecules and to regain thermodynamic balance. Hence, the surface tension γ_{LV} between the microemulsion and the atmosphere is a time-dependent characteristic. Thus, the contact angle θ between the microemulsion and the solid substrate can be expressed as described in Eq. 5.37 and Eq. 5.38, where h_0 is the coating thickness, D is the diffusion coefficient of the surfactant and t the time needed for the surfactant to diffusion through the whole coating thickness.

$$\cos\theta = \frac{\gamma_{SV} - \gamma_{SL}}{\gamma_{LV}(t)} \qquad \text{Eq. 5.37}$$

$$\gamma_{LV}(t) = \gamma_{LV}^{eq} + \left(\gamma_{LV}^{0} - \gamma_{LV}^{eq}\right) \exp\left(-\frac{tD}{{h_0}^2}\right) \qquad \text{Eq. 5.38}$$

Intermediate conclusions:

We evidenced that the contact angle of a microemulsion on various substrates can evolve as a function of the time. Such an evolution of the contact angle has to be considered for the dip-coating process in order to predict and control the dip-coating process of monomer microemulsion on polymer fibres. Indeed, the destabilisation phenomena of the liquid coating on the fibre are highly dependent on the contact angle between the solution coated and the solid substrates. We will then discuss two phenomena that can highly impact on the homogeneity of the resulting coating prior to polymerisation: the liquid capillary penetration and the liquid dewetting.

5.4.3.2.2 Coating capillary penetration into the hollow-fibres' porosity

Knowing the contact angle between the microemulsion and the Zeeweed™ (PVDF) and the MicroPES™ (PES, assumed to behave as PSU) it is possible to investigate the destabilisation of the coating upon deposition and before its polymerisation. We will first discuss the coating capillary penetration in the pores of the membrane, driven by the Young-Laplace capillary pressure difference in the pores of the substrate.

- Static penetration of the liquid

The deposited coating may penetrate the pore substrate after coating, it is therefore necessary to estimate to what extent the liquid film may be disrupted. To that end, we first estimated the maximum pore volume accessible by liquid for each fibre, if the fibre is exposed to the liquid long enough to reach equilibrium. To that end, we assumed perfect cylindrical pores, a homogeneous penetration and a fibre porosity – and thus surface density – of 80%. We then determined the associated minimum coating thickness to be deposited in order to saturate the porosity of each substrate, cf. Table 5.7. We were able to calculate the minimum coating thickness to be deposited in order to saturate the porosity of each substrate at equilibrium, cf. Table 5.6.

At equilibrium, a 280 µm thick and 80 µm thick coating have to be deposited on the Zeeweed™ and the MicroPES™ respectively in order to completely saturate the pores. Based on the results from section 5.4.1.2, we evidenced that the coating deposited on the surface of the MicroPES™ – for a fibre speed range of [0-19.8] $m.min^{-1}$ and a reservoir radius (excluding the fibre radius)

from 0.1 to 3.3 mm – is always thinner or equal to 80 µm. The same conclusion is drawn for the Zeeweed™, as the coating is always thinner than 280 µm for the investigated operating conditions. Therefore, the liquid may theoretically penetrate the totality of the porosity of both fibres, if the fibre is exposed to the liquid long enough to reach equilibrium. Such a behaviour can lead to non-homogeneous pore filling and defects, and ultimately to uncontrolled permeability and selectivity.

Table 5.6 – Estimation of the minimum coating thickness to saturate the pores at equilibrium – for the 1 m of fibre.

Hollow-fibre membranes	Zeeweed™	MicroPES™
Pore surface (m^2)	4.02E-03	1.26E-03
Wall thickness (µm)	350	100
Accessible pore volume of the fibre (m^3)	1.41E-6	1.26E-7
Minimum coating thickness to saturate the pores (µm)	280	80

- Dynamic penetration of the liquid

In order to fully assess the capillary penetration of the liquid into the fibre porosity, the dynamic aspect of this phenomenon has to be considered. The Washburn equation allows for the determination of the capillary penetration of the liquid depending on the time spent by the liquid on the substrate surface Δt [23]. This equation, presented in Eq. 5.39, is valid for a fibre pore radius strictly lower than the capillary length l_c for hydrophilic substrate, and for vertical coating process because the pores are considered as horizontal capillaries.

$$L_{cap} = \sqrt{\frac{\Delta t . \gamma . r_{pore} . \cos\theta}{2 . \eta}} \qquad \text{Eq. 5.39}$$

In order to predict the pore penetration by the microemulsion, we considered that the liquid was able to penetrate the substrate until its full polymer conversion at 80% lamp power, i.e. $\Delta t = 1.1$ s. The simulated penetration of the liquid depending on the contact angles of the microemulsion on the MicroPES™ and Zeeweed™ hollow-fibres is presented in Figure 5.14. Two observations can be immediately drawn from these results: first, liquid penetration will

be lower on Zeeweed™ than on MicroPES™ fibres – at most almost four times lower for superhydrophilic behaviour. We can therefore conclude the substrate pore size has a significant impact on the liquid capillary penetration into the fibre porosity, as suggested by Eq. 5.39. Secondly these results also demonstrate the huge impact of the contact angle between the coating and the fibre: indeed, the lower this contact angle the higher the pore penetration. Superhydrophilic behaviour leads to a capillary penetration in 1.1 s of about 200 and 760 µm for the Zeeweed™ and MicroPES™ fibres respectively. An increase in the contact angle then lowers the penetration – which will reach zero for hydrophobic liquid behaviour.

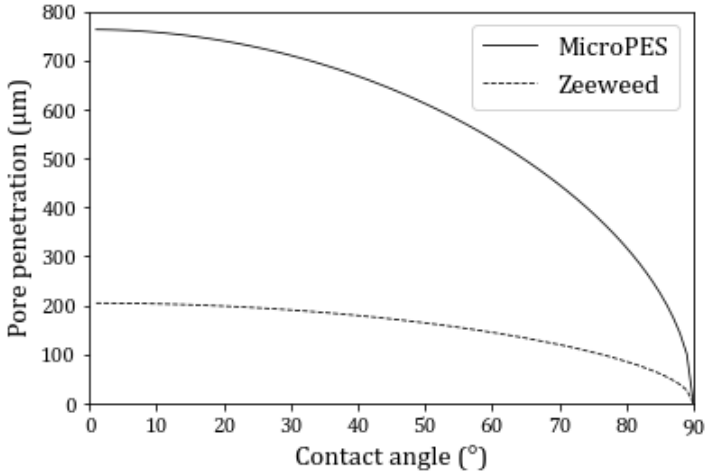

Figure 5.14 – Evolution of the dynamic capillary penetration of the microemulsion into the pores of the studied hollow-fibres in 1.1 s, depending on the contact angle between the liquid and the substrates.

In the last sub-section, we determined the contact angles between the microemulsion and PVDF, as well as PSU, polymer substrates. We assume that the behaviour of the MicroPES™ fibre – made of polyethersulfone (PES) – will be identical to that of PSU due to the chemical similarity of the polymers. These results indicate that the microemulsion will exhibit a 10 ± 5° and a 17 ± 4° contact angle with the PVDF and the PSU respectively at 1.1 s. We therefore expect the liquid to penetrate 203 µm into the Zeeweed™ and 746 µm – hence the full polymer wall – into the MicroPES™. Using the same reasoning as for the static part, we estimated in Table 5.7 the minimum coating thickness to be deposited in order to saturate the porosity of each substrate before the complete liquid polymerisation in 1.1 s.

Based on the results from section 5.4.1.2, we evidenced that coating deposited on the surface of the MicroPES™ – for a fibre speed range of [0-19.8] $m.min^{-1}$ and a reservoir radius (excluding the fibre radius) from 0.1 to 3.3 mm – is always thinner or equal to 80 µm. Therefore, the liquid

will penetrate the totality of the porosity in 1.1s, before the microemulsion full polymerisation. This conclusion is valid no matter the contact angle between the fibre and the liquid, as the liquid deposited will always penetrate the whole fibre wall in 1.1s based on Washburn equation. It is therefore impossible to maintain a continuous film on the surface of this MF fibre for the considered operating conditions.

Table 5.7 – Estimation of the minimum coating thickness to saturate the pores before full conversion at 80% lamp power – for the 1 m of fibre.

Hollow-fibre membranes	Zeeweed™ (θ = 10°)	MicroPES™ (θ = 17°)
Pore surface (m^2)	4.02E-03	1.26E-03
Wall thickness (µm)	350	100
Pore penetration in 1.1s (µm)	203	100 ($746\ \mu m > h_{fibre}$)
Maximum deposited thickness penetrating to the pores in 1.1 s (µm)	162	80

Unlike the MicroPES™ hollow-fibre membrane, the Zeeweed™ fibre exhibits thicker coatings – up to 164 µm – in the same investigated reservoir radius and fibre speed ranges. For specific operating conditions ($r_{reservoir} \geq 0.22 l_c = 0.4$ mm; $v_{fibre} = [0.8 - 19.8]\ m.min^{-1}$) it is therefore possible for the deposited coating thickness to be thicker than the liquid thickness that will penetrate the fibre porosity. Thus, it is possible to maintain a continuous film of low thickness on the UF fibre – which may however be subject to dewetting then, depending on the remaining continuous thickness.

In Chapter 4, we evidenced that the monomer solution effectively penetrates the deconditioned MicroPES™ flat-sheet membrane porosity, but is also photografted inside the supporting membrane due to the UV-sensitive nature of the polyethersulfone. We also note that the liquid solution is mainly retained in the smallest pores of the asymmetric membrane, due to a lower Laplace pressure. The penetration phenomenon can therefore block the support pores and decrease the composite permeability. The retention of the polymer microemulsion into the porosity of the PVDF membrane is to be investigated. Indeed, acrylate monomers will not covalently bind with the membrane material, which could lead to an elimination of the coating during the membrane use.

Intermediate conclusions:

We evidenced that, at equilibrium, the liquid can fully penetrate both fibres porosity. Considering the dynamic aspect of this phenomenon, we evidenced that the deposited coating will completely penetrate the MicroPES™ porosity no matter the contact angle of the microemulsion with the fibre (assuming a symmetric membrane). On the contrary, the microemulsion penetration into the porosity of the Zeeweed™ fibre is highly dependent on the contact angle with the coating. We evidenced that the considered microemulsion exhibits a low contact angle with the PVDF, which constitutes the Zeeweed™ membrane. The contact angle measurements between the polymer substrates and the microemulsion highlight that modifying the composition of the microemulsion might result in an increase of the contact angle, and thus a decrease in the fibre penetration. It is therefore of utmost concern to determine the microemulsion contact angle with the substrate to be coated in order to predict the coating behaviour. Indeed, it must be borne in mind that the coating will fill the microemulsion pores but could also create an additional thin-film over these saturated pores.

We also concluded that a coating thinner than 162 µm will completely penetrate the porosity of the Zeeweed™ fibre in 1.1s, before the complete monomer polymerisation. If this situation is mostly obtained according to the simulation carried out in this work, specific conditions allow to reach higher thicknesses. Working at larger radii of reservoir ($r_{reservoir} \geq 1.8 l_c = 3.3$ mm) and high fibre speeds ($v_{fibre} = [15.2 - 19.8]$ m. min^{-1}) allows to reach the saturation regime which leads to coatings of about 164 µm. It should be noted that, as explained in Section 5.4.1.2, the saturation regime cannot be precisely predicted and might lead to variations between theory and experience. It is therefore possible to obtain a ca. 2 µm continuous thin-film on the surface of the Zeeweed™ for these operating conditions. This film might however be subject to dewetting, which we will discuss in the following sub-section.

The penetration of the microemulsion coating is a major concern because the monomer solution is expected to cure through the entire wall thickness, as depicted in Chapter 4. Depending on the supporting membrane material, the coating can be grafted into the membrane porosity, which will then increase the effective thickness of the deposited coating, compared to the thickness calculated for non-porous fibres in Section 5.4.3, resulting in lower water permeabilities. If the microemulsion coating is not grafted into the membrane porosity, it can be eliminated during filtration, leading to a reversion to an unmodified membrane.

Finally, one must however keep in mind that the viscosity of the microemulsion will increase during the polymerisation process. Thus, if the liquid penetration is favoured for a zero-conversion rate, the occurrence of longer chains – increasing the liquid viscosity – will gradually limit the pore penetration. Indeed, the capillary penetration will probably be important for both hydrophilic and hydrophobic fibres, due to the co-existence of both hydrophilic and hydrophobic phases in the microemulsion, but will still be decreased when the microemulsion viscosity will increase, cf. Eq. 5.39. It is therefore likely that the liquid will stop penetrating the substrate before the full conversion, i.e. 1.1s.

5.4.3.2.3 Coating dewetting

It was discussed in the last sub-section that if a continuous coating remains on the fibre surface despite its penetration into the fibre porosity, this continuous coating may undergo dewetting. This thin-film will undergo dewetting as soon as its surface tension solid-gas γ_{SV} is lower than the sum of the liquid-gas γ_{LV} and the liquid-solid γ_{SL} surface tensions, cf. Eq. 5.40 [9], [19], [24]. Depending on the film thickness, two wetting regimes are to be differentiated: the metastable and the unstable regime.

$$\gamma_{SV} < \gamma_{LV} + \gamma_{SL} \qquad \text{Eq. 5.40}$$

The unstable domain can be overlooked once the coating h_i is thicker than 10 nm [9]. The metastable regime can be avoided once the coating reaches a minimum critical thickness h_c, cf. Eq. 5.41. This dry zone is assumed to be circular and will appear when the energy to create this dry zone is lower than the surface energy, i.e. when its radius $r_{dewetting}$ is equal to the coating thickness, cf. Eq. 5.42. Above this radius, the dewetting phenomenon occurs and the dry zone will expand, causing the liquid film surrounding this area to thicken until it reaches the critical value h_c, Eq. 5.43, stopping the dewetting propagation. This critical thickness h_c corresponds to the thickness at which the liquid flattens out under the effect of gravity and tends to form a gravity pool.

$$h_c = 2.l_c.\sin\left(\frac{\theta}{2}\right) \qquad \text{Eq. 5.41}$$

$$h_c > h_0 \qquad \text{Eq. 5.42}$$

$$h_0 < r_{dewetting} \qquad \text{Eq. 5.43}$$

Combining these last equations will allow for the determination of the minimum solid-liquid contact angle between the substrate and the liquid deposited to avoid the occurrence of a metastable dewetting phenomenon, cf. Eq. 5.44.

$$h_0 > 2.l_c.\sin\left(\frac{\theta_{min}}{2}\right) \qquad \text{Eq. 5.44}$$

The results presented in Figure 5.15 show that coatings with a contact angle of 1°, 2° and 3° with the substrate will undergo dewetting if they are thinner than 61, 123 and 184 µm respectively. In Section 5.4.1.2, we evidenced that the thickest possible coating deposited on the microPES™ and on the Zeeweed™ was 72 and 164 µm respectively. We therefore conclude that to avoid a dewetting phenomenon, the coating deposited on the MicroPES™ fibre must exhibit a contact angle with the fibre lower than 2°, while the contact angle with the Zeeweed™ must be lower than 3°. We also demonstrated that the microemulsion displays a superhydrophilic behaviour on the PVDF and PSU substrates after a few seconds on the fibre. However, when deposited on the polymer after 300 ms, the solution still exhibits a contact angle of 10° on PVDF and 17° on PSU, which would lead to a dewetting of the coating depending on the dynamic behaviour of the dewetting phenomenon.

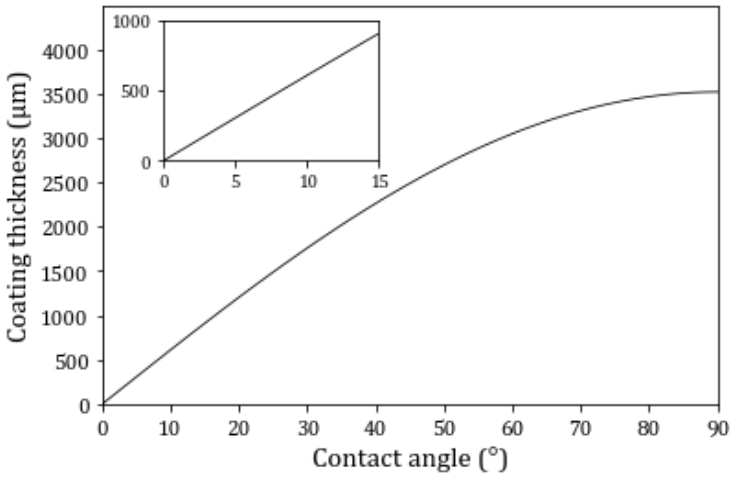

Figure 5.15 – Minimum coating thickness to avoid a dewetting phenomenon depending on the contact angle between the microemulsion and the substrate.

Noblin [24] differentiated two equations, depending on the coating thickness, to describe the dynamic dewetting phenomenon. If the deposited liquid thickness h is negligible compared to the critical thickness h_c, Eq. 5.45 should be used. Otherwise, Eq. 5.46 should be considered.

$$\mathbf{h_c \gg h}: \quad v_{dewetting} = \frac{\gamma}{6\eta l}\theta_E{}^3 \qquad \text{Eq. 5.45}$$

$$\mathbf{h_c \sim h}: \quad v_{dewetting} = \frac{\theta_D}{12\eta l}\rho g(h_c{}^2 - h_0{}^2) \qquad \text{Eq. 5.46}$$

θ_D and θ_E are the dynamic and static contact angles, l is a constant: $l = \ln\left(\frac{L_d}{d_m}\right) \sim 10 - 20$ with L_d the droplet size (m) and d_m molecular size (m). η, γ and ρ are the liquid dynamic viscosity (Pa.s), surface tension ($N.m^{-1}$) and density ($kg.m^{-3}$). g is the gravitational acceleration on Earth ($9.8\ m.s^{-1}$).

In the scope of our study, we did not evaluate the relative impact of the dewetting compared to the capillary penetration phenomenon. Further work should be carried out to fully assess the coating perturbation after fibre coating.

Intermediate conclusions:

The previous paragraphs highlighted that a continuous thin-film may remain on the surface of the Zeeweed™ fibre after pore penetration for specific operating conditions. The resulting continuous film thickness may be of ca. 2 µm and would therefore be too thin to avoid metastable dewetting, as depicted in Figure 5.15.

If the dynamic dewetting was not considered in our study, it would have to be considered for a full assessment of the evolution of the coating after its deposition on the fibre. As detailed in the last subsection, the liquid destabilisation may be contrasted because of the increase of microemulsion viscosity during polymerisation; which may prevent the dewetting phenomenon until achieving a full conversion. In order to fully assess this dynamic phenomenon, the continuous evolution of the viscosity of the monomer solution during the polymerisation should be considered in detail.

Beirnaert (2019) [9] also observed that the dip-coating of a PVDF hollow-fibre with a Teflon AF 2400® coating led to a severe vibration of the fibre on the coating module due to its own speed and the tension exerted by the pulley and reel system. These vibrations led to droplets ejections from the coating and thus to a possible decrease of the coating thickness. Such a phenomenon would therefore increase the probability to reach a heterogeneous system, which would then be subjected to a metastable dewetting regime for high fibre velocities.

5.4.4 Efficiency of the dip-coating process for microemulsions

Several conclusions can be drawn from the previous paragraphs are the following:

- ✓ The reservoir radius is a crucial factor up to $r_{cuve} \approx 1.85 l_c = 3.3$ mm in our case. Above this critical radius the meniscus will not be modified anymore and thus the reservoir width will not impact on the deposited coating thickness.
- ✓ For low reservoir radii lead to a divergence and saturation regimes at very low fibre speed, especially for thick fibre radii.
- ✓ Capillary penetration is the most impacting factor regarding the destabilisation of the coating after its deposition. The porosity of the MF fibre will be fully saturated when the deposited thickness will be thicker than 71 µm, while the UF fibre will be fully saturated when a coating thicker than 150 µm is achieved. A deposited coating thicker than these values will lead to the occurrence of an additional thin-film which will further decrease the permeability of the composite membrane.

One may now question the efficiency – permeability and selectivity – and thus the attractiveness of this process regarding the performance of the composite membrane: is the dip-coating of microemulsion on the surface of hollow-fibres a process of industrial interest? We will try to answer – at least partially – to this question by estimating the performances of such a composite hollow-fibre. Our reasoning will be based on the performances of the $(21{:}23{:}56)_{62:19:19}$ UV-TQ150 sample estimated in Chapter 4. We identified this sample as an ultrafiltration material regarding its selectivity. We will now discuss the permeability of the resulting composite membrane, as a function of the fibre substrate considered and of the coating thickness.

Using a series resistance model (cf. Eq. 4.5), we calculated the permeability of the final composite hollow-fibre membrane as a function of the coating thickness. Based on the manufacturer's data at 25°C and using Eq. 5.47 [25], we determined the water permeability of the MicroPES™ and the Zeeweed™ hollow-fibre membranes to be respectively of 19045 and 816 $L.h^{-1}.m^{-2}.bar^{-1}$ at 20°C.

$$L_P{}^{20} = \frac{L_P{}^{25}}{\exp\left(1708.1\left(\frac{1}{293.15} - \frac{1}{298.15}\right)\right)} \qquad \text{Eq. 5.47}$$

Using the permeability of the $(21:23:56)_{62:19:19}$ UV-TQ150 thin-film (as presented in Chapter 4, Section 4.2.2.2), we estimated permeability of the MicroPES™ and the Zeeweed™ composite hollow-fibres at 20°C, cf. Figure 5.16.

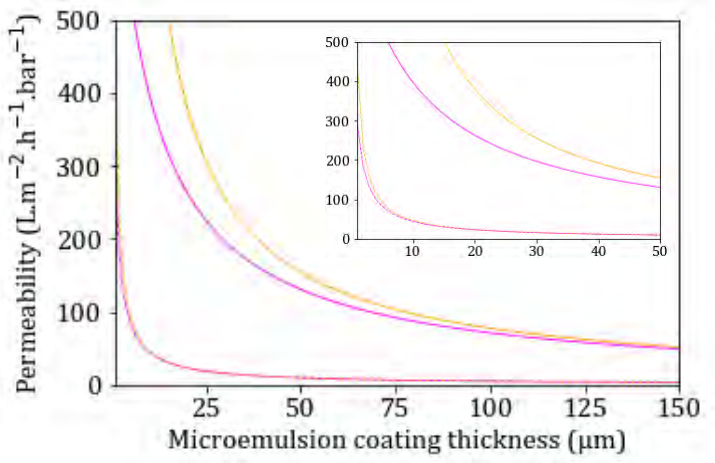

*Figure 5.16 – Water permeability at 20°C of the composite hollow-fibres depending on the $(21:23:56)_{62:19:19}$ UV-TQ150 coating thickness. (**magenta**) Zeeweed™ and (**orange**) MicroPES™ fibres; (**plain**) maximum and (**dashed**) minimum permeabilities.*

As a reminder, the maximum and minimum permeabilities of the $(21:23:56)_{62:19:19}$ UV-TQ150 polymer are determined using the most and least porous domains identified using cryo-SEM analysis and including a tortuous factor of 1.06 and 1.36 respectively. We expect the actual permeability of the sample to lie between these two extremes. One must however note that the interfaces are excluded from our prediction and can affect the estimated permeability of the composite membrane.

The simulated permeability highlights the dramatic decrease of the water permeability up to a 25 µm-thick coating, for which the water permeability falls below 225 and 305 L.h^{-1}.m^{-2}.bar^{-1} – at best – for the Zeeweed™ and MicroPES™ fibres respectively. Hence such a coating thickness will lead to a permeability decrease of at least 98.4% for the MicroPES™ and 72.4% for the Zeeweed™ fibres. This results stress, once again, the importance of the coating thickness. Such a low thickness can only be obtained for fibre speeds lower than 0.9 m.min^{-1} for the MicroPES™ fibre and 4.7 m.min^{-1}, regardless of the reservoir radius – if excluding the saturation regimes for reservoir radius lower than 0.4 mm.

We also observe that the permeabilities of the two fibres are in the same ranges, e.g. a difference in permeability of only 26% for a coating thickness of 25 µm. This last result brings to light the low impact of the substrate selection based on their initial permeability due to the really low

permeability of the deposited coating, which will predominantly govern the permeability decrease.

Intermediate conclusions:

The present simulation evidenced that the deposition of a microemulsion coating of a thickness below 25 µm is almost impossible to achieve on the presently investigated fibres. Indeed, such thicknesses would imply the use of a really small reservoir, and thus reaching the saturation and divergence regimes where the coating thickness is complicated to predict. Plus, we evidenced that the capillary penetration of the coating before its polymerisation may lead to an effective coating thickness thicker than the one deposited on the fibre surface, leading to further decreased permeabilities.

If we determined that reasonable permeabilities can be achieved when coating fibres with a $(21{:}23{:}56)_{62:19:19}$ microemulsion deposit thinner than 25 µm, the selectivity of the resulting composite membrane was estimated to be quite low – i.e. R=0.9 for a 145 kDa PEG – as detailed in Section 4.2.2.1. It should also be noted that experimental work performed by Galiano's team [26] evidenced the need to achieved coatings as thin as 4 µm to maintain a permeability higher than 75 $L.h^{-1}.m^{-2}.bar^{-1}$ (pristine supporting membrane permeability: Lp = 350 $L.h^{-1}.m^{-2}.bar^{-1}$). Such a low thickness is very difficult to achieve in the visco-capillary and visco-inertial regimes and is of little interest for industrial applications.

5.5 Conclusion

The well-known predictive laws of Landau-Levich-Derjaguin (LLD) for the dip-coating of a hollow-fibre membrane have been adapted in order to describe an emulsion, and more specifically a microemulsion ($d_{colloid}$ < 100 nm). A particular attention was paid to the impact of the liquid reservoir radius, which was evidenced as a decisive parameter for both the coating thickness and the critical speed boundaries limiting the applicability of the LLD and the visco-capillary domain.

- **To what extent does the width of the tank impact a linear liquid deposit?**

We incorporated the impact of the reservoir radius in our linear fluid coating numerical simulations, which led to the determination of an upper boundary radius, over which this factor does not evolve anymore. We decided to set this boundary value to $1.85l_c$, which corresponds to the reservoir width (fibre outer surface to tank wall) for which the maximum meniscus height is found – and thus the maximum meniscus width. Our results emphasised the necessity to incorporate the reservoir radius in the coating predictive models, as the saturation regime can be obtained for speed ranges way lower than expected from the mere determination of the Weber number. We can therefore conclude that the divergence and saturation regimes are impacted by two independent factors, namely the meniscus profile (i.e. the reservoir radius) and the Weber number (i.e. the fibre speed). A 3D model is thus expected for reservoir radii below $1.85l_c$ to fully apprehend the liquid coating behaviour.

- **Assuming the microemulsion behaves as a linear simple fluid, is the fibre coating a viable industrial solution for composite membranes manufacturing?**

Our work is – to our knowledge – the first which aims at the prediction of the coating thickness, homogeneity and stability for the dip-coating of a microemulsion solution. We evidenced that the main problem to overcome for such mixtures is the destabilisation of the coating after deposition. We discussed both the capillary penetration and dewetting destabilisation phenomena, which are dependent on the contact angle between the liquid and the solid substrate. We also evidenced the dynamic behaviour of the contact angle between the solid substrate and the monomer microemulsion, which decreases as a function of the time spent on the solid substrate due to the presence of surfactants. In order to consider this dynamic behaviour in our calculations, we considered the contact angle of the microemulsion with the substrate at 1.1 s, i.e. the time needed for the monomer coating to be fully cured. We therefore

considered a contact angle of 10 ± 5° and 17 ± 4° with the PVDF and the PSU respectively. Such low contact angles lead to a high capillary penetration of the liquid prior to its polymerisation. We however evidenced that – for some specific operating conditions – a liquid thin-film may also remain on the fibre surface, despite capillary penetration, due to the gelification of the polymer. We have shown that due to its thinness, the monomer coating deposited on the fibres can also be subject to dewetting. We have not investigated this problem further, because a joint assessment of the dynamic dewetting combined to the dynamic capillary penetration phenomena would be necessary to fully apprehend the liquid behaviour before its polymerisation.

We estimated that the pore penetration will always be significant and lead to a saturation of the pores, which will negatively impact on the permeability. Indeed, the penetrated distance into the fibre's porosity was estimated to be always higher than the thickness of the deposited coating. Indeed, preliminary coating tests carried out on flat-sheet MicroPES™ membranes evidenced that the microemulsion can be cured and grafted to the membrane over its entire thickness, i.e. 100 ± 10 µm. Such a penetration will block the substrate porosity and decrease the composite permeability. If the photopolymerisation of the microemulsion is carried out over the entire thickness of the Zeeweed™ fibre, the coating will not be grafted to the PVDF skeleton of the membrane, which is not photosensitive. We can therefore question the maintenance of the coating into the membrane during the filtration process. If the coating is eliminated from the sample, the composite membrane will be reversed to an unmodified Zeeweed™ fibre. In that case, a preliminary fibre modification will be needed to allow the grafting of the coating to the fibre and thus avoid the elimination of the coating upon filtration. In substance, the penetration of the coating negatively impacts on the dip-coating process, for both grafted and ungrafted coatings.

Finally, we estimated the impact of the coating thickness based on the permeability results from Chapter 4 for the $(21{:}23{:}56)_{62:19:19}$ UV-TQ150 sample. We highlighted the need for a maximum layer thickness of about 25 µm to avoid a dramatic decrease of the composite hollow-fibres permeability (below 305 and 225 $L.h^{-1}.m^{-2}.bar^{-1}$ for the MicroPES™ and the Zeeweed™ membranes respectively). Such a thickness is almost impossible to reach except for very low speed ranges below 0.9 and 4.7 $m.min^{-1}$ respectively. Plus, it remains uncertain whether the liquid would homogeneously penetrate the pores, and thus allow for an increased selectivity over the entire surface of the fibre. In the contrary situation, defects would appear and the

coating would drastically reduce the permeability without increasing the selectivity, as discussed by Quezada (2007) [27].

Our simulation therefore indicates a poor suitability of the process for separative applications, regardless of the initial substrate hydrophilicity, pore radii and fibre radii. Indeed, fibre wiring speeds below 0.9 and 4.7 $m.min^{-1}$ are not of high interest in the industrial scale and higher speed ranges will lead to thicker coatings with low permeabilities, which could be interesting for nanofiltration and reverse osmosis applications only. Plus, we evidenced the need of a fibre speed higher than 4.8 and 7.0 $m.min^{-1}$ to avoid the occurrence of the Plateau-Rayleigh instability. Therefore, the coated thin-films are expected to be thicker than 24 and 98 µm for the MicroPES™ and Zeeweed™ fibres respectively. Plus, we specified in Chapter 4 that the $(21:23:56)_{62:19:19}$ UV-TQ150 interconnected porous network belongs to the ultrafiltration selective range, and such low permeabilities are of no interest for UF membranes. In order to make the microemulsion dip-coating process industrially viable, other applications must then be considered, such as catalysis. We might, for example, consider trapping metallic (e.g. palladium or gold) nanoparticles, into the nanostructured system to enhance catalytic reactions [25], [28], [29].

- **What are the prospects for the microemulsion deposition on hollow-fibre membranes?**

We investigated the dip-coating process of fibres in the visco-capillary and visco-inertial domains and concluded on a poor suitability of the process in the case of microemulsion coating. Because the main challenge to overcome is the capillary penetration of the monomer coating into the substrate porosity, it seems unlikely that working in the viscous boundary regime might solve the problem.

If dip-coating processes are not the only processes that can lead to the synthesis of a thin-film composite membrane, we assume that pore penetration will always occur no matter how the thin film is deposited, due to both low surface tension and low viscosity of the microemulsion coating. It is therefore unlikely that other coating processes may be used to avoid capillary penetration of virgin porous fibres. However, in order to prevent spontaneous pore penetration we have identified two possible solutions to investigate.

The first one is to increase the viscosity of the coating by adding a pre-polymerisation step prior to coating. This solution might be adapted to both UV and RedOx initiation. However, this

solution will obviously impact the resulting thickness of the coating. Indeed, if the viscosity increases more than the surface tension decreases, then the capillary number Ca will increase. Such an increase would then lead to the deposition of thicker thin-films compared to the simulation presented here. Further work is therefore required on the intermediate properties of the polymerising microemulsion to fully assess the deposited thickness.

The second option considered would be to saturate the pores with a sacrificial solution, which would solidify before application of the coating and that can be easily eliminated from the pores after coating. This sacrificial solution must however be non-permeable and immiscible to the microemulsion, which might be quite challenging to obtain due to the hydrophilic and hydrophobic nature of the coating. *Prima facie*, we considered glycerol or sugar [30] to be interesting candidates. However, if the fibre surface is covered by a (dis-)continuous sacrificial layer, this may lead to a detachment of the polymer coating from the membrane surface after elimination of the sacrificial layer, which can reduce the selectivity of the composite membrane. One must therefore ensure that the resulting polymer coating is mechanically strong enough to withstand both the filtration and retro-filtration steps, especially if the coating is not grafted to the fibre surface. The results presented by Beirnaert (2019) [9] suggest that the Teflon AF 2400® thin film coatings – which are not covalently grafted on the hollow-fibre membrane – are mechanically strong enough to withstand the filtration steps, due to the sheath geometry of the coating. This encouraging result should however be confirmed for microemulsion coatings on fibres.

References

[1] S. K. Sahoo, B. Manoharan, and N. Sivakumar, 'Introduction: Why Perovskite and Perovskite Solar Cells?', *Perovskite Photovoltaics Basic to Adv. Concepts Implement.*, pp. 1–24, Jan. 2018, doi: 10.1016/B978-0-12-812915-9.00001-0.

[2] K. Kakaei, M. D. Esrafili, and A. Ehsani, 'Graphene and Anticorrosive Properties', *Interface Sci. Technol.*, vol. 27, pp. 303–337, Jan. 2019, doi: 10.1016/B978-0-12-814523-4.00008-3.

[3] M. N. Subramaniam, P. S. Goh, E. Sevgili, M. Karaman, W. J. Lau, and A. F. Ismail, 'Hydroxypropyl methacrylate thin film coating on polyvinylidene fluoride hollow fiber membranes via initiated chemical vapor deposition', *Eur. Polym. J.*, vol. 122, p. 109360, 2020, doi: 10.1016/j.eurpolymj.2019.109360.

[4] K. S. Goh, J. Y. Chong, Y. Chen, W. Fang, T. H. Bae, and R. Wang, 'Thin-film composite hollow fibre membrane for low pressure organic solvent nanofiltration', *J. Memb. Sci.*, vol. 597, p. 117760, 2020, doi: 10.1016/j.memsci.2019.117760.

[5] D. K. Mahalingam *et al.*, 'Spray-Coated Graphene Oxide Hollow Fibers for Nanofiltration', *J. Memb. Sci.*, p. 118006, 2020, doi: 10.1016/J.MEMSCI.2020.118006.

[6] E. Rio and F. Boulogne, 'Withdrawing a solid from a bath: How much liquid is coated?', *Adv. Colloid Interface Sci.*, vol. 247, pp. 100–114, 2017, doi: 10.1016/j.cis.2017.01.006.

[7] T. Goma-Bilongo, 'Modification de la surface de membranes fibres creuses par photogreffage en continu : simulation du procédé', PhD thesis, Université Toulouse 3 - Paul Sabatier, 2005.

[8] A. Akbari, S. Desclaux, J. C. Rouch, and J. C. Remigy, 'Application of nanofiltration hollow fibre membranes, developed by photografting, to treatment of anionic dye solutions', *J. Memb. Sci.*, vol. 297, no. 1–2, pp. 243–252, 2007, doi: 10.1016/j.memsci.2007.03.050.

[9] P. Beirnaert, 'Contacteurs membranaires pour la maîtrise des gaz dissous dans le vin', PhD thesis, Université Toulouse 3 Paul Sabatier, 2019.

[10] D. Quéré, 'Fluid Coating on a Fiber', *Annu. Rev. Fluid Mech.*, vol. 31, no. 1, pp. 347–384, 1999, doi: 10.1146/annurev.fluid.31.1.347.

[11] D. Quere and A. De Ryck, 'Hydrodynamic coating of a fiber', *Ann. Phys. (Paris).*, vol. 23, no.

1, p. pp.1+, 1998.

[12] E. Lasseuguette, J. C. Rouch, and J. C. Remigy, 'Hollow-fiber coating: Application to preparation of composite hollow-fiber membrane for gas separation', *Ind. Eng. Chem. Res.*, vol. 52, no. 36, pp. 13146–13158, 2013, doi: 10.1021/ie401874m.

[13] A. Gans, E. Dressaire, B. Colnet, G. Saingier, M. Z. Bazant, and A. Sauret, 'Dip-coating of suspensions', *Soft Matter*, vol. 15, no. 2, pp. 252–261, 2019, doi: 10.1039/c8sm01785a.

[14] G. Berteloot, A. Daerr, F. Lequeux, and L. Limat, 'Dip coating with colloids and evaporation', *Chem. Eng. Process. Process Intensif.*, vol. 68, pp. 69–73, 2013, doi: 10.1016/j.cep.2012.09.001.

[15] G. Jing, H. Bodiguel, F. Doumenc, E. Sultan, and B. Guerrier, 'Drying of colloidal suspensions and polymer solutions near the contact line: Deposit thickness at low capillary number', *Langmuir*, vol. 26, no. 4, pp. 2288–2293, 2010, doi: 10.1021/la9027223.

[16] M. Le Berre, Y. Chen, and D. Baigl, 'From convective assembly to landau - Levich deposition of multilayered phospholipid films of controlled thickness', *Langmuir*, vol. 25, no. 5, pp. 2554–2557, 2009, doi: 10.1021/la803646e.

[17] D. M. Warsinger *et al.*, 'A review of polymeric membranes and processes for potable water reuse', *Prog. Polym. Sci.*, vol. 81, pp. 209–237, Jun. 2018, doi: 10.1016/J.PROGPOLYMSCI.2018.01.004.

[18] Y. Tang and S. Cheng, 'The meniscus on the outside of a circular cylinder: From microscopic to macroscopic scales', *J. Colloid Interface Sci.*, vol. 533, pp. 401–408, Jan. 2019, doi: 10.1016/J.JCIS.2018.08.081.

[19] E. Lorenceau, T. Senden, and D. Quéré, 'Wetting of fibers', in *Molecular Gels: Materials with Self-Assembled Fibrillar Networks*, 2006, pp. 223–237.

[20] W. Wang, H. Wei, Z. Du, X. Tai, and G. Wang, 'Formation and characterization of fully dilutable microemulsion with fatty acid methyl esters as oil phase', *ACS Sustain. Chem. Eng.*, vol. 3, no. 3, pp. 443–450, Mar. 2015, doi: 10.1021/SC500667N.

[21] E. Golabi, F. S. Azad, S. S. Ayatollahi, S. N. Hosseini, and N. Akhlaghi, 'Experimental study of wettability alteration of limestone rock from oil-wet to water-wet using various

surfactants', *Soc. Pet. Eng. - SPE Heavy Oil Conf. Canada 2012*, vol. 1, pp. 746–761, 2012, doi: 10.2118/157801-MS.

[22] M. Von Bahr, F. Tiberg, and B. V. Zhmud, 'Spreading dynamics of surfactant solutions', *Langmuir*, vol. 15, no. 20, pp. 7069–7075, Sep. 1999, doi: 10.1021/LA990276O/ASSET/IMAGES/MEDIUM/LA990276OE00008.GIF.

[23] E. W. Washburn, 'The Dynamics of Capillary Flow', *Phys. Rev.*, vol. 17, no. 3, p. 273, Mar. 1921, doi: 10.1103/PhysRev.17.273.

[24] X. Noblin, 'Mouillage et démouillage inertiel : triplons , flaques vibrées , ondes de chocs', [PhD thesis], Université Paris 6, 2004.

[25] M. López Viveros, 'Influence des propriétés d'un réseau polymère sur la synthèse in situ de nanoparticules de palladium : application aux membranes catalytiques de grande efficacité en chimie fine - thesesups', PhD thesis, Université Toulouse 3 Paul Sabatier, 2018.

[26] F. Galiano *et al.*, 'UV-LED induced bicontinuous microemulsions polymerisation for surface modification of commercial membranes – Enhancing the antifouling properties', *Sep. Purif. Technol.*, vol. 194, pp. 149–160, 2018, doi: 10.1016/j.seppur.2017.10.063.

[27] M. L. Quezada Jiménez, 'Photo-greffage de membranes et distributuion initiale de taille des pores : Mise en évidence des limitations', PhD thesis, Université Toulouse 3 Paul Sabatier, 2007.

[28] C. Emin, 'Elaboration d'un réacteur membranaire catalytique par fonctionnalisation de surface de membranes polymères et intégration de nanoparticules métalliques : application à la chimie douce', PhD thesis, Université Toulouse 3 Paul Sabatier, 2013.

[29] Y. Gu, I. Favier, C. Pradel, D. L. Gin, J.-F. Lahitte, R. D. Noble, M. Gómez, and J.-C. Remigy, 'High catalytic efficiency of palladium nanoparticles immobilized in a polymer membrane containing poly(ionic liquid) in Suzuki-Miyaura cross-coupling reaction', *J. Memb. Sci.*, vol. 492, pp. 331–339, 2015, doi: 10.1016/j.memsci.2015.05.051.

[30] C. Stubenrauch, R. Tessendorf, R. Strey, I. Lynch, and K. A. Dawson, 'Gelled polymerizable microemulsions. 1. Phase behavior', *Langmuir*, vol. 23, no. 14, pp. 7730–7737, 2007, doi: 10.1021/la700685g.

General conclusions and perspectives

The present research work is positioned as a proof of concept for the synthesis of interconnected three-dimensional nanoporous polymer network for the manufacture of composite membranes, using non-ionic and non-polymerisable commercial surfactants. The main objective of this work was to carry on preliminary work developed by our research team in the Laboratoire de Génie Chimique. The formulation selected is composed of water as the aqueous phase, MMA as the organic monomer phase, HEMA as the co-solvent and co-surfactant monomer and an equimassic mix Synperonic™ A11 and Tergitol™ 15-S-12 non-polymerisable, non-ionic commercial surfactants. This dissertation aims to expand the scope of understanding of this quinary system, in both the initial monomer and the final polymer state.

To that end, we first led a comprehensive investigation of the monomer microstructure adopted by three systems of various composite surfactant phase (HEMA:Synperonic™ A11: Tergitol™ 15-S-12) compositions in Chapter 3. We chose to investigate the (0:50:50), (33:33:33) and (62:19:19) systems and constructed their associated pseudo-ternary phase diagrams. To that end, over 300 samples were investigated in each system using cross-polarised light observation, conductivity measurements, as well as PGSE-NMR and SAXS analyses. We first demonstrated **the existence of nanometric lamellar and hexagonal liquid crystal structures, in absence of HEMA**. Several unidentified domains remain to be studied to fully complete this preliminary work. We then demonstrated that the **addition of HEMA led to a disorganisation of the identified liquid crystal structures, to give rise to transparent non-birefringent domains.** Based on conductivity, PGSE-NMR and SAXS analyses, we hypothesised that the organised structure occurring in the (0:50:50) is distorted upon HEMA addition to create a bicontinuous structure for intermediate water contents. We further assumed from the analyses presented that **this bicontinuous monomer network swells when increasing the water content of the system, until its breakage when the aqueous channels cannot take in anymore water molecule**, and ultimately the occurrence of a W/O micellar structure.

In Chapter 4, we investigated the polymerisation of the $(21:23:56)_{62:19:19}$, $(46:8:46)_{33:33:33}$ and $(46:8:46)_{33:33:33}$ compositions. We investigated three polymerisation processes: one chemical (RedOx) and two photochemical (UV-LED and UV-TQ150) initiation methods. **Using SAXS and cryo-SEM analyses, we confirmed the evolution of the monomer systems during polymerisation for the three initiations tested, which was attributed to the blockage of the spinodal decomposition phenomenon taking place during the polymerisation of the system**. The resulting polymer systems either exhibited interconnected nanostructures with larger porous domains (5-230 nm) compared to the monomer microstructure, or displayed an

alternation of porous and dense structures, as a function of the composition and of the polymerisation method. We have also shown that the pore size of the samples varies with the initiation method selected, which is due to the different kinetics of these processes. **We also evidenced that the photochemical processes lead to an anisotropic bulk structure – due to the UV-penetration gradient – while the RedOx process leads to an isotropic bulk structure. Finally, we demonstrated the critical importance of interfaces, which modify the affinities of the monomer sample in contact and therefore affect the adjacent microstructure.** We therefore concluded that both the initial composition of the sample and the selection of the polymerisation process – i.e. the substrate where the microemulsion is deposited and the initiation method of the polymerisation – are to be investigated to give rise to the desired microstructure: **depending on the polymerisation kinetics and gel point on set – i.e. depending on the initiation method and system composition – the microemulsion may or may not give rise to a bicontinuous polymer structure.**

We then investigated the expected membrane performances of the homogeneous and uniform nanoporous structures polymerised from the selected monomer self-assembled systems: the $(21:23:56)_{62:19:19}$ RedOx, UV-LED and UV-TQ150 samples, as well as the $(46:8:46)_{62:19:19}$ UV-TQ150 sample. We first evidenced that the three $(21:23:56)_{62:19:19}$ samples display a MWCO of about 20, 22 and 145 kDa, respectively. **The three $(21:23:56)_{62:19:19}$ membranes can therefore be considered as UF membranes – low-UF for the UV-TQ150 sample – considering steric retention only.** The permeability associated to these three samples was estimated using Poiseuille's law and demonstrated **the need to polymerise films thinner than 25 µm to remain in a UF permeability range (i.e. $Lp > 50\ L.m^{-2}.h^{-1}.bar^{-1}$).** Such a result is consistent with other reported results from the literature [1]. Plus, the present simulation evidenced that **the anistropic nature of the UV samples led to a decreased permeability compared to the isotropic RedOx sample**. We then compared this numerical estimation to an experimental evaluation of the permeate flux through ca. 100 µm thick $(21:23:56)_{62:19:19}$ UV-TQ150 membranes. We concluded that for low applied pressure, the estimated fluxes were quite similar to the experimental ones. However, when increasing the pressure we observed a non-linear evolution of the flux as a function of the applied pressure, indicating **a – reversible – atypical elastic behaviour of the polymer network**.

The $(46:8:46)_{62:19:19}$ UV-TQ150 sample, in turn, was estimated to retain particles bigger than 68.4 nm with a retention coefficient of 0.9, associated to a permeability of 44,000-56,000 $L.m^{-2}.h^{-1}.bar^{-1}$ for a 38 µm-thick membrane. **We therefore conclude that the investigated**

$(46{:}8{:}46)_{62:19:19}$ UV-TQ150 sample has a potential to act as a low-MF membrane regarding the selectivity (ca. 3,200 kDa), while still having typical MF permeabilities. One of the main features of the investigated polymer network is its cross-linked nature. Providing a good mechanical resistance of this material – which will have to be tested in further work – **such a membrane could be of high interest for solvent filtration**.

Finally, in Chapter 5, we performed a numerical simulation of the microemulsion dip-coating process for the manufacture of composite hollow-fibre membranes. We adapted the predictive laws of Landau-Levich-Derjaguin (LLD) to describe microemulsified coatings on two commercial hollow-fibres: the MicroPES™ (MF-PES) and Zeeweed™ (UF-PVDF). We considered two different cases: a reservoir radius for which the meniscus is completely formed ($r_{reservoir} \geq 1.85 l_c$) and a reservoir radius for which the meniscus is impacted by the radius of the tank of liquid solution ($r_{reservoir} < 1.85 l_c$). In the former case, **a 2D model can be considered, using $\mathbf{r_{reservoir} = 1.85 l_c}$**. The latter case, in turn, has to be described using **a 3D model, in which both the fibre speed and the liquid reservoir radius are variables.**

Our simulation focused on the investigation of coatings carried out in the visco-capillary and visco-inertial domains. We evidenced the possibility to reach coatings thinner than 25 µm for a fibre speed below 0.9 and 4.7 $m.min^{-1}$ when coating the MicroPES™ and Zeeweed™ respectively. Such fibre speeds are too low to be interesting for an industrial scale-up. Thicker coatings obtained at higher fibre wiring velocities, in turn, result in permeability typical of NF or RO membranes. Plus, we evidenced that the fibre speed needs to be higher than 4.8 and 7.0 $m.min^{-1}$ respectively to avoid the Plateau-Rayleigh instability and remain homogeneous. **We therefore concluded on a poor suitability of the process for separative applications, no matter the initial substrate permeability and hydrophilicity, pore radii and fibre radii**. **For the investigated process to be industrially viable, other applications must then be considered, such as catalysis.** Plus, we evidenced that the coating will undergo both a capillary penetration and a dewetting phenomenon before being polymerised. The competition and the dynamic aspect of these two phenomena are beyond the scope of this project, but it should be noted that **these disturbances could result in the occurrence of heterogeneous coatings and defects, thus reducing the permeability without increasing the selectivity of the composite membrane** [2].

Overall, this research project allowed for:

- ***The proof that self-assembled systems stabilised with non-polymerisable non-ionic commercial surfactants can result in nanoporous and microporous interconnected cross-linked polymer networks.***
- ***The highlight of the utmost significance of the selection of both the polymerisation process and the substrate to be coated. For an identical composition, not all polymerisation processes will result in a homogeneous porous polymer structure.***
- ***An experimental determination of water permeability through the (21:23:56)$_{62:19:19}$ membrane and the evidence of its atypical elastic behaviour.***
- ***The evidence of the difficulty of adapting the microemulsion coating on hollow-fibre geometry using a dip-coating process in the visco-capillary and visco-inertial domains, for industrial separative applications.***

PERSPECTIVES

In the last sub-section of this manuscript we suggest future perspectives as a follow-up to the present research work:

- We were not able to reach a definitive conclusion on the microstructure adopted by the monomer system prior to polymerisation – which was not the inherent aim of this PhD project. In order to elucidate the structure adopted by the system, we first advise to simplify the system by using only one pure non-ionic non-polymerisable surfactant. Once such a system has been clarified, a second surfactant could be added. Finally, after these two steps a system consisting of mix of commercial surfactants could be thoroughly investigated.

- We suggest to further investigate the origin of the elastic behaviour of the $(21{:}23{:}56)_{62:19:19}$ polymer membrane we experimentally evidenced in Chapter 4 by monitoring the retention of PEOs as a function of the pressure and investigating the mechanical properties in compression. Depending on the results of these two analyses, the material may be considered for catalytic application. Indeed, if the pore size of the polymer network can be tuned as a function of the applied pressure, the entrapment of metallic (e.g. palladium or gold) nanoparticles could also be performed by filtration of a solution containing nanoparticles under successive pressure ranges. When increasing the pressure, the nanoparticles could penetrate inside the aqueous channels. Then, lowering the applied pressure could trigger their entrapment into those channels due to the reversible decrease of the pore size. Finally, the filtration of solutions at low pressures – to prevent the enlargement of the pores and the release of the trapped nanoparticles – may allow catalytic reactions at liquid state to be carried out [3]–[5].

- We first suggest to pursue the experimental work carried out on the $(21{:}23{:}56)_{62:19:19}$ UV-TQ150 membrane with the determination of the retention of the membrane, in relation to its elastic behaviour. We also recommend to experimentally assess the performances of asymmetric and composite membranes using the $(46{:}8{:}46)_{62:19:19}$ UV-TQ150 and of the $(21{:}23{:}56)_{62:19:19}$ RedOx, UV-LED formulations.

- In this manuscript, we detailed that both the interfaces (Marangoni effect) and the initiation method (polymerisation kinetics) impacted on the final polymer microstructure. We suggest to investigate both phenomena to better understand the modification of the self-

assembled microstructure upon polymerisation in contact with substrates of various hydrophilicity.

- As part of this research project, we investigated the impact of the composition of the system on the microstructure for a fixed temperature (i.e. 25°C). However, the temperature factor has a dramatic impact on the structure adopted by the quaternary and quinary systems, due to the polyethoxylated nature of both non-ionic surfactants. We would advise the investigation of this factor through the construction of fishtail diagrams.

- In this project, we highlighted the importance of the capillary penetration phenomenon on the coating prior to polymerisation, both for flat-sheet and hollow-fibre membranes. In order to prevent the spontaneous pore penetration we suggest two ideas for improvement. The first option is to saturate the pores with a sacrificial solid. This sacrificial compound must however be non-permeable and immiscible to the microemulsion, which is quite challenging due to the amphiphilic nature of the coating. Furthermore, this sacrificial filling must not be present on the supporting membrane surface, otherwise the deposited polymer coating could be heterogeneous or even detach from the substrate. The second option is to increase the viscosity of the monomer solution by adding a pre-polymerisation step before coating. Such a solution could however be challenging with regard to the dip-coating process. Indeed, modifying the viscosity of the solution would directly impact on the coating thickness. Plus, the coating deposited on the final polymer structure could be different than expected due – amongst other phenomena – to a Marangoni effect on the polymerising monomer bath. Finally, in the specific case of dip-coating process, we doubt that working in the viscous boundary regime will solve this problem, due to the low surface tension of the self-assembled solution used.

- We carried out a numerical simulation of the dip-coating process for the deposition microemulsion coatings cured under UV-light. We could extend the investigation to RedOx polymerisation, where other problematics could arise, such as how to avoid or limit the polymerisation burst – and its associated temperature increase – while limiting the penetration of the coating into the porosity of the membrane. The present simulation could also be extended to the viscous boundary regime to allow for higher fibre wiring speed. To that end, the experimental α-constant would have to be determined beforehand. Moreover, we suggest an experimental verification of the simulation presented in this work. Indeed, an experimental review of microemulsion dip-coating on fibres has – to our knowledge –

never be conducted. We hypothesise that some corrective factors may have be applied on the simulation presented to fit the experimental situation.

- A last perspective to this work is the comparison of the performances of microemulsion coatings to those achieved with block copolymers [6]. Indeed, both methods may result in composite membranes with increased performances. One may for example discuss the cross-linking of both polymer coatings, as well as their pore density and pore size or the possibility of dip coating the fibres using each method.

References

[1] F. Galiano, S. A. Schmidt, X. Ye, R. Kumar, R. Mancuso, E. Curcio, B. Gabriele, J. Hoinis, and A. Figoli, 'UV-LED induced bicontinuous microemulsions polymerisation for surface modification of commercial membranes – Enhancing the antifouling properties', *Sep. Purif. Technol.*, vol. 194, pp. 149–160, 2018, doi: 10.1016/j.seppur.2017.10.063.

[2] M. L. Quezada Jiménez, 'Photo-greffage de membranes et distributuion initiale de taille des pores : Mise en évidence des limitations', PhD thesis, Université Toulouse 3 Paul Sabatier, 2007.

[3] C. Emin, 'Elaboration d'un réacteur membranaire catalytique par fonctionnalisation de surface de membranes polymères et intégration de nanoparticules métalliques : application à la chimie douce', PhD thesis, Université Toulouse 3 Paul Sabatier, 2013.

[4] Y. Gu, I. Favier, C. Pradel, D. L. Gin, J. F. Lahitte, R. D. Noble, M. Gómez, and J. C. Remigy, 'High catalytic efficiency of palladium nanoparticles immobilized in a polymer membrane containing poly(ionic liquid) in Suzuki-Miyaura cross-coupling reaction', *J. Memb. Sci.*, vol. 492, pp. 331–339, 2015, doi: 10.1016/j.memsci.2015.05.051.

[5] M. López Viveros, 'Influence des propriétés d'un réseau polymère sur la synthèse in situ de nanoparticules de palladium : application aux membranes catalytiques de grande efficacité en chimie fine - thesesups', PhD thesis, Université Toulouse 3 Paul Sabatier, 2018.

[6] L. Upadhyaya, 'Self-assembled smart filtration membranes from block copolymers and inorganic nanoparticles', PhD thesis, Université de Montpellier; Universidad de Zaragoza, 2016.

Appendices

APPENDICES I

APPENDIX 1 – TECHNICAL DATA SHEET OF THE MICROPESTM TYPE 2F FLAT-SHEET MEMBRANE V

APPENDIX 2 – EMISSIVITY SPECTRA OF UV LAMPS USED IN THE LABORATORY VI

APPENDIX 3 – TUNING OF THE POROUS MATERIAL PROPERTIES: A NON-EXHAUSTIVE SURVEY OF THE POLYMERISATION OPERATING PARAMETERS VII

3.1 Oxygen elimination prior to polymerisation VIII
3.2 UV-initiation parameters XII
3.3 Polymer washing parameters XIV

APPENDIX 4 – EVOLUTION OF THE MICROSTRUCTURE OF THE ACRYLATE MONOMER SYSTEM UPON MMA:SURFACTANT PHASE DILUTION XVIII

APPENDIX 5 – TECHNICAL DATA SHEETS OF HOLLOW-FIBRE MEMBRANES DISCUSSED AS PART OF THE NUMERICAL SIMULATION XXII

Appendix 1 – Technical data sheet of the MicroPES™ Type 2F flat-sheet membrane

3M Science. Applied to Life.™

3M™ MicroPES™ Flat Membrane Type 2F

Chemical Composition	
Polymer	Polyethersulfone
Wetting property	Hydrophilic

Physical Properties	
Thickness	110 ± 10 µm (4.3 ± 0.4 mil)
Tensile strength	
Longitudinal	≥ 900 cN/15 mm
Transversal	≥ 800 cN/15 mm
Elongation at break	
Longitudinal	≥ 25%
Transversal	≥ 30%
Change of length (steam, 121 °C)	≤ 3 %

Membrane Performance Characteristics	
Bubble point (in water)	4.3 ± 0.54 bar (62.4 ± 7.8 psi)
Transmembrane flow (water, 25 °C)	≥ 35 ml/(min cm² bar) (≥ 2241 ml/(min ft² psi)) (≥ 15.57 ml/(min in² psi))
Retention of bacteria (Brevundimonas diminuta)	≥ 7 log /cm² reduction value

Available Make-up Configurations
Rolls

All specifications are based on 3M internal test procedures.

Technical Information: The technical information, guidance, and other statements contained in this document or otherwise provided by 3M are based upon records, tests, or experience that 3M believes to be reliable, but the accuracy, completeness, and representative nature of such information is not guaranteed. Such information is intended for people with knowledge and technical skills sufficient to assess and apply their own informed judgment to the information. No license under any 3M or third party intellectual property rights is granted or implied with this information.

Product Use: Many factors beyond 3M's control and uniquely within user's knowledge and control can affect the use and performance of a 3M product in a particular application. Given the variety of factors that can affect the use and performance of a 3M product, user is solely responsible for evaluating the 3M product and determining whether it is fit for a particular purpose and suitable for user's method of application.

Warranty, Limited Remedy, and Disclaimer: Unless a different warranty is specifically stated on the applicable 3M product packaging or product literature, 3M warrants that each 3M product meets the applicable 3M product specification at the time 3M ships the product. 3M MAKES NO OTHER WARRANTIES OR CONDITIONS, EXPRESS OR IMPLIED, INCLUDING, BUT NOT LIMITED TO, ANY IMPLIED WARRANTY OR CONDITION OF MERCHANTABILITY OR FITNESS FOR A PARTICULAR PURPOSE OR ANY IMPLIED WARRANTY OR CONDITION ARISING OUT OF A COURSE OF DEALING, CUSTOM OR USAGE OF TRADE. If the 3M product does not conform to this warranty, then the sole and exclusive remedy is, at 3M's option, replacement of the 3M product or refund of the purchase price.

Limitation of Liability: Except where prohibited by law, 3M will not be liable for any loss or damage arising from the 3M product, whether direct, indirect, special, incidental or consequential (including, but not limited to, lost profits or business opportunity), regardless of the legal theory asserted, including warranty, contract, negligence or strict liability.

3M and Membrana are trademarks of 3M Company. © 2019 3M Company. All rights reserved.

3M
Separation and Purification Sciences Division
13840 South Lakes Drive
Charlotte, North Carolina
28273 USA
Phone: +1 704 587 8888
Fax: +1 704 587 8610

3M Deutschland GmbH
Separation and Purification Sciences Division
Öhder Straße 28
42289 Wuppertal
Germany
Phone: +49 202 6099 – 0
Fax: +49 6099 - 241

IM-1008
Rev. 02/2020
www.3m.com/membrana

Appendix 2 – Emissivity spectra of UV lamps used in the laboratory

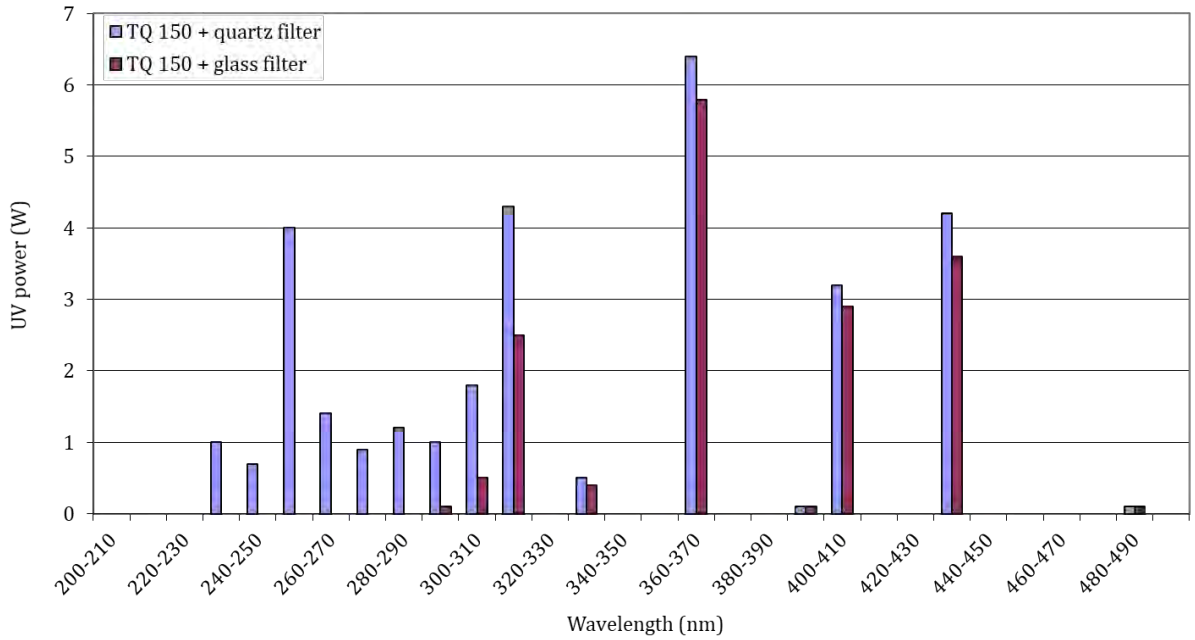

Figure A.1 – Emissivity spectra of the TQ 150 (Hereaus) UV lamp depending on the filter applied. (Manufacturers data)

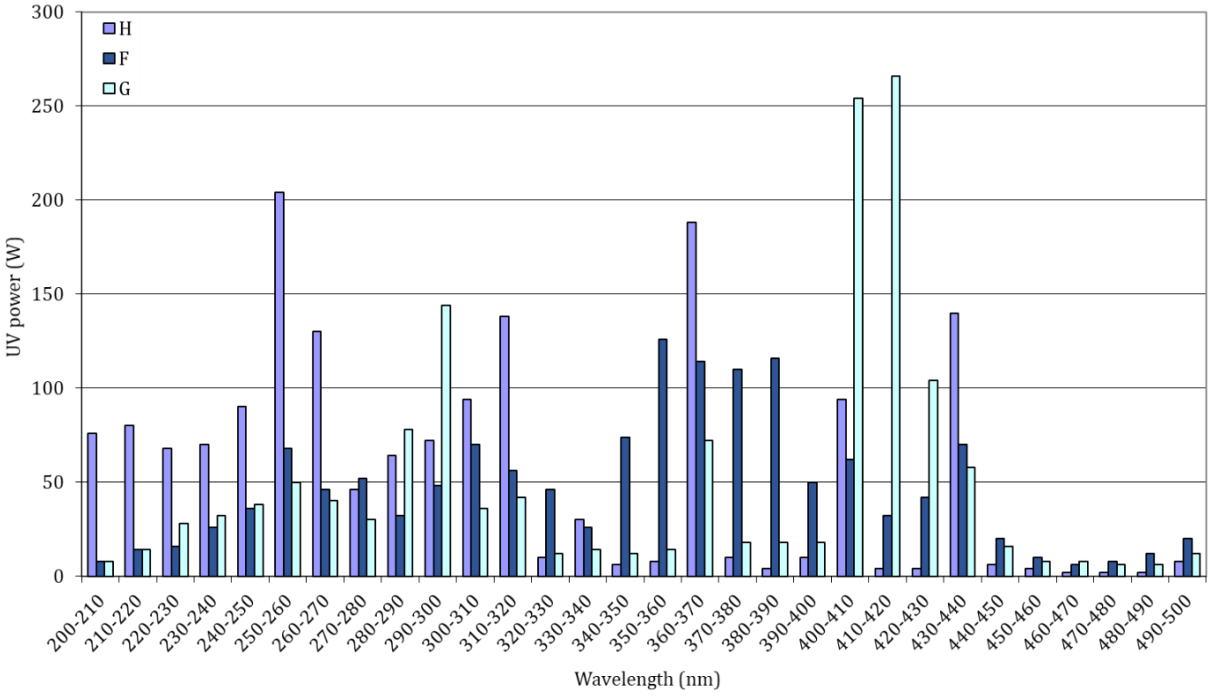

Figure A.2 – Emissivity spectra of the UVA PRINT-LE (Hoenle) UV lamp depending on the doping of the lamp. (Manufacturers data

Appendix 3 – Tuning of the porous material properties: a non-exhaustive survey of the polymerisation operating parameters

One of the aim of this project was to investigate and better control the various operating parameters that have an impact on the polymer microstructure resulting from microemulsion polymerisation. Indeed, to our knowledge – apart from the choice of the initiator [1], [2] – no work has been carried out on the selection of the polymerisation operating parameters prior to the polymerisation of the nanostructured microsystem. Therefore, the following sections will detail in a non-exhaustive way the impact of the operating parameters of the microemulsion polymerisation on the final polymer microstructure.

We will first discuss how the oxygen depletion method can modify the monomer composition prior to polymerisation. Will then investigate the impact of the substrate hydrophilicity on the final polymer microstructure. The influence of the UV the lamp module as well as the photoinitiator used will then be discussed. Finally, the washing step following polymerisation will be discussed and the polymer conversion method evaluated.

This appendix will answer the following questions:

- *How to combine both oxygen depletion and composition preservation?*
- *How will the properties of the substrate impact on the final polymer microstructure?*
- *Why is the washing step crucial when polymerising microemulsified templates?*

3.1 Oxygen elimination prior to polymerisation

In order to eliminate the oxygen of the atmosphere – to increase the polymer conversion – several options can be considered. The most common method used in the literature is working under inert conditions, e.g. under argon or nitrogen atmosphere. We however evidenced that the microemulsion evaporates when exposed to a dry argon gas flux (1.5 ± 0.9 $L.min^{-1}$), leading to a 20% weight loss in less than 10 min for a thin-film of 100 µm. This loss is attributed to the evaporation of MMA – and to a lesser extent water – as presented in Figure A.3.

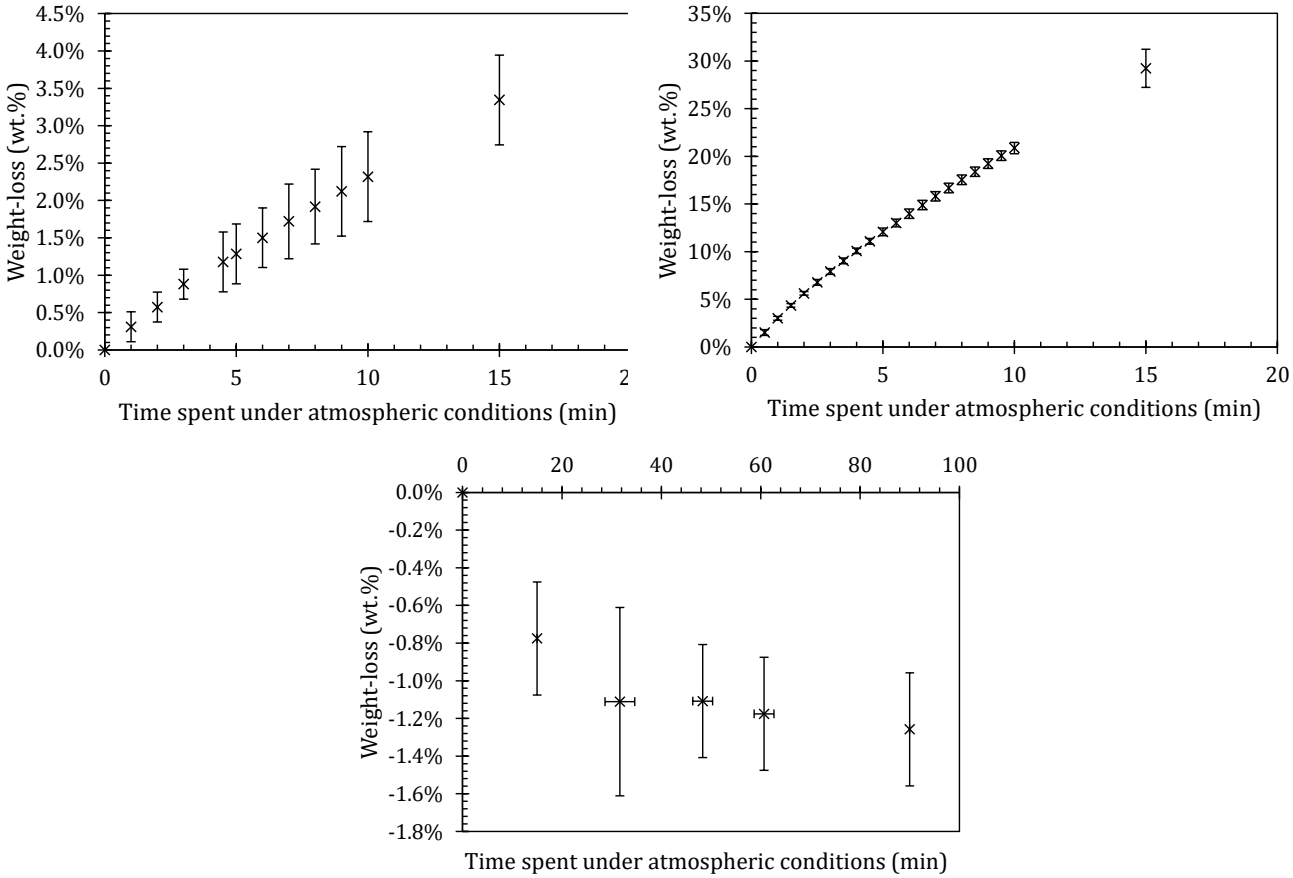

Figure A.3 – Evolution of the liquid weight loss due to the evaporation of the liquid (top-left) water, (top-right) MMA and (bottom) HEMA under atmospheric conditions (T=22.8°C, %RH=20).

Therefore, casting a microemulsion thin-film under inert conditions will result in the partial evaporation of the liquid microemulsion and as a result the modification of its composition. In order to avoid this side-effect, some solutions have been discussed: bubbling of the inert gas into a sacrificial microemulsion solution before its introduction into the inert UV-chamber, utilisation of oxygen scavengers or polymerisation of the microemulsified solution into a closed mould transparent to the UV radiations.

- Saturation of the inert atmosphere

The first solution involves the saturation of the atmosphere with the microemulsion. This approach presents however a severe drawback that is the possibility to polymerise the monomer in suspension in the vapour phase when irradiating the UV-chamber. However, working with the LED lamp allows to avoid the wavelength range where the acrylate will react with the UV-radiation. This solution is therefore viable, but not applicable to our set-up which requires a continuous gas flush and therefore will lead to the continuous depletion of the microemulsion monomers and water and a variation of the saturated gas composition.

- Addition of oxygen scavengers

The second solution consists of the addition of oxygen scavengers into the solution. These species will react preferentially with the oxygen and prevent the premature termination of the polymerisation process. Two oxygen scavengers have been considered in our study: the triethanolamine (TEOA) and the triethylamine (TEA). To determine their respective impact on the polymer conversion, we determined the conversion rate as a function of the oxygen scavenger quantity using ATR-FTIR analyses. The microemulsion was polymerised for 180 s under the Hoenle LED Cube 100 UV. The resulting upper surface of the sample – in contact with the air – was immediately analysed using an ATR-FTIR apparatus.

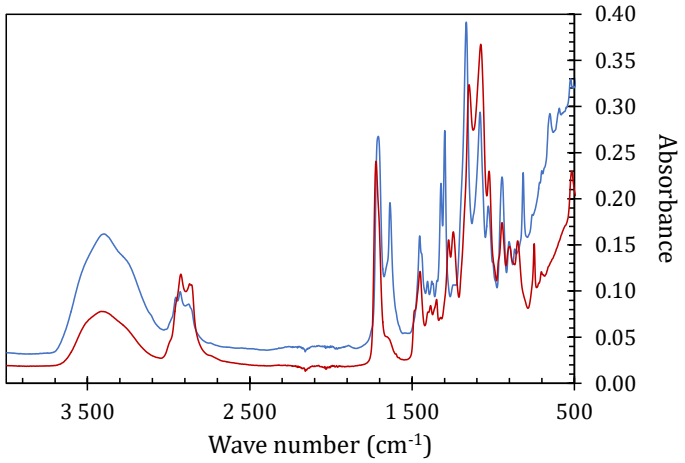

*Figure A.4 – ATR-FTIR spectra of the (21:23:56)$_{62:19:19}$ (**blue**) monomer and (**red**) polymer microemulsion.*

The conversion rate π is determined using the Eq. A.48, using the area $A_{C=C}$ under the characteristic peak of the vinyl bond of the monomers at 817 cm^{-1}, cf. Figure A.4. We must keep in mind that the conversion rate obtained is the maximum conversion rate obtained in the system: the UV penetration will decrease with the microemulsion thickness and so will the polymer conversion.

$$\pi = \frac{h_{C=C}^{t=0} - h_{C=C}^{t}}{h_{C=C}^{t=0}} = \frac{A_{C=C}^{t=0} - A_{C=C}^{t}}{A_{C=C}^{t=0}} \qquad \text{Eq. A.48}$$

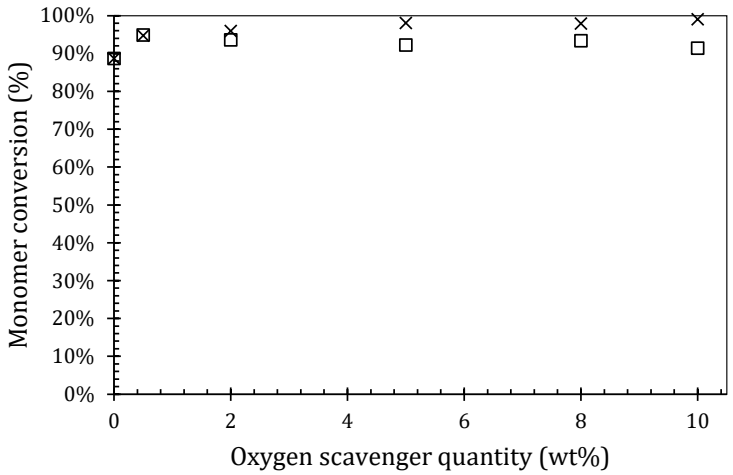

Figure A.5 – Monomer conversion of the microemulsion measured on the upper surface exposed to UV-radiation for 180 s under the Hoenle LED Cube 100 UV as function of the quantity of (×) TEOA and (△) TEA added in solution.

We evidenced that both the TEA and TEOA led to an increase in the conversion rate by ca. 10% as soon as 0.5 wt.% of oxygen scavengers are added, as seen in Figure A.5. The addition of these compound may however destabilise the system and modify the microstructure. Hence, a small amount of the compound must be added to increase the polymerisation process, without significantly impacting the initial microstructure. Both products seem to increase the polymer rate in quite similar ways. However, the TEOA molecules are less sensitive to the temperature, unlike the TEA whose boiling point is 89°C. As seen in the previous section, the temperature of the solution increases greatly during the polymerisation reaction. Therefore, using the TEA might lead to partial evaporation of the scavenger, which is toxic. For safety concerns, the TEOA is more suitable for our application. Plus, this compound is highly soluble in water below 15°C and can therefore be easily removed from the polymer network.

The weight loss of a 100 µm-thick microemulsion thin-film in contact to the atmosphere was then determined by gravimetric analyses, cf. Figure A.6. Considering a UV-polymerisation of 180 s at most, the maximum liquid weight loss would be limited to 3 wt.% at most. This second alternative to an inert atmosphere is therefore feasible, considering an addition of 0.5 wt.% of TEOA.

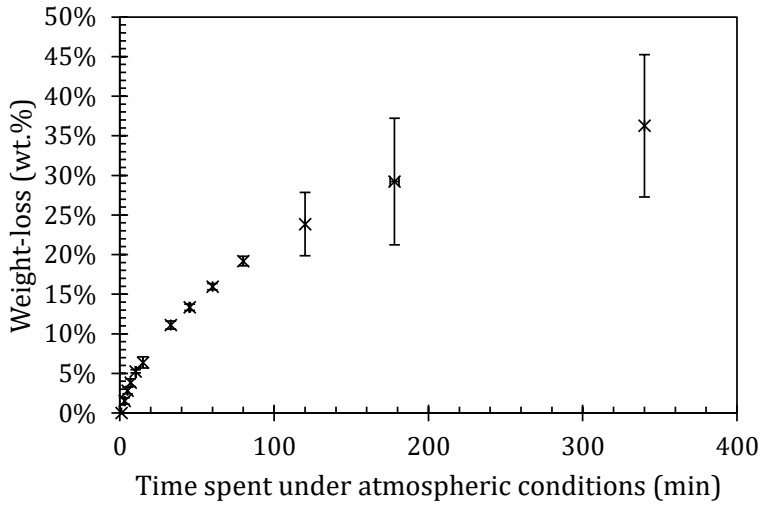

Figure A.6 – Evolution of the weight loss of a 100 µm-thick microemulsion thin-film in contact to the atmospheric environment (non-inert conditions).

We only considered using oxygen scavengers for photopolymerisation reaction. Indeed, these species can act as a reductor in presence of the oxidant compound and start the RedOx initiation and their role as an oxygen scavenger would therefore be affected.

- Utilisation of a UV-transparent mould

The last alternative we discussed is the use of a UV transparent mould as an alternative to the casting knife. Using a mould is an interesting solution as it allows to polymerise the microemulsion into inert conditions, without needing an inert gas chamber. The UV intensity received by the microemulsion might be slightly lower because borosilicate and quartz both interact somewhat with the UV-radiation. The main drawback of this method is the impossibility of adapting this method for the deposition of thin layers without increasing the capillary penetration of the liquid into the substrate pores.

Plus, Chieng's work [3] brings to light a microstructure's gradient depending on the medium surrounding the liquid microemulsion. When in contact with the glass plate, a smaller porosity is observed compared to the bulk polymer. In the same way the microemulsion surface exposed to the inert gas present a more open porosity which can be attributed to the partial evaporation of the liquid solution. Applying a blade to both surfaces would alter the liquid/medium interactions and thus result in different polymer microstructures compared to the previous sections.

3.2 UV-initiation parameters

- Photoinitiator choice

Several photoinitiators have been considered in order to initiate the polymerisation of our system under UV-radiation. Both Norrish type I (i.e. 2,2-dimethoxy-2-phenylacetophenone (DMPA), 2-hydroxy-2-methylpropiophenone (HMP) and Irgacure® 819) and Norrish type II photoinitiators (i.e. benzophenone and 4-hydroxybenzophenone) were diluted into methanol to achieve mass compositions corresponding to the proposed operating values and were analysed using UV-vis spectrometry. The wavelength of the LED lamp is presented as a black dotted line. The UV absorption spectra presented in Figure A.7 were determined using a quartz UV-cuvette. The UV detector saturated when analysing all samples, indicating a strong interaction of the molecules with UV-light in the 200-300 nm range.

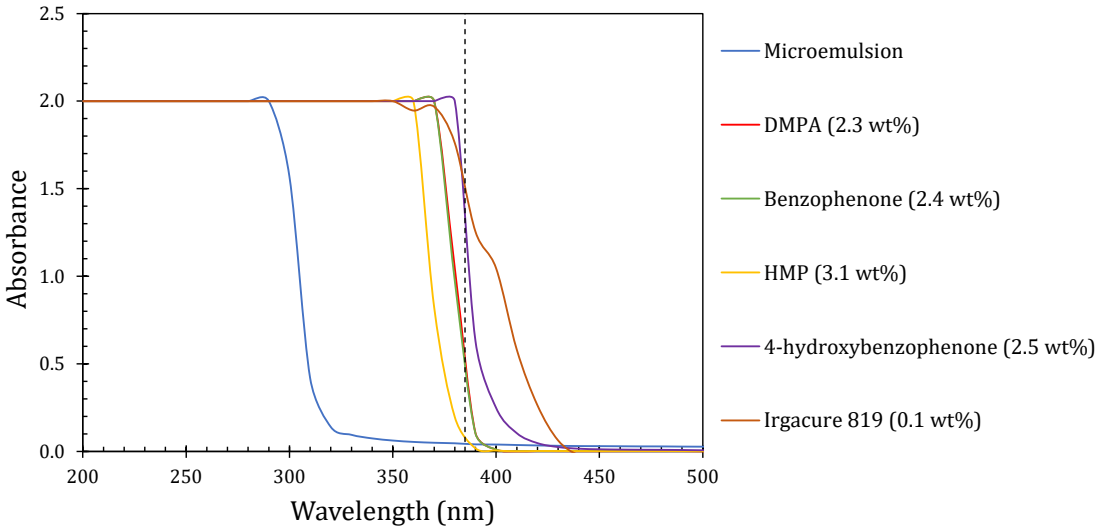

Figure A.7 – UV-absorption spectra of the microemulsion and of various photoinitiators.

Due to the wavelength of the Hoenle UV LED Cube 100 of 385 nm, the HMP is out of range for our application as its absorbance is too low to trigger the initiation step. Both the DMPA and the benzophenone display an absorbance of 0.5 at the LED UV lamp wavelength, while the 4-hydroxybenzophenone and the Irgacure® 819 display an absorbance higher than the unity. These photoinitiators may therefore be suitable for our polymerisation process.

Only the Norrish type I photoinitiators will be now considered as they do not require an extra initiation step, unlike the type II photoinitiators. The photoinitiator choice is thus narrowed to the DMPA ($\lambda_{max} \approx 250$ nm) [7] and the Irgacure® 819 ($\lambda_{max} \approx 290$ nm) [8]. Considering the absorbance of both product at 285 nm as a function of the quantity of product added in solution, one might be tempted to directly choose the Irgacure® 819 to initiate our system. However, we

observed some difficulty to polymerise our system using this photoinitiator. The same behaviour was reported by Galiano [1] and was attributed to the sensitivity of the chemical compound to the non-binding doublets of the oxygen and thus of the inert conditions during the polymerisation. Our experiments revealed that the inert operating conditions available in our laboratory where not sufficient to avoid the compound inhibition.

We therefore decided to work with the DMPA photoinitiator which is not as sensitive to the inert conditions. The quantity of photoinitiator added was chosen based on Galiano's work [1] for a similar acrylate bicontinuous system. Both TQ 150 (Hereaus, Germany) and LED Cube 100 (Hoenle, Germany) UV sources (cf. Appendix 2) can be used to initiate the photopolymerisation in the microemulsion system. However the latter will need the addition of 2 wt.% of DMPA whereas the former can be used without any addition of photoinitiator, as the acrylate compounds will react with the UVC radiation [5], [6]. It should be noted that even if the microemulsion can polymerise spontaneously under the TQ150 irradiation, the addition of DMPA may enhance the reaction, and increase the conversion rate, as reported in Figure A.8.

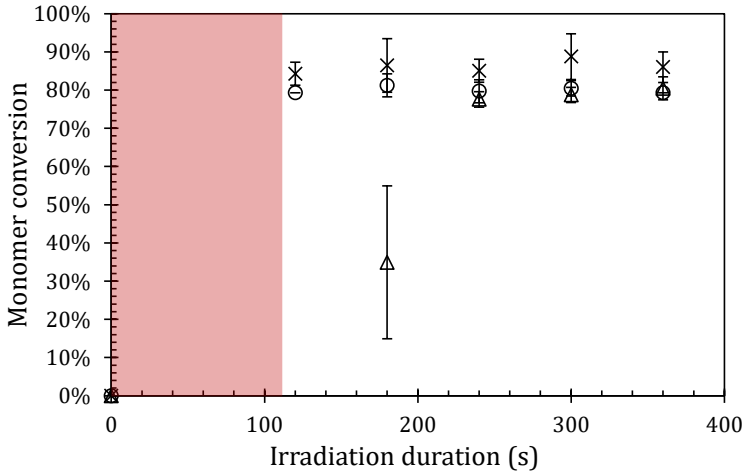

Figure A.8 – Polymer conversion of the (21:23:56)$_{62:19:19}$ microemulsion as a function of the TQ150 UV lamp irradiation duration with (△) 0 wt.%, (○) 0.5 wt.% and (×) 2 wt.% DMPA. Red zone: lamp warming period.

- **Comparison of the TQ150 and the LED UV-lamps**

The polymer networks obtained using the polychromatic mercury high-pressure TQ 150 and the LED Cube 100 UV sources have been compared. The main difference between these two lamps is their poly- or monochromatic feature. The TQ150 lamp emits over a wide range of wavelengths, cf. Appendix 2, while the Hoenle lamp only radiates at a wavelength of 385 nm. If the polychromatic radiations may lead to a quicker initiation, we note that the lamp exhibit a warm-up period of ca. 100 s during which only IR-radiation are emitted that may result in an

increase of the sample's temperature. A temperature increase in the sample may lead to various phenomena such as a variation of structure or the liquid evaporation prior to its polymerisation.

We investigated the top surface (i.e. the surface in direct contact with the UV-radiation) of a microemulsion sample polymerised under both the TQ150 polychromatic and the UV-LED monochromatic lamps, without a top glass surface preventing evaporation. The SEM images of both samples presented in Figure A.9 show that the polymer obtained using the polychromatic lamp exhibits surface defects – i.e. nanometric holes – unlike the sample obtained using the monochromatic lamp. We assume that this behaviour can be due to either an increase of the sample temperature or a different polymerisation kinetics. Thus, the choice of the lamp used during the curing is crucial.

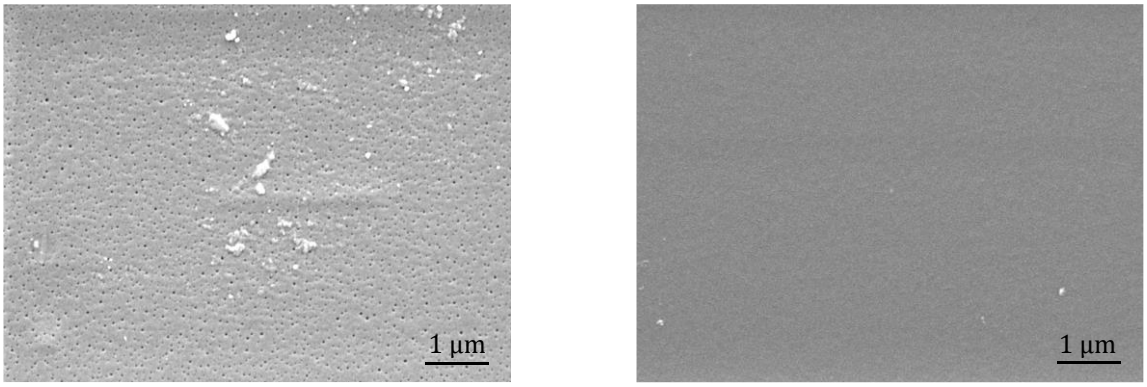

Figure A.9 – SEM images of the upper surface of the microemulsion exposed to air atmosphere, cured (left) under the UV-TQ150 polychromatic lamp and (right) under the UV-LED monochromatic lamp.

3.3 Polymer washing parameters

Most of the articles relating the synthesis of polyacrylate networks based on a microemulsified template report the use of organic solvents – such as toluene, acetone and methanol – to wash the resulting polymer from the unreacted monomers and surfactants. The classical polymer washing process is presented in Figure A.10 below.

It is well known that acetone alters the properties of polymeric membranes and must not be used for their washing. We might therefore wonder if the organic solvents commonly used for the cross-linked polymer network are appropriate for our system. If one of the polymer is damaged due to the exposure to the washing solvent, the investigated complex polymer network might also be affected to some unknown extent.

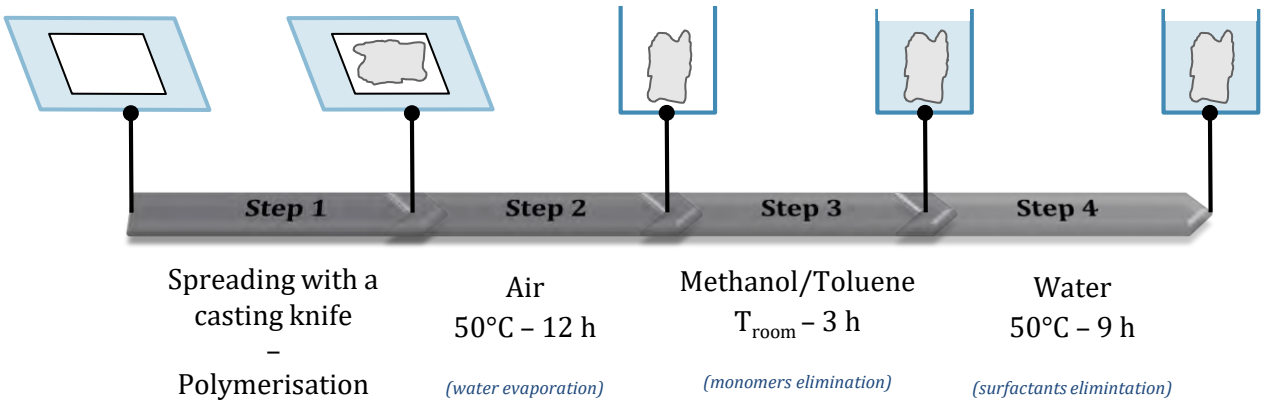

Figure A.10 – Schematic representation of the polymer washing process used as part for the determination of the polymer conversion in the literature.

In order to determine the stability of the homopolymer found in our microemulsified polymer template, we synthesised several PHEMA and PEGDMA thin-films using UV-polymerisation (DMPA: 2wt% – Δt = 180 s) and used commercial PMMA beads to carry out solvent resistance tests. The polymer samples were dried in oven at 30°C one day before being immersed into the organic solvent bath for four hours. Each polymer sample was subjected to the exposure of methanol, ethanol, acetone or water. The resulting polymer are presented in Figure A.11.

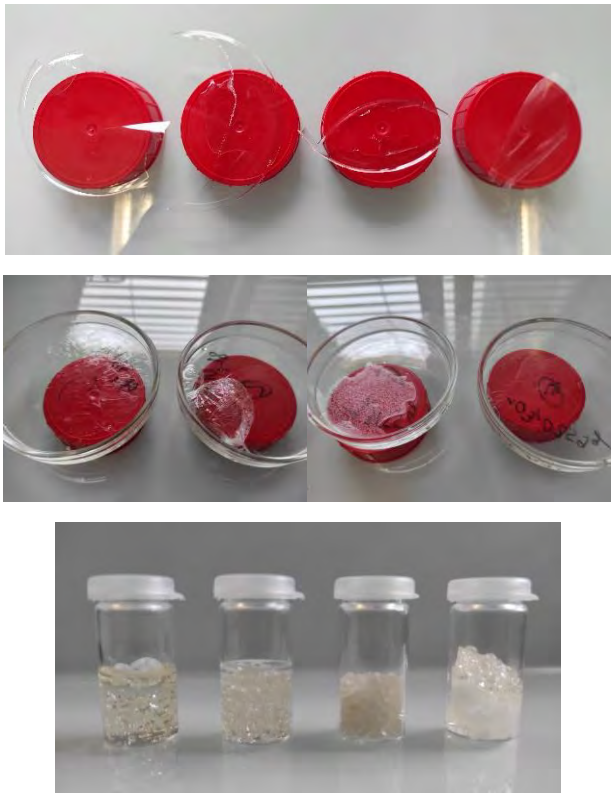

Figure A.11 – (top) PEGDMA, (middle) PHEMA and (bottom) MMA polymer after being immersed for four hours in: (from left to right) ethanol, acetone, water and methanol.

We observe that ethanol, acetone and methanol all deteriorate the PHEMA and PMMA structure. Water is the only solvent to maintain both PHEMA and PMMA polymer integrity. We decided not to test any other solvents, as we expect a similar impact of organic solvent on these quite sensitive homopolymers. PEGDMA however was not affected by any of the investigated solvent, due to its cross-linked structure. We therefore assume that the use of these solvents on the cross-linked polyacrylate system will have no – or little – impact on the microstructure, especially if the organic solvent is diluted and applied for a short period of time.

However, in order to avoid any possible damages on the cross-linked polyacrylate network synthesised, water was chosen as the exclusive washing solvent. This solvent is also cheaper and less toxic than the considered organic solvents. Plus, as we know that MMA evaporates quickly upon heating, we assume that only unpolymerised HEMA, EGDMA and surfactants are to be eliminated from the polymer system. The HEMA being miscible with both EGDMA, water and the surfactants, we can therefore safely conclude that several successive water baths will be sufficient to completely remove the unreacted compounds from the cross-linked polymer network.

Finally, some authors also use a gravimetric method in order to determine the polymer conversion of their system [5], [7], [8]. To do so the polymer is weighed after each step of the washing process presented in Figure A.10, in order to determine the loss unpolymerised material. Note that a drying step is also applied after the organic and water washing. The polymerisation rate is most of the time determined using the third step, based on the assumption that the unreacted monomer will be removed by immersion in an organic solvent bath. We however evidenced that MMA molecules are highly volatile and therefore can be removed during the drying step. One might therefore question the appropriateness of the gravimetric method for the determination of the conversion rate for this type of system. In our work, the ATR-FTIR monitoring was adopted to determine the conversion rate of the monomer system, as reported in the previous sections.

References

[1] F. Galiano, S. A. Schmidt, X. Ye, R. Kumar, R. Mancuso, E. Curcio, B. Gabriele, J. Hoinis, and A. Figoli, “UV-LED induced bicontinuous microemulsions polymerisation for surface modification of commercial membranes – Enhancing the antifouling properties,” *Sep. Purif. Technol.*, vol. 194, pp. 149–160, 2018, doi: 10.1016/j.seppur.2017.10.063.

[2] C. H. Chew, T. D. Li, L. H. Gan, C. H. Quek, and L. M. Gan, "Bicontinuous-nanostructured polymeric materials from microemulsion polymerization," *Langmuir*, vol. 14, no. 21, pp. 6068–6076, 1998, doi: 10.1021/la970990a.

[3] T. H. Chieng, L. M. Gan, C. H. Chew, S. C. Ng, and K. . L. Pey, "Formation of microporous polymeric materials by microemulsion polymerization of methyl methacrylate and 2-hydroxyethyl methacrylate" *J. Appl. Polym. Sci.*, vol. 60, pp. 1561–1568, 1996, doi: https://doi.org/10.1002/(SICI)1097-4628(19960606)60:10<1561::AID-APP6>3.0.CO;2-H.

[4] Y. Makita *et al.*, "Electrochemical investigation of dynamic solution structures of bicontinuous microemulsion at solid interfaces," *Chem. Lett.*, vol. 39, no. 11, pp. 1152–1154, 2010, doi: 10.1246/cl.2010.1152.

[5] M. López Viveros, "Influence des propriétés d'un réseau polymère sur la synthèse in situ de nanoparticules de palladium : application aux membranes catalytiques de grande efficacité en chimie fine" PhD thesis, Université Toulouse 3 Paul Sabatier, 2018.

[6] Y. Gu, "Membranes polymères fonctionnalisées par des poly(liquide ionique)s et des nanoparticules de palladium: applications au captage de CO2 et aux membranes catalytiques," Université Toulouse 3 Paul Sabatier, 2015.

[7] Sigma–Aldrich, "Applications : Free Radical Initiators."

[8] T. E. Bishop, "Multiple Photoinitiators for Improved Performance."

Appendix 4 – Evolution of the microstructure of the acrylate monomer system upon MMA:surfactant phase dilution

In order to further investigate the transparent domains in the (62:19:19) and (33:33:33) system, we studied two MMA:surfactant phase ratio dilution lines in each phase diagram. The total quantity of MMA in these solutions varied from 8 to 33 wt.% depending on the MMA to surfactant phase ratio, as depicted in Figure A.12. To that end, DOSY-NMR and SAXS analyses were performed.

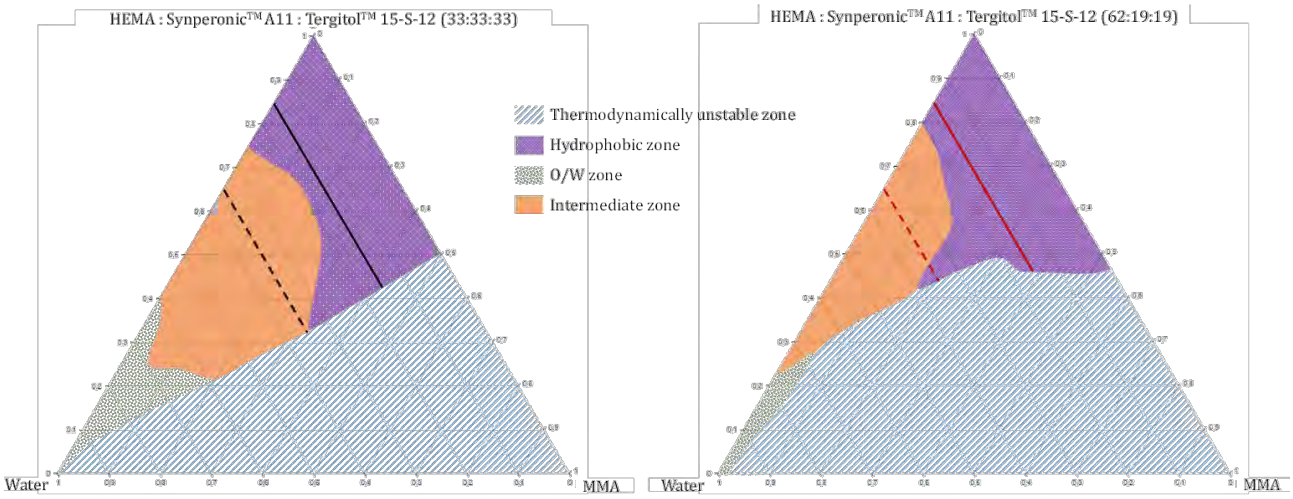

*Figure A.12 – Pseudo-ternary phase diagrams from conductivity measurements and the (plain) (15:85) and (dashed) (35:65) MMA:surfactants dilution lines, in the (**black**) (33:33:33) and (**red**) (62:19:19) acrylate systems.*

- **DOSY-NMR analyses**

The DOSY-NMR analyses of the (15:85) and (35:65) MMA:Surfactant phase dilution lines are presented in Figure A.13 and Figure A.14, for both (62:19:19) and (33:33:33) systems. We first note that the (62:19:19) and (33:33:33) exhibit a similar behaviour on both dilution lines. Along the (15:85) MMA to the surfactant phase dilution line, HEMA, water and MMA exhibit similar values of self-diffusion coefficient in the range of 1E-10 to 7E-10 $m^2.s^{-1}$. We also observe that the MMA, water and HEMA self-diffusion coefficients all increase when the amount MMA in the ratio MMA to the surfactant phase is increased above 25 wt.%. This increase is consistent with the position of this dilution line on the pseudo-ternary diagram: increasing the ratio of MMA implies decreasing the surfactant quantity in the system and therefore approaching the transition to an emulsion structure, where the structures are bigger due to the lower amount surfactant molecules in the system.

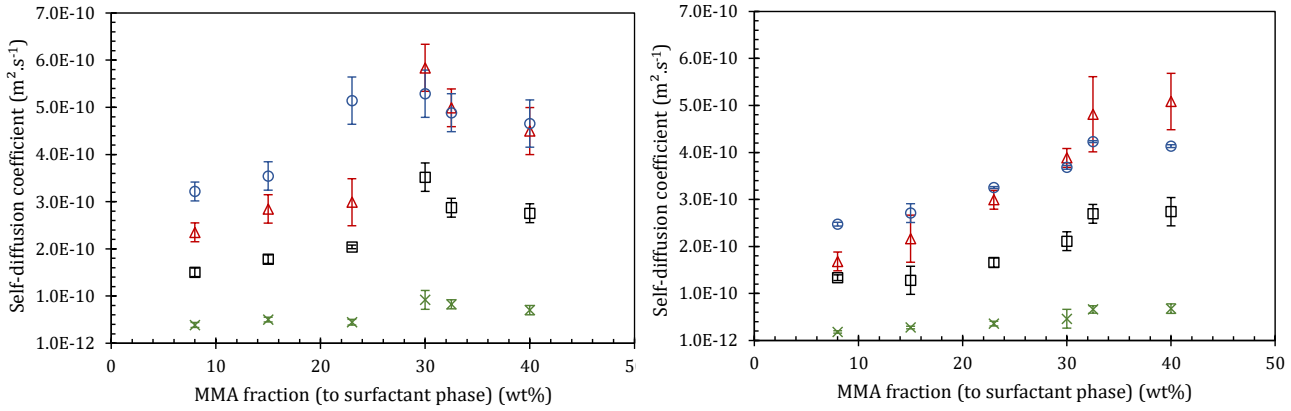

*Figure A.13 – Self-diffusion coefficient of (△) MMA, (□) HEMA, (○) water and (×) non-ionic surfactants at 25°C, along the (15:85) dilution line in the (**left**) (62:19:19) and (**right**) (33:33:33) systems.*

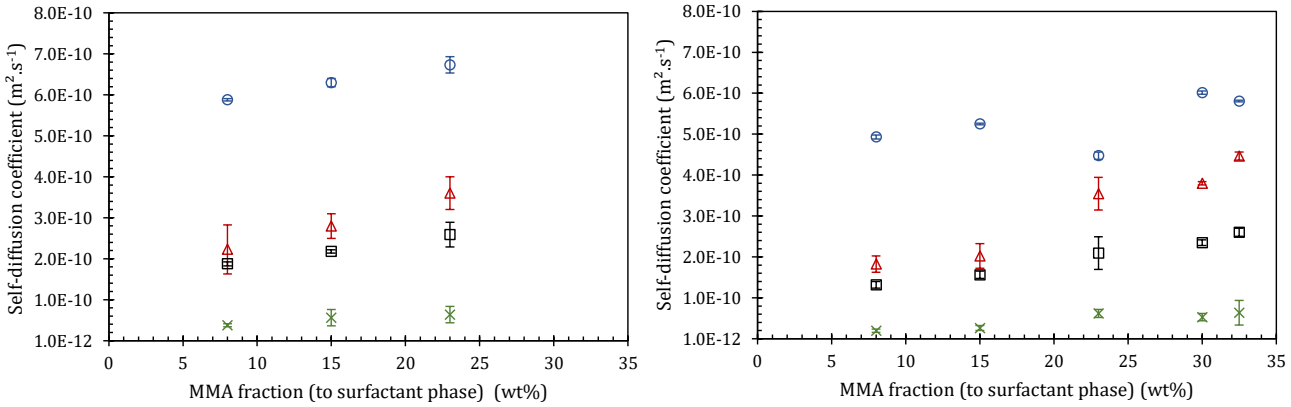

*Figure A.14 – Self-diffusion coefficient of (△) MMA, (□) HEMA, (○) water and (×) non-ionic surfactants at 25°C, along the (35:65) dilution line in the (**left**) (62:19:19) and (**right**) (33:33:33) systems.*

Along the (35:65) MMA to the surfactant phase dilution line, in both systems, water diffusion coefficients lay between 5E-10 and 6E-10 $m^2.s^{-1}$. The self-diffusion coefficients of MMA increase from 2E-10 to 4E-10 $m^2.s^{-1}$ and, while those of HEMA remain stable to about 2E-10 $m^2.s^{-1}$. We then note that the water self-diffusion coefficients are two to five times higher than the coefficients of MMA and HEMA.

One must note that this dilution line is shortened in the (62:19:19) system compared to the one of the (33:33:33) system, due to the smaller transparent and non-birefringent area, cf. Figure A.12. Similarly to the (15:85) dilution line presented in Chapter 3, Section 3.4.2, we observe an increase in the MMA and HEMA self-diffusion coefficients above 25 wt.% MMA in the MMA to the surfactant phase ratio, due to the decrease in the surfactant quantity compared to the hydrophobic phase. We finally note that the self-diffusion coefficients of the non-ionic surfactants remain stable around 10E-11 $m^2.s^{-1}$ in both systems, for both dilution lines considered.

Similarly to the conclusion drawn in Chapter 3, Section 3.4.2.1, none of the self-diffusion determined in these dilution lines are consistent with the occurrence of a continuous phase.

- **SAXS analyses**

The small-angle X-ray scattering curves of the (15:85) and (35:65) MMA:Surfactant phase dilution lines are presented in Figure A.15 and Figure A.16, for both (33:33:33) and (62:19:19) systems. The X-ray source used for these analyses was less powerful than the one presented in Chapter 2 and produced a flow of 18.10^6 ph.mm^2.s^{-1}. Each sample was exposed to the X-ray beam 1200 s at room temperature (23°C). We first note that the scattering curves obtained are quite similar for both surfactant compositions.

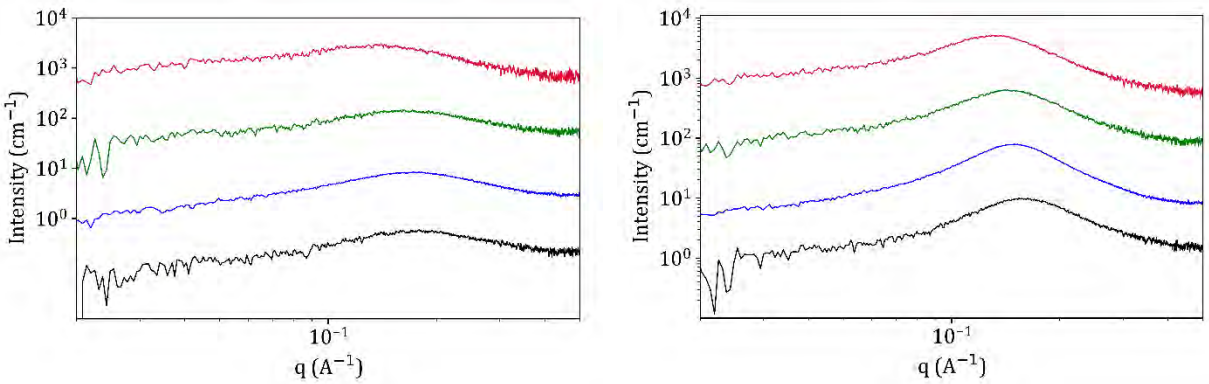

*Figure A.15 – SAXS scattering curves of the (15:85) MMA to the surfactant phase ratio along for the (**left**) (62:19:19) and (**right**) (33:33:33) acrylate systems at 25°C. Legend of the curves: (**black**) (8:92), (**blue**) (15:85), (**green**) (23:77) and (**red**) (32.5:67.5) MMA to surfactant phase ratios.*

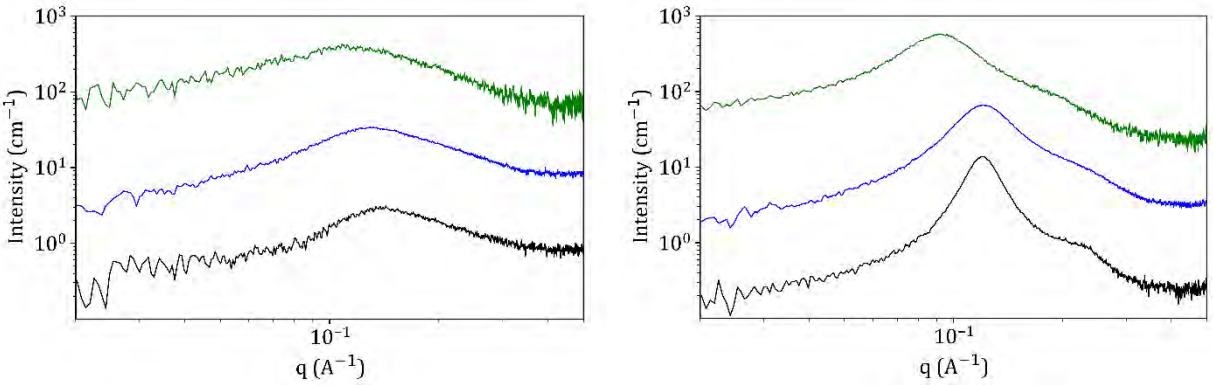

*Figure A.16 – SAXS scattering curves of the (35:65) MMA to the surfactant phase ratio along for the (**left**) (62:19:19) and (**right**) (33:33:33) acrylate systems at 25°C. Legend of the curves: (**black**) (8:92), (**blue**) (15:85) and (**green**) (23:77) MMA to surfactant phase ratios.*

In both systems, along the (15:85) MMA to the surfactant phase dilution line, a single broad peak is observed. In the (62:19:19) system, no peak shift is observed, indicating that the

structure remains quite identical in size when increasing the MMA amount in the MMA to surfactant phase ratio. As for the (33:33:33) system, a slight displacement towards lower scattering vectors can be seen, indicating a slight increase in the structure size. All the scattering curves are quite similar to those for a similar water content in the (15:85) water dilution lines, cf. Chapter 3, Section 3.4.2.2.

As for the (35:65) dilution line, two broad peaks are observed for both systems. These peaks are more or less well-defined as a function of the MMA to the surfactant phase ratio. Once again, all scattering curves are quite similar to those for a similar water content in the (15:85) water dilution lines. We also observe that increasing the ratio of MMA broadens the peaks and decreases its intensity, especially for the (33:33:33) system. This indicates a less stiff interface and a decrease of the long-range order in the system. The peaks also shift towards smaller scattering vectors values, indicating an increase of the size of the structure when decreasing the ratio of surfactant phase to MMA.

Intermediate conclusions:

The DOSY-NMR and SAXS analyses highlight a similar behaviour to the monomer self-assembled system discussed in Chapter 3 as the MMA to surfactant phase ratio was modified. Logically, we observed that an increase of MMA in this ratio leads to an increase of the organic structure size but also did not modify the microstructure of the systems. This behaviour is consistent with the pseudo-ternary phase diagram of the quinary system, as an increase of MMA to the surfactant phase brings the system closer to the emulsion boundary, and thus creates bigger structures.

The results presented in this appendix tend to indicate the occurrence of an identical structure in the transparent non-birefringent domain of each system, for similar water content. The only significant difference we identified when modifying the MMA to surfactant phase ratio is the increase of the organic structure upon decrease of the surfactant quantity and therefore the receding towards the emulsified zone, and thus the micrometric structures.

Appendix 5 – Technical data sheets of hollow-fibre membranes discussed as part of the numerical simulation

3M | MEMBRANA Medical Membranes

3M™ Membrana™ MicroPES™ Capillary Membrane, Type TF10

Chemical Composition	
Polymer	Polyethersulfone

Physical Properties	
Wall thickness	m 100 µm d ± 25 µm
Inner diameter (nominal)	m 300 µm d ± 40 µm
Tensile strength	≥ 50 cN
Elongation at break	≥ 30 %

Membrane Performance Characteristics	
Transmembrane flow (water, 25°C)	≥ 35 ml/[min x cm² x bar]
Maximum pore size (calculated from BP)	m 0.5 µm d ± 0.1 µm
Bubble point (Isopropylalcohol, 23°C)	m 1.22 bar d +0.31/-0.20 bar

Available Make-up Configurations
Single-thread spools Bundles (customer specified) Mats

All specifications are based on 3M internal test procedures and represent average lot performance.

m = mean value
d = deviation of the mean value

Technical Information: The technical information, guidance, and other statements contained in this document or otherwise provided by 3M are based upon records, tests, or experience that 3M believes to be reliable, but the accuracy, completeness, and representative nature of such information is not guaranteed. Such information is intended for people with knowledge and technical skills sufficient to assess and apply their own informed judgment to the information. No license under any 3M or third party intellectual property rights is granted or implied with this information.

Product Use: Many factors beyond 3M's control and uniquely within user's knowledge and control can affect the use and performance of a 3M product in a particular application. Given the variety of factors that can affect the use and performance of a 3M product, user is solely responsible for evaluating the 3M product and determining whether it is fit for a particular purpose and suitable for user's method of application.

Warranty, Limited Remedy, and Disclaimer: Unless a different warranty is specifically stated on the applicable 3M product packaging or product literature, 3M warrants that each 3M product meets the applicable 3M product specification at the time 3M ships the product. 3M MAKES NO OTHER WARRANTIES OR CONDITIONS, EXPRESS OR IMPLIED, INCLUDING, BUT NOT LIMITED TO, ANY IMPLIED WARRANTY OR CONDITION OF MERCHANTABILITY OR FITNESS FOR A PARTICULAR PURPOSE OR ANY IMPLIED WARRANTY OR CONDITION ARISING OUT OF A COURSE OF DEALING, CUSTOM OR USAGE OF TRADE. If the 3M product does not conform to this warranty, then the sole and exclusive remedy is, at 3M's option, replacement of the 3M product or refund of the purchase price.

Limitation of Liability: Except where prohibited by law, 3M will not be liable for any loss or damage arising from the 3M product, whether direct, indirect, special, incidental or consequential (including, but not limited to, lost profits or business opportunity), regardless of the legal theory asserted, including warranty, contract, negligence or strict liability.

3M and Membrana are trademarks of 3M Company. © 2018 3M Company. All rights reserved.

3M
Separation and Purification Sciences Division
13840 South Lakes Drive
Charlotte, North Carolina
28273 USA
Phone: +1 704 587 8888
Fax: +1 704 587 8610

3M Deutschland GmbH
Separation and Purification Sciences Division
Öhder Straße 28
42289 Wuppertal
Germany
Phone: +49 202 6099 – 0
Fax: +49 6099 - 241

MM-1005
Rev. 09/2019
www.3m.com/membrana

Water Technologies & Solutions
fact sheet

ZeeWeed* 500S module

ultrafiltration membrane module

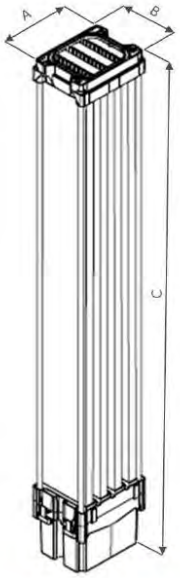

module dimensions

Product	Depth A mm (in)	Width B mm (in)	Height C mm (in)
ZW500S	277 (10.9)	217 (8.5)	1780.3 (70.1)

module weight and membrane properties

Nominal Surface Area m^2 (ft^2)	Maximum Shipping Weight[1] kg (lb)	Max. Lifting Weight[2] kg (lb)	Membrane Material	Nominal Pore Size (µm)	Surface Properties	Fiber Diameter (mm)	Flow Path
27.9 (300)	22 (49)	58 (128)	PVDF	0.04	Non-ionic & hydrophilic	OD: 1.9 (0.07) ID: 0.8 (0.03)	Outside In

[1] Packaged; [2] Varies with solids accumulation

operating & cleaning specifications

Application	TMP Range kPa (psig)	Max. Operating Temp. °C (°F)	Operating pH Range	Max. Cleaning Temp. °C (°F)	Cleaning H Range	Max. Cl_2 Concentration
MBR	– 55 to 55 (– 8 to 8)	40 (104)	5.0 to 9.5	40 (104)	2.0 to 10.5 (<30°C) 2.0 to 10.0 (30-40 °C)	1000 ppm
Non-MBR	– 90 to 90 (– 13 to 13)					

Find a contact near you by visiting www.suezwatertechnologies.com and clicking on "Contact Us."

*Trademark of SUEZ; may be registered in one or more countries.
©2018 SUEZ. All rights reserved.

FSmbrZW500S_Module_EN.docx Sep-18